UNIVERSITAT POLITÈCNICA DE VALÈNCIA

Departamento de Ingeniería Electrónica

Sound Scattering by Lattices of Heated Wires.

Por Mitko Ivanov Angelov

Dirigida por

Francisco Cervera Moreno

y

José Sánchez-Dehesa Moreno-Cid

Enero 2016

Agradecimientos

En primer lugar me gustaría agradecer a mis directores de tesis, profesor Francisco Cervera y profesor José Sánchez-Dehesa, todo el esfuerzo, paciencia, confianza y dedicación que han invertido en enseñarme, guiarme por el camino de investigación y ayudarme en el desarrollo de la tesis doctoral. Sin ellos este trabajo no habría sido posible.

También doy gracias a mis compañeros del grupo Dani, Andreas, Ellios, Victor, Alfonso, Jorge y Roge por la ayuda que me prestaron en cada momento que la necesité y también por los buenos momentos que hemos pasado juntos. No pueden faltar los agradecimientos a Abel y Hector por sus consejos y charlas sobre los problemas que habían surgido durante el desarrollo de la tesis. Tampoco puedo olvidar la gran ayuda de Lourdes en los momentos más decisivos.

A nivel personal, quiero agradecer a mi familia todo el apoyo durante mi carrera académica.

Difracción de sonido por redes de hilos calientes

de

Mitko Ivanov Angelov

Doctor por la Universitat Politècnica de València,

Valencia, Enero 2016

El objetivo de este trabajo es demostrar teoréticamente y experimentalmente como la propagación de ondas acústicas puede ser controlada por gradientes de temperatura. Empezando con el caso más simple de dos hilos calientes en aire, el estudio se extiende sobre estructuras periódicas conocidas como cristales sónicos (CS). Se ha utilizado el Método de Elementos Finitos (FEM) para realizar simulaciones numéricas con el objetivo de demonstrar la colimación y focalización de ondas acústicas en CS bidimensionales (2D) cuya fracción de llenado es ajustable mediante gradientes de temperatura.

Como parte de la investigación se ha analizado la reflexión de Bragg y el efecto de tipo Fabry-Perot asociados con los CSs estudiados. Entre los ejemplos tratados figuran un CS con una transmitancia ajustable a voluntad, dentro de ciertos límites. También se han estudiado lentes acústicas bidimensionales de gradiente de índice, basadas en gradiente de temperatura. Utilizando cortinas paralelas de hilos calientes cuya temperatura varía según una ley dada se puede diseñar una lente GRIN con propiedades determinadas. Por otra parte, cambiando la temperatura de los hilos se puede lograr un cambio en la fracción de llenado dentro del GRIN CS. Así, el índice de refracción local, que está directamente relacionado con la fracción de llenado, se cambia también y se obtiene una variación de gradiente de índice dentro del GRIN CS. Este GRIN CS es una analogía directa de medios con gradiente, observados en la naturaleza. Como sus analogías ópticas, las lentes, estudiadas en este trabajo, tienen las superficies planas y son más fáciles de fabricar que las lentes curvadas. La deflexión de las ondas acústicas obtenida mediante una lente de gradiente GRIN se puede utilizar para focalizar o colimar haces de sonido.

Otro aspecto de este trabajo trata sobre el ajuste de algunas propiedades de un SC como el índice de refracción efectivo o la densidad efectiva con el objetivo de obtener unas propiedades deseadas del cristal. Como el ajuste activo de los bandgaps fonónicos es ciertamente deseado para futuras aplicaciones con funcionalidades mejoradas, hasta ahora se han hecho varios intentos de desarrollar CSs de características ajustables. Hay una gran necesidad de un método más práctico desarrollado para un ajuste activo de las propiedades de CSs. Controlando el ángulo de incidencia o la frecuencia de funcionamiento, un GRIN CS puede ajustar dinámicamente la curvatura de la trayectoria de propagación dentro de la estructura CS para demonstrar el efecto "espejismo acústico" en la escala de longitud de onda pero es muy difícil modificar la fracción de llenado. Entre los últimos estudios de CSs las fracciones de llenado se ajustaron mediante una deformación física directa de la estructura o mediante estímulos externos (por ejemplo campos eléctricos o magnéticos). El primero es poco práctico para una gran parte de las aplicaciones y el segundo a menudo requiere estímulos muy fuertes para ajustes modestos. En este trabajo se propone otra forma de ajustar las propiedades de un CS. Las propiedades acústicas del medio de propagación (densidad, índice de refracción) dependen de la temperatura, por tanto, introduciendo gradientes de temperatura dentro de dicho medio pueden ajustarse a voluntad las propiedades del CS dentro de ciertos límites. La manera de

obtener gradientes de temperatura dentro del CS, propuesta en este estudio, es mediante hilos de nicrom calentados con corrientes eléctricas. Hay algunas ventajas importantes de este método. En primer lugar, cambiando la intensidad de corriente eléctrica que circula por los hilos se puede conseguir cambiar dinámicamente las propiedades del CS. En segundo lugar, es relativamente más fácil de cambiar la fracción de llenado simplemente ajustando la intensidad de la corriente eléctrica que modificar físicamente la estructura o aplicar fuertes campos eléctricos o magnéticos.

En conclusión, el método propuesto en esta tesis permite, en principio, conseguir materiales y estructuras con propiedades acústicas ajustables dinámicamente mediante el control de la temperatura a través de la corriente eléctrica en los hilos, dentro de ciertos límites. De esta forma se puede experimentar fácilmente a escala macroscópica fenómenos de propagación de ondas análogos a los que ocurren en estructuras microscópicas para la propagación de ondas electromagnéticas de alta frecuencia (microondas y luz).

Todo este trabajo se enmarca en el contexto de la investigación básica y amplia nuestras capacidades para el estudio y mejor comprensión de la propagación de ondas en metamateriales y estructuras complejas y nos capacita para poder aplicar dichos conocimientos al diseño de dispositivos de focalización de energía acústica para usos médicos y ensayo no destructivo de materiales, así como para problemas de aislamiento y control de ruido, como por ejemplo el "cloaking" acústico.

RESUM DE LA TESI DOCTORAL

Difracció de so per xarxes de fils calents

de

Mitko Ivanov Angelov

Doctor per la Universitat Politècnica de València,

Valencia, Gener 2016

L'objectiu d'este treball és demostrar teorèticament i experimentalment com la propagació d'ones acústiques pot ser controlada per gradients de temperatura. Començant amb el cas més simple de dos fils calents en aire, l'estudi s'estén sobre estructures periòdiques conegudes com a cristalls sónics (CS) . S'ha utilitzat el Mètode d'Elements Finits (FEM) per a realitzar simulacions numèriques amb l'objectiu de demonstrar la col·limació i focalització d'ones acústiques en CS bidimensionals (2D) la fracció de omplit de la qual és ajustable per mitjà de gradients de temperatura.

Com a part de la investigació s'ha analitzat la reflexió de Bragg i l'efecte de tipus Fabry-Perot associats amb els CSs estudiats. Entre els exemples tractats figuren un CS amb una transmitancia ajustable a voluntat, dins de certs límits. També s'han estudiat lents acústiques bidimensionals de gradient d'índex, basades en gradient de temperatura. Utilitzant cortines paral·leles de fils calents la temperatura de la qual varia segons una llei donada es pot dissenyar una lent GRIN amb propietats determinades. D'altra banda, canviant la temperatura dels fils es pot aconseguir un canvi en la fracció d'ompliment dins del GRIN CS. Així, l'índex de refracció local, que està directament relacionat amb la fracció d'ompliment, es canvia també i s'obté una variació de gradient d'índex dins del GRIN CS. Este GRIN CS és una analogia directa de mitjans amb gradient, observats en la naturalesa. Com les seues analogies òptiques, les lents, estudiades en este treball, tenen les superfícies planes i són més fàcils de fabricar que les lents corbades. La deflexión de les ones acústiques obtinguda per mitjà d'una lent de gradient GRIN es pot utilitzar per a focalitzar o colimar feixos de so.

Un altre aspecte d'este treball tracta sobre l'ajust d'algunes propietats d'un SC com l'índex de refracció efectiu o la densitat efectiva amb l'objectiu d'obtindre unes propietats desitjades del cristall. Com l'ajust actiu dels bandgaps fonónicos és certament desitjat per a futures aplicacions amb funcionalitats millorades, fins ara s'han fet diversos intents de desenrotllar CSs de característiques ajustables. Hi ha una gran necessitat d'un mètode més pràctic desenrotllat per a un ajust actiu de les propietats de CSs. Controlant l'angle d'incidència o la freqüència de funcionament, un GRIN CS pot ajustar dinàmicament la curvatura de la trajectòria de propagació dins de l'estructura CS per a demonstrar l'efecte "mirall acústic" en l'escala de longitud d'ona però és molt difícil modificar la fracció d'ompliment. Entre els últims estudis de CSs les fraccions d'ompliment es van ajustar per mitjà d'una deformació física directa de l'estructura o per mitjà d'estímuls externs (per exemple camps elèctrics o magnètics) . El primer és poc pràctic per a una gran part de les aplicacions i el segon sovint requerix estímuls molt forts per a ajustos modestos. En este treball es proposa una altra forma d'ajustar les propietats d'un CS. Les propietats acústiques del mig de propagació (densitat, índex de refracció) depenen de la temperatura, per tant, introduint gradients de temperatura dins del

dit mitjà poden ajustar-se a voluntat les propietats del CS dins de certs límits. La manera d'obtindre gradients de temperatura dins del CS, proposta en este estudi, és per mitjà de fils de Nicrom calfats amb corrents elèctrics. Hi ha alguns avantatges importants d'este mètode. En primer lloc, canviant la intensitat de corrent elèctric que circula pels fils es pot aconseguir canviar dinàmicament les propietats del CS. En segon lloc, és relativament més fàcil de canviar la fracció d'ompliment simplement ajustant la intensitat del corrent elèctric que modificar físicament l'estructura o aplicar forts camps elèctrics o magnètics.

En conclusió, el mètode proposat en esta tesi permet, en principi, aconseguir materials i estructures amb propietats acústiques ajustables dinàmicament per mitjà del control de la temperatura a través del corrent elèctric en els fils, dins de certs límits. D'esta manera es pot experimentar fàcilment a escala macroscòpica fenòmens de propagació d'ones anàlegs a què ocorren en estructures microscòpiques per a la propagació d'ones electromagnètiques d'alta freqüència (microones i llum) .

Tot este treball s'emmarca en el context de la investigació bàsica i àmplia les nostres capacitats per a l'estudi i millor comprensió de la propagació d'ones en metamateriales i estructures complexes i ens capacita per a poder aplicar els dits coneixements al disseny de dispositius de focalització d'energia acústica per a usos mèdics i assaig no destructiu de materials, així com per a problemes d'aïllament i control de soroll, com per exemple el "cloaking" acústic.

ABSTRACT OF THE DOCTOR THESIS

Sound scattering by lattices of heated wires

by

Mitko Ivanov Angelov

Doctor by The Universitat Politècnica de València,

Valencia, January 2016

The aim of this work is to demonstrate theoretically and experimentally how acoustic wave propagation can be controlled by temperature gradients. Starting with the simplest case of two hot wires in air the study extends over periodic structures known as Sonic Crystals (SCs). The Finite Elements Method (FEM) has been employed to perform numerical simulations in order to demonstrate collimation and focusing effect of acoustic waves in two-dimensional (2D) SC whose filling fraction is adjusted by temperature gradients.

As a part of the research, Bragg reflection and Fabry-Perot type of acoustic effects are investigated for the proposed type of SC. As example, a SC with desired transmittance can be tailored. Also, gradient index (GRIN) 2D sonic lenses are studied. Using parallel rows of heated wires whose temperatures vary according to a prefixed gradient index law a GRIN lens can be designed with a given performance. Moreover, by changing the temperature of the wires a change in the filling fraction inside the GRIN SC can be achieved. Thus, the local refraction index, which is directly related to the filling fraction, is changed too and an index gradient variation inside the GRIN SC is obtained. This GRIN SC is a direct analogy of gradient media observed in nature. Like their optical counterparts, the investigated 2D GRIN SC lenses have flat surfaces and are easier for fabrication than curved SC lenses. The bending of sound waves obtained by GRIN acoustics structures can be used to focusing and collimating acoustic waves.

Another aspect of this work is about tuning some SC properties as effective refractive index, effective mass density, etc. in order to obtain a SC with prefixed properties. Since active tuning of the phononic band gaps is certainly desirable for future applications with enhanced functionalities, few attempts have been made to develop tunable SCs thus far. There is a strong need in developing a more practical method to actively tune the SC properties. By controlling the incident angle or operating frequency, a GRIN SC can dynamically adjust the curved trajectory of acoustic wave propagation inside the SC structure to demonstrate the “acoustic mirage” effect on the wavelength scale but it is quite difficult to model the filling fraction. Among the last studies of tunable SCs, the filling fractions were tuned either by direct physical deformation of the structure or external stimuli

(e.g. electric or magnetic fields). The former is impractical for most applications and the latter often requires very strong stimuli to produce only modest adjustment. In this work another way to tune the SC properties is proposed. Hot and cold media have different density, speed of sound, refractive index, etc. in comparison with the same properties at normal conditions, so inserting temperature gradients inside the medium can be used to tune the SC properties in certain limits. The proposed way to obtain temperature gradients inside SC is by wires made of Nicrom which are heated by electrical currents. There are some important advantages of this method. First, changing the electrical current intensity through the wires the SC properties can be changed dynamically. Second, it is relatively easier to change the filling fraction simply by adjusting the current intensity than physically changing the structure or applying strong electric or magnetic fields.

In conclusion, the method proposed in this thesis allows us, in principle, to get materials and structures with dynamically adjustable acoustic properties using the temperature control through electric current in the wires, within certain limits. Thus, it is easy to carry out experiments of wave propagation phenomena in a macroscopic scale similar to those that occur in microscopic structures for the propagation of electromagnetic waves of high frequency (microwaves and light).

This work can be considered in the context of basic investigation and it increases our capabilities to study and better understand the propagation of waves in Metamaterials and complex structures and enables us to apply such knowledge to design devices for focusing of acoustic energy for medical applications and non-destructive testing of materials, as well as problems of isolation and control of noise, as for example the acoustic cloaking.

Contents

Outline of the PhD manuscript and Methodological strategy

The manuscript is divided in three main parts. They cover the main topics of the thesis: Focusing effect of two hot wires, Sonic crystals made of heated wires and Gradient-Index sonic crystals.

I. **Focusing effect of two hot wires**: In this first part of the thesis a focusing effect resulting from the scattering of ultrasounds by glass tubes, considered as multilayered scatterers is investigated. The model is based on the theory of multiple scattering in multilayered scatterers. An appropriate experimental set-up has been developed in order to demonstrate experimentally the focusing effect of multilayered scatterers. The control of airborne sound propagation has great potential for some applications where large concentration of acoustic pressure is needed, such as fine ultrasonic cleaning, nondestructive material testing and etc.

II. **Sonic crystals made of heated wires**: Here a SC based on heated wires is described. This part is divided to theoretical modeling and experimental part. The theoretical model of the proposed SC is built using FEM based simulations including natural convection, thermal conduction and acoustic wave propagation. Some properties of thus formed SC, like reflectance and transmittance, are investigated theoretically. Next, an adapted to the investigated physical phenomena experimental set-up is prepared. A map of the standing wave in front of the SC is made. From the obtained data the reflection coefficients are calculated.

III. **Gradient-Index sonic crystals**: A 2D model of GRIN lens with hyperbolic secant profile of refractive index is proposed. The conventional rigid scatterers are replaced with heated wires that change the local refractive index. In addition, the temperature of the wires can be dynamically adjusted and this can be an important step to dynamically tuning of sonic crystals.

Furthermore, FEM based simulations of the bending wave inside the crystal are performed. It is demonstrated that the wave inside the crystal can be focused. The position of the focus is previously analytically calculated and it is in very good agreement with the FEM simulation.

Finally, some fundamental theoretical concepts about Acoustics, Theory of multilayered scatterer, Heat transfer, and Finite Element Method are treated in the appendices A, B, C and D, resp.

Methodological strategy

1. Solving the thermal natural convection of a hot wire and obtaining the radial distribution of the temperature of the air surrounding the wire. COMSOL Multiphysics, which is a package of scientific software based on finite element method (FEM) is used for this purpose.

2. Study using COMSOL Multiphysics of the propagation of waves in a two-dimensional periodic array of hot wires, i.e., the study of wave propagation in a medium where scatterers are made of hot air cylinders whose radial distribution of temperature has been obtained in step 1 and from which the radial distribution of density and propagation speed can be calculated.

3. Construction of a SC consisting of a slab of wires of nichrome of 0.2 mm. in diameter and 30 cm. in length each, distributed periodically. This slab measures 26 x 28 x 36 cm. and is made up of 12 layers of 10 wires each separated by a distance of 22 mm.

4. Installation of voltage regulators to supply each one of the layers of the SC, in order to be able to set the electric current and therefore the working temperature.

5. Construction of a horn attached to the tweeter in order to achieve a collimated beam with a width adapted to the slab dimensions.

6. Construction of a positioning system for the microphone, controlled by computer using LabView environment.

7. Development of a program under the LabView environment that coordinates the positioning of the microphone, the signal generation and the measurement of the sound. The instrumentation for the generation of the excitation signal as well as the measurement of the signal captured by the microphone is based on National Instruments PXIe work station, equipped with a computer under Windows XP, a signal generation card and another 16-bit precision data acquisition card.

Part I
Focusing Effect of Two Hot Wires

Introduction

I.1 Temperature gradient as a natural phenomenon

Bending of light waves by changes in the refraction index of air is an effect encountered in the natural phenomenon of *mirage* – a visual illusion of the sky reflected on a distant land surface in a hot day. The origin of mirage is the existence of a temperature gradient in the air. Usually the atmosphere has a vertical gradient of about -1ºC per 100 meters of altitude. The value is negative because it gets colder as altitude increases. For a mirage to happen the temperature gradient must be much greater than that – it can be perceived at 2ºC per meter and get stronger at more than 5ºC per meter. These conditions do occur when there is strong heating at ground level or when the sun has been shining a long time on sand or asphalt. Because of that an inferior mirage (i.e. the mirage is formed bellow the true position of the real object) can be observed in the desert or on the highway. As a rule the real object is the sky or any distant object in that direction. Warm air is less dense than cool air and the variation between the hot air at the surface of the road and the denser cool air above creates a gradient in the refractive index of the air. Light from the sky at a shallow angle to the road is refracted by the index gradient making it appear as if the sky is reflected by the surface of road. The result looks to the human mind like a pool of water on the road, since water also reflects the sky.

If there are several temperature layers, several mirages may mix together, perhaps causing double images. In any case, mirages are usually not larger than about half a degree high and from objects only a few kilometers away.

Temperature also causes changes in the refraction index of sound waves. Some sonic phenomena associated with temperature gradient on the Earth's surface and in the ocean have been reported [Woo41]. In acoustics it is not easy to tailor the refractive index of acoustic materials like in optics using optical materials. However, gradient index acoustic lenses have been proposed by using acoustic metamaterials [Tor07]. Also, it has been predicted that heated wires could be used to focus

airborne sound and produce a microlenses array [Cai07]. The high temperature changes radially the air

properties (mass density, speed of sound, refractive index, etc) near the wires and several layers of different properties are created. In this case, the so called multilayer scatterer is formed. Therefore, sound guiding and focusing are controlled by temperature gradient around the wires. Hence, the temperature can be used as a means to control the propagation of airborne sound.

I.2 Some applications of multilayer scatterer

Interests in the effects of the interface between the fiber and the matrix in a fiber-reinforced composite material have a long history in the research efforts in composite materials [Cai04a]. In these efforts, a fiber is often modeled as a layered circular elastic cylinder, with the outer layer representing the intermediate material phase that is introduced physically or chemically between the fiber and the matrix [Bog94, Yim95a]. Such a model is also suitable for analyzing a fiber that naturally possesses a layered structure, such as a silicon-carbide (SiC) fiber.

A micromechanical model for composites uses the scattering by a single fiber as the basis to analyze problems concerning multiple fibers. A single layered scatterer subjected to a plane-strain wave, often referred to as P/SV wave (longitudinal wave, also referred to as vertically polarized shear wave in the context of seismic waves) has been studied [Yim95b, Bog93, Sin93]. For the case of antiplane shear wave, often referred to as SH wave (horizontally polarized wave in the context of seismic waves), only a multilayer model has been considered [Mal94, Shi96]. Later, an exact solution for dual-layer cylindrical scatterer for multiple scattering of elastic waves in fiber-reinforced composite materials has been proposed [Cai99].

The applications of such a dual-layer cylindrical model are not limited to modeling composites. At a larger scale, such a model can be modified to analyze cylindrical shell structures found in many civil engineering applications such as underground pipeline and cable systems, in which the SH wave case has been of major concern from an earthquake engineering perspective. Furthermore, since the equation that governs elastic SH waves and acoustic waves is the same, extending such a model to the field of acoustics is straightforward.

I.3 Objectives

In this first part of the thesis we shall investigate a focusing effect resulting from the scattering of ultrasounds by glass tubes, considered as multilayered scatterers. The model is based on the theory of multiple scattering in multilayered scatterers [Cai04a, Cai04b, Cai05, Cai07]. An appropriate experimental set-up has been developed in order to demonstrate experimentally the focusing effect of multilayered scatterers. The control of airborne sound propagation has great potential for some applications where large concentration of acoustic pressure is needed, such as fine ultrasonic cleaning, nondestructive material testing and etc.

Chapter 1
A brief introduction to acoustics

Sound is a small perturbation (p, ρ) of a steady state (p_0, ρ_0) of a compressible ideal fluid, where p and ρ are the pressure and the density of the fluid, respectively. At any arbitrary point **x** of the fluid the functions $P(\boldsymbol{x}, t)$ and $\rho(\boldsymbol{x}, t)$ represent oscillations with small amplitude. These oscillations interact in such a way that energy propagates through the medium. An oscillatory motion can be excited by a change from an equilibrium state of a mass particle, by acting on it with a certain force. An oscillating mass particle always forms a system with the surrounding medium in which the particles are bound together by elastic bonds. An oscillation or a wave motion of the elastic medium is caused by a displacement and an oscillatory motion of a particle group which act on their neighboring particles through elastic bonds. The disturbance propagates in the medium as a wave motion with a certain velocity which depends on the physical properties of the medium.

The governing equations are obtained from fundamental laws of compressible fluids in appendix A.

1.1 Acoustic Wave Equation

Sound waves in a lossless medium are governed by the following equation for the acoustic pressure p [Mor86]:

$$\frac{1}{\rho_0 c^2}\frac{\partial^2}{\partial t^2} + \nabla \cdot \left(-\frac{1}{\rho_0}(\nabla p - \boldsymbol{q}) \right) = \boldsymbol{Q} \qquad (1.1.\ 1)$$

Here ρ refers to the density, $\boldsymbol{q}$ and $\boldsymbol{Q}$ are the dipole and monopole sources, resp., and c denotes the speed of sound. The product $\rho_0 c^2$ is called adiabatic bulk modulus, commonly denoted K.

An important special case is a time-harmonic wave, for which the pressure varies with time as:

$$p(\boldsymbol{x}, t) = p(\boldsymbol{x}, t)e^{i\omega t} \qquad (1.1.\ 2)$$

where $\omega = 2\pi f$ is the angular frequency, with f denoting the frequency. Assuming the same harmonic time dependence for the source terms, the wave equation for acoustic waves reduces to an inhomogeneous Helmholtz equation:

$$\nabla \cdot \left(-\frac{1}{\rho_0} (\nabla p - \boldsymbol{q}) \right) - \frac{\omega^2}{\rho_0 c^2} = \boldsymbol{Q} \qquad (1.1.\ 3)$$

In the absence of monopole and dipole sources, for spatially varying density $\rho = \rho(r)$ and speed of sound $c = c(r)$ the wave equation can be formulated in the time-harmonic case as

$$\nabla \cdot \left(-\frac{1}{\rho_0} \nabla p \right) - \frac{k^2}{\rho_0} = 0 \qquad (1.1.\ 4)$$

where $k = \omega / c(r)$ is the wave vector.

1.2 Ultrasound in Real and Ideal Gases

Normally, the human ear distinguishes sounds with frequency between 20 Hz and 20 kHz. Sound waves with frequencies higher than the upper limit of human hearing are called ultrasounds. Ultrasound devices operate with frequencies from 20 kHz up to several gigahertz.

In an ideal gas the velocity of ultrasound propagation is often expressed as [Coc96]:

$$c = \sqrt{\chi \frac{p_a}{\rho}}, \qquad (1.2.\ 1)$$

where $\chi = c_p/c_v$ is the ratio of specific heats at constant pressure and constant volume (Poisson's constant), p_a is total atmospheric pressure and ρ is the density of the gas. The propagation velocity can also be expressed by adiabatic and isothermal coefficients of compressibility, β_{ad} and β_{is}, and Poisson's constantχ:

$$c = \sqrt{\frac{1}{\beta_{ad}\rho}} = \sqrt{\chi \frac{1}{\beta_{is}\rho}} \qquad (1.2.\ 2)$$

where $\chi = \beta_{is}/\beta_{ad} = c_p/c_v$.

For many purposes the air can be considered an ideal gas.

Any change in some real gas that affects the actual particle velocity has some influence on the speed of sound in the gas. These changes usually are temperature, density (which is proportional to the pressure) or any other alteration of the medium of propagation.

The increasing of temperature leads to an increase of the velocity of the particles in the medium. Hence, the speed of sound increases. In practice the following formulas for sound speed in air and mass density of air are used [Cai07]:

$$c = 331.3 \sqrt{1 + \frac{T}{273.15}} \qquad (1.2.\ 3)$$

$$\rho = \frac{p}{R(T+273.15)} \qquad (1.2.\ 4)$$

where T is the temperature in ºC, p is the atmospheric pressure, which is 101.325 kPa at 0ºC, and R= 287.05 J/(kgK) is a gas constant.

Another possibility of alteration of the medium of propagation is the humidity of air. With increasing humidity the propagation velocity increases approximately linearly. For example, at the level of humidity of 50% the velocity increases by 1%, at 100% by 2%.

1.3 Reflection and transmission of acoustic waves

In this paragraph we follow the theory explained in [Kin00] and [Rec00]. When an acoustic wave traveling in some medium encounters the boundary of another medium, reflection and refraction effects occur. Let the incident and reflected waves travel in a fluid of characteristic acoustic impedance $r_1=\rho_1 c_1$, where ρ_1 is the equilibrium density of the fluid and c_1 is the speed of sound in the fluid (fig.1.3.1). Let us assume that the transmitted wave travels in a fluid of characteristic acoustic impedance $r_2=\rho_2 c_2$. If the complex pressure amplitude of the incident wave is p_i, the reflected wave p_r, and the transmitted wave p_t, then we can define the pressure transmission and reflection coefficients:

$$T = \frac{p_t}{p_i}, \tag{1.3.1}$$

$$R = \frac{p_r}{p_i}. \tag{1.3.2}$$

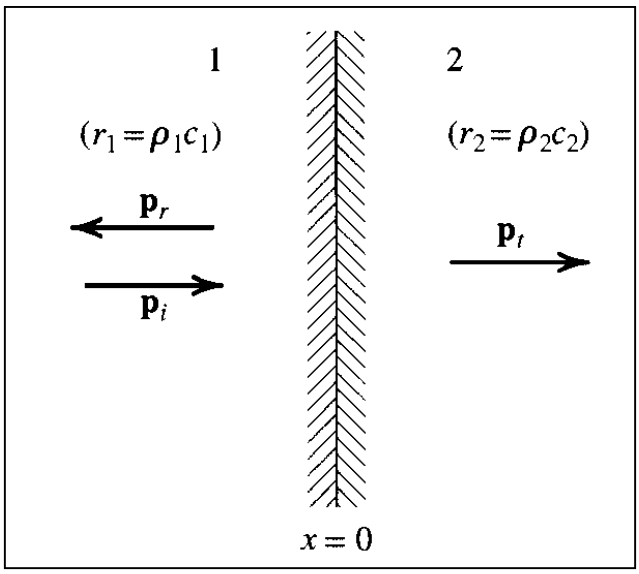

Figure 1.3.1 Reflection and transmission of a plane wave normally incident on a planar boundary between fluids with different characteristic impedances.

The mathematical derivation of the formulas of reflection and transmission is obtained in appendix A. Here we only present the final result. The intensity reflection and transmission coefficients are:

$$R_I = \left(\frac{r_2 - r_1}{r_2 + r_1}\right)^2 = \left(\frac{r_2/r_1 - 1}{r_2/r_1 + 1}\right)^2, \tag{1.3.3}$$

$$T_i = \frac{4r_2r_1}{(r_1+r_2)^2} = \frac{4r_2/r_1}{(r_2/r_1+1)^2}\,. \qquad (1.3.4)$$

If the speed of sound in air at normal conditions is simply *c*, then the ratio

$$n_1 = \frac{c}{c_1} \qquad (1.3.5)$$

is so called refractive index of medium 1. In the same way refractive index n_2 can be defined for medium 2.

1.4 Transmission Through a Fluid Layer: Normal Incidence

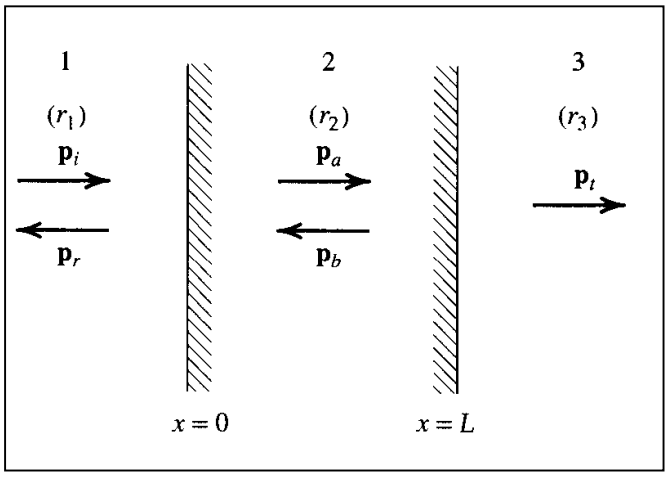

Figure 1.4.1 Reflection and transmission of a plane wave normally incident on a layer of uniform thickness.

Assume that a plane fluid layer of uniform thickness L lies between two dissimilar fluids and that a plane wave is normally incident on its boundary (fig.1.4.1). Let us assume that the characteristic impedances of the fluids are r_1, r_2 and r_3, respectively.

When an incident signal in fluid 1 arrives at the boundary between fluids 1 and 2, some of the energy is reflected and some transmitted into the second fluid. The portion of transmitted wave will proceed through fluid 2 to interact with the boundary between fluids 2 and 3, where again some of the energy is reflected and some transmitted. The reflected wave travels back to the boundary between fluids 2 and 1, and the whole process is repeated. If the duration of the incident signal is less than $2L/c_2$, an observer in either fluid 1 or 3 will see a series of echoes separated in time by $2L/c_2$ whose amplitudes can be calculated by applying the results of the previous section the appropriate number of times. Otherwise, if the incident wave train has a monofrequency carrier and has duration much greater than $2L/c_2$, it can be assumed that:

$$P_i = p_i e^{i(\omega t - k_1 x)}. \qquad (1.4.1)$$

The various transmitted and reflected waves now combine so that in the steady state the wave reflected back into fluid 1 is:

$$P_r = p_r e^{i(\omega t + k_1 x)} \qquad (1.4.2)$$

The transmitted and reflected waves in fluid 2 are

$$P_a = Ae^{i(\omega t - k_2 x)} \tag{1.4.3}$$

$$P_b = Be^{i(\omega t + k_2 x)} \tag{1.4.4}$$

and the wave transmitted into fluid 3 is

$$P_t = P_t e^{i(\omega t - k_3 x)} \tag{1.4.5}$$

Continuity of the normal specific acoustic impedance at $x=0$ and at $x = L$ gives:

$$\frac{p_i+p_r}{p_i-p_r} = \frac{r_2}{r_1}\frac{A+B}{A-B}, \quad \frac{Ae^{-ik_2L}+Be^{ik_2L}}{Ae^{-ik_2L}-Be^{ik_2L}} = \frac{r_3}{r_2}. \tag{1.4.6}$$

Some algebraic manipulations yield to:

$$R = \frac{(1-r_1/r_3)cosk_2L+i(r_2/r_3-r_1/r_2)sink_2L}{(1+r_1/r_3)cosk_2L+i(r_2/r_3+r_1/r_2)sink_2L} \tag{1.4.7}$$

For the particular case when $r_1=r_3$, it can be obtained after substitution $\eta=r_2/r_1$:

$$\boxed{R = \frac{i\left(\eta-\frac{1}{\eta}\right)}{2ctgk_2L+i\left(\eta+\frac{1}{\eta}\right)}.} \tag{1.4.8}$$

The intensity transmission coefficient is found by using (1.3.1) - (1.3.2), (A.3.1) - (A.3.5) from the Appendix A and noting that $A_t=A_i$:

$$T_I = \frac{4}{2+(r_3/r_1+r_1/r_3)cos^2k_2L+(r_2^2/r_1r_3+r_1r_3/r_2^2)sin^2k_2L}. \tag{1.4.9}$$

1.5 Bragg Condition

Now let consider a medium consisting of alternate layers of high and low refractive indices of $n_0+\Delta n$ and $n_0-\Delta n$ of equal thickness d [Gha09]. Such a medium is called a periodic medium and the spatial period of the refractive index variation is given by

$$\Lambda = 2d. \tag{1.5. 1}$$

Now if $\Delta n << n_0$, and if the thickness of each layer is chosen to be

$$d = \frac{\lambda}{4n_0} \approx \frac{\lambda}{4(n_0+\Delta n)} \approx \frac{\lambda}{4(n_0-\Delta n)}, \tag{1.5. 2}$$

then the reflections arising out of individual reflections from the various interfaces should result in a strong reflection. Thus for strong reflection at a chosen wavelength λ_B, the period of the refractive index variation should be:

$$\Lambda = 2d = \frac{\lambda_B}{2n_0}. \tag{1.5. 3}$$

This is referred to as the Bragg condition and is very similar to the Bragg diffraction of X-rays from various atomic layers [Kit56]. Equation (1.5.3) corresponds to the Bragg condition for normal incidence. The quantity λ_B is often referred to as the Bragg wavelength.

Chapter 2

Fundamentals of the Heat Transfer Theory

Generally speaking, there are three types of heat transfer processes – conduction, convection and radiation. Heat conduction is the process of molecular heat transfer by microparticles (molecules, atoms, ions, etc.) in a medium with a non-uniform temperature distribution. Convection is the process of heat transfer by displacing of microelements of a medium (molar volumes). Finally, the radiation is process of heat transfer from one object to another by electromagnetic waves. In our physical model of hot wire only the thermal conduction and free convection will be considered. Also, only the laminar part of the convection movements will be taken in account.

A detailed deduction of the governing laws and formulas is presented in Appendix C

2.1 The heat equation

The fundamental law governing all heat transfer is the first law of thermodynamics, commonly referred to as the principle of conservation of energy. However, internal energy, *U*, is a rather inconvenient quantity to measure and use in simulations. Therefore, the basic law is usually rewritten in terms of temperature, *T*. For a fluid, the resulting heat equation is [Bei93]:

$$\rho C_p \left(\frac{\partial T}{\partial t} + (\boldsymbol{u} \cdot \nabla) T\right) = -(\nabla \cdot \boldsymbol{q}) + \tau : S - \frac{T}{\rho}\frac{\partial \rho}{\partial T}\Big|_p \left(\frac{\partial p}{\partial t} + (\boldsymbol{u} \cdot \nabla) p\right) + Q \qquad (2.1.1)$$

where

- ρ is the density (kg/m3)
- *Cp* is the specific heat capacity at constant pressure (J/(kg·K))
- *T* is absolute temperature (K)
- **u** is the velocity vector (m/s)
- **q** is the heat flux by conduction (W/m2)
- *p* is pressure (Pa)
- τ is the viscous stress tensor (Pa)
- **S** is the strain rate tensor (1/s):

$$S = \frac{1}{2}(\nabla \boldsymbol{u} + (\nabla \boldsymbol{u})^T)$$

• Q contains heat sources other than viscous heating (W/m3)

In deriving Equation (2.1.1), a number of thermodynamic relations have been used. The equation also assumes that mass is always conserved, which means that density and velocity must be related through:

$$\frac{\partial \rho}{\partial t} + \nabla \cdot (\rho \boldsymbol{v}) = 0 \qquad (2.1.2)$$

The Fourier's law of conduction states that the conductive heat flux, **q**, is proportional to the temperature gradient:

$$q_i = -k\frac{\partial T}{\partial x_i} \qquad (2.1.3)$$

where k is the thermal conductivity (W/(m·K)). In some cases, the thermal conductivity (2.1.2) can be different in different directions. Then k becomes a tensor and the conductive heat flux is given by:

$$q_i = -\sum_j k_{ij}\frac{\partial T}{\partial x_j} \qquad (2.1.4)$$

The second term on the right of equation (2.1.1) represents viscous heating of a fluid. The operation ":" is a contraction and can be written in this case on the following form:

$$a{:}\,b = \sum_n \sum_m a_{nm} b_{nm}$$

The third term represents pressure work and is responsible for the heating of a fluid under adiabatic compression and for some thermo-acoustic effects.

Inserting equation (2.1.3) into (2.1.1), reordering the terms and ignoring viscous heating and pressure work puts the heat equation on a more familiar form for two-dimensional steady state case of conductive and convective heat transfer:

$$\rho C_p \boldsymbol{u} \cdot \nabla T + \nabla \cdot (-k\nabla T) = Q \qquad (2.1.5)$$

A strict derivation of the heat transfer equations is presented in appendix C.

2.2 Boundary conditions

The heat equation accepts two basic types of boundary conditions: specified temperature and specified heat flux. The former is of Dirichlet type and prescribes the temperature at a boundary

$$T = T_0, \qquad (2.2.1)$$

while the latter is of Newmann type and specifies the inward heat flux

$$-\boldsymbol{n} \cdot \boldsymbol{q} = q_0 \qquad (2.2.2)$$

where:

•**q** is the total heat flux vector (W/m2),

$$\boldsymbol{q} = -k\nabla T + \rho C_p \boldsymbol{u} T$$

- **n** is the normal vector of the boundary,
- q_0 is inward heat flux (W/m2), normal to the boundary.

When convective heat transfer occurs, the heat flux boundary condition is a mixed, or Robin type, boundary condition rather than a pure Neumann boundary condition.

The special case $q_0 = 0$ is called thermal insulation. Another special case is $q_0 = -\rho C_p \mathbf{u} T$, or equivalently, $-n \cdot (-k\nabla T) = 0$, which is known as convective flux. This is usually the appropriate condition on an outflow boundary in a model with convection. If the velocities are zero, thermal insulation and convective flux are equivalent conditions.

In this work, depending on the model, we will use all of the types of boundary conditions mentioned above.

Chapter 3

Focusing of Ultrasonic Waves by an Array of Hot Wires

In this chapter we consider the focusing effect resulting from the scattering of ultrasounds by a grid of electrically heated wires. To do this we need to model the temperature gradient around the heated wire where the air properties change as a function of the temperature.

A basic tool for heat conduction analysis is so called heat equation:

$$\frac{\partial}{\partial \mathrm{x}}\left(\mathrm{k}\frac{\partial \mathrm{T}}{\partial \mathrm{x}}\right)+\frac{\partial}{\partial \mathrm{y}}\left(\mathrm{k}\frac{\partial \mathrm{T}}{\partial \mathrm{y}}\right)+\frac{\partial}{\partial \mathrm{z}}\left(\mathrm{k}\frac{\partial \mathrm{T}}{\partial \mathrm{z}}\right)+\dot{\mathrm{q}}=\ \rho \mathrm{c_p}\frac{\partial \mathrm{T}}{\partial \mathrm{t}}$$

It is derived in details in Appendix C. From its solution we can obtain the temperature distribution *T(x, y, z)* in some medium as a function of time. It describes an important physical condition, that is, conservation of energy.

The heat equation (C.1.13 in Appendix C) can be solved in several techniques. It can be satisfied for [Car59]:

$$T(t)=\frac{Q}{8(\pi k t)^{\frac{3}{2}}}e^{-\{(x-x')^2+(y-y')^2+(z-z')^2\}/4kt} \qquad (3.\ 1)$$

where T is the temperature rise, t is the time, Q is the strength of the heat source and k is the thermal conductivity. When $t\rightarrow 0$ this expression tends to zero at all points except (x', y', z'), where it becomes infinite.

Also the total quantity of heat in the infinite region is

$$\int_{-\infty}^{\infty}\int_{-\infty}^{\infty}\int_{-\infty}^{\infty}\rho cT\,dxdydz=\frac{Q\rho c}{8(\pi k t)^{\frac{3}{2}}}\int_{-\infty}^{\infty}e^{-(x-x')^2/4kt}dx\int_{-\infty}^{\infty}e^{-(y-y')^2/4kt}dy\int_{-\infty}^{\infty}e^{-(z-z')^2/4kt}dz=Q\rho c \qquad (3.\ 2)$$

Thus, the solution (3.1) may be interpreted as the temperature in an infinite region due to a quantity of heat $Q\rho c$ instantaneously generated at t=0 at a point (x', y', z').

Now we search a solution for instantaneous line source of heat. We consider a distribution of instantaneous point sources of strength Qdz' at t=0, parallel to the z-axis and passing through the point (x', y'), at z' along the line. The temperature is obtained by integrating (3.1) and it is

$$T(t) = \frac{Q}{8(\pi k t)^{\frac{3}{2}}} \int_{-\infty}^{\infty} dz' e^{-\{(x-x')^2+(y-y')^2+(z-z')^2\}/4kt} = \frac{Q}{4\pi k t} e^{-\{(x-x')^2+(y-y')^2\}/4kt} \quad (3.3)$$

For the case of a continuous line source we assume that heat is liberated at the rate $\rho c \phi(t)$ per unit time per unit length of a line parallel to the z-axis and through the point (x', y'). If the heat supply starts at t=0 the temperature at time t is, using (3.2):

$$\frac{1}{4\pi k} \int_0^t \phi(t') e^{-r^2/4k(t-t')} \frac{dt'}{t-t'} \quad (3.4)$$

where $r^2 = (x-x')^2 + (y-y')^2$.

If $\phi(t)$ = Q (Q = constant) this becomes:

$$T(t) = \frac{Q}{4\pi k} \int_{r^2/4kt}^{\infty} \frac{e^{-u} du}{u} = -\frac{Q}{4\pi k} Ei(-\frac{r^2}{4\alpha t}) \quad (3.5)$$

where $-Ei(-x) = \int_x^{\infty} \frac{e^{-u} du}{u}$ is the exponential integral function.

This solution is very important since it gives the temperature in an infinite region which is heated by a line source; that is by an ideal thin wire carrying electric current.

First, let us consider the case of a single heated wire. Assume that the temperature in the air surrounding the heated wire is similar to that due to an ideal line heat source, which gives (in accordance with (3.5)):

$$T(r,t) = -\frac{Q}{4\pi k_{th}} E_i\left(-\frac{r^2}{4\alpha t}\right), \quad (3.6)$$

where T is the temperature rise, *r* is the distance from the wire, *t* is the time, k_{th} and α are the thermal conductivity and thermal diffusivity on the air, respectively and Q represents the strength on the heat source. This temperature distribution neglects al possible effects on ambient airflow that might be caused by the temperature rise. Let's make the follow substitution:

$$F_0 = \frac{4\alpha t}{a^2}, \quad (3.7)$$

where a is a length parameter, which in this case is the radius of the wire. F_0 is so called Fourier number that has a meaning of dimensionless time. Also, let's denote $T_0=Q/(4\pi k_{th})$ and $\bar{r} = r/a$, then the expression for the temperature distribution is [Car59]:

$$T(r,t) = T_0 E_1 \frac{\bar{r}^2}{F_0}, \qquad (3.8)$$

where E_1 is alternative but more common form of exponential integral function defined as $E_1(x) = -Ei(-x)$.

The scattering of ultrasonic wave from hot wire is treated by using the method of multiple scattering in a single scatterer described in Appendix B. In his model the heated wire and portion of surrounding air are considered as the scatterer. The scatterer has a rigid core (the wire) surrounded by a cylindrical shell of air with radially varying properties. This scatterer is approximated as multiple layers of concentric uniform thin shells. The multilayer structure is constructed as follows. The outer edge of the multilayer structure is the concentric zone where the sound speed exceeds 1% of the sound velocity in the environment. A new layer toward the core is located at the next position where the speed of sound varies with another 1%. Each layer is assumed to be uniform, having the values of sound speed and mass density at its edge in its continuous profile.

The solution follows the multiple scattering processes in the layered scatterer, hence it is formally applicable for all types of waves and adapting that solution for acoustic wave is straightforward. The recursive process is as follows. In the first step, the innermost two layers are considered as the core and intermediate layer, and the second layer from the core is considered as the host. In the next step, the core and the intermediate layer are treated as a composite new core and one more layer is added to form another dual-layer scatterer. This process is repeated until all the layers are included.

The amplitude of the acoustic pressure due to a planar incident wave is shown in Figure 3.1 for two selected Fo numbers, as well as the unheated wire, at normalized frequency ka = 4, where k is the wavenumber. The white circles delineate boundary of the scatterer and outline of the wire.

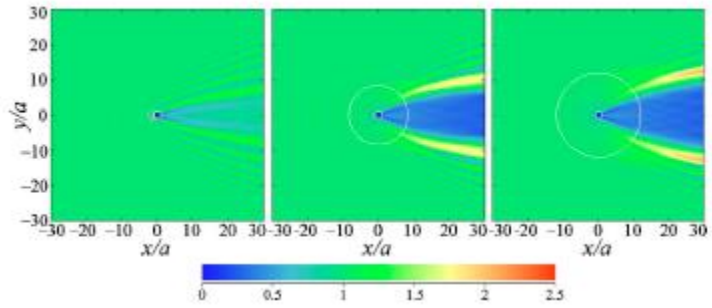

Figure 3.1. Amplitude of acoustic pressure due to a planar incident wave travelling in X direction scattered by a heated wire. Left: cold wire (Fo=0). Center: Fo=50. Right: F0=100

The heated wire splits the impinging wave into two strong beams on either side of the wire, creating a large shadow zone.

Let's consider now arrays of wires arranged along a straight line to form an evenly spaced grid. The model assumes that the temperature fields due to the individual wires do not interfere with each other. For that reason the wires are 20*a* apart. Multiple scattering of a planar incident wave by such a grid is analyzed [Cai99]. The amplitude of acoustic pressure distributions due to the impingement of planar ultrasonic wave normally onto the grid at two selected Fo numbers are shown in (Figure 3.2). It can be seen a series of narrow regions where the ultrasonic wave is focused. These elongated focused regions are located in the forward direction along the lines bisecting the line segment that connects the centers of two adjacent wires. Similar patterns are observed for a range of computed frequencies up to *ka*=10. The distance of these focused regions from the grid of wires decreases when the temperature increases, but it does not change noticeably as the frequency varies. As the frequency increases, the focused regions become narrower and have higher Intensity. The pressure amplitude can reach 3 or 4 times of that of incident. In essence, the heated wire grid behaves like an array of microlenses with tight focusing spots and a great "field of depth".

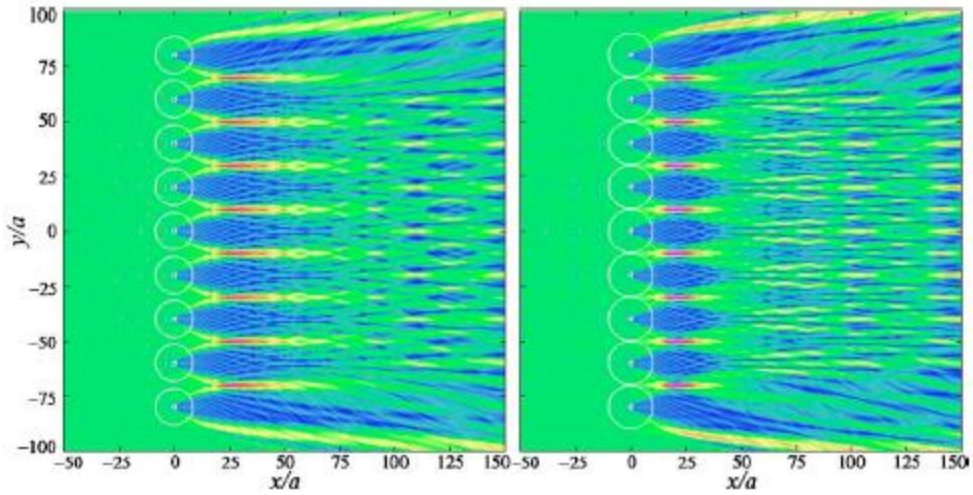

Figure 3.2. Amplitude of acoustic pressure due to a planar incident wave propagating in X direction scattered by a grid of heated wires. Left: Fo = 50. Right: Fo = 100.

The focused regions have been also analyzed. Figure 3.3 shows the cross sections of one of the focused regions near the center for a series of frequencies from *ka*=1 up to 10. The figure on the top shows the cross-section parallel to the *x* axis, defined by the line segment $x/a \in (0,50)$ and y/a=10. It can be observed that the peaks of the focus regions are located in the neighborhood of $x/a \approx 30$, and is essentially unchanged within the computed frequency range. The cross section parallel to the y axis is located at $x/a \approx 30$ and $y/a \in (0,20)$. At low frequencies such as *ka*=1, the focusing effect is not strong. However, as the frequency increases beyond *ka*=2, the focusing regions became narrower and shorter and the peak value increases as the energy is focused onto a smaller area.

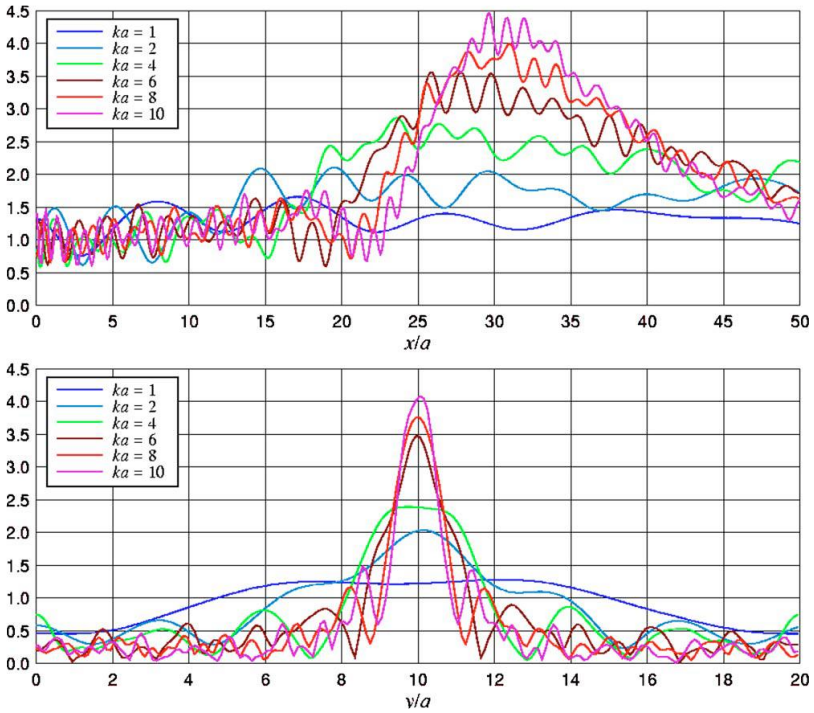

Figure 3.3 Cross-section of a focus region for the case F_0=50. Top: cross-section cut parallel to the x axis at y/a=10. Bottom: cross-section cut parallel to the y-axis at x/a=30.

In the next chapter the focusing effect theoretically predicted above will be demonstrated experimentally.

Chapter 4

Experimental Confirmation of the Focusing Effect Produced by Heated Wires

In this chapter we describe the experimental setup employed to demonstrate the focusing effect predicted previous chapter. Glass tubes with radius 5mm are used as cores of the multilayer scatterers and this radius is our length parameter *a* in equation (3.7). Inside the tube a nichrome wire connected to electrical current provides high temperature. The maximum temperature inside the tube, which is approximately 400 °C, has been determined by using a Varioscan 3021ST infrared camera. At the surface the temperature of the tube is about 300ºC.

It is shown that a couple of heated wires separated by an appropriate distance produce a focal spot for the impinging ultrasound waves.

4.1 Temperature Measurements

A: Experimental setup for temperature measurements.

The temperature measurements were performed using the experimental setup shown in Figure 5.1. The wire is inserted in a glass tube with 1 cm of diameter and 50 cm length (1). The tube is supported at both extreme and is kept in vertical position by a stand (3) that held it at a distance

approximately 1 meter from the floor. A PT100 temperature sensor (4) made from platinum resistance and mounted

at robot arm (5) is responsible for temperature measurements. The robot arm can move at two axes and it permits to scan a plane area with dimensions 60x90cm. A Motors Control Card (9) does control of the movement of the robot arm. The temperature sensor is connected with a multimeter digital HP34401A (7) that permits to be measured the resistance of PT100 and hence – the temperature. The multimeter can be connected to the computer (11) by serial port RS-232 or parallel port GPIB using an adapter GPIB-USB. The measurements by USB connection are sent to the computer and saved to files. The results are presented using Origin 7.5. The programs that manage the robot and the multimeter and co-ordinate the measurements and the movement of the robot arm are made in LabView8.2 environment.

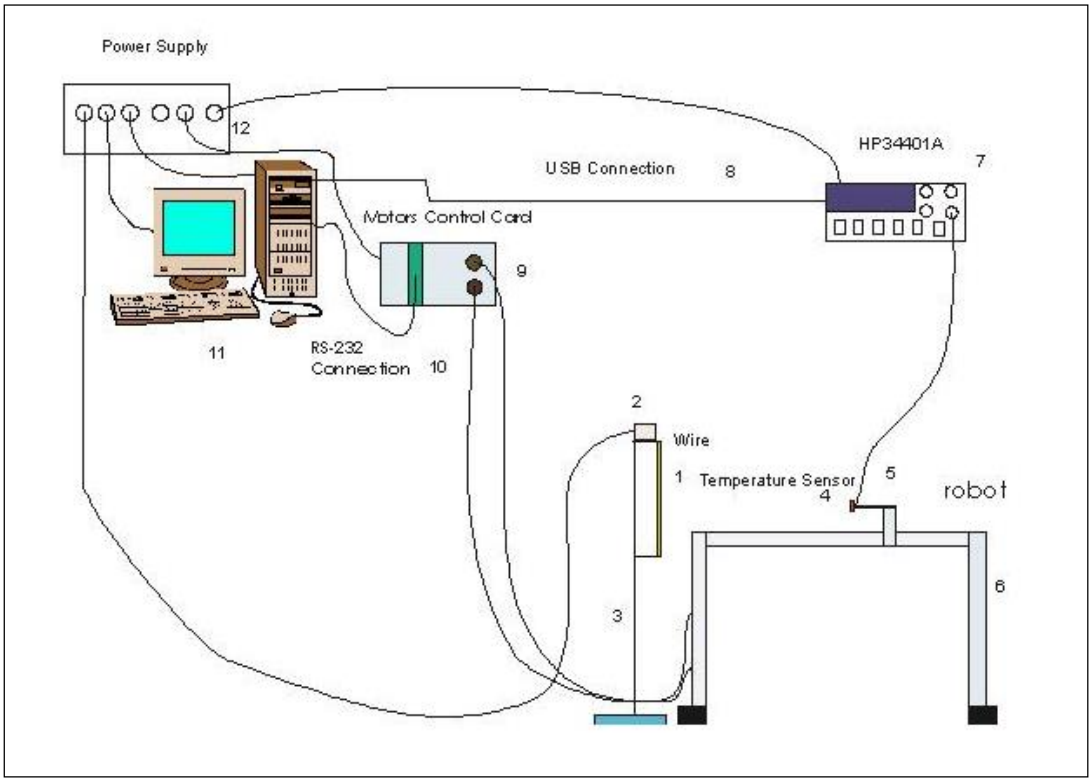

Figure 4.*1.1* Experimental setup for temperature measurements

1. Wire from nicrom inserted in a glass tube with diameter 1 cm
2. Power supply and power regulator
3. Stand
4. Temperature sensor PT100
5. Robot arm
6. Robot
7. Digital multimeter HP34401A
8. USB/GPIB connection between the computer and the multimeter
9. Motor control card
10. RS-232 connection
11. Computer (CPU 3GHz, 1GB RAM Memory, Windows XP Operating system, LabView, Origin and other software of interest installed)
12. Power supply for experimental setup

B: Experimental setup for measurements of ultrasonic waves

The experimental setup for ultrasound measurements is presented in Figure 4.2. The exciting signal that consists of a brief Gauss pulse with amplitude -100V and frequency of repetition 20 Hz is generated from HV Pulser/Receiver Panametrics 5058. The signal is sent to a transducer Murata MA40S4S (1) where a longitudinal vibration is generated. The transducer responds emitting an ultrasonic wave with length 8.5 mm and nominal frequency 40 kHz. The generated ultrasonic beam is incident perpendicularly to the wires plane. A receiver type transducer Murata MA40S4R (3) is mounted on the robot arm (4), designed and carried out by the research team. The receiver transforms the received wave in an electrical signal with amplitude proportional to the wave pressure. Therefore it can be made a map of the transmitted wave. The measurements are taken in an equatorial plane perpendicular to vertical plane defined by the two tubes. From the receiver the signal backs again to the HV Pulser/Receiver where is amplified and sent to the digital oscilloscope PicoScope3224 (7). By USB connection the measured data are sent to the computer (11) y saved in files. LabView based program controls and co-ordinates the signal parameters (amplitude, Nº samples, triggering y etc.) and the robot movement.

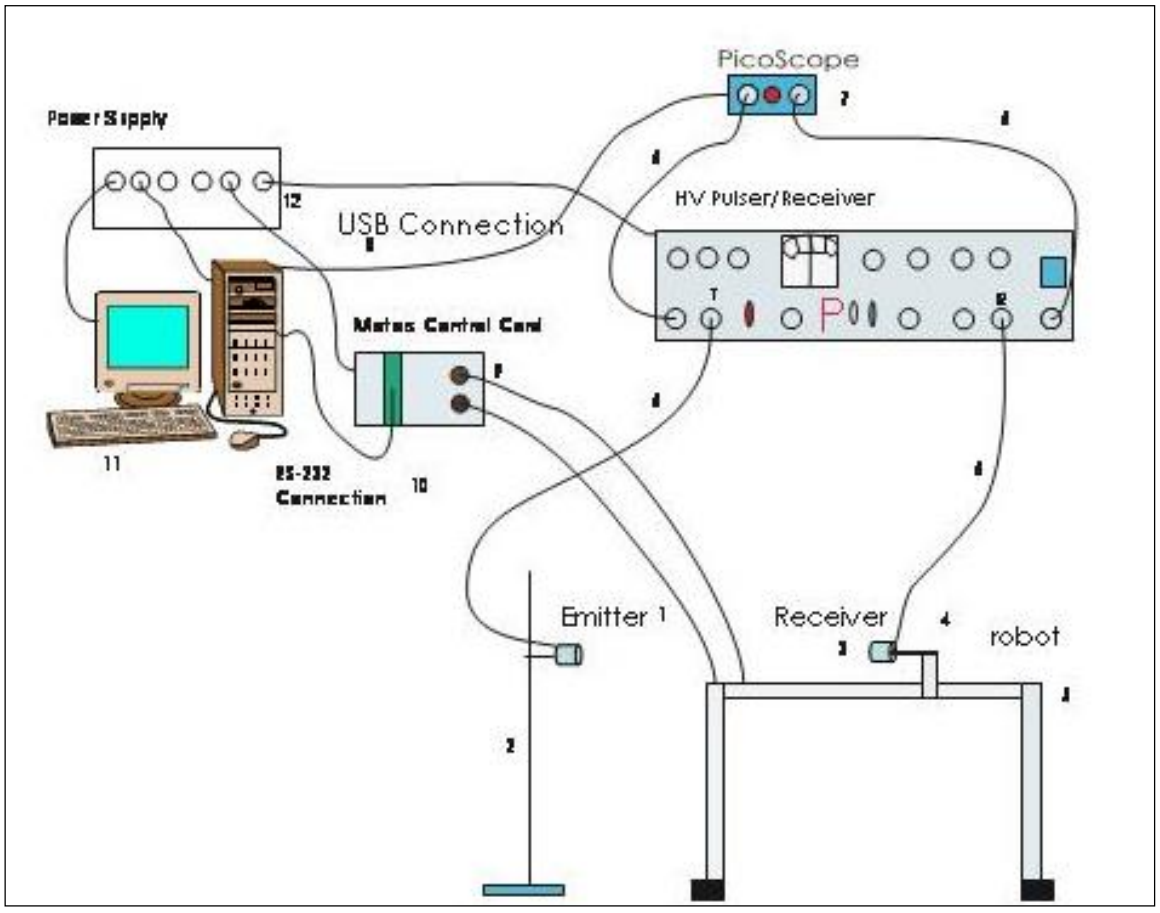

Figure 4.1.2 Experimental setup for measurements of ultrasonic waves

1. Emitter Murata MA40S4S

2. Hot wire

3. Receiver Murata MA40S4R

4. Robot arm

5. Robot

6. BNC connection

7. Oscilloscope digital PicoScope 3224

8. USB connection between the oscilloscope and the computer

9. Motor control card

10. Serial port connection between the computer and Motor control card

11. Computer

12. Power supply

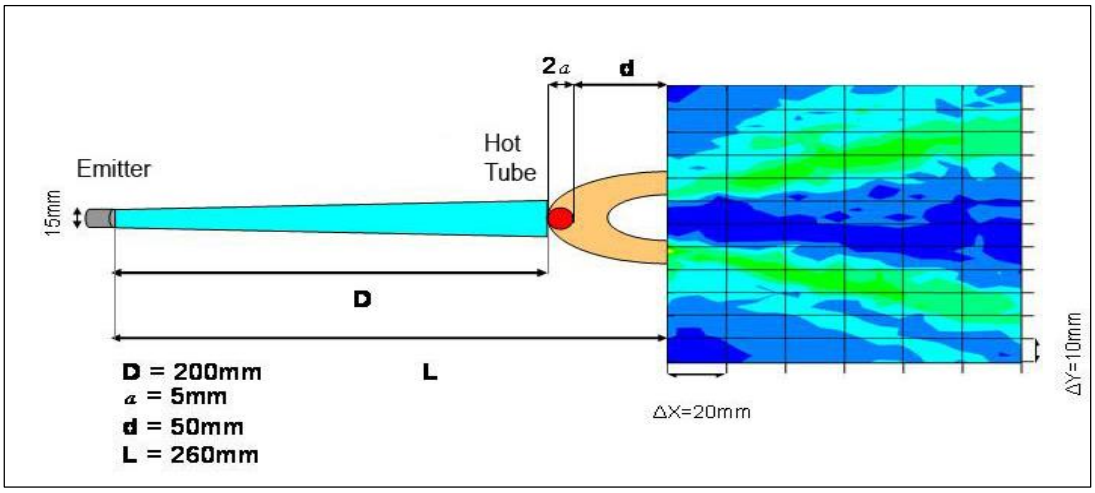

Figure *4.1.3* Scheme of a typical measurement.

The emitter emits an ultrasonic wave in a cone with approximately 15º aperture. The tube(s) with diameter 10 mm (i.e. the plane of wires) is situated 200 mm from the emitter. The initial point of the measurements is 50 mm from the tube surface placed; this distance is necessary for protection of the receiver from the high temperature of the wires. Hence the total distance between the emitter and initial point of measurements is 260 mm. In case of temperature measurements the initial distance between the tube surface and the sensor PT100 is 1 mm. The robot step is 20 mm in direction X and 10 mm in direction Y.

4.2 Basic formulas verification

The theory considers the thermal conductivity coefficient k_{th} and the thermal diffusivity coefficient α as constants but in fact they are not. Figure 4.2.3 and Figure 4.2.2 show the dependency of k_{th} and α from the temperature.

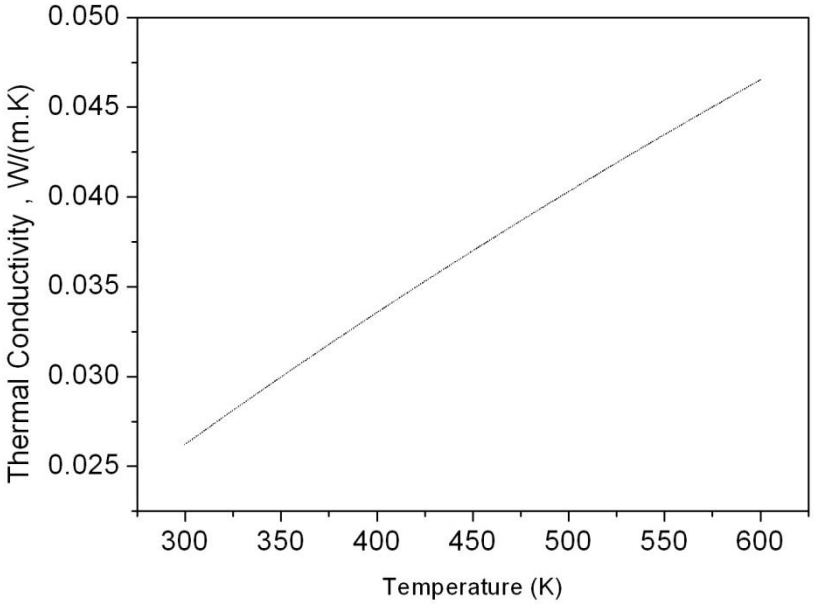

Figure 4.2.1 Thermal conductivity coefficient k_{th} as a function of the temperature.

The condition "Fo=const" means α = const in equation (3.7). Therefore, we consider that k_{th} only depends on the temperature. Figure 4.2.3 shows the experimental data for the temperature distribution around a cylinder with radius a = 5mm (black curve) and calculated values (the red, green and blue curves) for different Fo. It can be observed a good approximation between theoretical and experimental data.

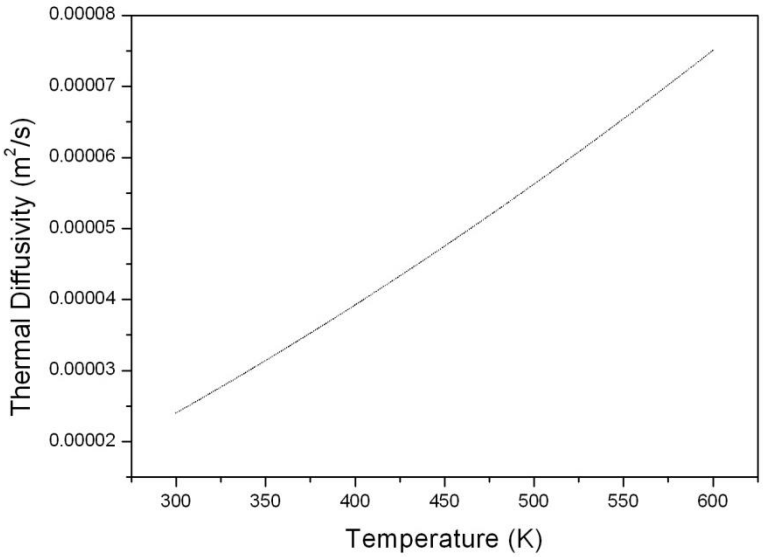

Figure 4.2.2 Thermal diffusivity coefficient α as a function of the temperature.

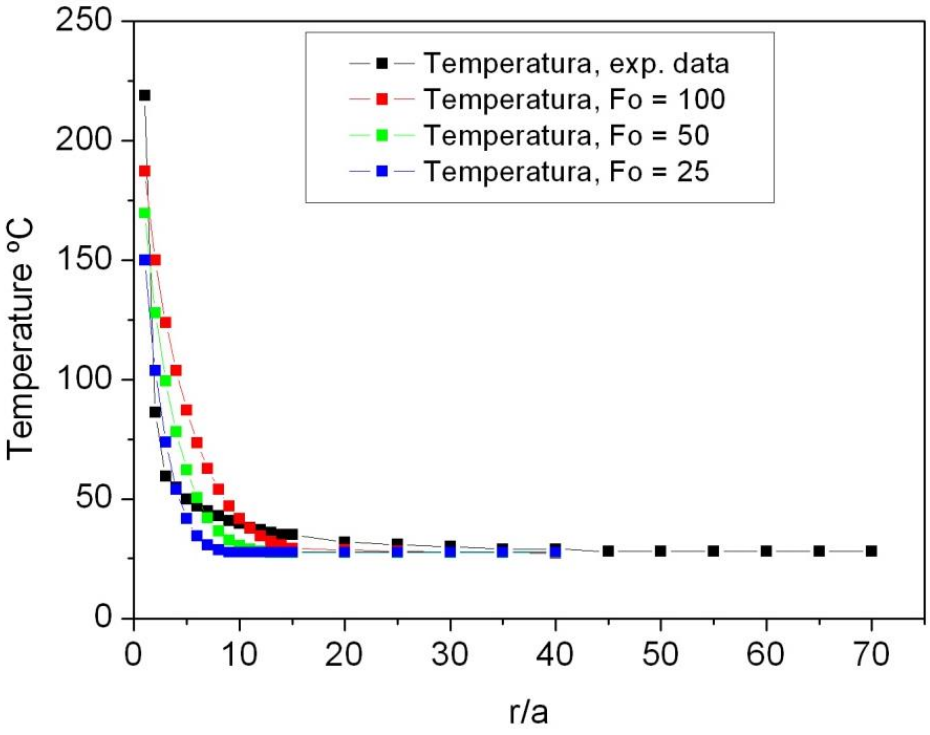

Figure 4.2.3 The temperature measured as a function of the radial distance r normalized by the radius a = 5mm of the hot tube (black curve) and calculated values for different Fo.

The experiment was performed as follows. The initial point of the measurement was situated of 1 mm from the surface of the tube. Every step of the robot arm with the mounted sensor was 1 mm backwards. 350 points in radial direction were measured. The room temperature was reached at a distance 20 cm. A posterior analysis performed using a FEM based software package COMSOL showed that the temperature, measured by the sensor, was higher than the temperature of the air in contact with it. Most probably, the discrepancy comes from the fact that during the experiment the temperature sensor was receiving from the tubes additional heat by radiation.

In the experiment the strength of the heat source is Q=23 W/m, the radius of the tube is 5 mm and Fo is 25. The temperature sensor is connected with the multimeter using "4 wires" method. The scale of the multimeter is 61/2 digits in kΩ range. The dependency between the measured resistance R and the temperature is lineal:

$$T = m*R+n \qquad (4.2.1)$$

It is got average of 5 measurements. The precision of the measurements is 1ºC.

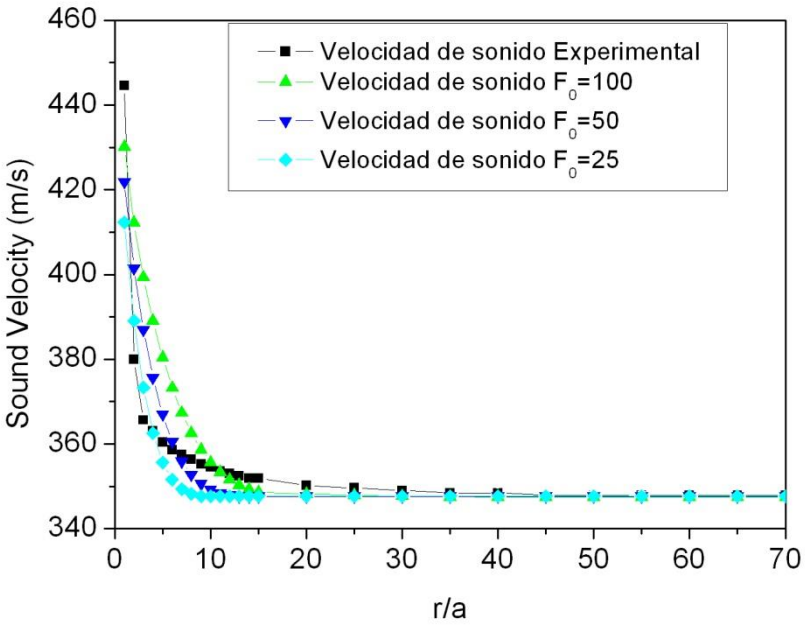

Figure 4.2.4 The speed of sound in air as a function of the distance radial normalized by the radius a of the hot tube for different values of Fo (green, deep blue and light blue curves) and experimental data (black curve)

The expression (1.2.3) permits the calculation of the sound speed in air as a function of the temperature. Figure 4.2.4 presents the speed of sound calculated for different values of Fo (the green, deep blue and light blue curves) and the experimental measurements (the black curve). The experimental data show a good agreement with the theory and therefore we consider that formula (1.2.3) works correctly in the case of hot wire.

4.3 Temperature and Pressure Measurements Near the Heated Wires

4.3.1 Temperature measurements

Temperature maps in the *XY*-plane, *T(x, y)*, are measured prior to ultrasonic measurements. We use a platinum wire temperature sensor, which measures the temperature in range of −50 °C up to 600 °C with an error of ±1 °C. The shortest distance between PT-100 sensor and the tube is 1 mm. The maximum temperature on the tube surface, which is 300 °C, has been determined by using a Varioscan 3021ST infrared camera. The temperature around the tube decreases rapidly with increasing distance due to the thermal conductivity of air.

The results are presented in Fig. 4.3.1.1 and Fig.4.3.1.2. The temperature of the wire inside is approximately 400ºC but on the surface of tube it is approximately 305ºC.The isotherms are situated concentrically around the tube.

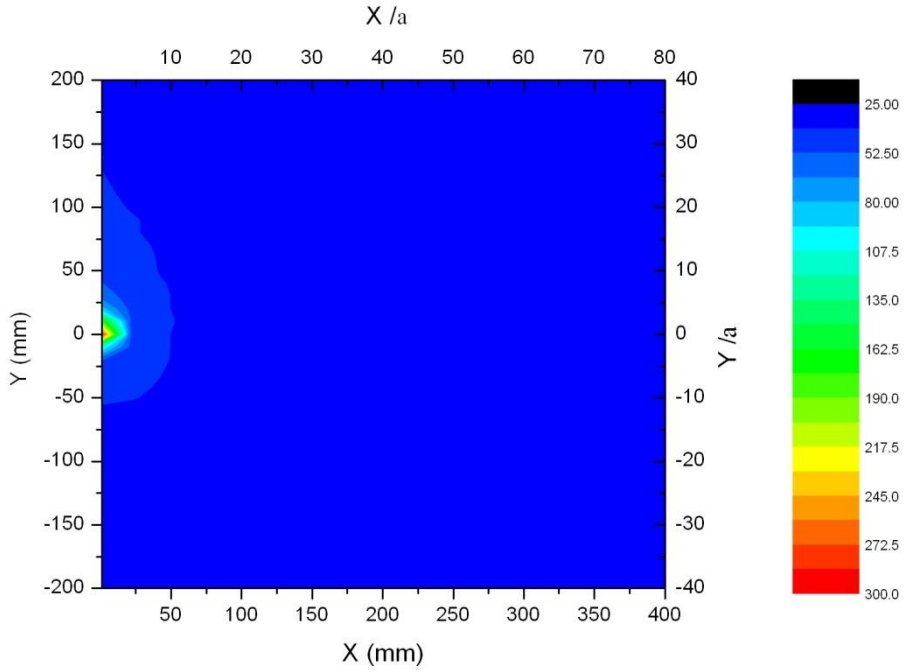

Figure 4.3.1.1. A map of the temperature distribution around a single heated tube

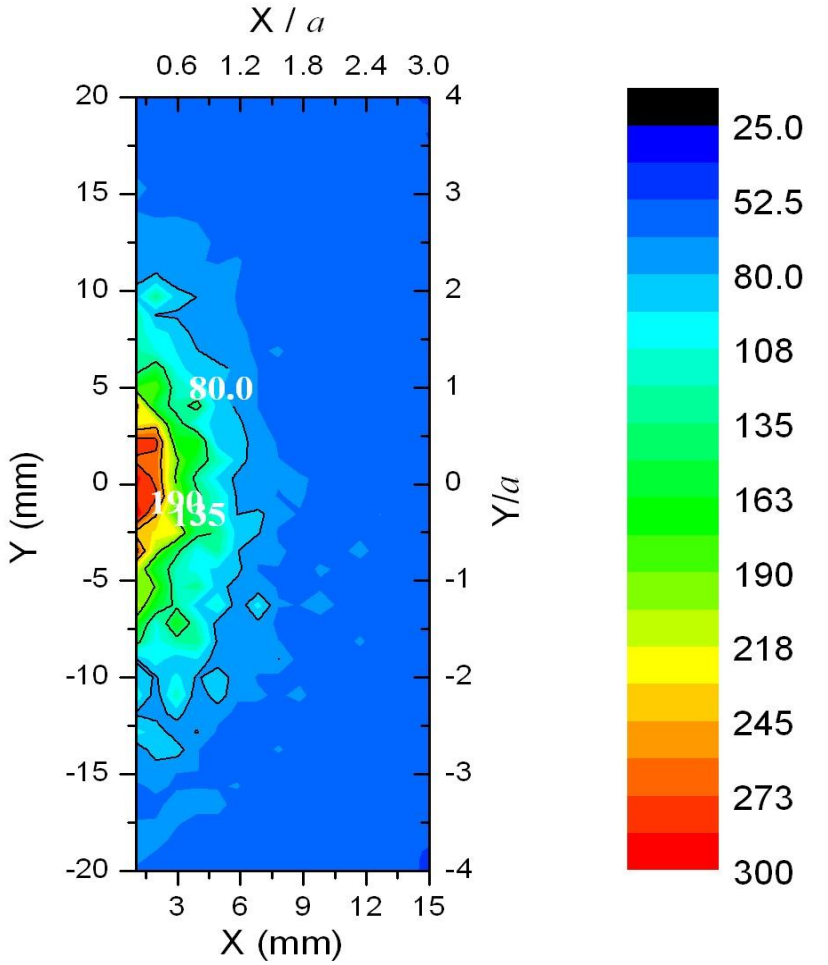

Figure 4.3.1.2. Zoom of the zone near to the hot tube. The isotherms are concentrically situated around the tube.

The experiment was performed as follows. The initial point of the temperature sensor was situated of 1 mm from the surface of the tube in direction X and 200 mm in direction Y. It was explored an area 400x400 mm. The robot step was 20 mm in X and 10 mm in Y.

Fig.4.3.1.3 shows temperature distribution around 2 hot tubes placed at distance 270 mm between the surfaces of the tubes. It can be seen that even at this large distance the measurements indicate that the temperature in the middle between the tubes is higher than the ambient temperature, i.e. the thermal fields of the tubes overlap. Once again, a posterior analysis showed that the temperature, measured by the sensor, was higher than the temperature of the air in contact with it. Most probably, it is due to the additional heat transfer by radiation that the temperature sensor was receiving from the tubes during the experiment.

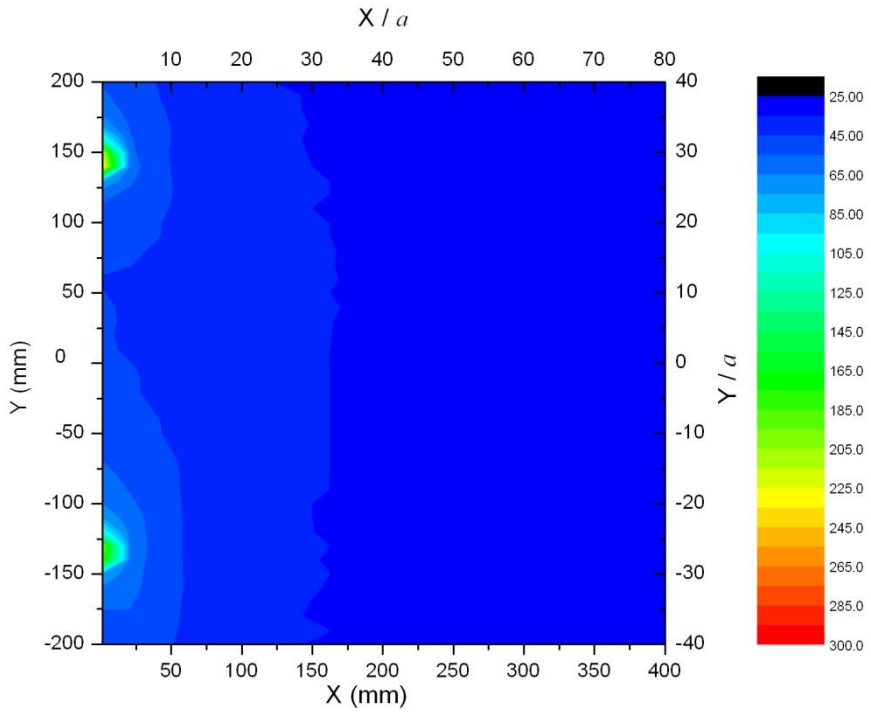

Figure 4.3.1.3 Two-dimensional temperature map near two hot tubes.

4.3.2 Ultrasonic measurements

The experimental setup is described in Fig. 4.1.2. A MURATA SCmt transducer is used as emitter to generate an ultrasonic pulsed beam nominally centered at 40 kHz. The beam impinges onto two cylindrical glass tubes containing a spiral metallic wire that can be heated by applying an alternating current to its ends. Both tubes are 30cm long and 5 mm radius, d defines the distance (center to center) between tubes along the *y*-axis, and D is the distance from the emitter to the origin of coordinates along the *x*-axis. D=20.5 cm is chosen in order to avoid the transducer near field amplitude oscillations (Fig.4.3.2.1 a). Another MURATA SCmt transducer is used as receiver, detecting the signal scat erred by the tubes. A computer controlled robot arm is used to sweep the receiver through a grid of measuring points. Two stepped motors with a maximum resolution of 0.25mm per step allows the movement along each X- and Y- axis in the equatorial plane perpendicular to that defined by the tubes. The nearest distance between heated tube and the receiver is x_0=5.5 cm since the operational temperature of transducers is under 60°C. In fact, temperature above 60°C can produce irreparable damages of the receiver. A repetition rate of 20 cps is used for the pulses generated by the emitter. The signal (in volts) at the receiver is amplified in a high-voltage pulser/receiver and it is send to a digital oscilloscope, which makes a temporal averaging of 16 pulses. The data acquired is transferred to a computer that makes a fast Fourier transform in order to represent the pressure amplitude as a function of frequency. Fig 4.3.2.1 b shows the pressure map of the beam generated by the emitter in an area 45x40 cm^2. It has been obtained by using a grid of 1134 points; 14 points spaced Δx=50 mm along the X-axis and 81 points spaced Δy=5 mm along the Y-axis.

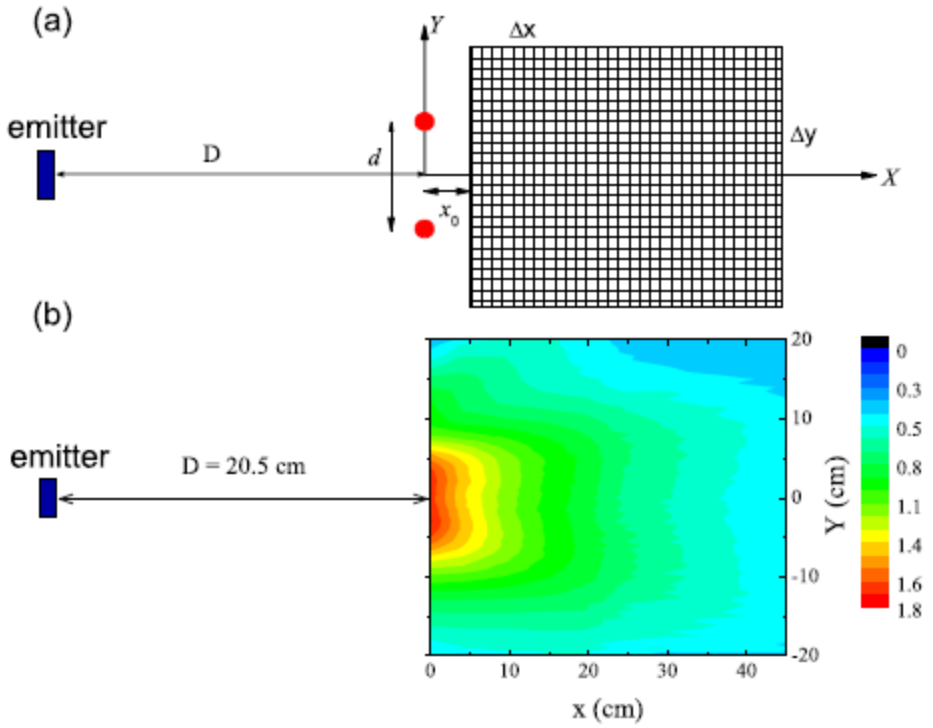

Figure 4.3.2.1 (a) Schematic drawing of the experimental set-up. (b) Two-dimensional pressure map of the field generated by the emitter transducer employed in the experiments

The original produced ultrasonic beam is clearly distorted from a tube situated at some place where it propagates (figure 4.3.2.2top). The incident wave is divided on two beams. The regions of high amplitude are situated near to the tube. Also there is no shadowed zone behind the tube. If the tube is hot (figure 4.3.2.2bottom) the beam still is divided but the regions of maximum amplitude are situated of some distance from the tube. It is formed a shadowed zone behind the hot tube exactly as the theoretical model predicts.

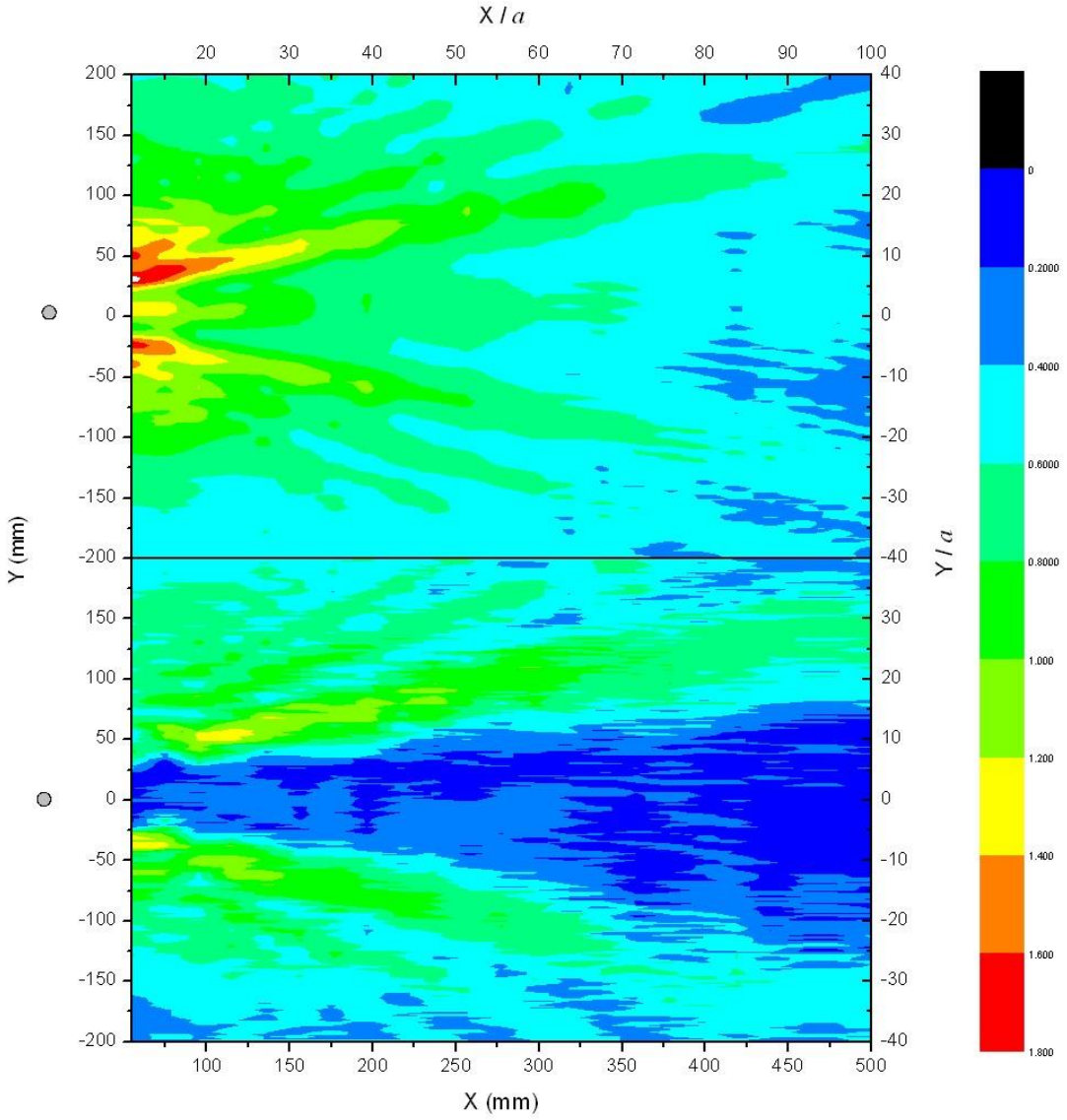

Figure 4.3.2.2 A map of the ultrasonic wave distorted by one tube at room temperature (top) and a hot tube (bottom). The grey circles point the position of the tube.

The experiments about ultrasound were performed for 5 different distances: - 270, 150, 100, 80 and 60 mm between the tubes. Decreasing the distance the internal beams get closer. Figure 4.3.2.7 shows that the focalization is reached for 60 mm distance between the tubes, approximately at the predicted distance. The position of the tubes is marked on the left in the figures with two gray little circles.

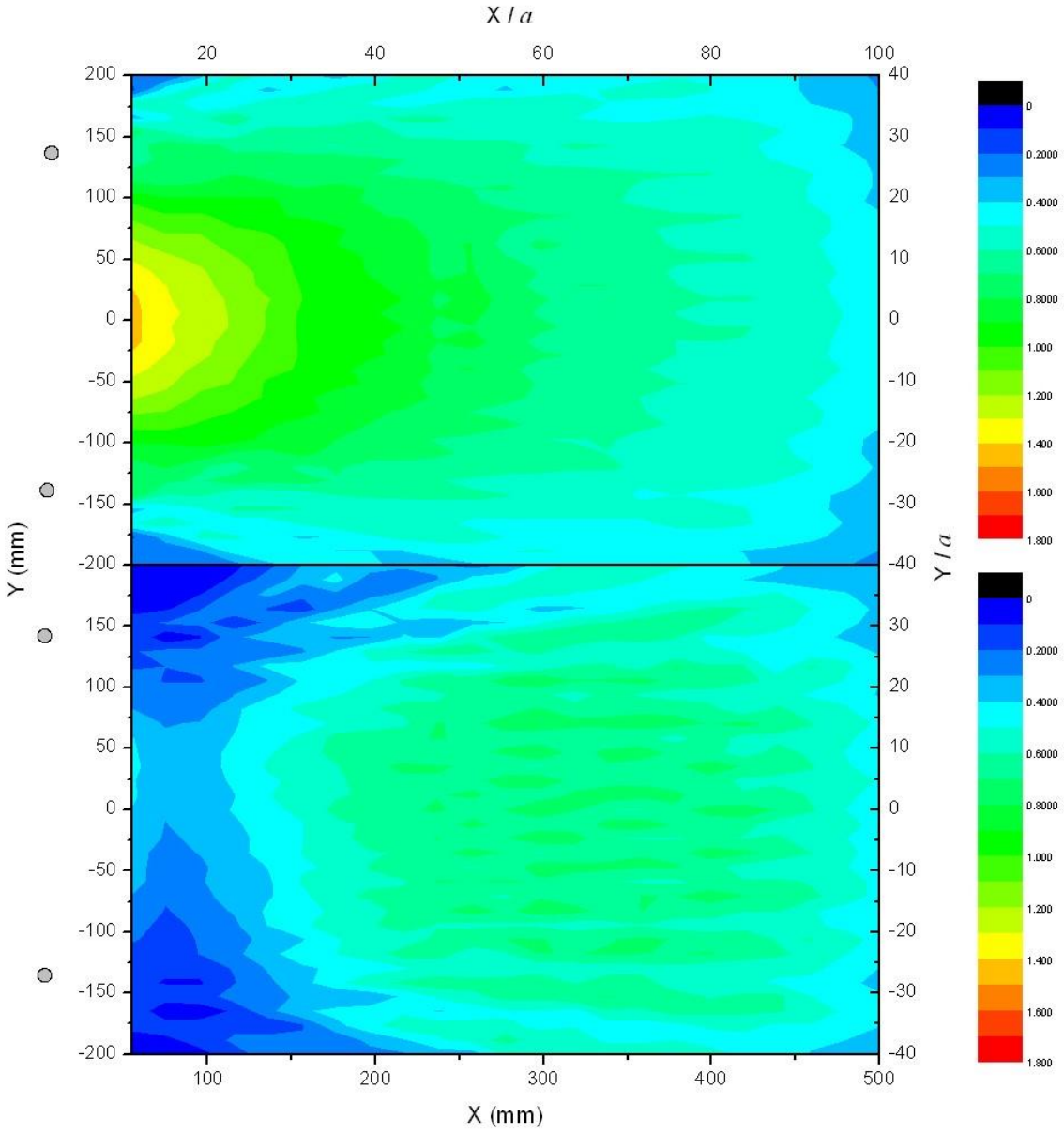

Figure 4.3.2.3 Ultrasound wave incident on two tubes at room temperature (top) and hot tubes (bottom). The distance between the tubes is 270 mm. The hot tubes displace the zone of high pressure amplitude but there is not a focal zone. The position of the tubes is marked on the left in the figures with two gray little circles.

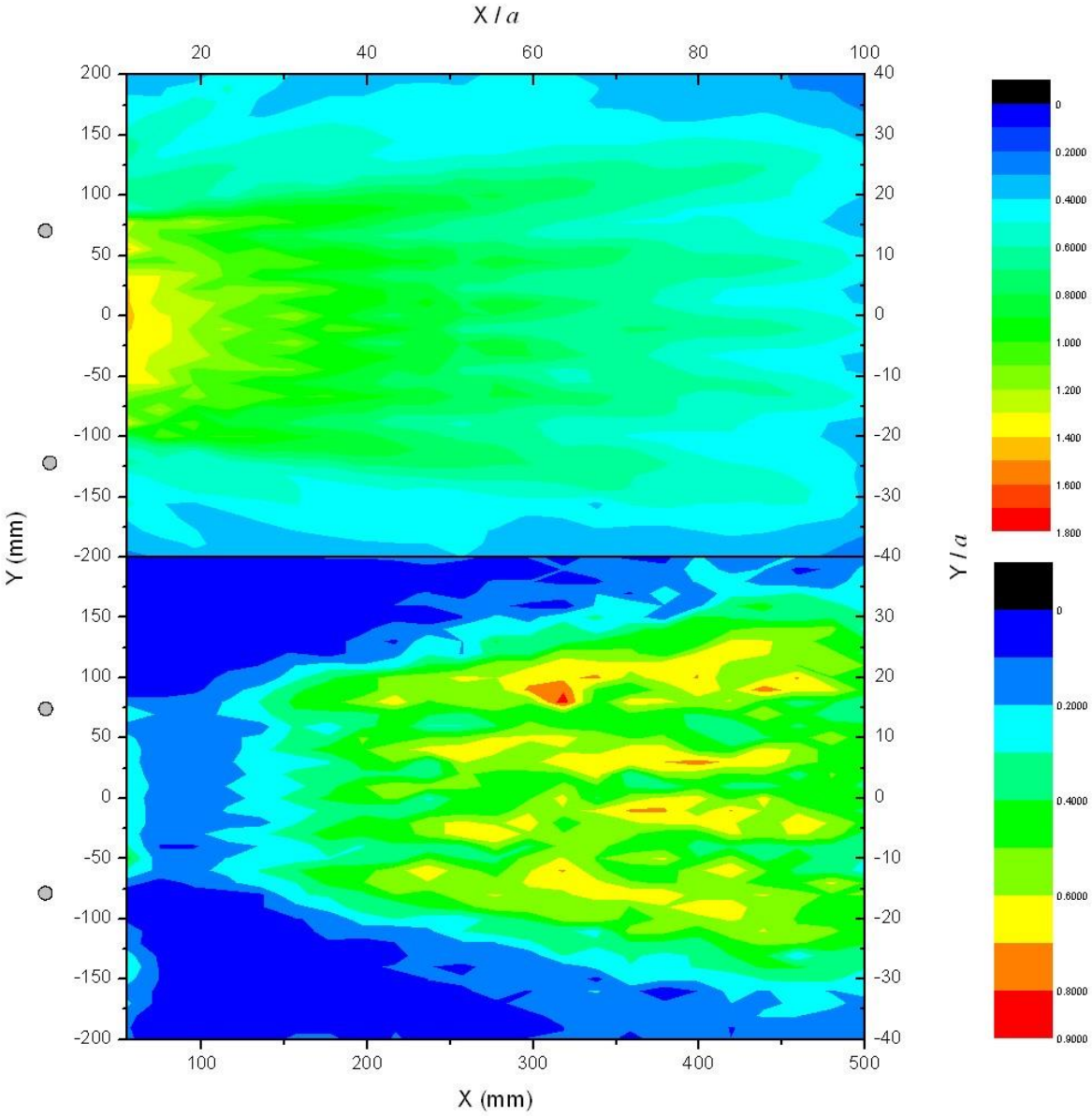

Figure 4.3.2.4 Ultrasound wave incident on two tubes at room temperature (top) and hot tubes (bottom). The distance between the tubes is 150 mm. The hot tubes displace the zone of high pressure amplitude but there is not a focal zone. The position of the tubes is marked on the left in the figures with two gray little circles.

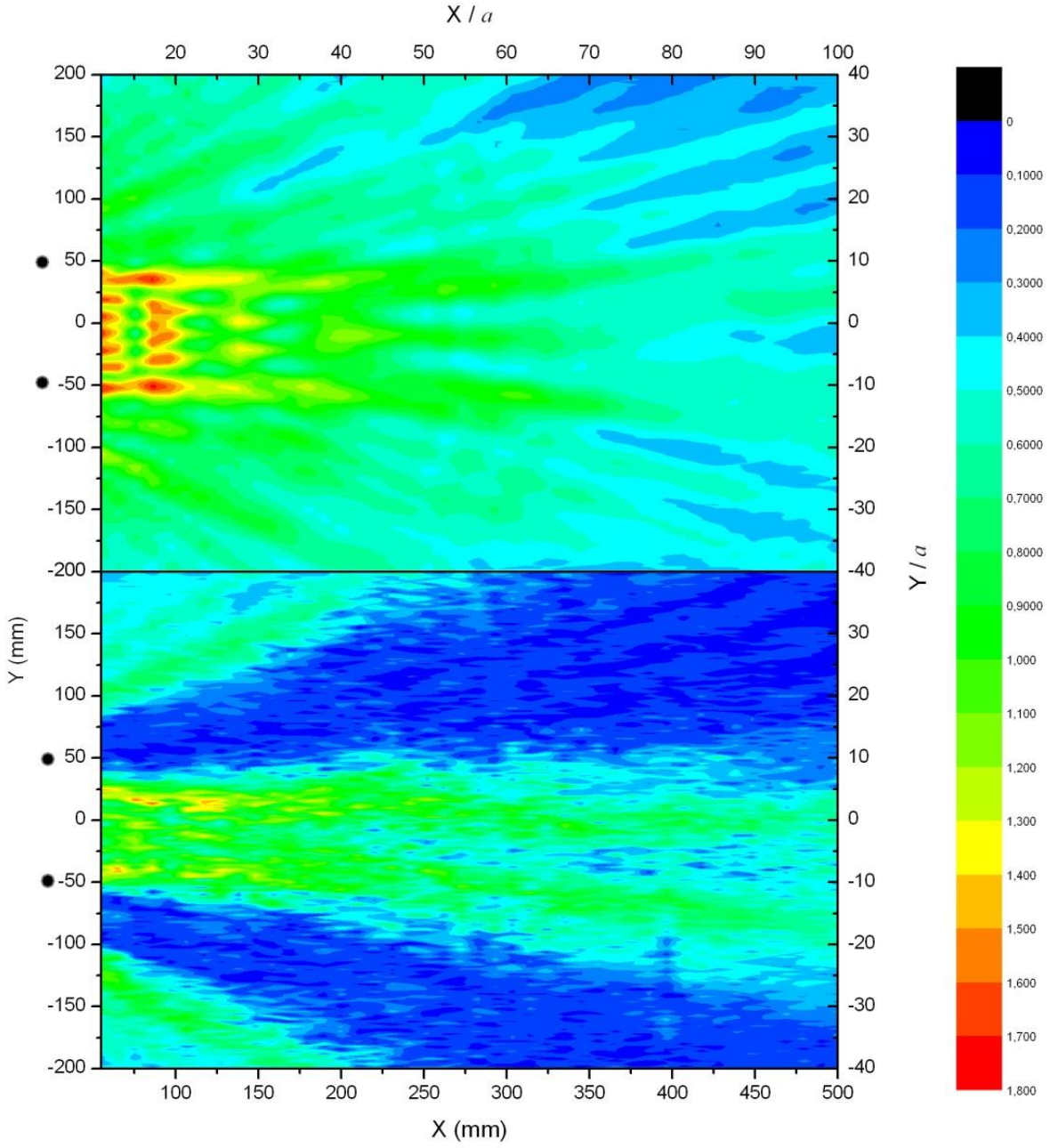

Figure 4.3.2.5 Ultrasound wave incident on two tubes at room temperature (top) and hot tubes (bottom). The distance between the tubes is 100 mm. The central beams are stronger than the lateral beams. The position of the tubes is marked on the left in the figures with two gray little circles.

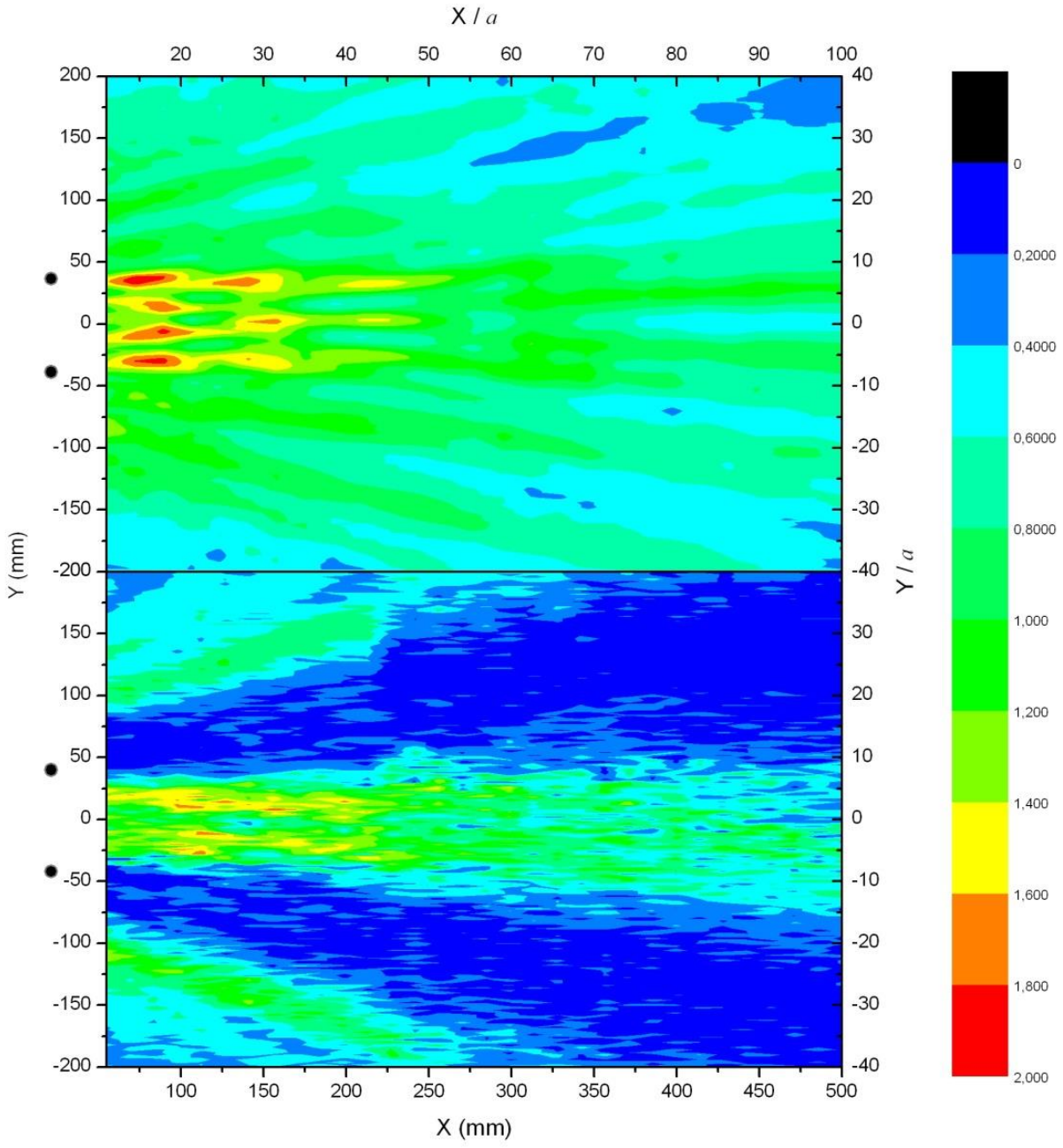

Figure 4.3.2.6 Ultrasound wave incidents on two tubes at room temperature (top) and hot tubes (bottom). The distance between the tubes is 80 mm. The central beams are getting stronger and closer. The position of the tubes is marked on the left in the figures with two gray little circles.

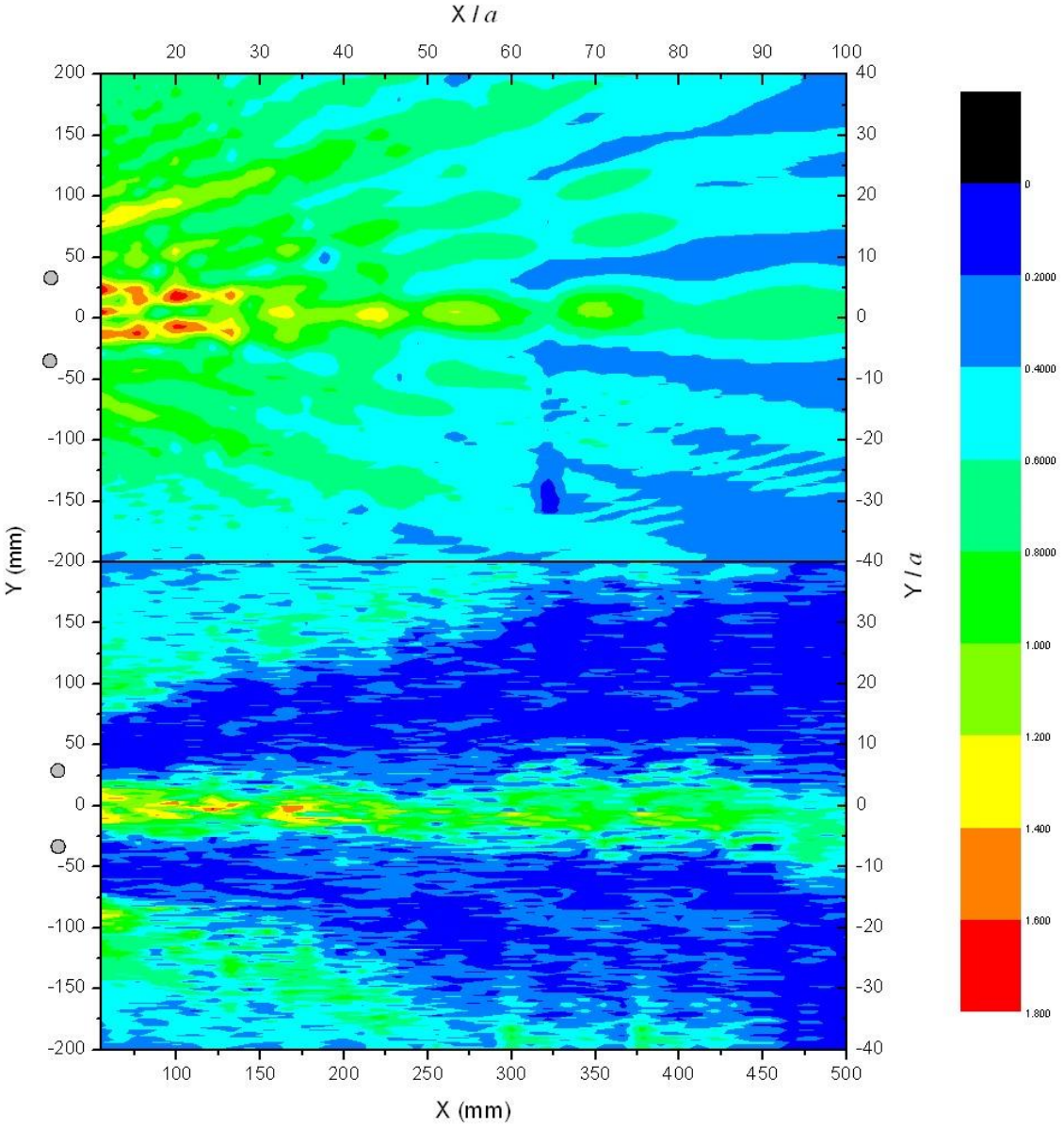

Figure 4.3.2.5 Ultrasound wave incidents on two tubes at room temperature (top) and hot tubes (bottom). The distance between the tubes is 60 mm. The central beams are joined in focal zone. The position of the tubes is marked on the left in the figures with two gray little circles.

4.4 Comparison between Theory and Experiments

Some comparisons between the simulated amplitude profiles and experimental data are depicted below. There are showed cross-sections along the y-axis at 5 (near to the surfaces of the tubes), 9, 11 (around the focus), 25 and 45 cm from the vertical plane formed of the surfaces of the tubes. The continuous lines represent COMSOL Multiphysics simulated profiles and the dashed lines represent the experimentally obtained profiles. The frequency is 40.6 kHz. These profiles are obtained by using in the simulation a Gaussian beam fitted to the transducer beam depicted in Figure 4.3.2.1. Dashed lines correspond to the tubes positions. Figure 5.4.5 shows the focusing features of the collimated beam produced by two heated tubes. Qualitatively the agreement between simulations and experiments is fairly good.

Also it can be noted that the amplitudes measured for the heated tubes are smaller than that obtained for the tubes at room temperature. It can be explained with the additional losses of energy due to the increasing of viscosity associated to sound propagation in hotter air [Cro98].

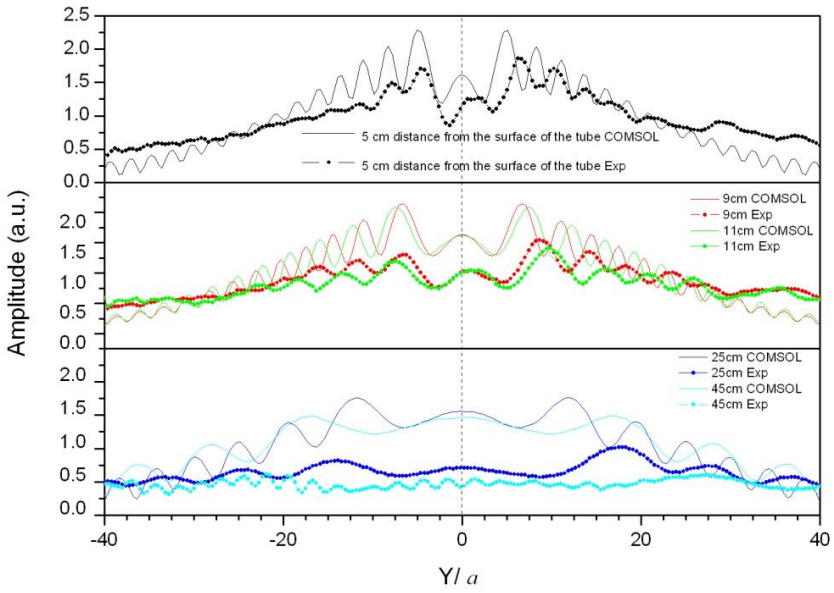

Figure 4.4.1. Cross-sections along the y-axis, one tube, room temperature. It can be seen the splitting of the incident ultrasonic wave to two lateral beams and the small central peak due to the interference.

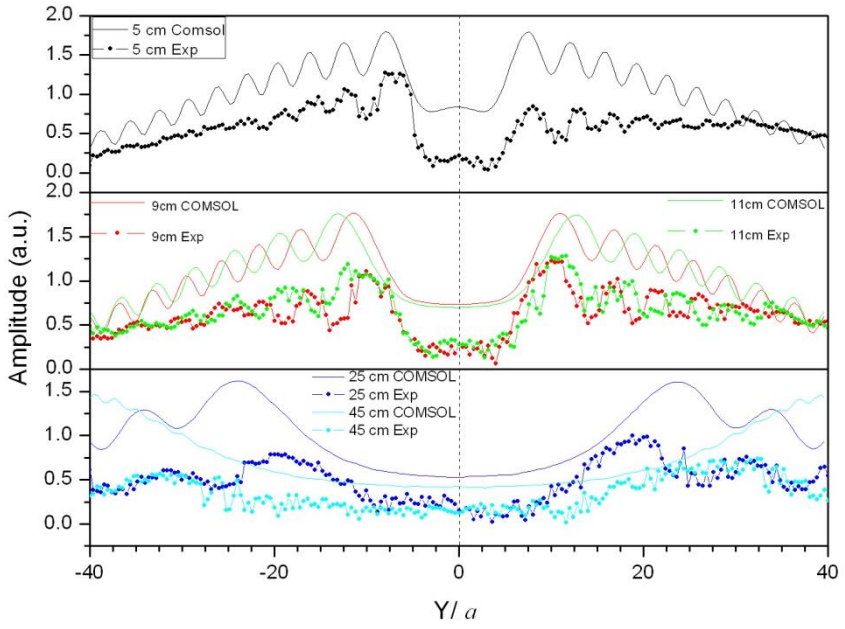

Figure 4.4.2. Cross-sections along the y-axis. The lateral beams are stronger and the central peak vanishes.

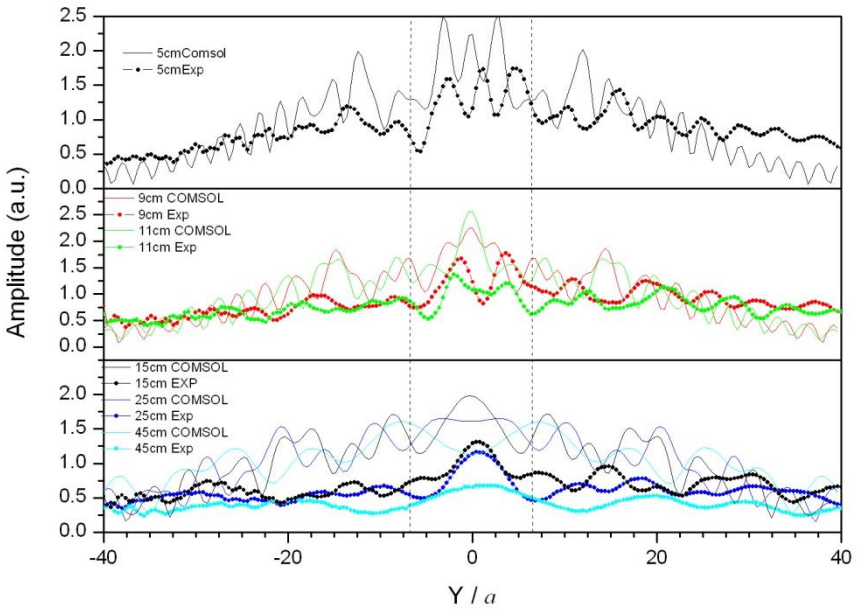

Figure 4.4.3. Cross-sections along the y-axis, two tubes, room temperature. Some discrepancies between the simulated and measured profiles can be observed. They are mainly due to thermal losses not included in the simulations.

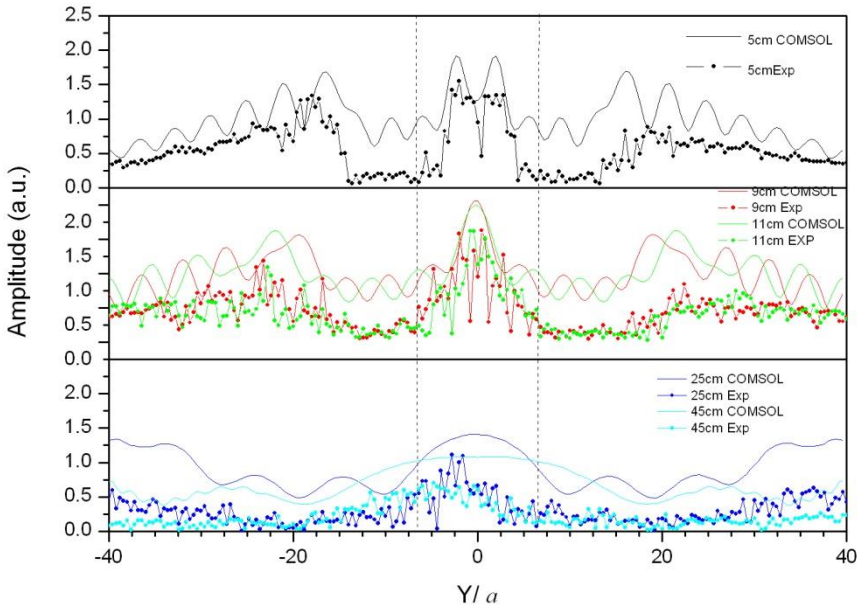

Figure 4.4.4 Cross-sections along the y-axis, two hot tubes. It can be seen that near to the hot tubes are formed two internal lateral beams that turn into the focal zone along the x axis.

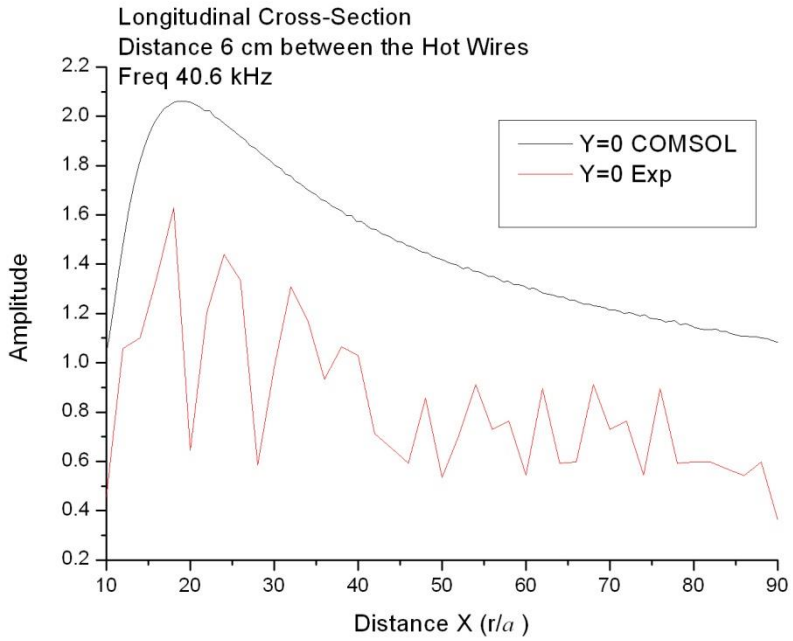

Figure 4.4.5 Focusing features of the collimated beam produced by two heated tubes. The distance between the tubes is 6 cm. The continuous line defines FEM simulations. The dashed line represents the experimental data. It can be seen that the point of maximum amplitude is located at x=19a.

4.5 Conclusions

Guiding of sound waves by temperature gradients has been theoretically and experimentally demonstrated. It is shown that an ultrasonic wave interacting with the heated tubes produces a highly collimated bean that is also focused along its propagation direction. A grid of such tubes has the capability of focusing an incident ultrasonic wave into series of tightly focused spots in toward direction. As the optical microlens array, such a microlens array has great potential for innovative applications. For example, in ultrasonic cleaning applications, focusing would enable to remove of finer dusts from hardly accessible surfaces; in ultrasonic transducers for nondestructive testing of materials and etc.

The focusing features described in this work are qualitatively similar to that obtained by other mechanisms like, for example, refraction by lenticular clusters of cylinders or by multiple scattering of specially designed arrangements of cylinders [Cer01]. The simulations based on multiple scattering methods are unable to include in its algorithm the temperature gradient existing in the region between the tubes. In this work Finite Element Method (FEM) is used to simulate the temperature gradient between the tubes and the scattering of Gaussian beam ultrasonic wave. The FEM simulations and the experiments are in good qualitative agreement. The main discrepancy comes from the fact that COMSOL simulations do not include the thermal losses expected in this type of structures.

Part II

Sonic Crystals Made of Heated Wires

Introduction to Sonic Crystals

II.1 Introduction

Sonic Crystals (SC) are structures made of sound scatterers periodically arranged in a lattice [Dow92] (Figure I.1). SCs forbid sound propagation for some frequency bands, named bandgaps. The physical mechanism behind the bandgaps formation is the destructive interference between waves reflected by consecutive planes of sound scatterers (for acoustic waves) or atomic planes (for electromagnetic waves). Transmittance and reflectance measurements for sound waves impinging arrays of solid cylinders in air demonstrated that, at bandgap frequencies, a low transmittance and a high reflectance are simultaneously observed due to Bragg scattering [San98,San01].

Practical devices like, for example, acoustic filters or waveguides based on SCs have been proposed and demonstrated [Miy01,Khe04]. Taking advantage of the low acoustic impedance of SCs with low filling fractions, it is possible to implement convergent lenses [Cer01] and Fabry-Perot interferometers [Sán03]. Also, recently, Garcia-Chocano et al. [Gar12] reported a theoretical possibility to build a reduced acoustic cloak that uses a temperature gradient in order to obtain sound speeds larger than in air. The cloak consists of a circular acoustic crystal made of concentric layers of rigid cylinders whose surfaces are heated or cooled in order to get the temperature gradient needed for cloaking behavior.

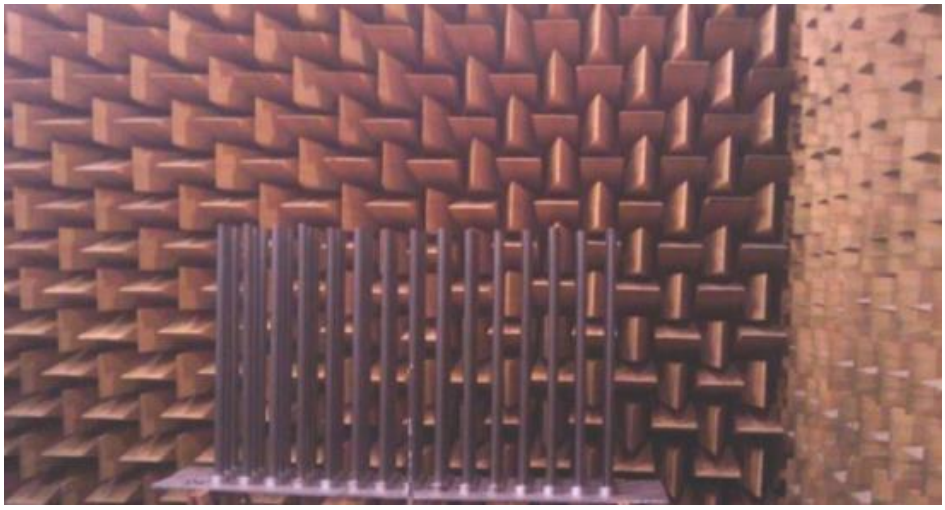

Figure I.1 An example of Sonic Crystal made of a periodic array of rigid cylinders in air

II.2 Objectives

In this part a SC based on heated wires is proposed. Some properties of thus formed SC, like reflectance and transmittance, are proposed to be investigated. FEM based simulations are used for better understanding of the SC properties. An adapted to the investigated physical phenomena experimental set-up is prepared.

Chapter 5

Brief Theoretical Introduction to the Sonic Crystals

Generally, the theory of this part is based on the concepts described in paragraphs 1.3, 1.4, 1.5 and Appendix 1. Here, it is extended over some practical cases like Fiber Bragg Grating and interferometers. Acoustic analogues of the optical devices are investigated.

5.1 Fiber Bragg Grating

Some artificial materials have periodically changed refractive index [Joa08]. When the material is a long glass core with radius usually less than 10 μm it is called Fiber Bragg Grating (FBG) [Gha09]. Many of the challenges associated with electrical detection using light instead of electricity and standard optical fiber instead of copper wire can be solved using FBG devices. An optical Bragg grating is a device with a periodic variation of the refractive index, so that a large reflectivity may be reached in some wavelength range around a certain wavelength which fulfills the Bragg condition (1.5.3). Expressing the Bragg wavelength we obtain:

$$\boldsymbol{\lambda_B = 2n_{eff}\Lambda} \qquad (5.1.\ 1)$$

At each periodic refraction change a small amount of light is reflected. All the reflected light beams combine coherently to one large reflection at a particular wavelength – the Bragg wavelength - when the grating period is approximately half the input light's wavelength. Light beams at wavelengths other than the Bragg wavelength, which are not phase matched, are essentially transparent. This principle is shown in Fig.5.1.

Therefore, light propagates through the grating with negligible attenuation or signal variation. Only those wavelengths that satisfy Bragg condition are affected and strongly back-reflected. A fiber

Bragg grating can be therefore used as an optical filter to block certain wavelengths, or as a wavelength-specific reflector.

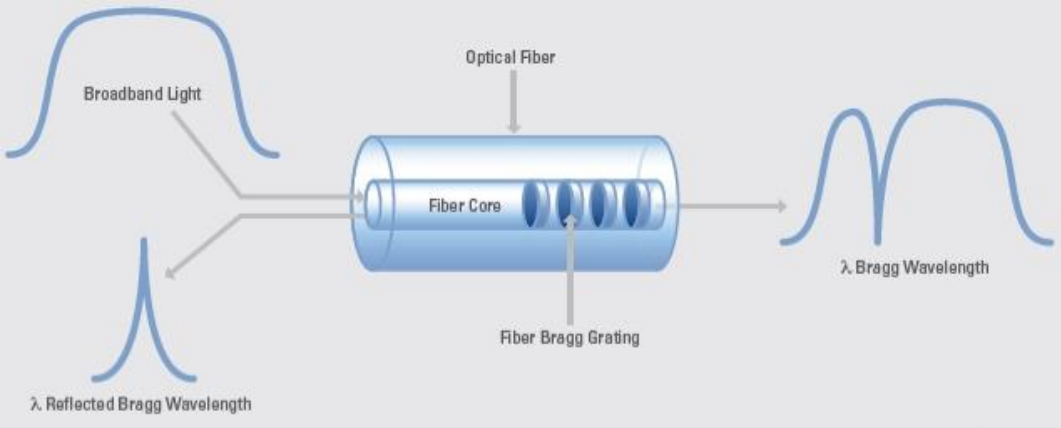

Source: *National Instruments official page*

Figure 5.1 Concept of Bragg wavelength. Almost all incident spectrum (left, up) passes through the optical fiber(right) except the waves with wavelength approximately equal to half the input wave's wavelength (left, down).

The ability to accurately preset and maintain the grating wavelength is a fundamental feature and advantage of FBG. Due to the temperature and strain dependence of the parameters n_{eff} and Λ, the wavelength of the reflected component will also change as function of temperature and/or strain. This dependency is well known and it allows determining the temperature or strain from the reflected FBG wavelength. Hence, FBG can be used temperature and strain sensors. As well as strain and temperature detection, FBGs can be used for pressure, acceleration and displacement measurements. Another applications of FBG are in fiber lasers, transducers and etc.

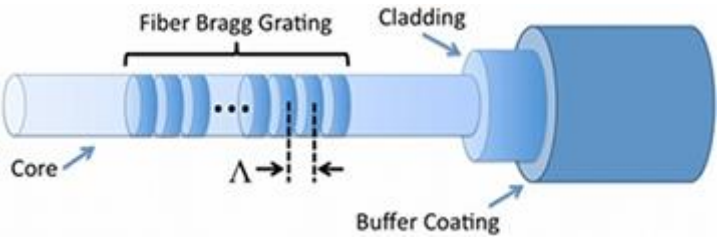

Source: *National Instruments official page*

Figure 5.2 Parts of a FBG device. The most important part is a very thin glass core where the light propagates.

The main part of optical detection technology is optical fiber – a thin strand of glass that transmits light at its core. An optical fiber is made up of three main components: a very small inner core (normally of 4 to 9 μm), cladding and protective coating (Fig.5.2). Cladding reflects light back to the core, ensuring the transmission of light in the core with minimal loss. This is achieved with a higher refractive index in the core, resulting in a total internal reflection of light. Creating a periodic variation in the refractive index of the fiber core the Bragg condition is fulfilled for certain wavelengths. Protecting coating serves to protect the fiber from external conditions and physical damage.

5.2 Standing wave and acoustic interferometers

A standing wave is formed by the interference of two waves of the same nature with equal amplitude and wavelength (or frequency) which move in the same medium but in opposite directions. Also, a standing wave is formed in front of the SC. This wave can be understood as due to the reflection suffered by the incident wave at the air/SC interface. This is general result at any frequency. Below, we describe how the reflectance R is obtained from the standing wave.

At a given frequency ω, the standing wave can be reduced to the general one-dimensional form:

$$\boldsymbol{P(x) = Ae^{i(kx-\omega t)} + Be^{-i(kx-\omega t)}}. \qquad (5.2.1)$$

The standing wave ratio SWR, which is defined as the ratio between the maximum pressure to the minimum pressure, can be expressed as a function of the reflection coefficient R=(B/A) [Deh03]:

$$\boldsymbol{SWR = \frac{P_{max}}{P_{min}} = \frac{A+B}{A-B} = \frac{1+R}{1-R}}. \qquad (5.2.2)$$

Then, solving for R we obtain:

$$\boxed{\boldsymbol{R = \frac{SWR-1}{SWR+1}}} \qquad (5.2.3)$$

Though our samples are finite in the direction perpendicular to the impinging wave (the y-axis), the pressure pattern along the x axis effectively behaves as an ideal standing wave and therefore, the expression for R above can be applied.

Chapter 6

2D Model of a Sonic Crystal Made of Heated Wires. Numerical Simulations

In our model we shall consider a 2D infinite along y-axis SC made of hot wires. To perform the numerical analysis we take advantage of the definition of crystal lattice [Kit56] and the translation symmetry. Thus, we take a part of the crystal that can be repeated infinitely in *y* direction. The standing wave in front the SC is studied and some properties as reflectance, transmittance and Bragg frequency are analyzed.

6.1 Crystal definition.

With the aim to optimize the time of calculus and computational resources in this model the tubes in Chapters 3 & 4 are substituted with wires. The radius of the wires is a half of mm.

First, we make a model of temperature distribution around a hot wire. This is the simplest possible case and it is a good starting point for theoretical building of our problem. In order to obtain the temperature distribution we perform some Finite Element Method (FEM) based simulations using COMSOL Multiphysics.

COMSOL Multiphysics is a software package for various physics and engineering applications which allows to couple different physical problems. Also, COMSOL Multiphysics allows for entering coupled systems of partial differential equations from different parts of the physics, for example heat transfer and acoustics.

Figure 6.1.1 a, b, c and d show the temperature and velocity distribution around one heated wire with surface temperature of 400ºC simulated using COMSOL Multiphysics. In this simulation equations (C.3.20) and (C.3.28) are simultaneously resolved taking advantage in COMSOL Multiphysics' virtue to couple physical phenomena – in this case General Heat Transfer and Navier-Stokes Weakly

Compressible Non-Linear Flow. In the first one the boundary conditions of "temperature" (673ºK) are imposed on the wire surface and "convective flux" on the background boundary; in the second one are imposed "wall" and "open" boundary conditions, respectively. Figure 6.1.1b shows that room temperature is completely reached at 27 mm from wire surface although it can be considered approximately reached even before - about at 13 mm (Figure 6.1.1c). Also the similarity between model (Figure 6.1.1d) and theory (Figure C.3.5) can be seen.

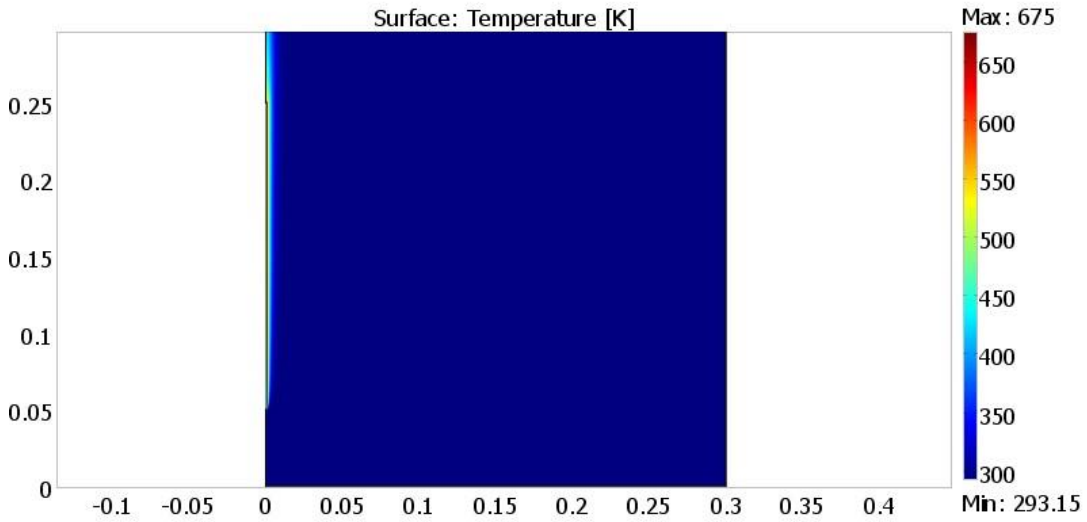

Figure 6.1.1. Temperature distribution around a wire heated to 400ºC and it decreases dramatically due to the thermal conductivity of air.

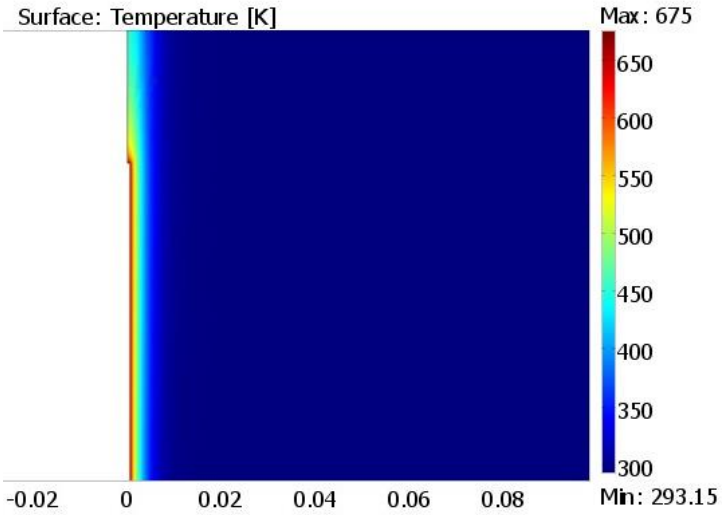

Figure 6.1.1a. Zoom of the previous figure

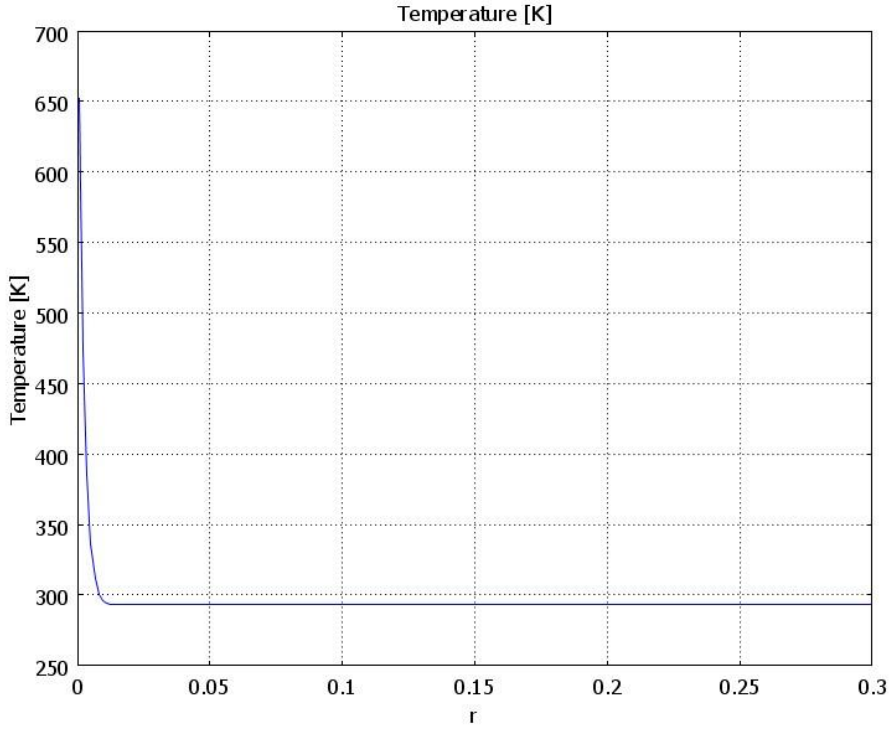

Figure 6.1.1 b. Profile of the temperature distribution in radial direction, z=0.15m. Surface temperature of the wire is 400ºC and it reaches the ambient temperature at 0.025 m.

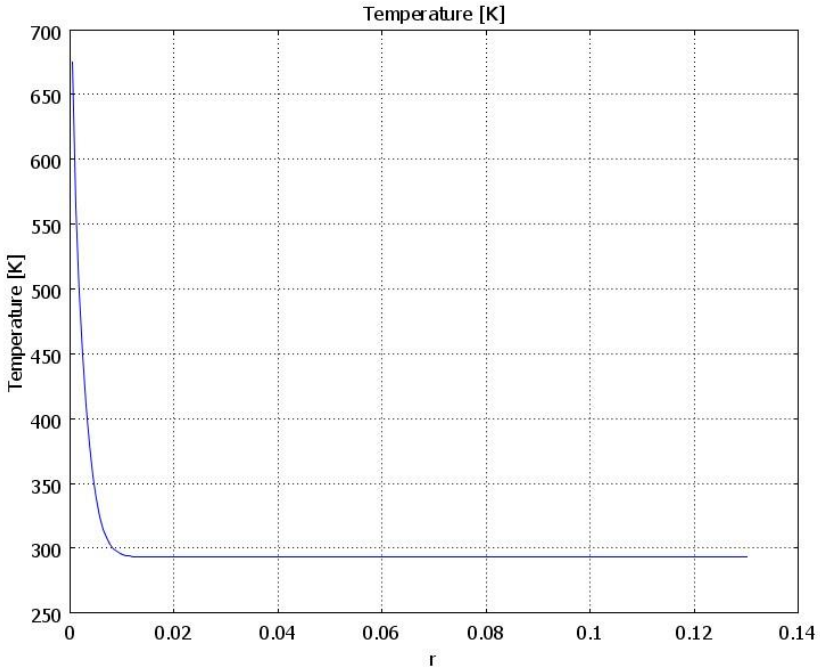

Figure 6.1.1 c. Zoom of the temperature distribution shown in the figure above. At 0.013 m from the wire the ambient temperature is practically reached.

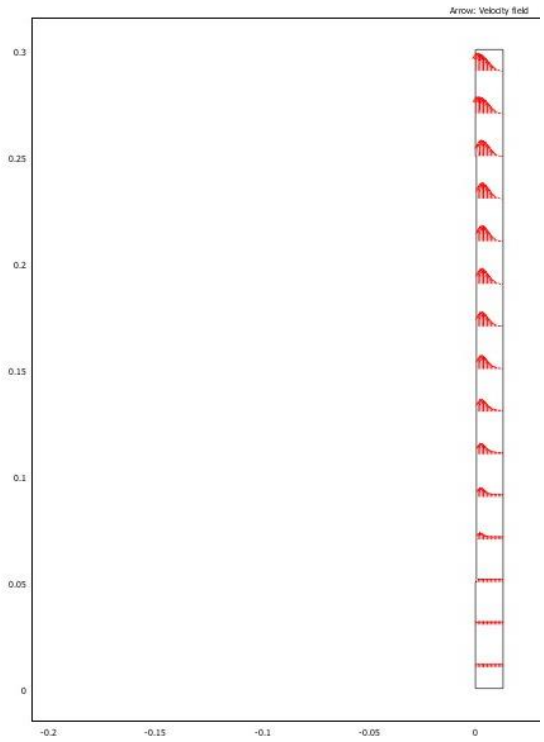

Figure 6.1.1 d. Velocity profile near to the heated wire, z=0.15m. The velocity is 0 at the wire surface and at infinity and has a maximum value at certain distance from the surface.

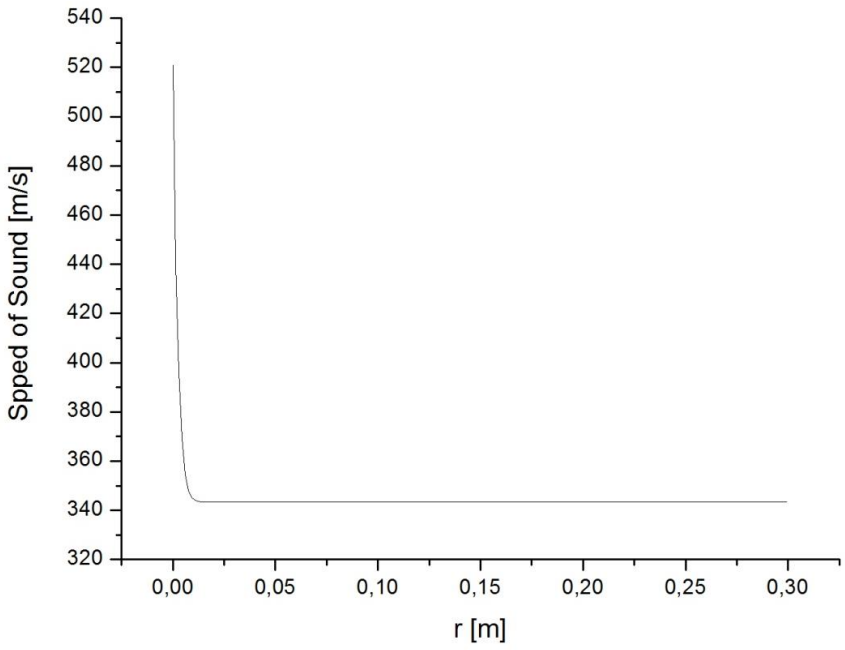

Figure 6.1.2 a Speed of sound around a hot wire as a function of the temperature. The wire is heated to 400ºC (673K)

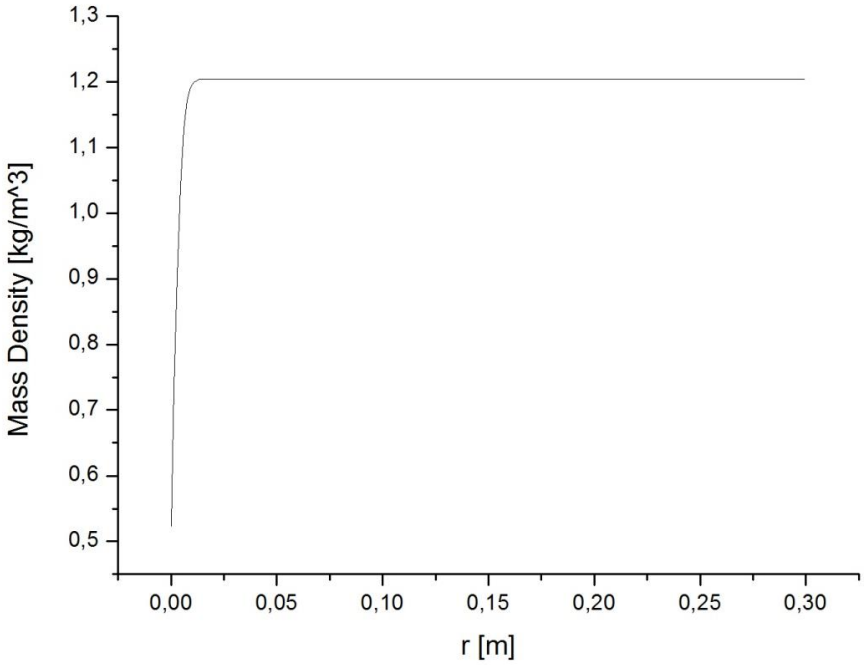

Figure 6.1.2 b Mass density of air around a hot wire as a function of the temperature. The wire is heated to 400ºC (673K)

From the temperature distribution around a hot wire it can be obtained the profile of the sound speed and the air density as a function of the distance using their temperature dependence according to Eqs. (1.2.3) and (1.2.4). Then these profiles are used to build the multilayer model. Figure 6.1.2a shows the change in speed of sound and figure 6.1.2b - the change in density of air.

It is appropriately to take care again of computational effort and time. Although the simulation indicates that room temperature is almost reached at 13 mm, it is suitable to reduce more this distance. Thus, the radius of subdomain where a single hot wire changes the properties of ambient air is considered 12 mm. Therefore, in our model we consider each wire with radius 0.5 mm inscribed in another circular domain with radius 12 mm, but the distance between the wires is maintained 13 mm. Then, applying the Pythagorean Theorem we obtain the distance between the vertical rows of our SC and it is d=22.5 mm. Fig.6.1.3 shows the SC structure and the dimensions.

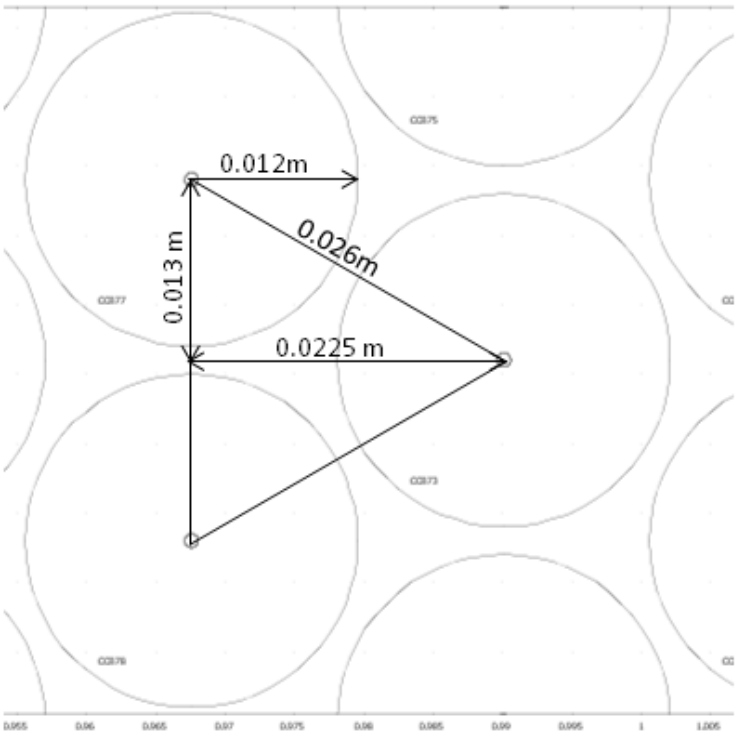

Figure 6.1.3 The structure of proposed SC made of heated wires. The distance between the large circles is 26 mm. The radius of the small circles which represents the wires is 0.5 mm. The radius of the subdomain where the air properties are considered affected is 12 mm. Finally, the calculated distance between the vertical rows of the SC is 22.5 mm.

6.2 Temperature field inside the SC

Now we must investigate the thermal field inside the SC. Heat conduction and natural convection are considered again and the temperature of the hot wires is 400ºC. First, we make a profile of the temperature distribution around the heated wires and then we calculate the mass density and speed of sound inside each circular subdomain as a function of the temperature following eq. (1.2.3) and (1.2.4). For this goal, we build an axisymmetric FEM based model of 3 heated wires inside the crystal for temperature T=400ºC. Fig.6.2.1 shows the model in 2D geometry. The heated wires are positioned at the vertexes of the equilateral triangle. The distance between each pair of wires is 0.0225 m. Next, 2D geometry is extruded to 3D in order to add the natural convection witch acts vertically. The final geometry is shown in Fig.6.2.2.

In FEM simulations, the General heat transfer and Weakly compressible Navier-Stokes are coupled. We assume that the ambient air entries only from the lower surface and leaves the geometry as hot air through the upper surface. The set of hot wires around the considered model impedes that heat transfer in horizontal direction occurs.

In General heat transfer as boundary condition on the wires is imposed the temperature 400ºC. Room temperature condition for lower surface and convective flux for the upper surface are considered. On all other surfaces is symmetry condition imposed. In Weakly compressible Navier-Stokes on the wires the boundary condition is that all the velocity components must be zero (Figure C.3.5). On the

lower surface is inlet condition imposed, and on the upper one - open boundary. The rest of the boundaries is completed with symmetry condition. Thus, the eq. *(C.3.20)* and *(C.3.28)* are resolved simultaneously and the solution is shown in Figure 8.2.3. It can be seen how the temperature of the air between the wires increases with the height of the wires. Red line at half height corresponds to the plane where some horizontal cuts are made in order to describe the temperature distribution inside. These cuts are shown on figure 6.2.3 and 6.2.4. It can be seen that the lowest temperature inside the model at z=0.15 m is about 32ºC

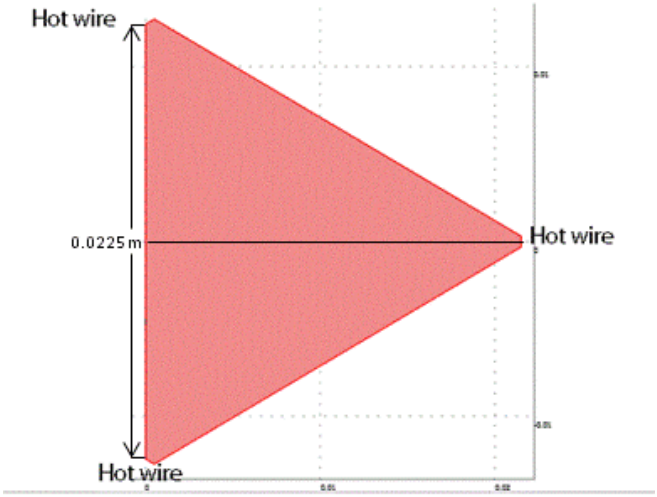

Figure 6.2.1 2D model of 3 heated wires. The wires are positioned at the vertexes of the equilateral triangle and the distance between them is 0.0225 m.

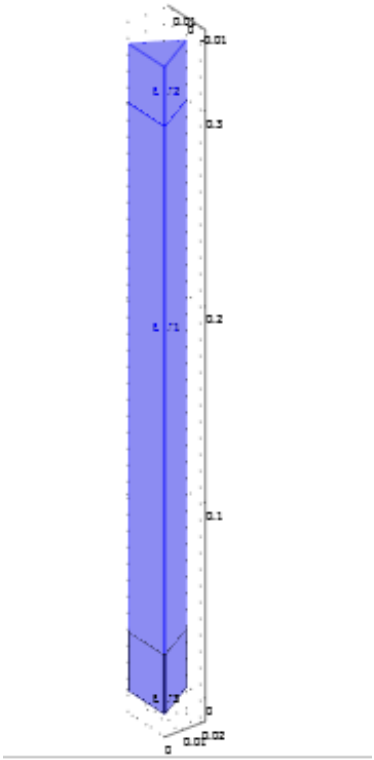

Figure. 6.2.2 3D model of three heated wires. The wires are positioned at the edges of the geometry. High and low additional subdomains are added with aim to make lighter the FEM calculus.

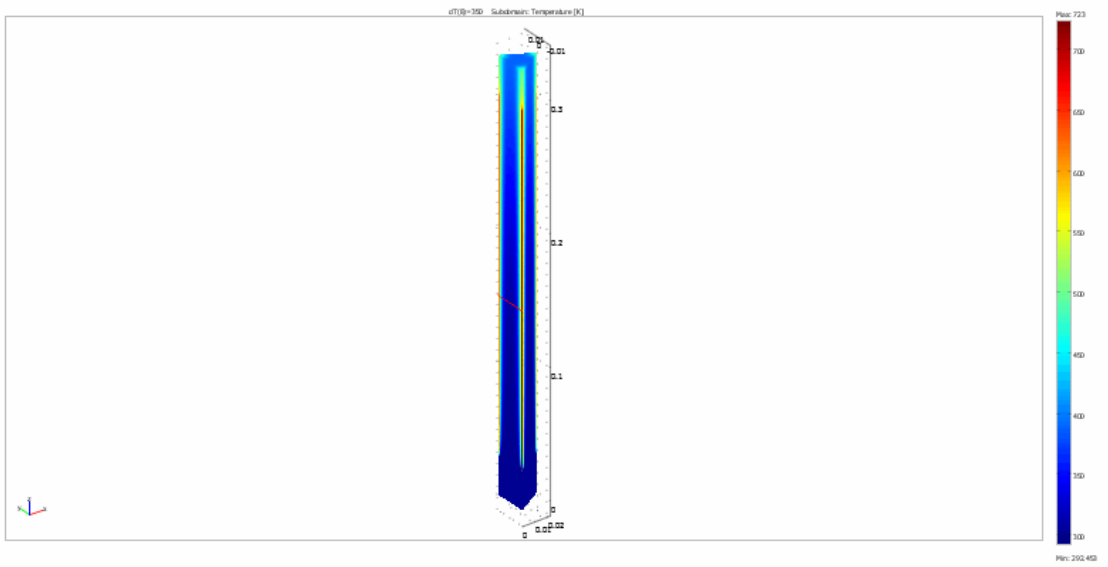

Figure 6.2.3a Temperature distribution of air between 3wires heated to 400ºC. In accordance with the eq. (C.3.20), the temperature increases from the bottom to the top of the model.

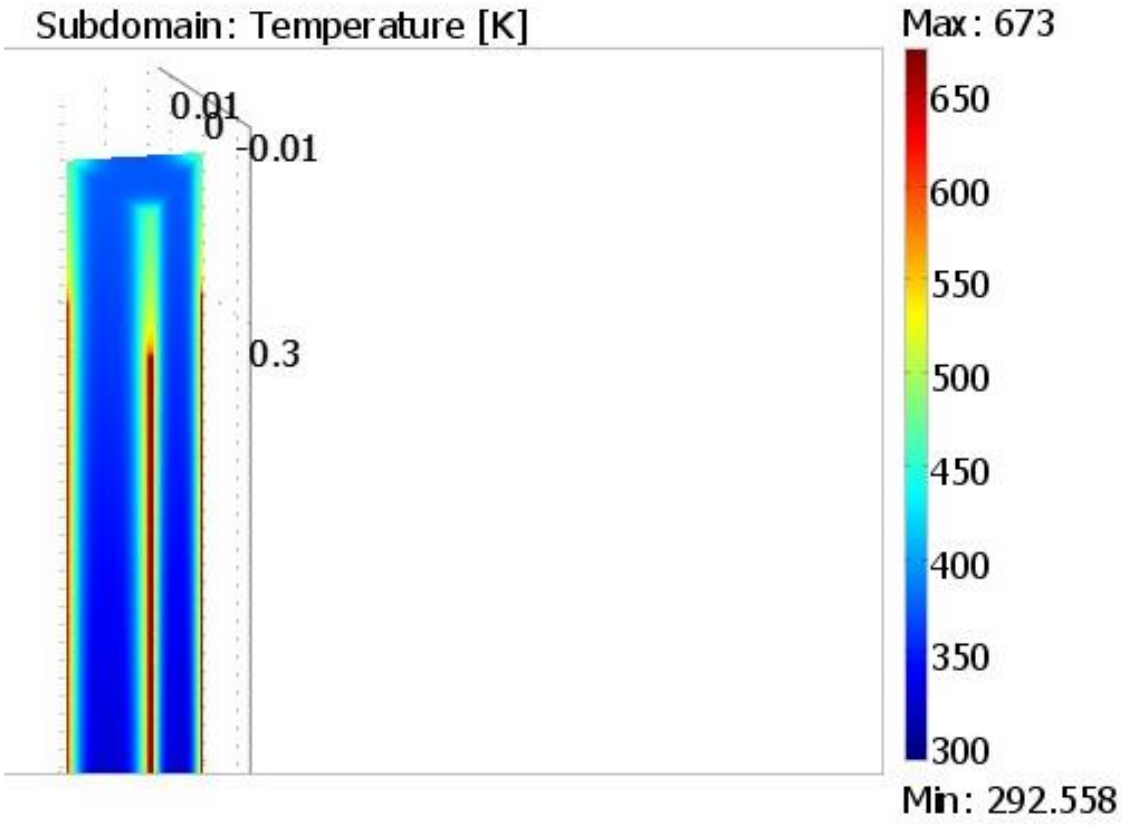

Figure 6.2.3b Zoom of the temperature distribution of air between 3 hot wires showed in figure 6.2.3a In accordance with the eq. (C.3.20), the temperature increases from the bottom to the top of the model.

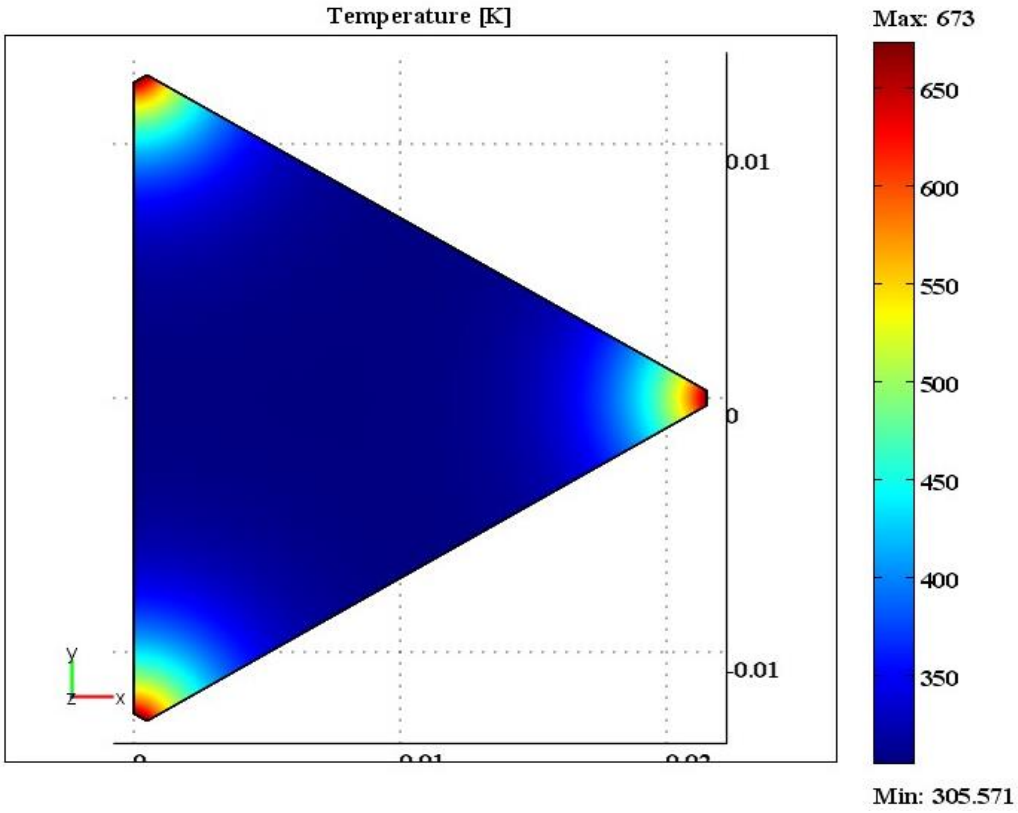

Figure 6.2.3c Horizontal cross-section at z=0.15m. of 3 hot wires showed in figure 6.2.3a

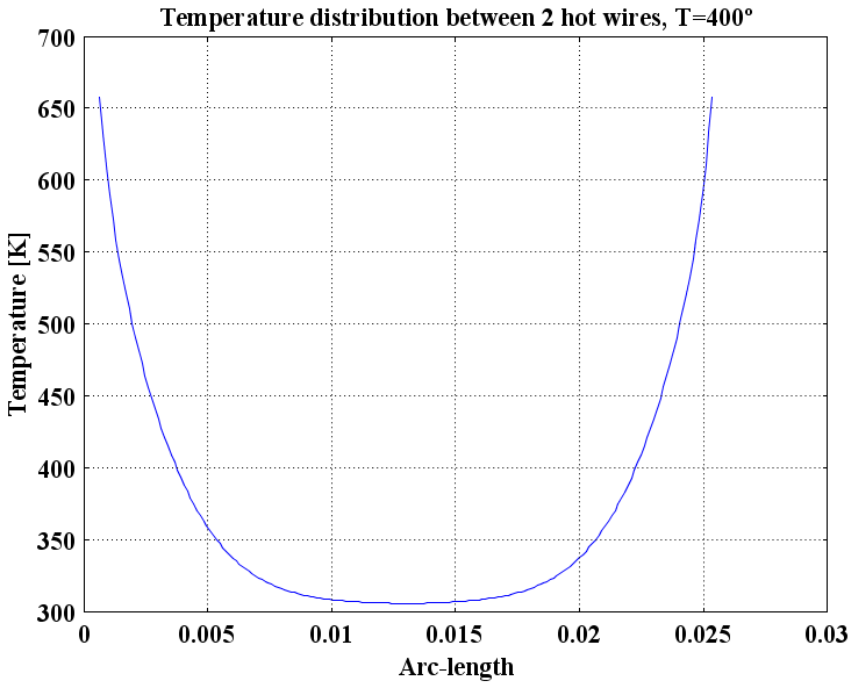

Figure 6.2.4 Horizontal lateral cut between 2 wires heated to 400ºC. The height of the cut is z=0.15m from the bottom of model, which corresponds to the red line in Fig.6.2.3a. The temperature reached between the wires is about 305K.

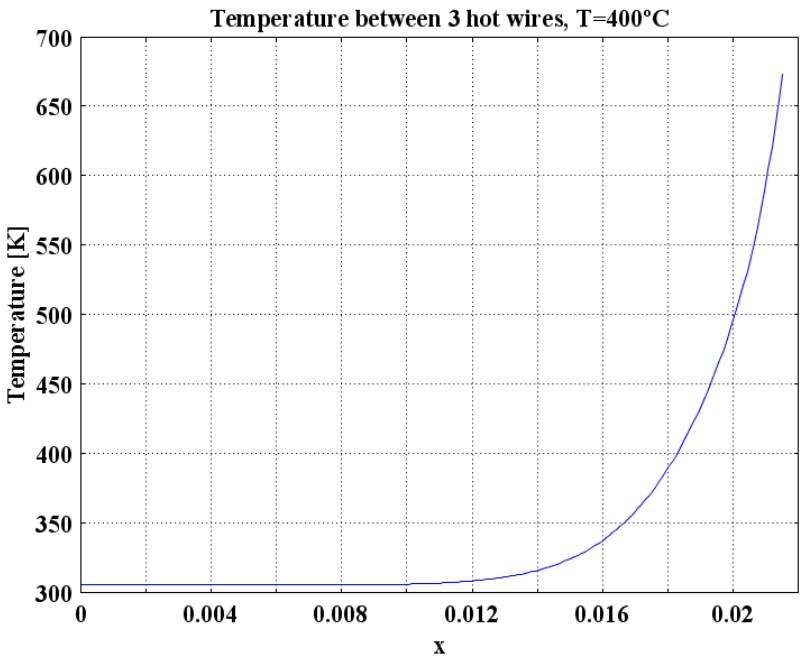

Figure 6.2.5 Horizontal cut from one wire heated to 400ºC to the opposed edge of the investigated subdomain. The height of the cut is z=0.15m from the bottom of model. The reached temperature is about 305K

The cut of Figure 6.2.5 is approximated with a mathematical function which best fits the data. For temperature of 400ºC a Boltzmann sigmoidal function is used (eq. 6.2.1). Figure 6.2.6 shows the fit with a Boltzmann function for T=400ºC.

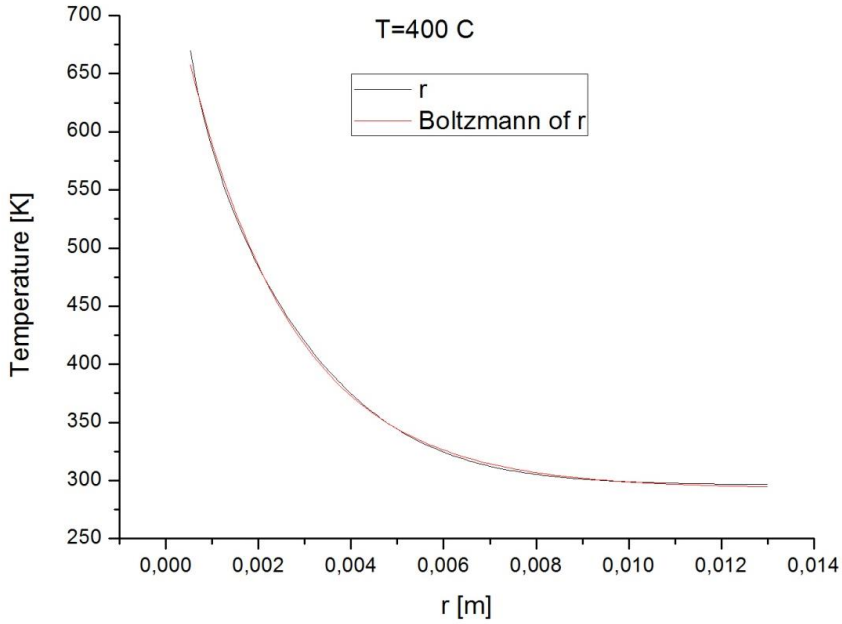

Figure 6.2.6 A fit of the data obtained for wire heated to 400ºC. For fitting is used a Boltzmann sigmoidal function.

The Boltzmann sigmoidal function can be written as:

$$T = A_2 + \frac{(A_1 - A_2)}{1 + e^{\frac{r - x_0}{dx}}}, \qquad (6.2.\ 1)$$

where A_1, A_2, dx, and x_0 are given coefficients and r represents the current coordinates.

For T=400ºC the coefficients of Boltzmann function are described in the next table:

Temperature (°C)	A1	A2	x0	dx
400	35352.34485	293.11019	-0.00983	0.00227

Table 6.2.1 Table of coefficients for T=400°C

Now we only need to add the data from the table to the circular subdomains of Figure 6.1.3. Inside each subdomain the air has properties, e.g. speed of sound and mass density, changed by the high temperature of the wire in center. Therefore, the heated wire can be considered as a scatterer with radially changed properties. Figures 6.2.7 (top) and (bottom) show the density and speed of sound inside the subdomain with radius 12 mm. It can be seen that the values of density and speed of sound are slightly lifted because the room temperature between the hot wires is not completely reached.

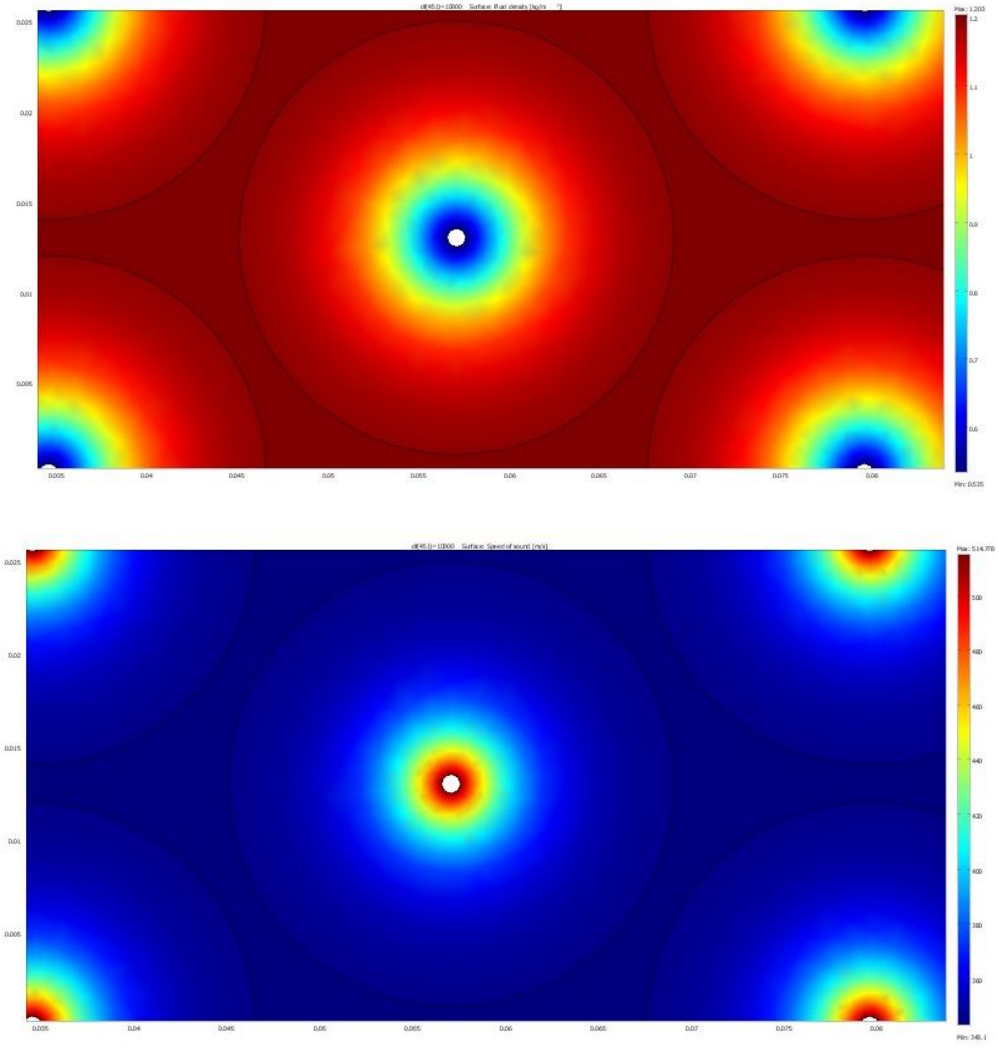

Figure 6.2.7. Top: Density around the hot wire as a function of the temperature inside the subdomain with radius 0.012 m. Bottom: Speed of sound inside the subdomain.

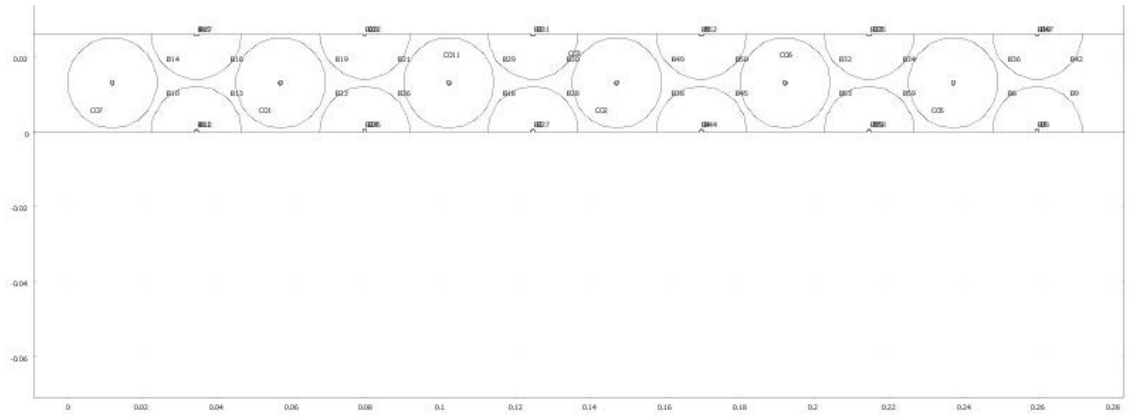

Figure 6.2.6 Geometry of 12 layers SC**.**

The rest of the domain has the properties of air at normal conditions (T=20ºC, density ρ=1.19 kg/m^3 and speed of sound c = 343 m/s).

6.3 Acoustic pressure simulations

In our model three different SCs are investigated: with 6, 9 and 12 layers. Fig. 6.2.6 shows the geometry of SC with 12 layers. On the both sides the crystal is considered symmetrical and hence the sample acts as an infinite crystal in vertical direction. On the boundaries of subdomains conditions of continuity are imposed and the boundaries of wires are considered as sound hard boundaries, i.e. the normal component of the particle velocity vanishes.

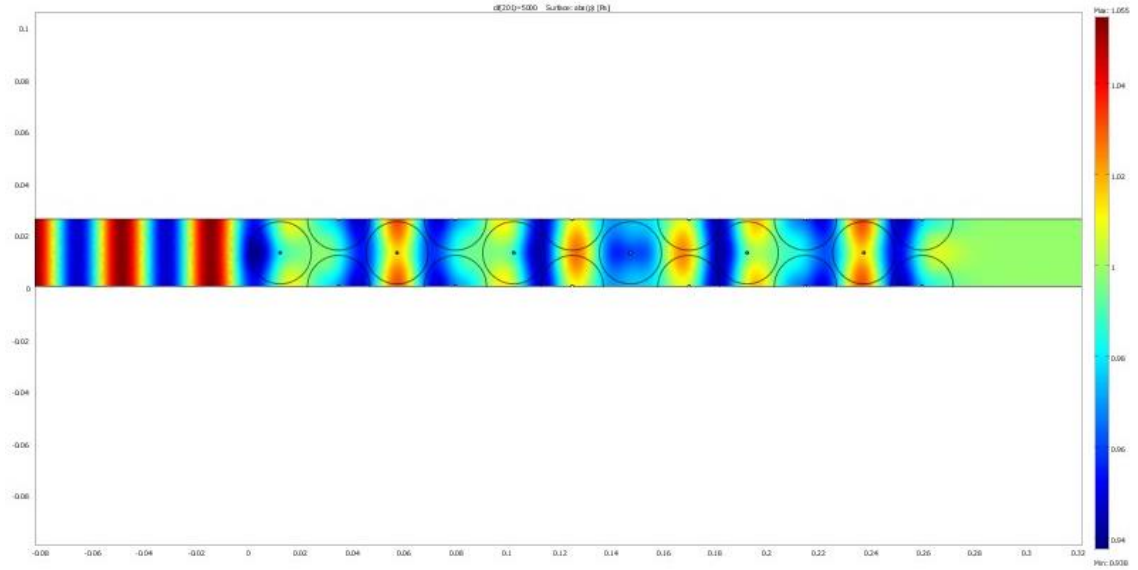

Figure 6.3.2 A standing wave formed in front of the crystal for 5 kHz

We use a plane wave in frequency range of 1 up to 10 kHz as an incident wave. Fig. 6.3.2 shows a standing wave formed in front of the crystal. Studying its maxima and minima the reflectance can be obtained by equation (5.2.3). In addition, behind the crystal the amplitude of the transmitted wave is constant and it is easy to obtain.

Figure 6.3.3 shows the transmission coefficients for different frequencies and number of layers. It can be observed a minimum for frequency about *f*=7900. This is the Bragg frequency when the Bragg condition (2.5.3) is satisfied and a strong reflectance occurs. As the distance between the layers is 0.0225 m, we can easily calculate the Bragg frequency from (A.2.8). For T=400ºC the average speed of sound in the chosen subdomain is about 356 m/s, and the wavelength must be two times the distance between the layers. Then:

$$f = \frac{C}{2d} = \frac{356\,m/s}{2*0.0225m} \approx 7911 s^{-1} \qquad (6.3.\ 1)$$

Apparently, the simulation and the analytical calculation are in good agreement.

Also, it can be seen that the minimum is stronger when the number of layers increases.

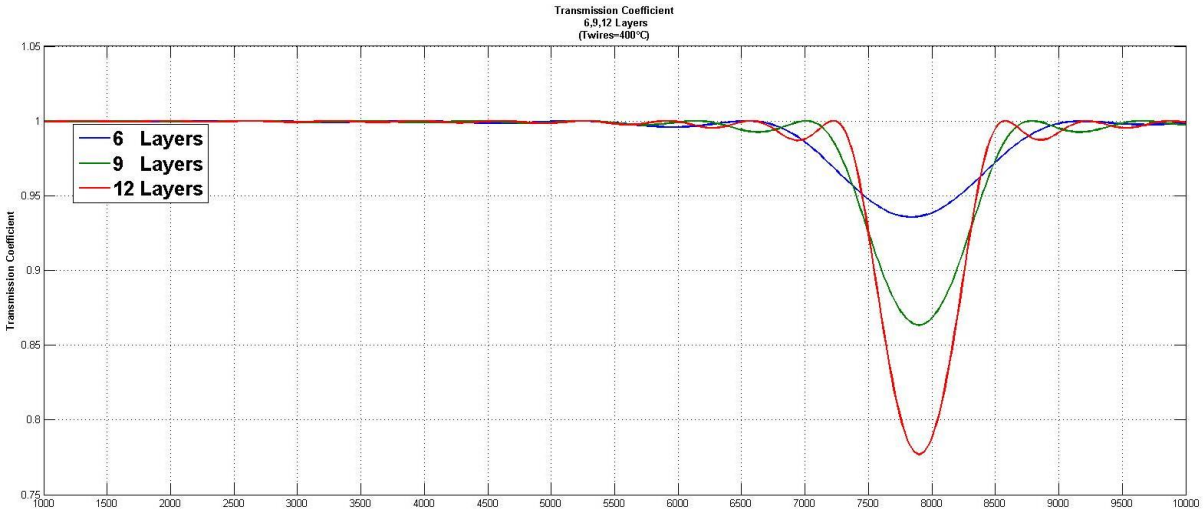

Figure 6.3.3 Transmission coefficients as a function of the frequency and number of layers.

If the transmission coefficients are known, it is easy to calculate the reflectance coefficients. As $R = \sqrt{1 - T^2}$, we only need to substitute T in the equation. Fig.6.3.4 shows the reflection coefficients as a function of the frequency and layers number, and Fig.6.3.5 - a zoom in the area of maximum.

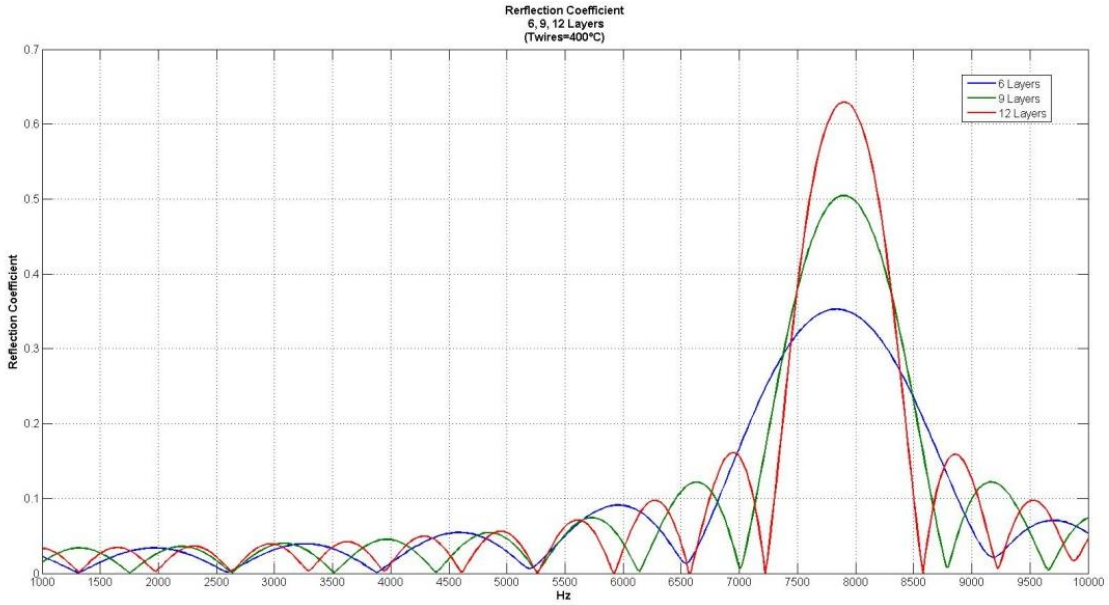

Figure 6.3.4 Reflection coefficients for 6, 9 and 12 layers.

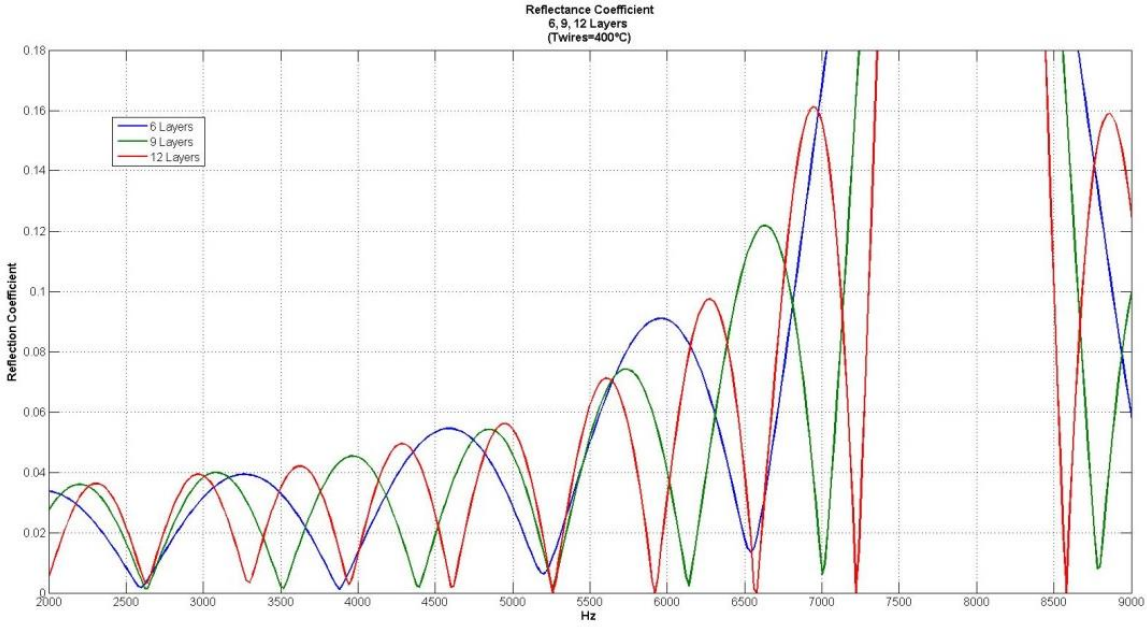

Figure 6.3.5 Zoom of the previous figure.

6.4 Acoustic analogue of FBG

An acoustic analog of the Fiber Bragg grating can be a SC shown in Fig. 6.4.1. It has 12 layer, but not all of wires are heated. First three layers are formed by hot wires, but next three are at room

temperature. Then this configuration is repeated. Thus, a periodic change of refractive index is achieved.

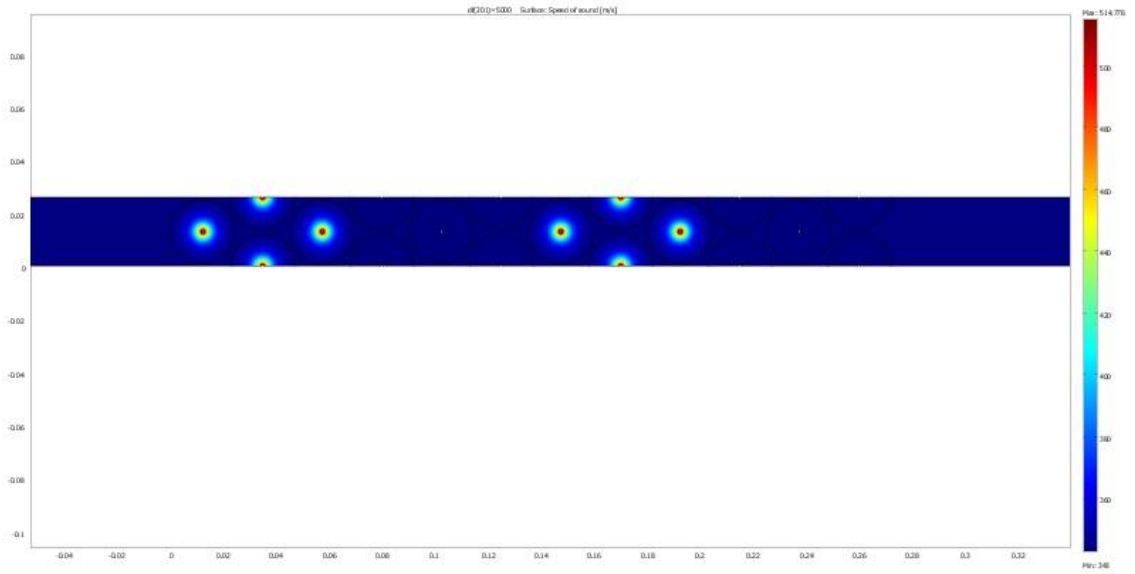

Figure 6.4.1 SC as an analog of optic Fiber Bragg Grating.

Figure 6.4.2 shows the acoustic pressure map in this case and figure 6.4.3 presents the reflection coefficients. It can be observed that at frequency f = 3955Hz, which is the half of the original SC Bragg frequency, a moderate reflection (R=0.15) appears; this peak would increase if more alternating layers are added.

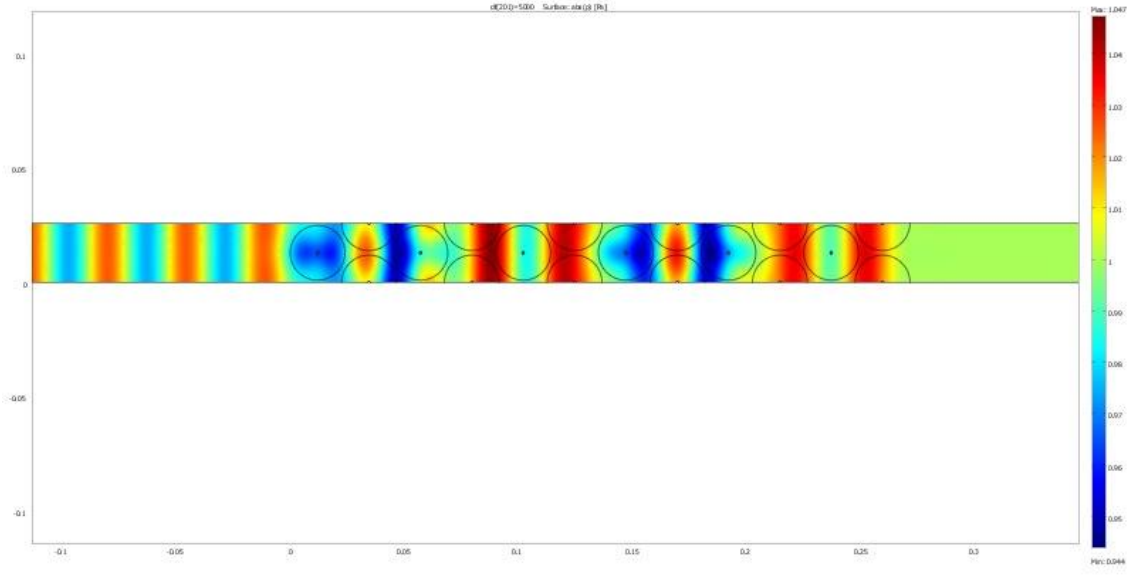

Figure 6.4.2 Acoustic pressure map, FBG SC

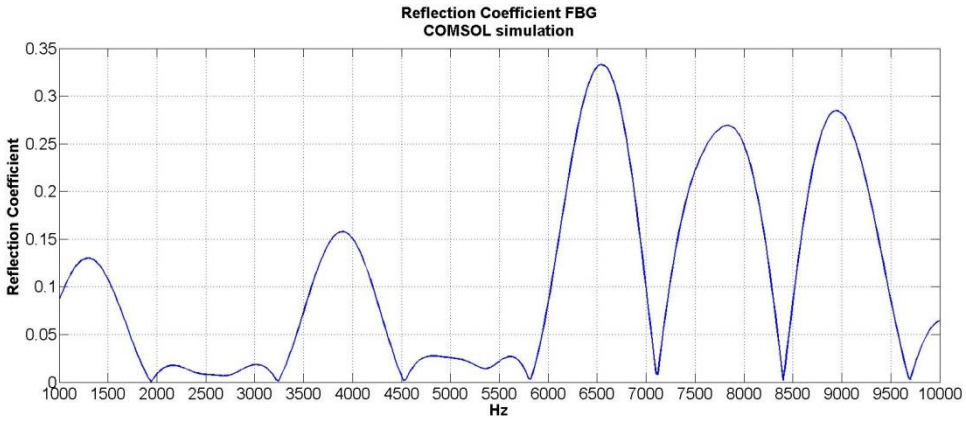

Figure 6.4.3 Reflection coefficients for FBG SC

6.5 Reflection coefficients as a function of the temperature for an equivalent homogeneous medium.

For wavelengths, much larger than the distance between the layers, i.e. for frequencies considerably lower than the Bragg frequency, the SC can be considered as an effective homogeneous medium with an average temperature, density, speed of sound, refractive index, etc.

Equation (1.4.8), applied for a homogeneous medium, shows that the reflectance depends on the thickness L of the medium. For a given SC L= (*N-1)*d*, where *N* is the number of layers, and *d* is the distance between the layers. Thus, for SC of 6 layers in our model L= (6-1)*0.0225 m =0.1125 m. For 9 layers L=0.18 m and for 12 L=0.2475 m.

The maximum reflectance is obtained when the cotangent function in the denominator is 0. It is fulfilled for $k_2 L = (2m+1)\frac{\pi}{2}$. Then

$$R_{max} = \frac{\eta^2 - 1}{\eta^2 + 1}. \qquad (6.5.1)$$

where η is:

$$\eta = \frac{\rho_2 c_2}{\rho_1 c_1}, \qquad (6.5.2)$$

where both ρ and c depend on the temperature accordingly to (2.2.3) and (2.2.4). Hence, the reflection coefficients must depend on the temperature.

Figures 6.5.1, 6.5.2 and 6.5.3 show the frequency dependence of the reflection coefficients as a function of the temperature and number of layers. When the temperature increases the reflection coefficients increase too. Adding more layers does not contribute to obtain higher values of reflectance but it increases the number of frequencies where the reflectance is 0. This conclusion is true only for wavelengths larger than the lattice parameter *d*. In this case the crystal can be considered homogeneous.

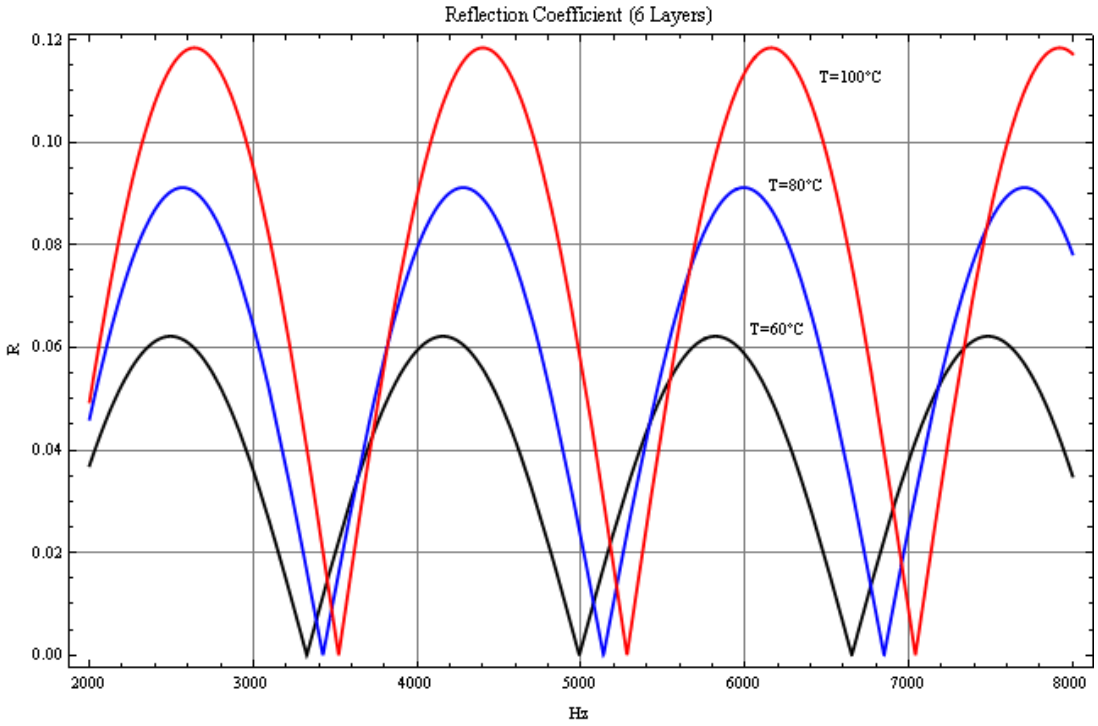

Figure 6.5.1 Reflection coefficients for L= 0.1125 m which corresponds to 6 layers at three different temperatures

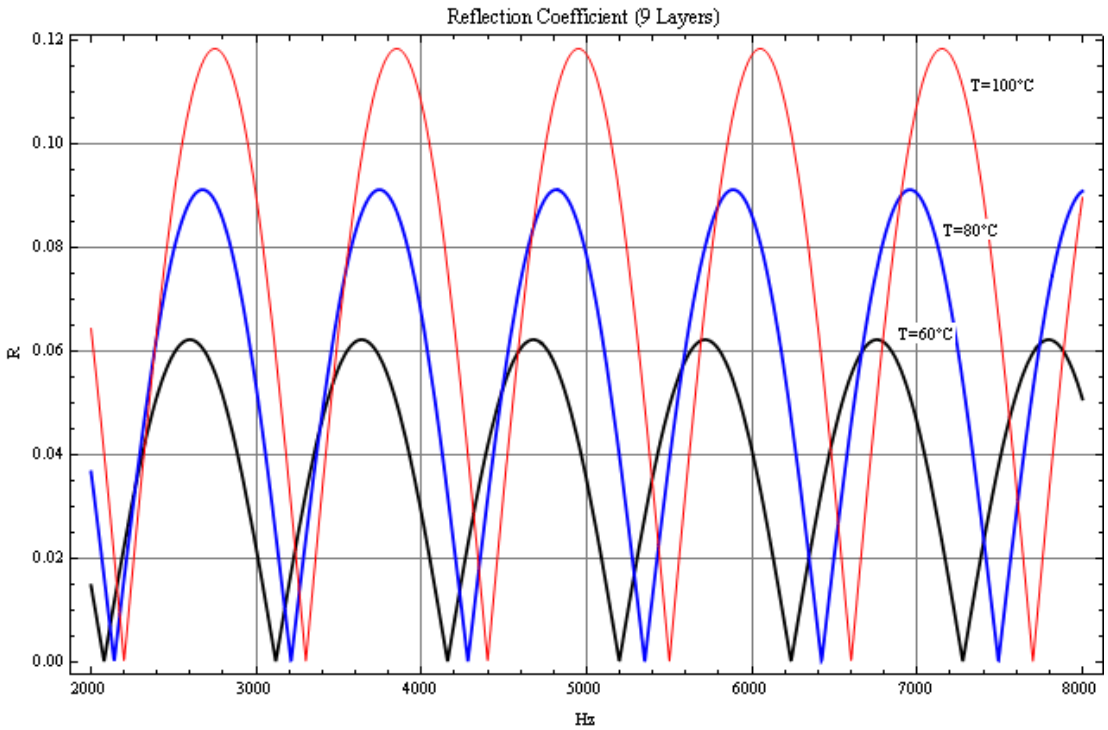

Figure 6.5.2 Reflection coefficients for L= 0.18 m which corresponds to 9 layers at three different temperatures. The maximum reflectance has the same value as in figure 6.5.1 but the number of frequencies with R=0 has increased.

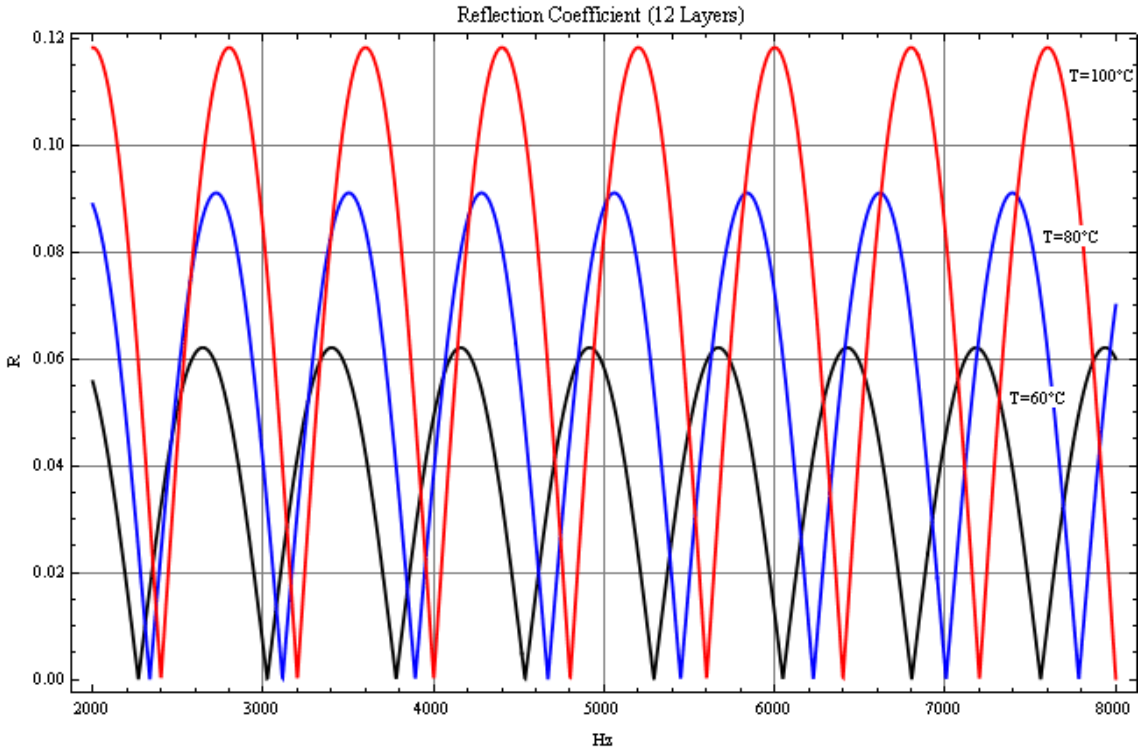

Figure 6.5.3 Reflection coefficients for L=0.2475 m which corresponds to 12 layers at three different temperatures. The maximum reflectance has the same value as in figure 6.5.2 but the number of frequencies with R=0 has increased

Chapter 7

Experimental Study of the Properties of SC Made of Heated Wires

A specific experimental setup is developed with the aim to demonstrate the properties of a SC of heated wires, theoretically studied in the previous chapter. Nichrome wires with diameter 0.2 mm, vertically positioned, are used as hot scatterers. The lattice of wires consists of 12 layers with hexagonal geometry (Fig.7.1). An aluminum support with dimensions 26x28x36 cm is prepared for the measurements. Each wire can be heated by applying ac current to its ends. The temperature of the wires can be modified controlling the electric current intensity. Next, some measurements results are presented.

Fig.7.1 The cage formed by the wires from nichrome and aluminum support

7.1 Experimental setup

The experimental setup is shown in Figure 7.1.1 (a) and (b). The most important parts are:

1. A computer controlled positioning system
2. Fiber glass acoustic absorber
3. Horn
4. Power Amplifier Samson Servo 300
5. Graphic Equalizer DBX 1231
6. Workstation NI-PXIe with two data acquisition cards.
7. Preamplifier Brüel&Kjaer 2694
8. Microphone Brüel&Kjaer type 4958
9. Step Motor Controller
10. Cage supporting the lattice of wires (SC) (Fig.7.1)
11. Speaker

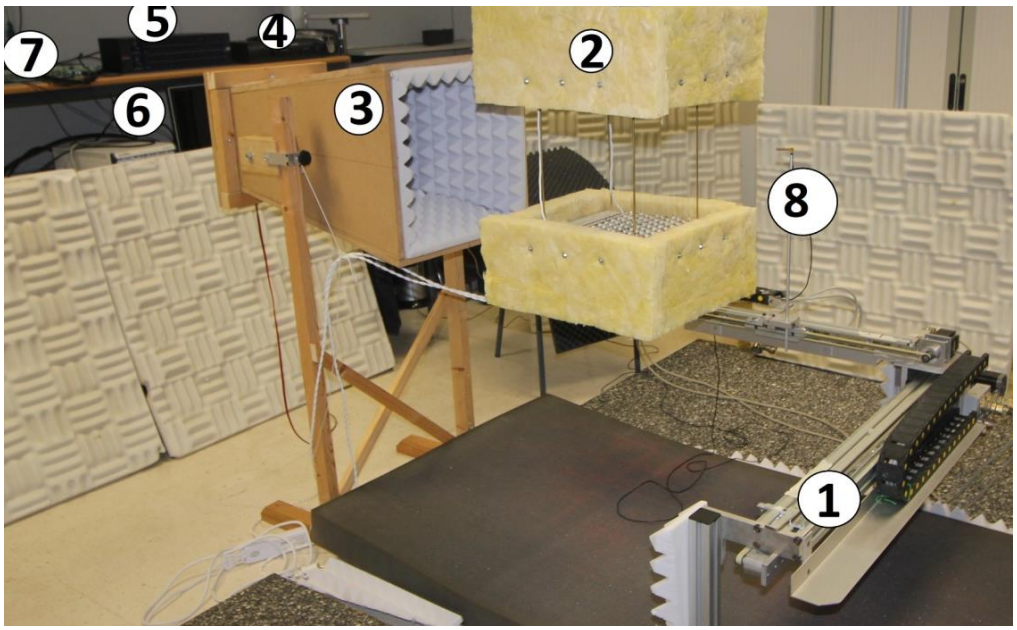

Figure 7.1.1 (a) Experimental setup

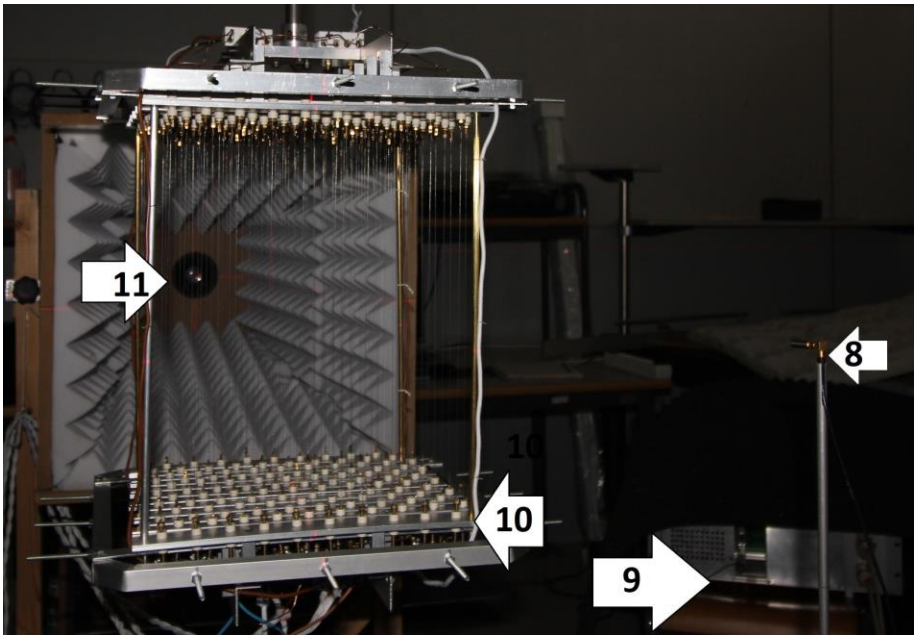

Figure 7.1.1 (b) Experimental setup

The data acquisition cards in the workstation have different functions. One generates the signal and sends it to the speaker and another analyzes the measured signal and saves the data into the hard disc. A computer controlled positioning system is used to move the microphone through a grid of measurement points with a maximum resolution of 0.25 mm per step. The cage with wires is hung on a frame. A special horn is prepared with purpose to obtain a better collimation of the incident beam and to avoid undesired scattering. A chirp signal with duration 75 ms and amplitude 0.1 V is send to the crystal and subsequently measured after scattering by the wires. Five chirp signals are averaged and a frequency analysis is performed. The obtained data are saved for frequencies from 500 Hz to 10 kHz with a resolution of 5 Hz.

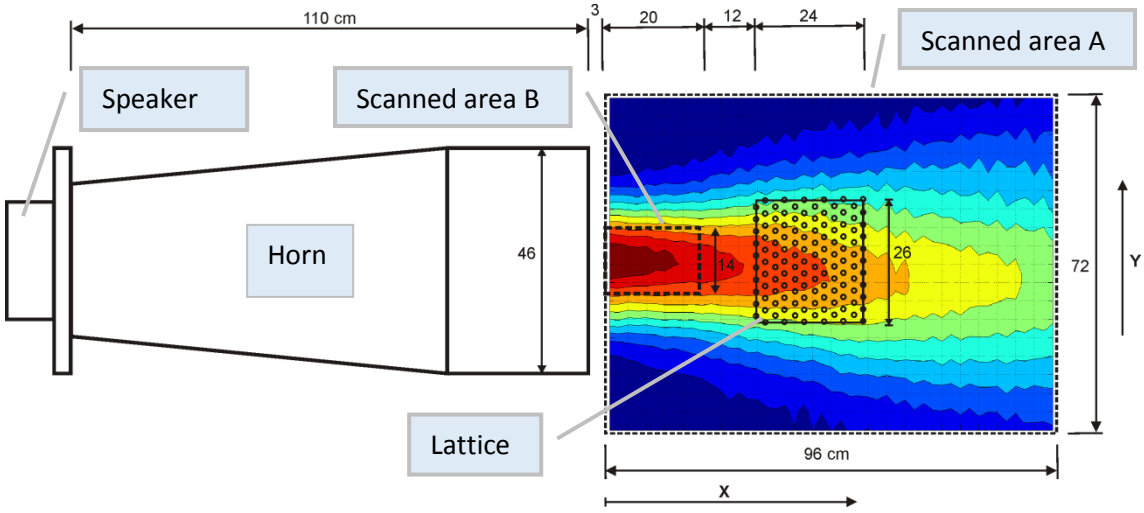

Figure 7.1.2 Scheme of the experimental setup

7.2 Acoustic measurements

First of all, we need to measure the acoustic field produced by the speaker together with the horn in order to check the quality and regularity of the emitted sound. Also, it is necessary to evaluate the changes in the scattered pressure field originated by the SC. A scanned area A of 96x72 cm is considered for the measurements (Fig. 7.1.2). The grid step is 2 cm in both axis. The obtained map for 5 kHz is showed in Figure 7.2.1

The Fig.7.2.2 shows the incident spectrum at three specific distances - in front of the crystal, inside the crystal and behind the crystal. Blue line corresponds to the distance of 35 cm from the horn border where the left edge of the crystal is supposed to be positioned. The green line corresponds to the center of the SC and the red one - to the back.

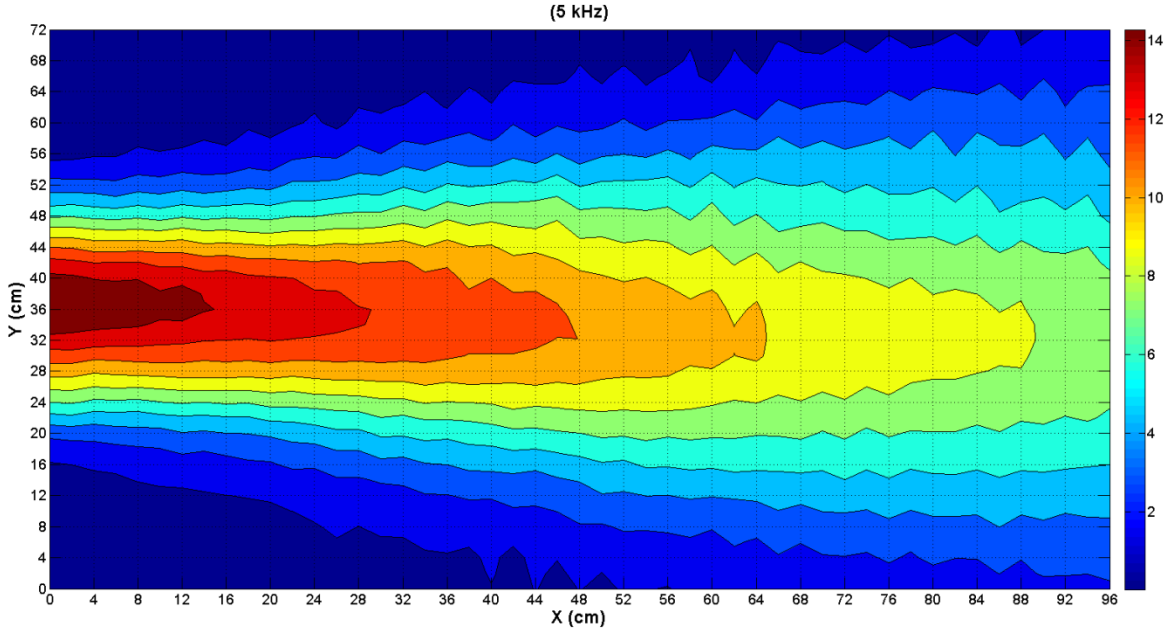

Figure 7.2.1. Map of the acoustic pressure field produced by the loudspeaker with the horn at 5 kHz (arbitrary units).

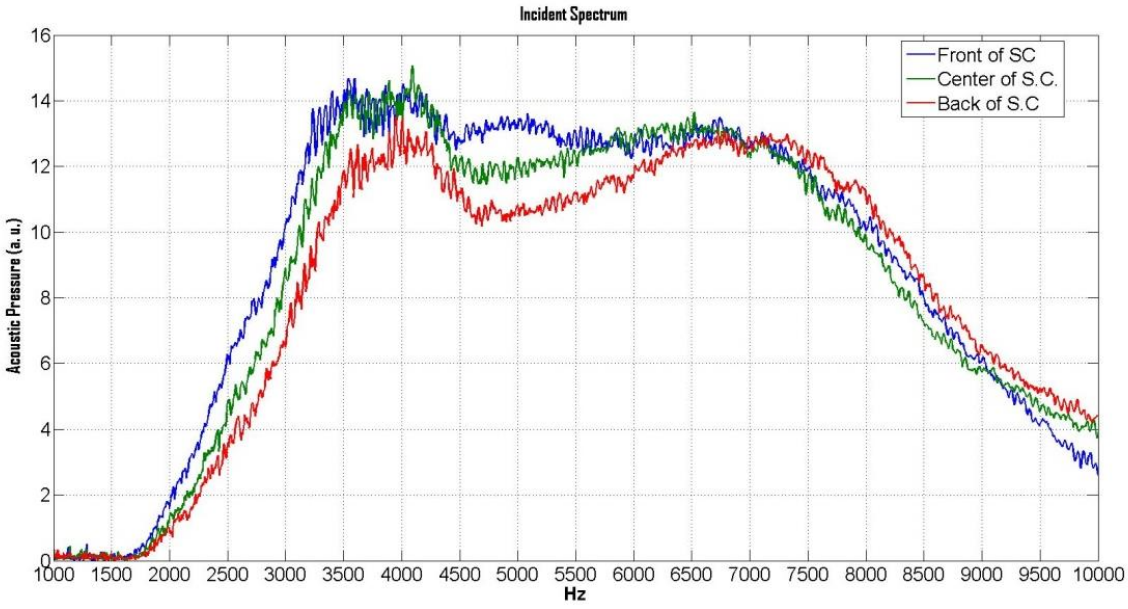

Figure 7.2.2 Spectrum of the incident wave after five times averaged chirped signals.

With measurements of the standing wave in front of the crystal (see scanned area B in Fig. 7.1.2) and applying eq. (7.2.2) it can be obtained the reflection coefficient. Figure 7.2.3 represents a map with dimensions 20x14 cm (with step 0.5 cm in X axis and 2 cm in Y axis) in front of the crystal where a standing wave can be observed. Figure 7.2.4 is a longitudinal cross-section of the map. In order to estimate the average amplitude of the standing wave we use the dominant component of the Fourier analysis of the measured signal shown in the figure.

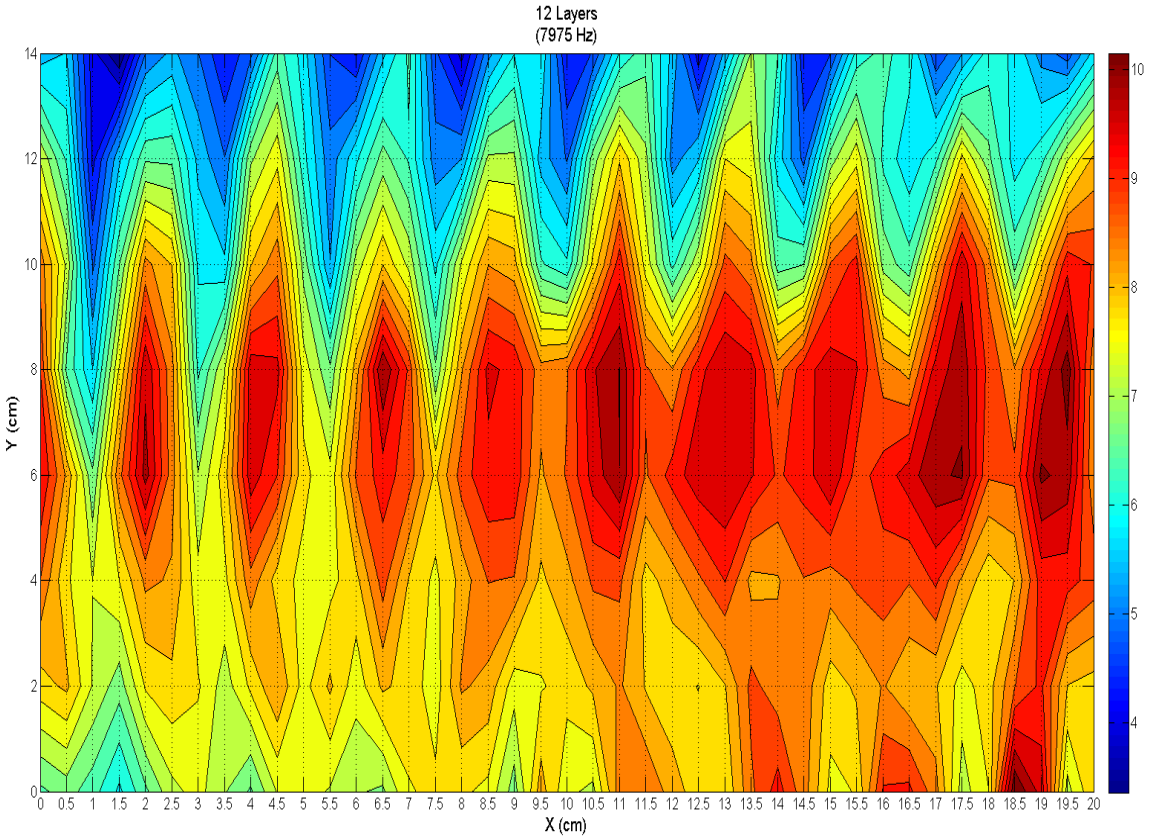

Figure 7.2.3 Acoustic pressure map at 7975 kHz obtained in the scanned area B, in front of the crystal with 12 layers (arbitrary units)

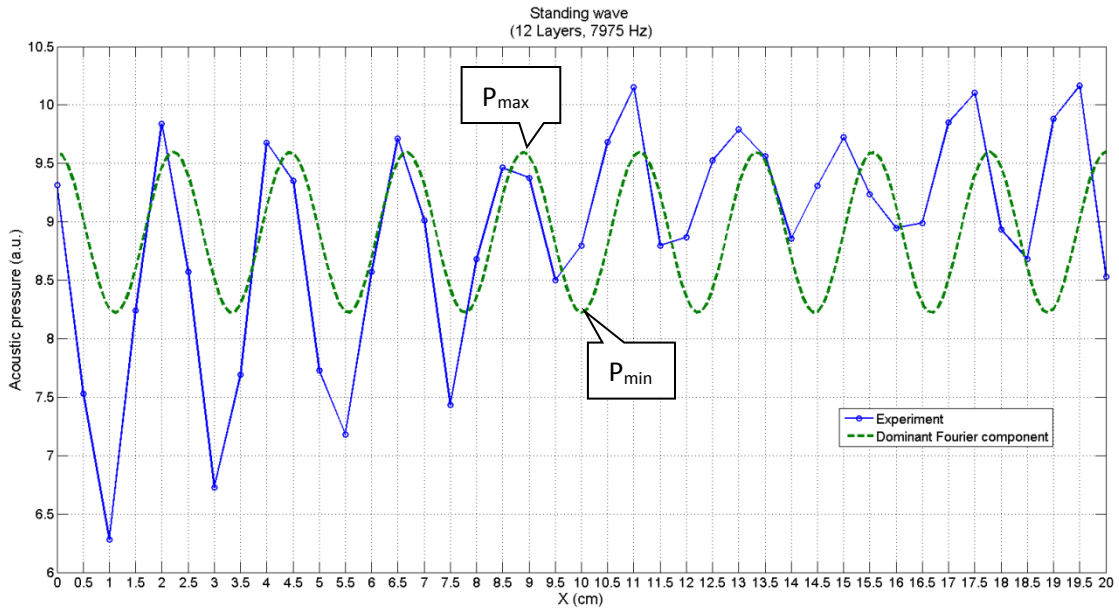

Figure 7.2.4 Cross-section along the symmetry axis of the previous figure. The average amplitude of the standing wave is obtained from the dominant component of the Fourier analysis of the measured signal shown in the figure.

The figure 7.2.5 shows the measured reflection coefficient for 3 different SCs: of 6, 9 and 12 layers. The results can be compared with corresponding numerical simulations shown in Figure 6.3.4. The measured reflection peaks are below the simulated ones. Probably the reason is that the viscosity of the air increases with the temperature and consequently, the absorption. For frequencies above 6400 Hz the reflection coefficients for heated wires are considerably greater than the ones for cold wires. Three prominent peaks appear in this frequency range for the three crystals. The maximum reflection occurs for each of the SCs at about 8300 Hz. This frequency is higher than the predicted Bragg frequency of 7911 Hz (see figure 6.3.4). Perhaps it is due to the possibility that not all the wires have the same temperature. The displacement toward higher frequency indicates that the wires have higher temperature than the simulated.

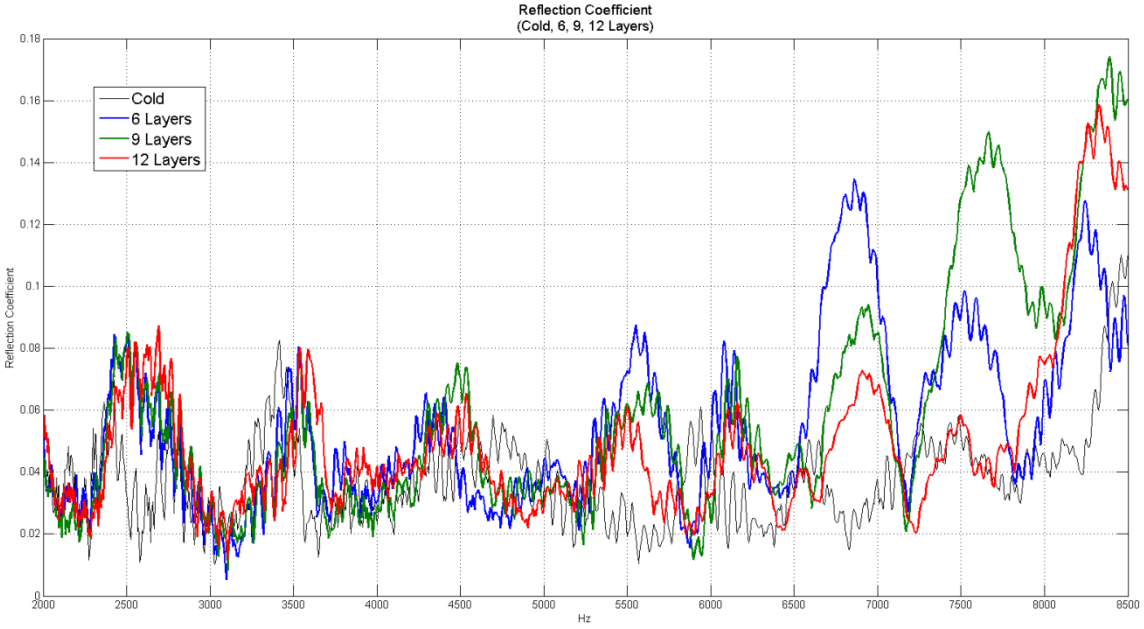

Figure 7.2.5 Reflection coefficient for 3 different numbers of layers of SC. Blue line corresponds to 6 layers, green - to 9 and red one to 12.

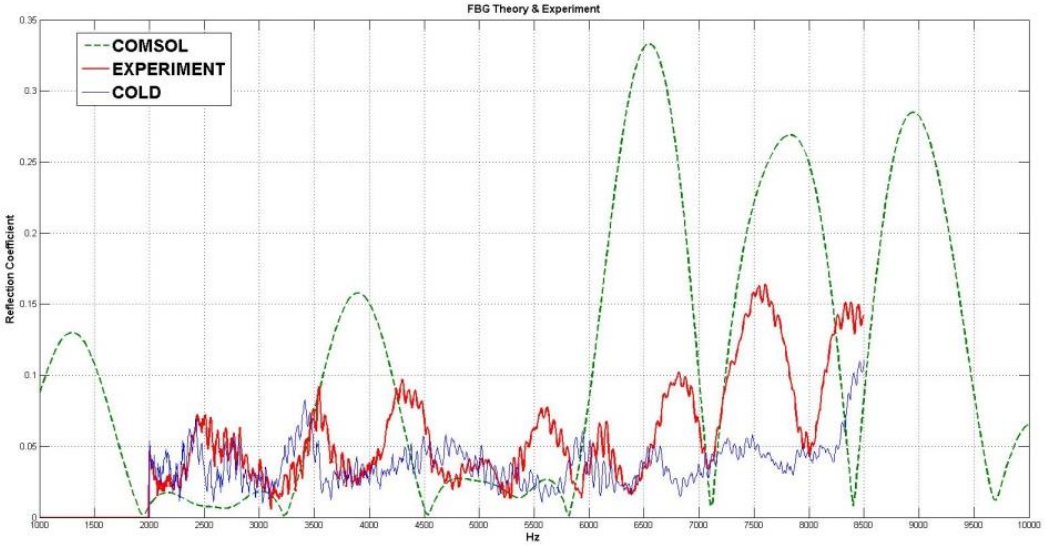

Figure 7.2.6 A comparison between the FEM simulations and experimental data for an acoustic FBG

A very interesting case is about acoustic analogue of FBG, described in section 8.4. Fig. 7.2.6 shows a comparison of the numerical simulations and experimental data. The measured reflection peaks are below the simulated ones. Once again, probably the reason is that the viscosity of the air increases with the temperature and consequently, the absorption. Unfortunately, there is no good agreement between the measured and simulated data.

7.3 Conclusions

The frequency where the reflection coefficients are maxima denotes the existence of Bragg frequency for SCs made of heated wires. The Bragg frequency of the measured peaks is shifted toward higher frequencies in comparison with the simulation. It can be explained assuming that the temperature of the wires is higher than the simulated one.

Because of the natural convection it exists a temperature gradient inside the SC from the bottom to the top (see figure 6.2.3a). When a plane wave impinges on the left side of the crystal (see figure 7.1.2) its wave vector points in the horizontal direction, but while the wave propagates inside the crystal the wave vector bends toward the bottom of the SC. Then it is difficult to predict the shape of the reflected wave.

The average temperature for each horizontal plane inside the crystal is different for different heights. Then the reflection coefficient is different for different heights. When we try to measure an effective reflection coefficient for the whole crystal in fact we obtain a complicated composition of different coefficient values.

Part III

Gradient-Index Sonic Crystals

Chapter 8

Fundamentals of Gradient-Index Sonic Crystals

8.1 Introduction and objectives

The properties of SCs have been employed to design refractive devices like, for example, acoustic lenses whose focusing properties are based on their external curved surfaces [Mey72, Cer01] or Fabry–Perot type acoustic interferometers [Sán03]. Recently, gradient index (GRIN) sonic lenses based on homogenized 2D SCs have been proposed [Tor07, Lin09, Lin12]. A GRIN SC is a crystal with variable properties in order to obtain given propagation characteristics. The index gradient can be obtained by changing the SC filling fraction, which is directly related to the local refraction index. The hyperbolic secant law is especially known to result in focusing of an incident plane wave [Lau15]. 2D GRIN SCs composed of different cylinder materials along different rows have been also theoretically and experimentally demonstrated [Lin09, Cli10]. In optics, the index of refraction is a measure of the slowness of light in a material as compared to the vacuum. Since light rays tend to bend toward the regions with higher index of refraction, engineering the index distributions leads formations of new type of devices.

Like their optical counterparts, the proposed 2D GRIN SC lenses have flat surfaces and are of easier fabrication than curved SC lenses. The bending of sound waves obtained by GRIN acoustics structures have been also proposed to produce acoustic mirages in a laboratory [Lin09].

In this part a 2D GRIN lens based on temperature gradients produced by heated wires in air is proposed. Numerical simulations are made with the aim to confirm the focusing effect of GRIN lens and its positioning inside the crystal. Also, a comprehensible method to describe the change in the medium properties due to temperature gradient is developed and applied in acoustic modeling. Finally, as the temperature of the wires is easy to control in relatively wide range a dynamically tuning of SC properties by temperature gradients is proposed.

8.2 Brief theory of GRIN SCs

An acoustic gradient index lens is an acoustic lens in which the refractive index n varies gradually along the axis transverse with respect to the propagating wave (Fig.8.1). The lens is symmetrical to the wave propagation direction and, by not having curvature, it is relatively easy to build. In optics it is usually fabricated by superposition of homogeneous horizontal layers. Each layer has a different refractive index. Thus, the thickness and number of layers define the quality of the lens. The propagation axis of the GRIN lenses considered here is defined along the x-axis and, therefore, the proposed lens is built by superpositioning layers in y-direction. Thus, the refractive index n_y changes along the y-axis.

The physical principle behind the GRIN lenses is the delay introduced by each layer in the wave that impinges its entrance. The refractive index of the upper layers n_h is smaller than the one of the center n_0, so the particles travel faster there than the ones traveling through the center. This forces the wave front to bends inside the lens. Additionally, upon exiting, when the refractive index inside the lens is larger than the one outside the mismatch of refractive index between the lens and the background forces the beam to further bend. But in our model of SC made of heated wires the refractive index inside is less than the one in the background and then the outgoing beams tend to diverge and it is impossible to find a true focus outside the lens, only a collimation of the beam can be observed. Therefore, we must search the focusing effect inside the lens.

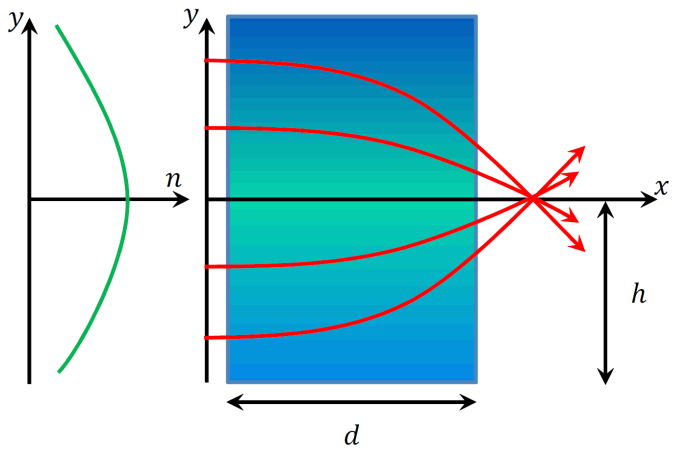

Figure 8.1 Scheme of gradient index lens with length d and width 2d. Left: Refractive index values. Right: Ray trajectory as a function of y-position.

Once the trajectory is known, a refractive index has to be chosen. The simplest profile is of parabolic form, and it is widely studied and used in optical devices [Lin09]. In this work, a refractive index profile in form of a hyperbolic secant (of which a parabolic profile can be considered as the first-order Taylor series approximation) is chosen. This refractive index is theoretical studied [Lin12] in achieving internal focusing in large enough GRIN structures. Following the model described in the reference above, it can be written:

$$\boldsymbol{n(y)} = n_0 \boldsymbol{sech(\alpha y)}\ , \qquad (8.1)$$

where

$$\boldsymbol{\alpha = \frac{1}{h} arcosh\left(\frac{n_0}{n_h}\right).} \quad (8.2)$$

Here h is the semi-width of the lens, n_0 is the refractive index along the x-axis and n_h is the refractive index at the edge of the lens.

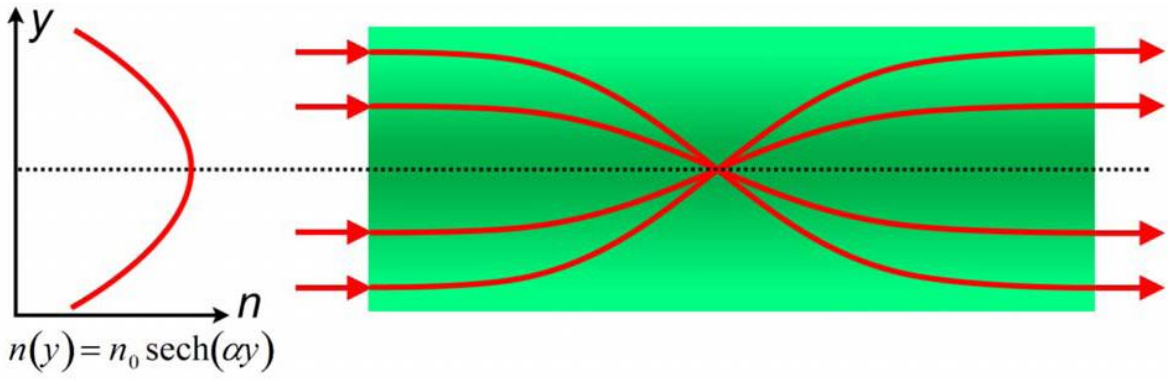

Source: Sz-Chin Lin et al., Gradient-index phononic crystals, Physical review B, **79**, 094302.

Figure 8.2. Within the GRIN medium, the paraxial incident beams bent gradually toward the center axis where refractive index is highest (per Snell's law) and converged at a focal spot. Beyond that spot, the focused beams are redirected parallel to the direction of propagation. A flat GRIN medium can thereby serve as a flat lens for focusing or collimation.

The beam trajectory within a GRIN medium can be analytically derived from the hyperbolic secant refractive index profile [Rom13]:

$$\boldsymbol{y(x) = \frac{1}{\alpha} sinh^{-1}[u_0 H_f(x) + \dot{u}_0 H_a(x)],} \quad (8.3)$$

where u_0 is the hyperbolic space at x=0 such that $u_0 = sinh(\alpha y_0)$, $\dot{u}_0$ is the derivative of u_0 with respect to x; and $H_a(x)$ and $H_f(x)$ are the positions of axial and field rays written as:

$$\boldsymbol{H_a(x) = \frac{sin(\alpha x)}{\alpha}, \qquad H_f = cos(\alpha x).} \quad (8.4)$$

The sinusoidal path through the GRIN medium described by (8.3) features a focal length (the distance to focus paraxial incident beams within the GRIN medium) of:

$$\boldsymbol{f = \frac{\pi}{2\alpha}.} \quad (8.5)$$

The focal length is independent of the incident position along the y direction (y_0). Thus, a focusing within a GRIN medium by the gradient coefficient α can be characterized.

A 2D GRIN SC can be considered as a transversely discretized medium where each row is independent. This discretized medium can be physically realized by adjusting the refractive index in each row to fit a hyperbolic secant profile. In this work the fit is achieved by adjusting the temperature of the heated wires.

Chapter 9

Modeling of GRIN Sonic Crystals

In this chapter some FEM based simulations of GRIN SC are shown. The hyperbolic secant profile of the refractive index for a GRIN lens is designed by heated wires. Also, a model of temperature distribution inside the lens is investigated. The obtained temperature distribution is further used for obtaining a map of acoustic pressure inside the crystal. It is demonstrated that the acoustic wave propagating in sonic crystal with gradient-index changing of the refractive index bends toward the central axis of the crystal and thus it can be focused.

9.1 GRIN lens design

In our model we shall use again as in Chapter 6 circular domains with radius 0.12 m. The distance between the centers of the wires is 0.13 m and the distance between the vertical rows is 0.0225 m. An initial adjusting of the width of the incident gauss beam with the width of the crystal suggests that 11 horizontal layers (or rows) per side are needed (Fig.9.1.1). Totally, 23 layers (with a central layer placed on the axis of symmetry which coincide with the *x*-axis), arranged hexagonally. It means that *h* in equation (8.2) must be 0.156m (11 layers *0.13m between the centers +half width of the central layer). A maximum reasonable temperature of the hot wires that can be reached is about 400-450ºC. The average temperature of 425ºC is chosen, hence the maximum speed of sound inside the domain is about 530 m/s (eq. 1.2.3), the average speed of sound is about 350 m/s and the refractive index has a value n_h= 0.95 approximately (eq.1.3.5). A finer adjusting of the values yields to final temperature 428ºC which leads to insignificant change in the refractive index.

Now we are ready to calculate α from eq. 8.2. In this case h=0.156m, n_h=0.95 and n_0=1, so α = 2.07 m^{-1}. Figure 9.1.2 shows refractive index as a function of the vertical position *y*. It can be seen the profile of hyperbolic secant function.

Table 9.1 contains data for the hot wire temperature, maximum speed of sound inside the domain and refractive index.

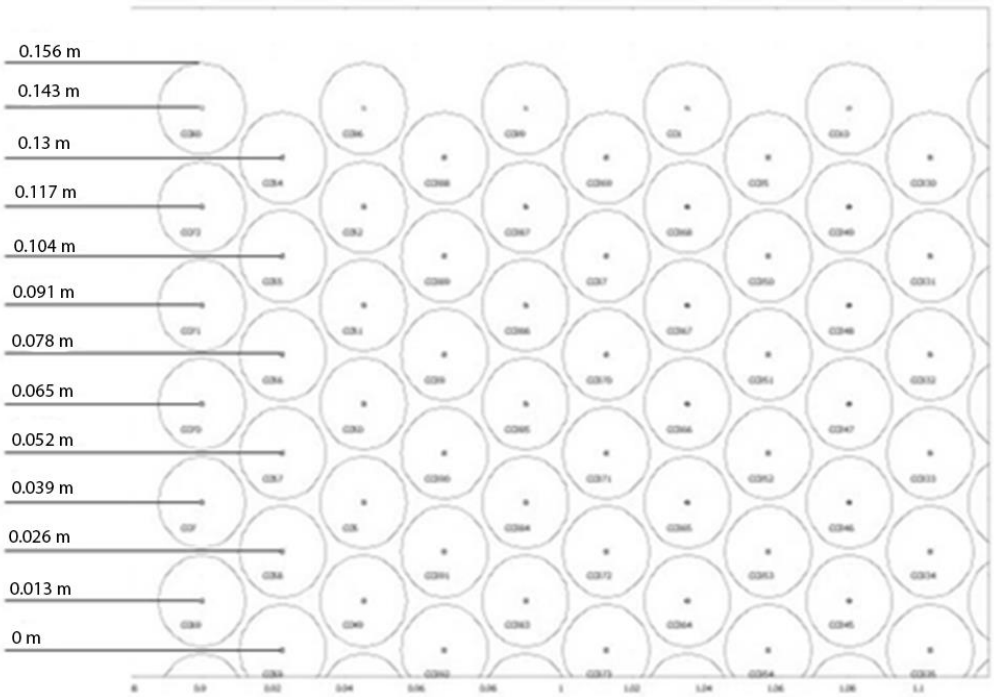

Figure 9.1.1. Layer positions in y-direction

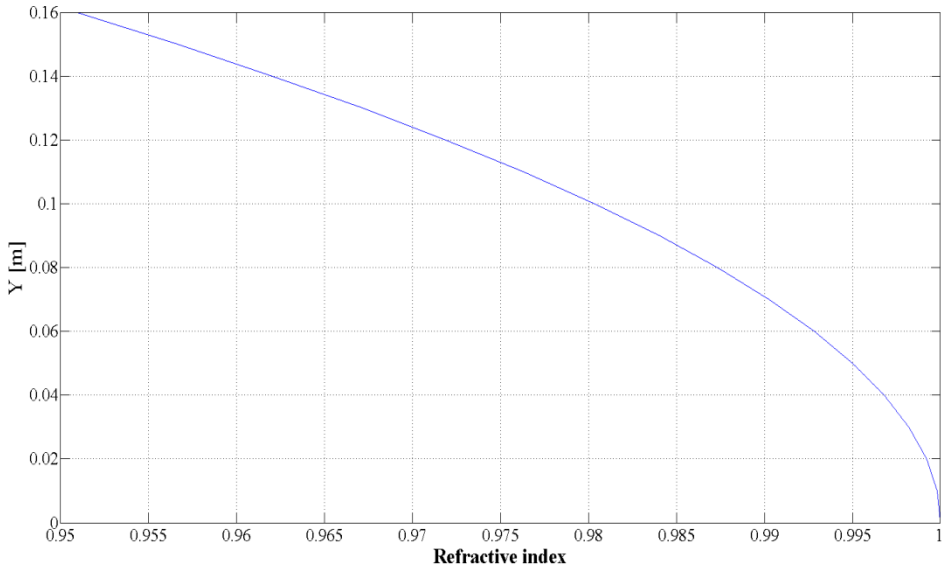

Figure 9.1.2 The refractive index as a function of the crystal width. The profile of the temperature is a hyperbolic secant function.

Distance y[m]	Refractive index	Max Speed of sound[m/s]	Temperature[°C]
0.143	0.9605	531	428
0.13	0.9671	503	357
0.117	0.9732	476	290
0.104	0.9788	449	229
0.091	0.9837	424	176
0.078	0.988	402	129
0.065	0.9916	382	90
0.052	0.9946	364	57
0.039	0.997	359	47
0.026	0.9986	356	38
0.013	0.9997	348	29
0	1	343	20

Table 9.1.1. Temperature of the hot wires, maximum speed of sound and refractive index for each vertical position of the subdomains. Red numbers correspond to internal column and blue numbers - to the external one of the Fig.9.1

Taking into account eq. (8.5), we conclude that the focus is positioned at 0.76 m from the left edge of the crystal. As the distance between the wires is 0.0225 m we need 0.76/0.0225 = 34 vertical layers (or columns) to complete the crystal with the focus inside (Fugure 9.1.3).

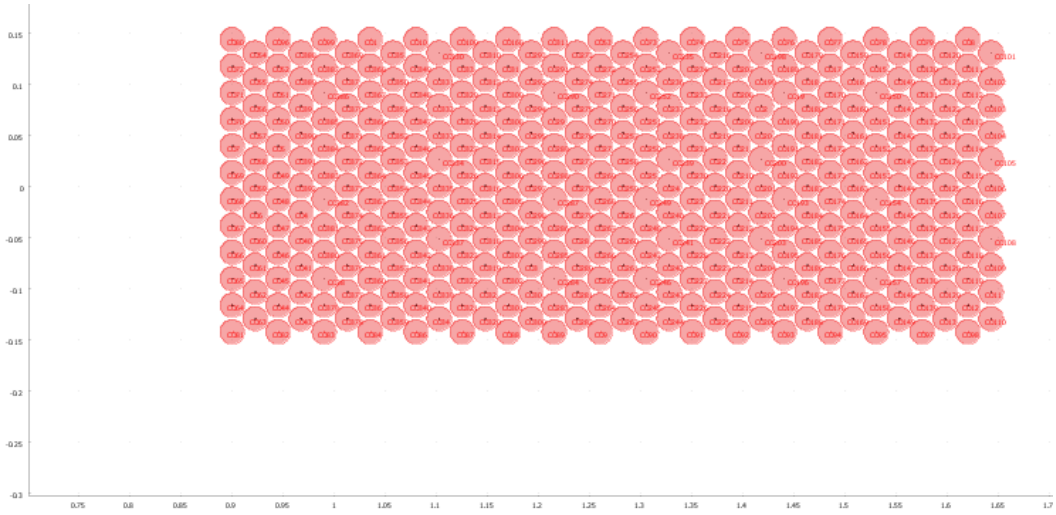

Figure 9.1.3. Complete geometry of our GRIN sonic crystal. It contains 23 horizontal rows and 34 vertical columns.

The most important part of the model is to describe correctly the temperature distribution inside each circular subdomain. Again, we build an axisymmetric FEM based model of 3 heated wires inside the crystal for each temperature from the table 9.1.1. All the steps described in chapter 6.2 are repeated but for different wire temperatures. Once again, we take advantage of the symmetry of the model and it leads to significant reduction of time, effort and resources of calculus.

The solution is shown in Figure 9.1.4. It can be seen how the temperature of the air between the wires increases with the height of the wires. Red line at half height corresponds to the plane where some horizontal cuts are made in order to describe the temperature distribution inside. These cuts are shown on figure 9.1.5 and 9.1.6. It can be seen that the lowest temperature inside the model at z=0.15 m is about 32ºC

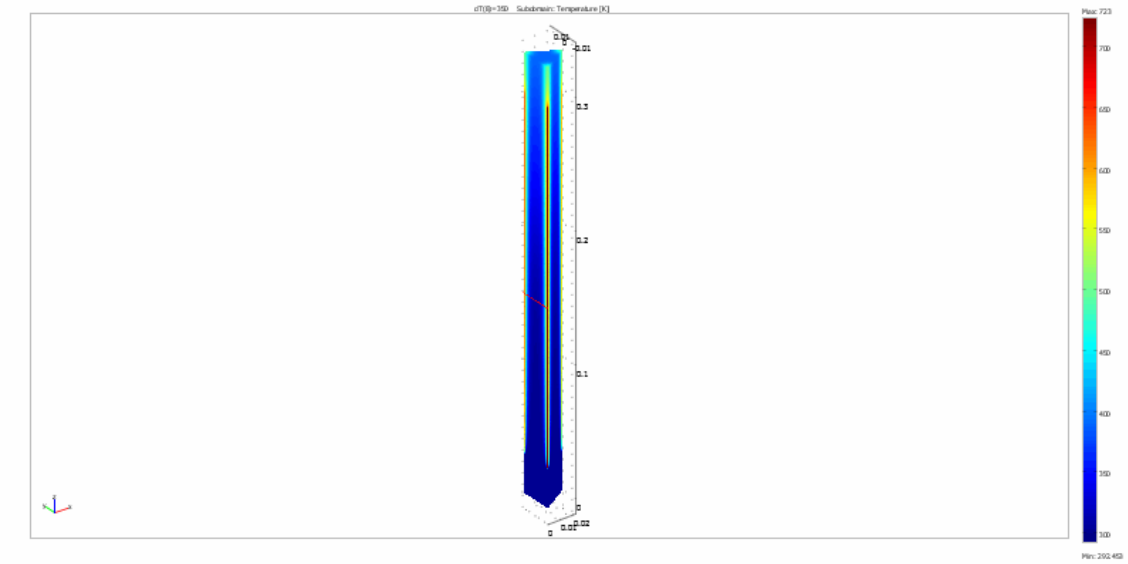

Figure 9.1.4 Temperature distribution of air between 3wires heated to 428ºC. In accordance with the eq. (4.3.20), the temperature increases from the bottom to the top of the model.

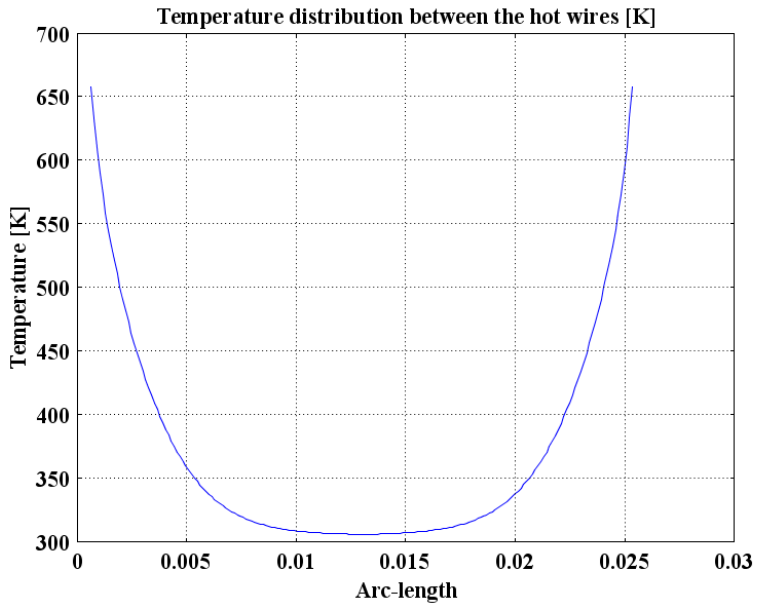

Figure 9.1.5 Horizontal lateral cut between 2 wires heated to 428ºC. The height of the cut is z=0.15m from the bottom of model, which corresponds to the red line in Fig.9.1.4. The temperature reached between the wires is about 305K.

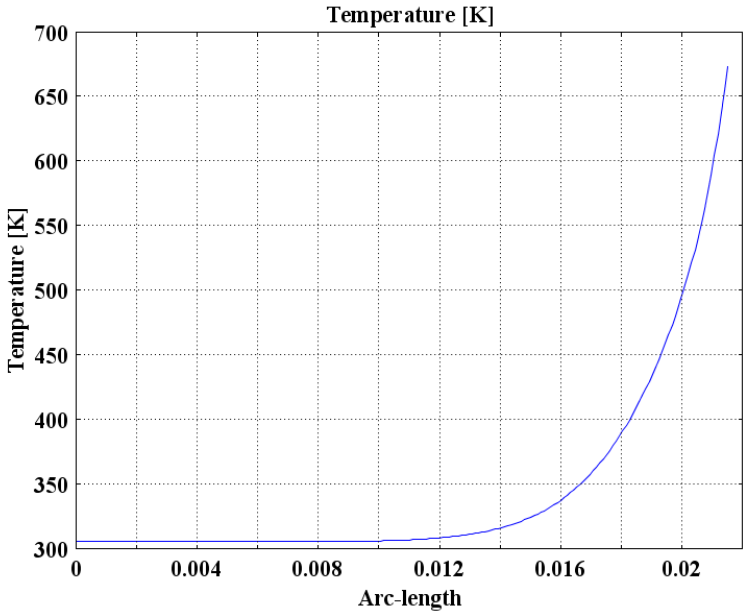

Figure 9.1.6 Horizontal cut from one wire heated to 428ºC to the opposed edge of the investigated subdomain. The height of the cut is z=0.15m from the bottom of model. The reached temperature is about 305K

For each temperature of the wires cuts like these are taken. Then they are approximated with some mathematical function which best fits the data. For temperatures above 50ºC a Boltzmann sigmoidal function is used (eq. 6.2.1) and for temperatures below 50ºC - exponential function (eq. 9.1). Figure 9.1.7 shows the fit with a Boltzmann function for T=428ºC.

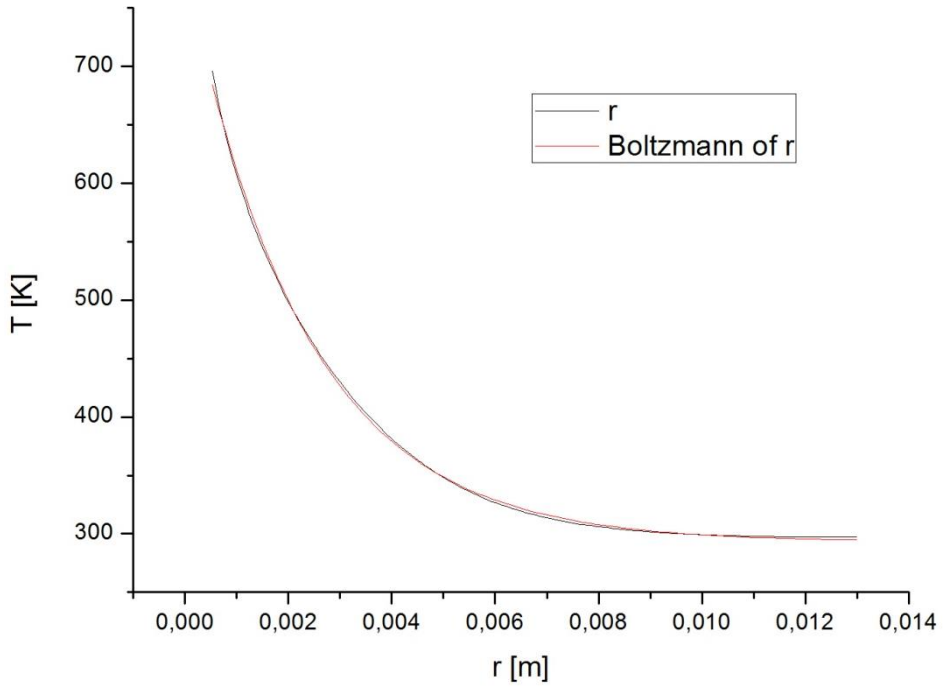

Figure 9.1.7 Fit of data obtained for wire heated to 428ºC. For fitting is used a Boltzmann sigmoidal function.

The exponential approximation function can be written as:

$$T = A_1 e^{-\frac{r}{t_1}} + A_2 e^{-\frac{r}{t_2}} + y_0, \qquad (9.1)$$

where A_1, A_2, t_1, t_2, and y_0 are given coefficients and r represents the current coordinates. Next tables contain all values of the wires temperature and the corresponding coefficients of Boltzmann sigmoidal function for hyperbolic secant temperature profile:

Temperature,°C	*A1*	*A2*	X_0	*dx*
428	1640.95646	292.7274	-0.00118	0.00201
357	1552.06996	292.94267	-0.00155	0.00203
290	1486.71236	293.09775	-0.00203	0.00206
229	1490.44162	293.19463	-0.0028	0.00213
176	1682.2785	293.23961	-0.00409	0.00222
129	3672.16989	293.24376	-0.00758	0.00238
90	30834.78628	293.29777	-0.01487	0.00253
57	34042.99244	293.31685	-0.01833	0.00276

Table 9.1.2. Table of the Boltzmann coefficients in the temperature fitting for values above 50ºC.

Temperature, °C	*A1*	*A2*	*t1*	*t2*	*y0*
47	16.20073	16.84046	0.004	0.00194	293.02962
38	11.7995	10.15626	0.0043	0.00182	293.02839
29	4.9484	5.96488	0.00179	0.00513	293.02341

Table 9.1.3. Table of the Boltzmann coefficients in the temperature fitting for values below 50ºC.

Thus, the design of the GRIN lens is completed. Now we only need to add the data from the tables to the circular subdomains of Fig.9.1.1. Inside each subdomain the air has properties, e.g. speed of sound and mass density, changed by the high temperature of the wire in the center. Therefore, the refractive index is changed and the desired profile is obtained. The rest of domain has the properties of air at normal conditions (T=20ºC, density ρ=1.19 kg/m^3 and speed of sound c = 343 m/s). Figure 9.1.8 shows the density as a function of the temperature and the position. The profile is hyperbolic secant function.

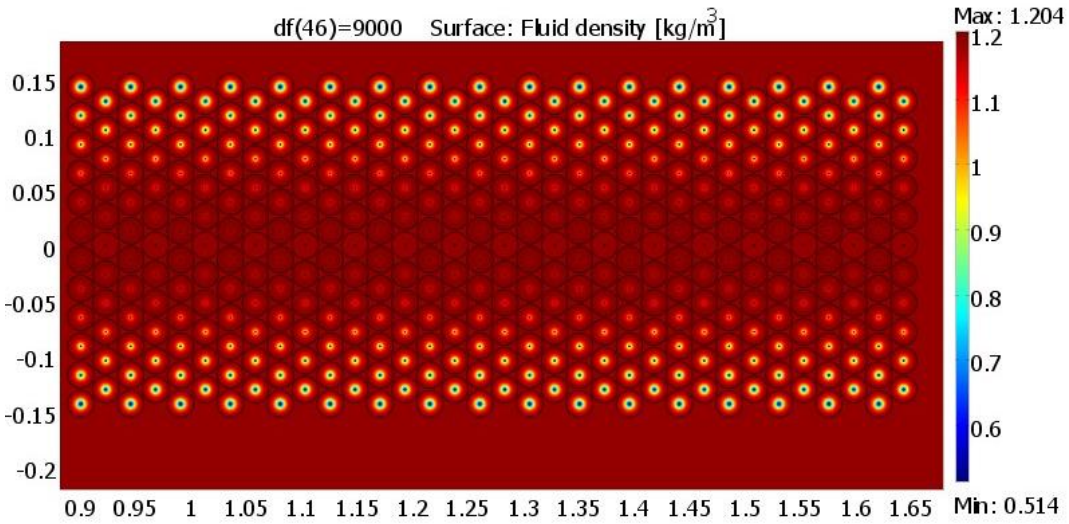

Figure 9.1.8. Density distribution inside the SC as a hyperbolic secant function. The temperature of the central row is 20ºC and of the two lateral rows is 428ºC

9.2 Acoustic pressure simulations

In our model we use Gauss waves in range of frequencies from 1 up to 10 kHz in Time-Harmonic analysis of Pressure Acoustics. To model the rigid surfaces of the nichrome wires in the analysis we consider the walls of the wires as ideally hard walls, i.e. the normal component of the particle velocity vanishes at the boundaries. Because there is no acoustic drift velocity, this condition is equivalent to the normal acceleration being equal to zero. At the boundaries of the investigated area we use the radiation condition option that allows an outgoing wave to leave the modelling domain with no or minimal reflections.

In order to perform the calculations correctly it is necessary to choose the size and form of the mesh element. As the working frequency is in range from 1 to 10 kHz the wavelength of the acoustic wave is between 3.4 and 34 cm. Following the rule that the length of the mesh element must be 4 – 5 times less than the wavelength the chosen size for mesh element can be about 7 mm in the domain. But taking into account how rapidly changes the temperature around the hot wire with the distance the maximum mesh element size is chosen to be 0.0034 m.

Next figure (Fig. 9.2.1) shows a solution of the amplitude of acoustic pressure (eq. A.2.4) in the domain of modelling. The white rectangle indicates approximately the crystal borders. The small white circles inside are the hot wires. It can be seen a focal spot, enclosed in white, near to the back side of the crystal. Longitudinal cuts along *x*-axis confirms that the focus is obtained near to the previously calculated position. For example, for frequency f=7 kHz its position is at 0.77 m from the left crystal edge. Longitudinal cuts for all other frequencies also show focal positions near to the theoretically calculated.

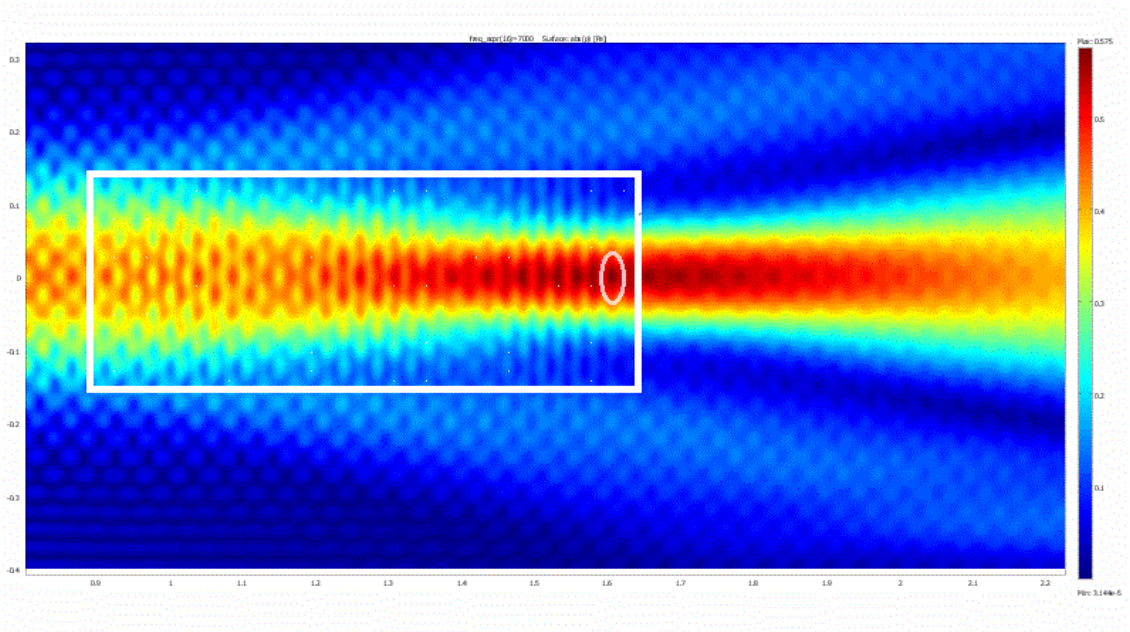

Figure9.2.1 A map of the acoustic pressure inside the GRIN SC.

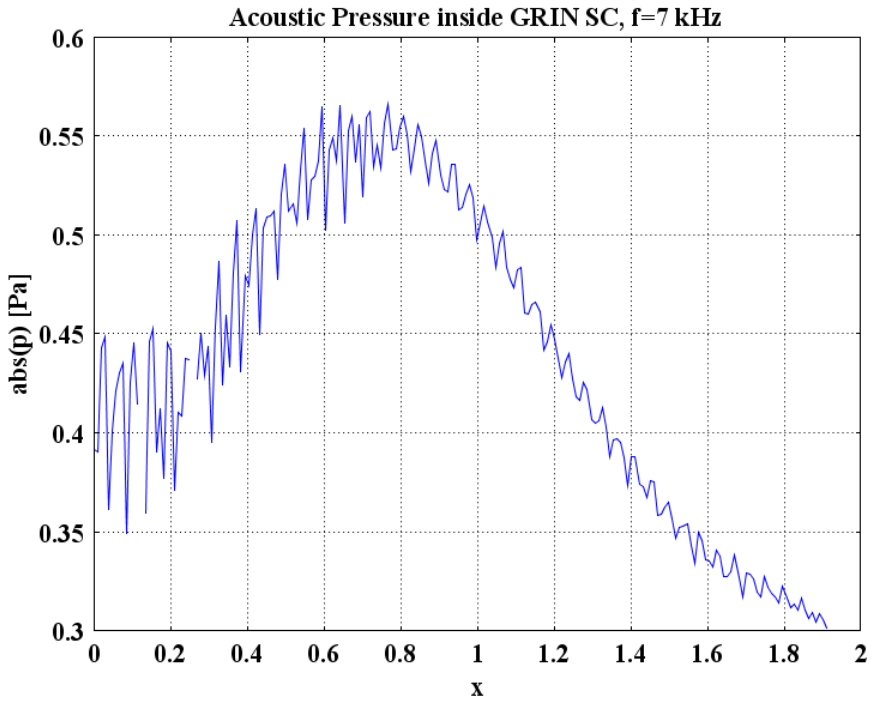

Figure 9.2.2 Longitudinal cross-section for y=0 inside the GRIN SC. The maximum amplitude value is obtained at approximately 0.77 m from the edge of the crystal.

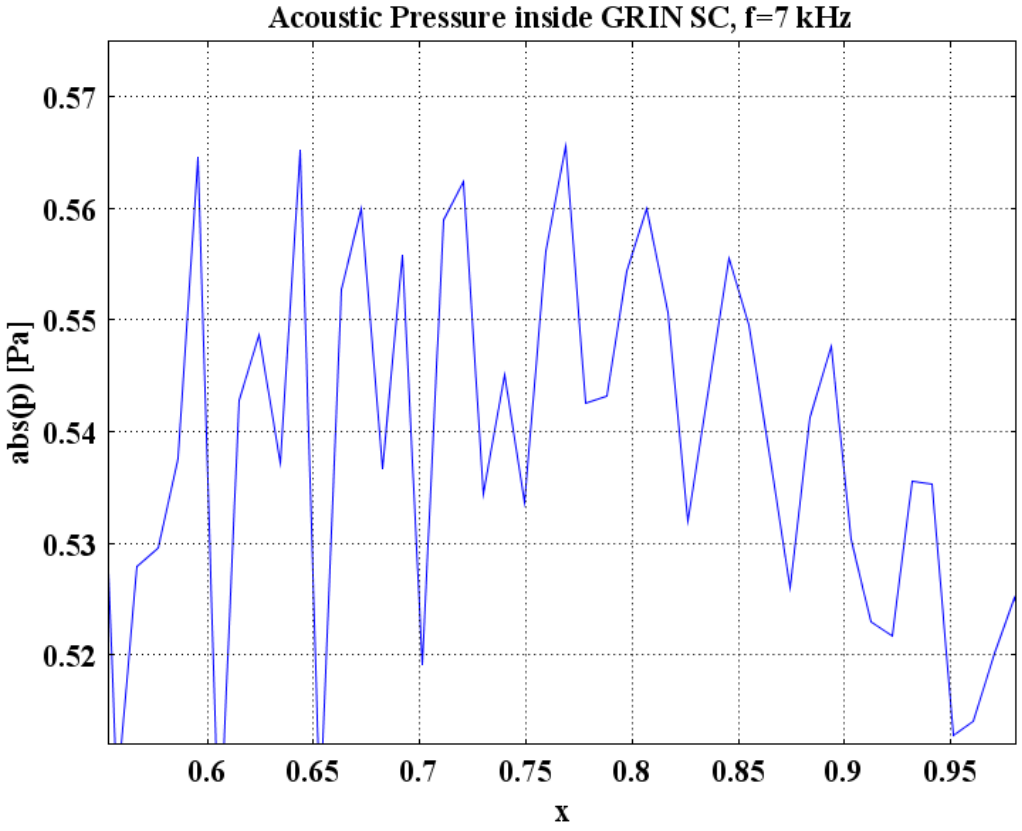

Figure.9.2.3 Zoom of the longitudinal cross-section from Fig.9.2.2. The maximum amplitude value is obtained at approximately 0.77 m from the edge of the crystal.

9.3 Some special cases

One important advantage of this method is that the focus position can be adjusted in some limits. For example, if the last two horizontal rows of wires are disconnected (Fig.9.3.1) the focus line can be deviated of approximately 7º. But if the half of rows are disconnected then the deviation of the focus line is about 13º (Fig.9.3.2).

The refractive index profile can be arbitrarily chosen. Figure 9.3.3 shows a GRIN lens with linear profile of refractive index. The central row has temperature of 25ºC and the last lateral rows up and down have the temperature of 300ºC. The temperature step between the rows is 25ºC. The focus of this kind of lens can be observed approximately at the same position as in the case of hyperbolic secant function (Fig.9.3.4).

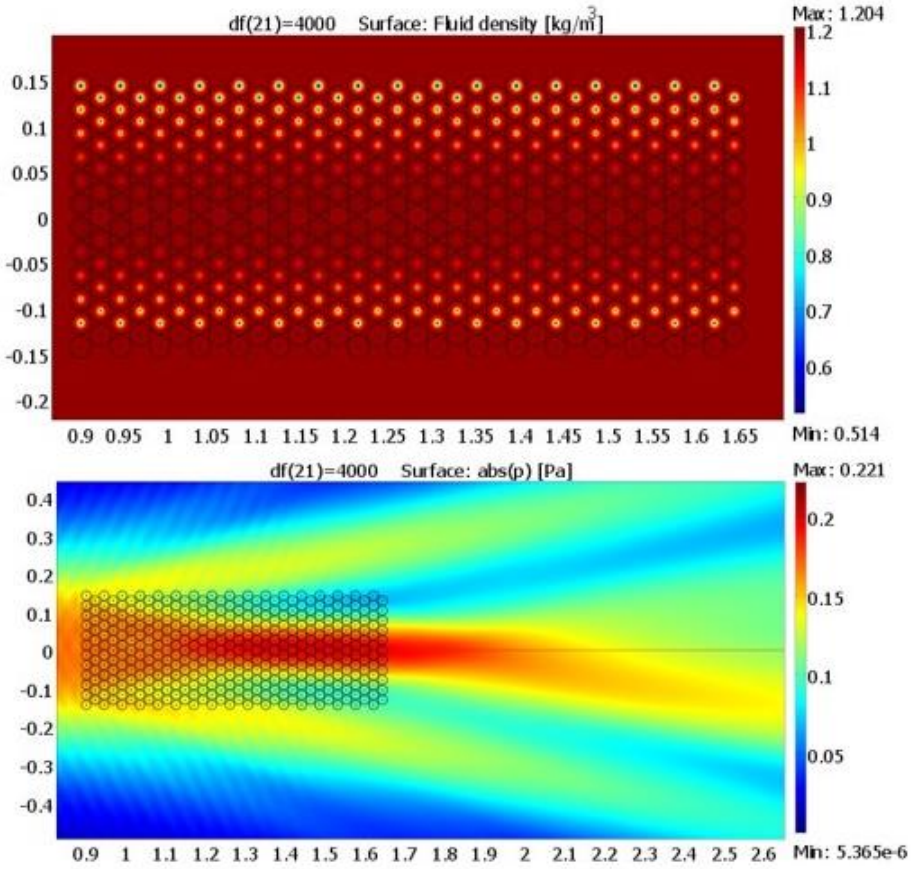

Figure 9.3.1. The last two rows of the SC are disconnected (up). Then, the focus line is deviated of 7º (down).

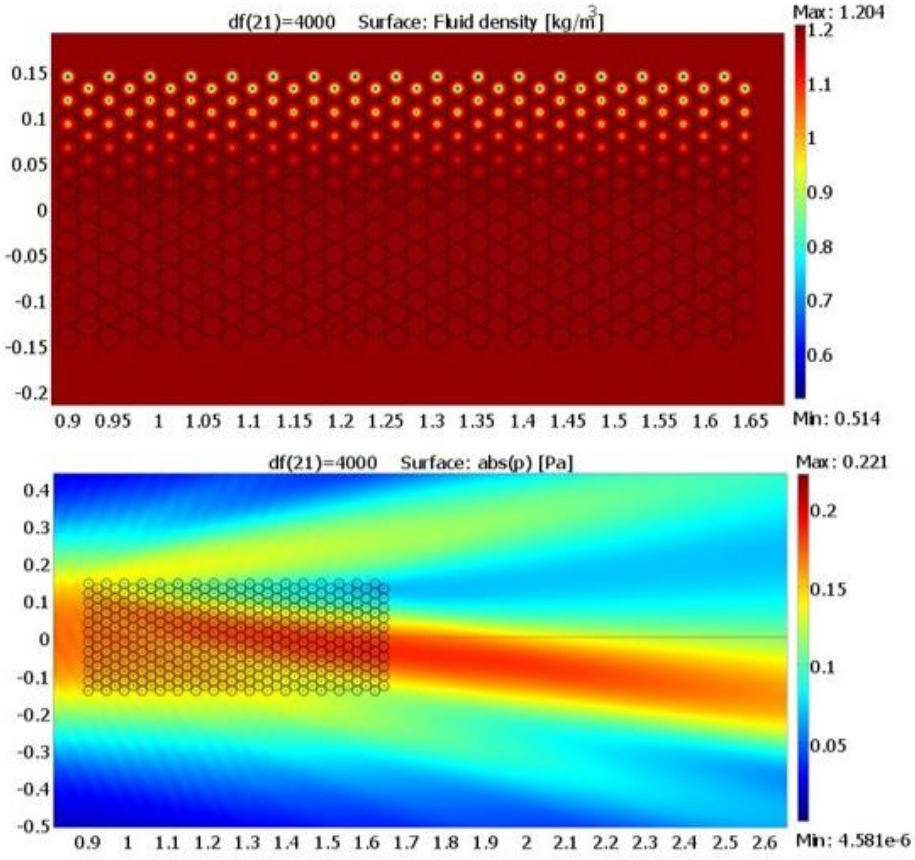

Figure 9.3.2. The half of the rows of the SC are disconnected (up) and the focus line deviation is about 13º (down).

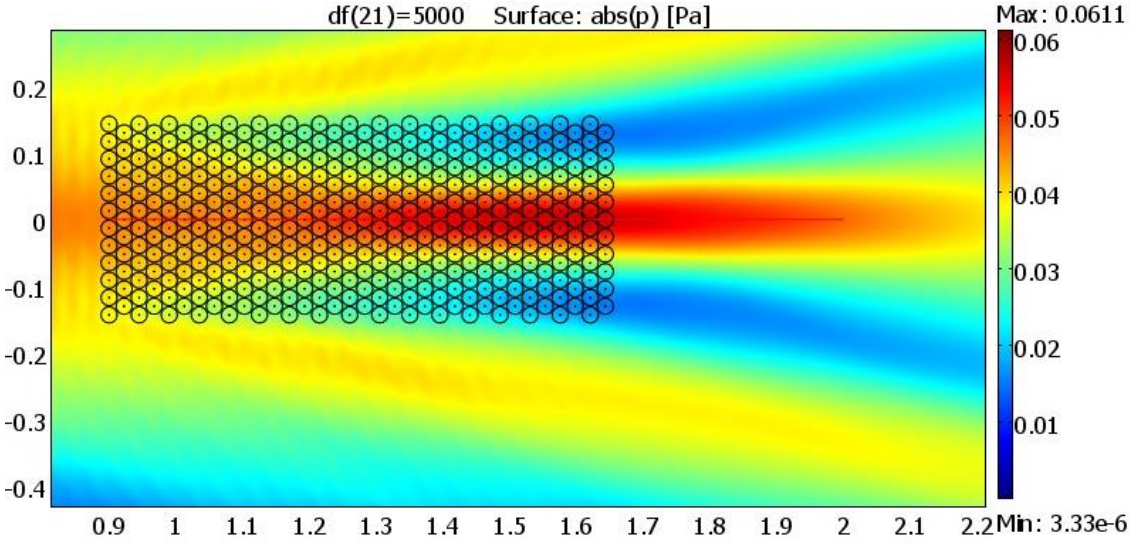

Figure 9.3.3 Focusing effect of acoustic GRIN lens with a linear profile of the refractive index.

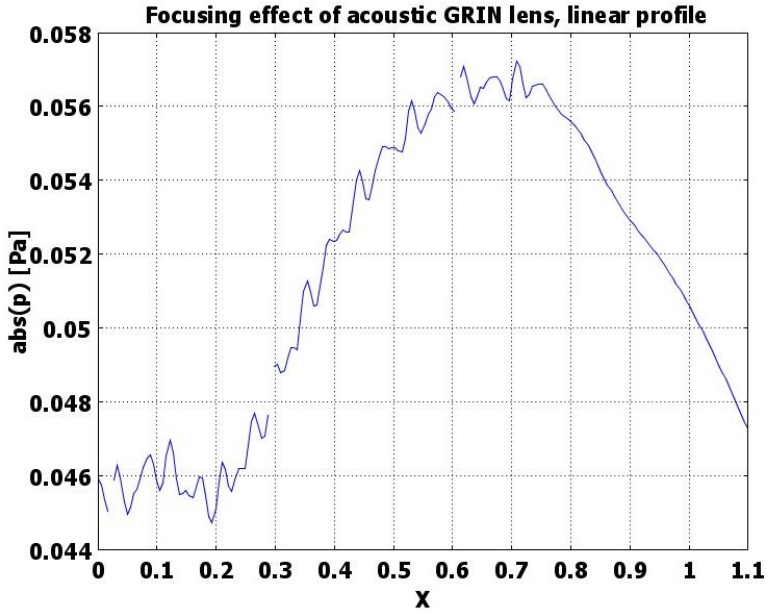

Figure 9.3.4 Focusing effect of acoustic GRIN lens with a linear profile of the refractive index. The focus can be observed approximately at 0.7 m from the left edge of the crystal. The longitudinal cross-section is taken at y=0 and corresponds to the red line of the fig. 9.3.3

9.4 Experimental part

It would be very difficult to perform some experimental confirmation of the focusing features of so built GRIN lens because too much time and too high electrical power are required. Nevertheless, it is possible to demonstrate that some collimation with a smaller GRIN lens can be obtained. In this part we use again the experimental setup shown in Fig. 7.1, 7.1.1 and 7.2. The GRIN lens consists of 126 vertical nichrome wires arranged in 12 horizontal rows and 21 vertical columns (Fig.9.4.1).

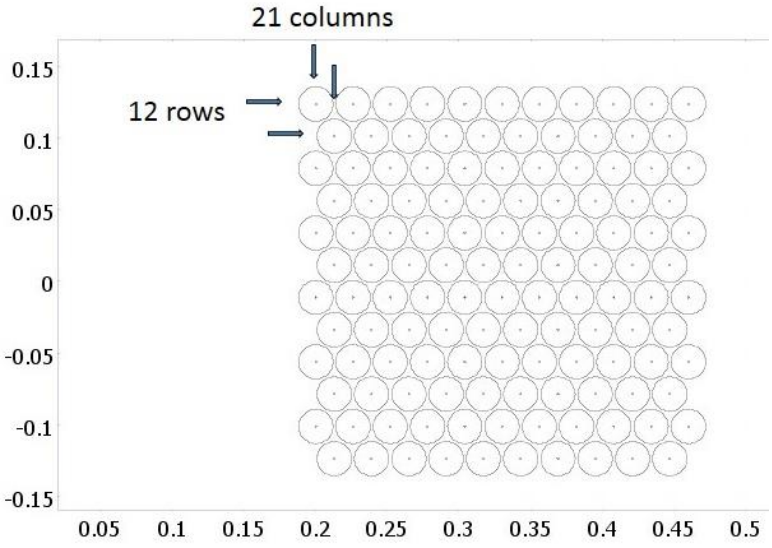

Figure 9.4.1 A scheme of the wires arrangement. It consists of 6 rows with 11 wires and 6 rows with 10 wires, hexagonally arranged.

First of all, it is necessary to adjust the incident wave in the model to the wave produced by the speaker used in the experimental setup. Although the goal of this work is to demonstrate only qualitatively the focusing features of the GRIN acoustic lenses the acoustic pressure amplitude of the simulated incident wave is multiplied by a corresponding factor in order to obtain the same amplitude as the experimental one (Fig. 9.4.2). The theoretical cross-section is taken at the left edge of the crystal (fig. 9.4.3, the red line) and it is adjusted to the cross-section of the acoustic field produced by the loudspeaker at the corresponding position, as it is shown in fig. 7.1.2. The chosen frequency is 5 kHz.

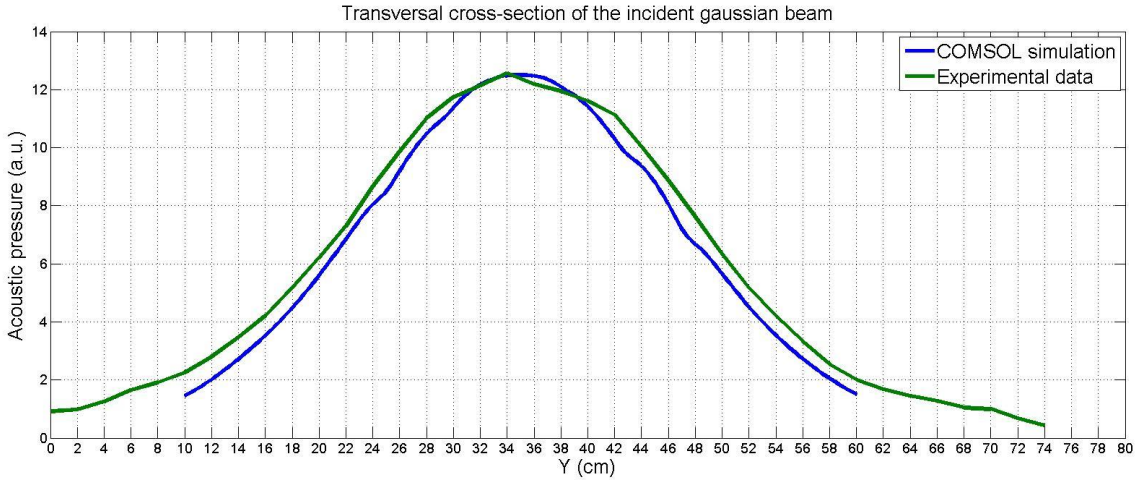

Figure 9.4.2. Comparison between the COMSOL simulated (blue line) and the experimental (green line) incident wave. The frequency is 5 kHz.

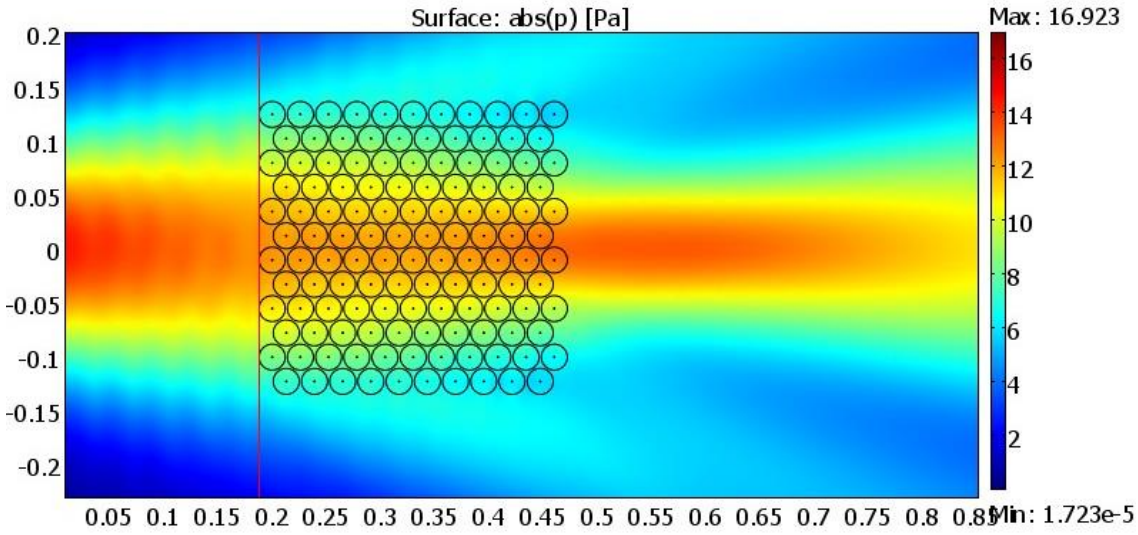

Figure 9.4.3. COMSOL simulation of the collimating feature of an acoustic GRIN lens with linear profile of the refractive index. The frequency is 5 kHz.

Taking into account some technical difficulties, a linear profile of the refractive index is chosen. Thus, in the simulation the wires in the central rows have the temperature of 25ºC and 525ºC in the rows at the borders. The step between the rows is 100ºC. Fig. 9.4.3 shows a clear collimating effect behind the crystal in a FEM simulation at 5 kHz.

Voltage regulator were added to the original setup in order to obtain fine adjustment of the temperature of the wires. They can be seen in the red circle in the fig. 9.4.4. The wires in each row are connected in series with a corresponding regulator (fig. 9.4.4, right down). Thus, the same (or approximately the same) temperature for every row is achieved and the temperature of each row is independent on the rest of rows.

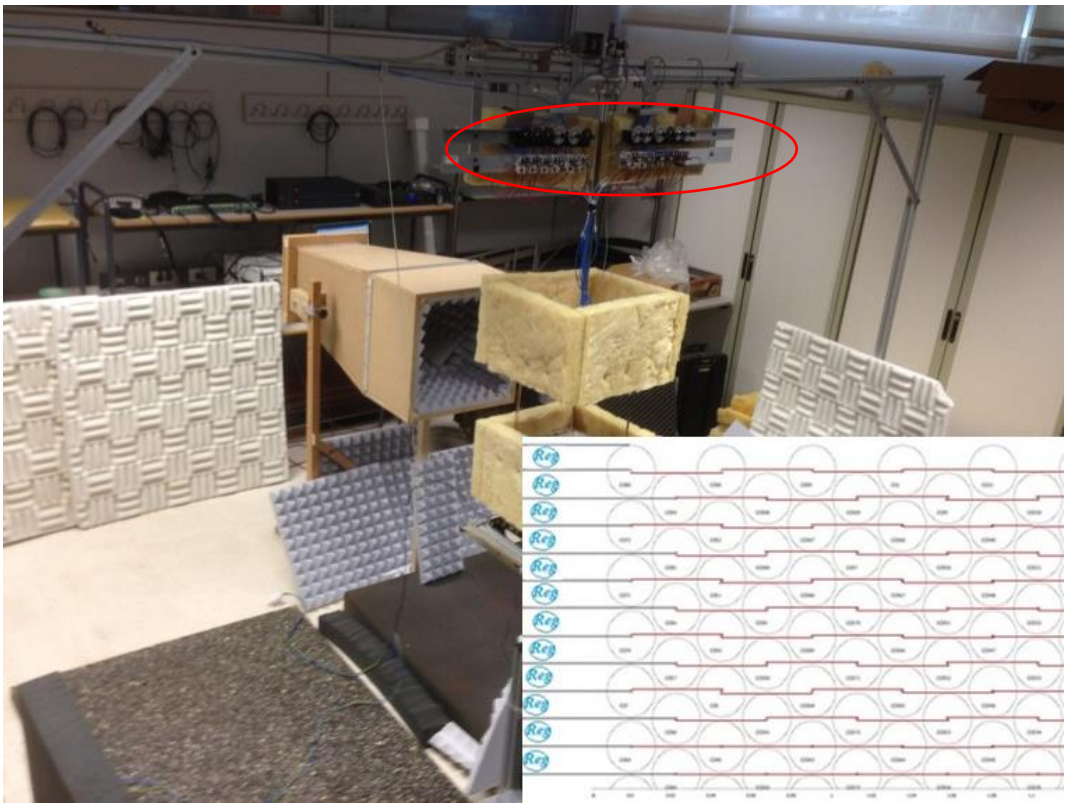

Figure 9.4.4 Experimental setup for demonstrating the collimating feature of GRIN acoustic lens. In the red circle are the voltage regulators added to the setup with the aim of achieving different temperature for each row.

Fig.9.4.5, top, shows the acoustic field produced by the loudspeaker. It is measured behind the area where the GRIN lens should be positioned. Bottom, the acoustic field measured behind the SC at room temperature is shown. The comparison shows that the acoustic field suffers very small perturbations when the temperature of the wires is equal to the room temperature. When all the wires have the same temperature, higher than the room temperature, then the acoustic field changes. Behind the lens a small zone of high acoustic pressure is formed, as well as two lateral beams (fig.9.4.6, top). And if inside the SC the refractive index has a linear profile then the lateral beams get weaker and in the central zone behind the crystal a clear collimated beam is formed (fig.9.4.6, bottom).

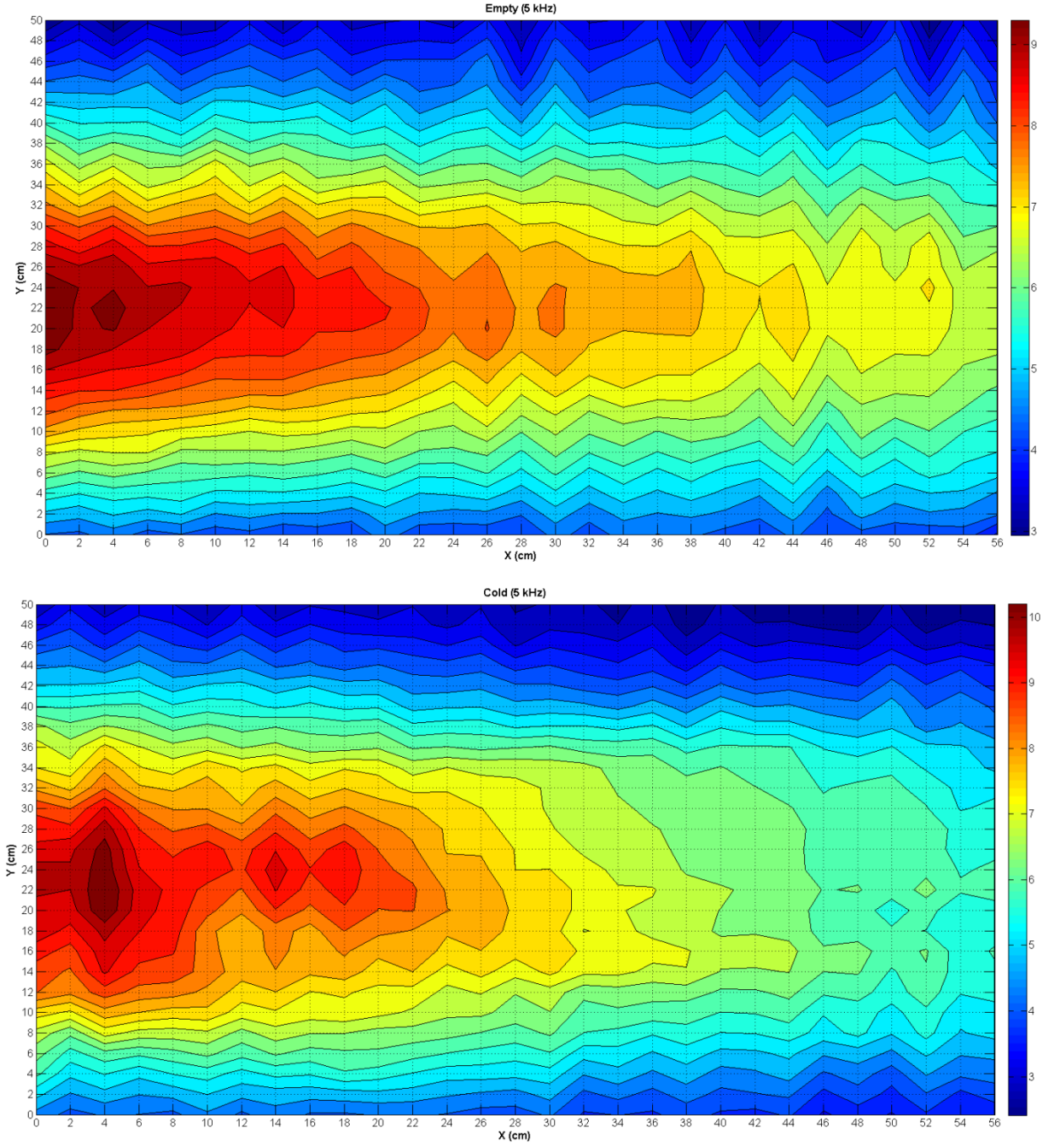

Figure 9.4.5, top: the acoustic field produced by the loudspeaker at 5 kHz. Bottom: the acoustic field measured behind the crystal at room temperature. It can be seen that the acoustic field is practically the same.

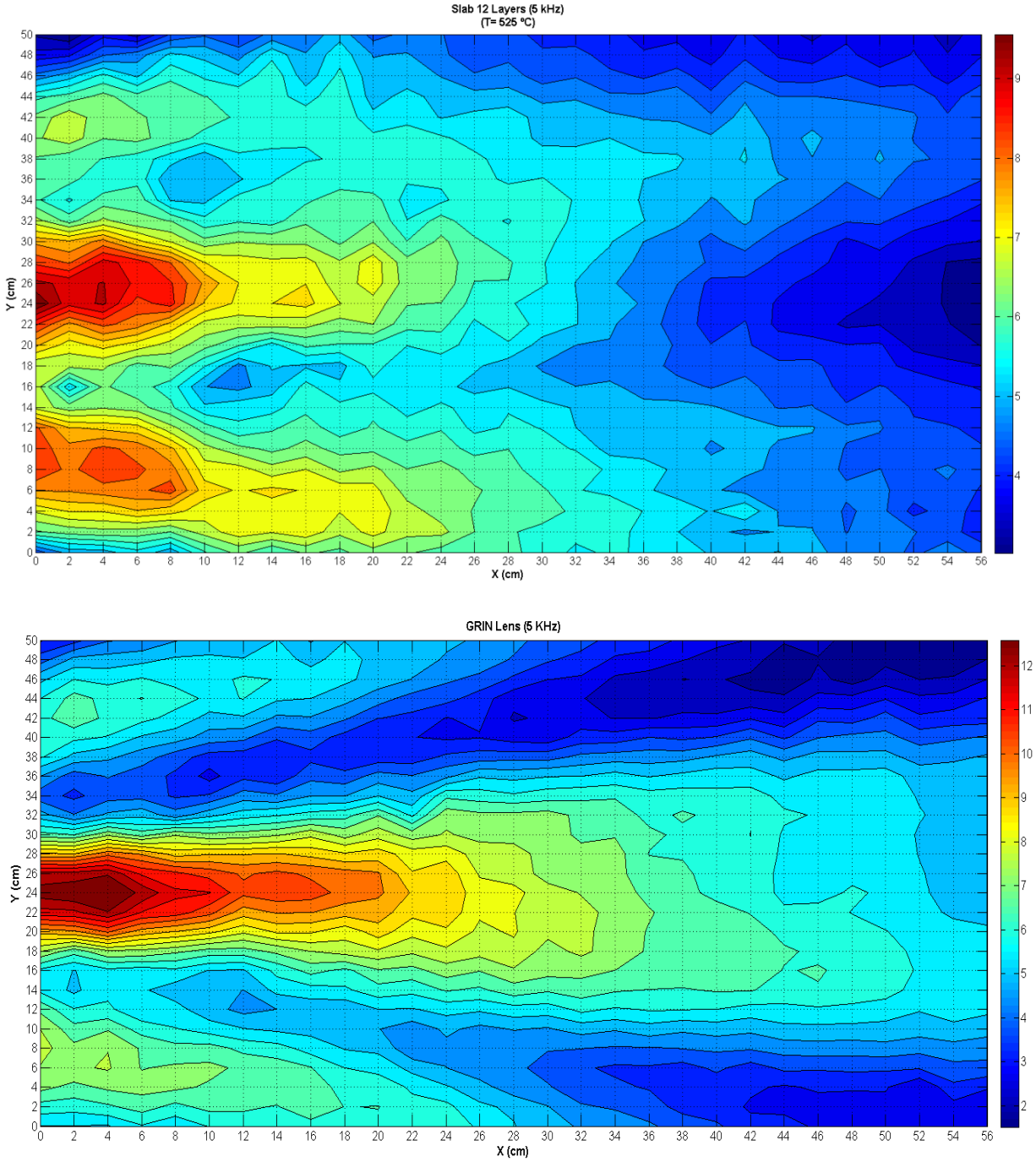

Figure 9.4.6, top: the acoustic field measured at uniform temperature of the wires, T=525ºC. Bottom: the acoustic field measured behind the GRIN crystal with linear profile of the refractive index. It can be observed that the lateral beams are getting weaker and in the central zone behind the crystal a clear beam of collimation is achieved.

Fugure 9.4.7 shows a comparison between the experimental data measured along a transversal cross-section at 4 cm behind the lens and the corresponding FEM simulation. A satisfactory agreement can be observed. The discrepancy in the peak positions probably is due to small differences in the true temperature of the wires which are difficult to control.

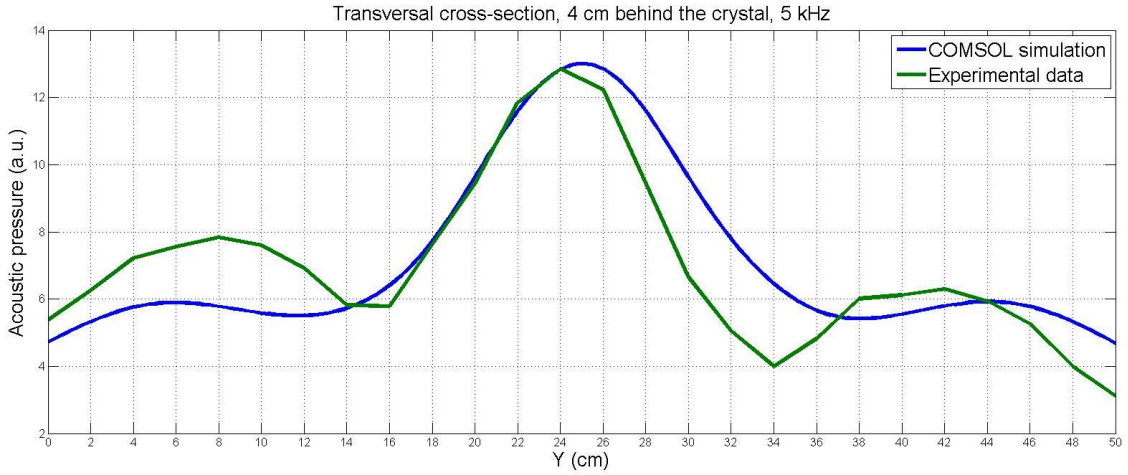

Figure 9.4.7 Transversal cross-section at 4 cm behind the lens. It can be observed a significant agreement between the FEM simulation and the experimental measurements.

9.5 Conclusions

A 2D model of GRIN lens of 34 layers with hyperbolic secant profile of refractive index is proposed. The conventional rigid scatterers are replaced with heated wires that change the local refractive index. In addition, the temperature of the wires can be dynamically adjusted and this can be an important step to dynamically tuning of sonic crystals.

Furthermore, FEM based simulations of the bending wave inside the crystal are performed. It is shown that the wave inside the crystal can be focused. The position of the focus is previously analytically calculated and it is in very good agreement with the FEM simulation.

The practical implementation of this GRIN SC would be very difficult to perform because of the following main reasons. First, building the crystal requires too much time and tedious work. Second, the needed electrical power is too high - it is about 3500W. Third, the produced heat requires special conditions for the laboratory. And finally, trying to measure inside the crystal may produce some damage of the microphone.

Nevertheless, a clear collimation with a smaller GRIN lens of only 12 layers has been experimentally demonstrated. A SC with a refractive index linear profile forms a clear collimated beam behind the crystal.

Conclusions

This work reports focusing effect from arrangements of heated wires. First, a focusing effect of ultrasonic wave by two hot wires, previously theoretically predicted, is demonstrated experimentally. In the next step, a sonic crystal with hot wires as scatterers is introduced. In this case the hot wires can be considered as scatterers with radially variation of the properties. An acoustical analogue of fiber Bragg grating is proposed and studied. An experimental set-up including a home-made computer controlled positioning system for the microphone has been prepared with the aim to verify experimentally the FEM simulations.

Next, an acoustic lens with temperature gradient is designed. The numerical simulations show that a lens like this can be used for focusing and collimating of sound waves. Modifying the refractive index of air by temperature gradients an acoustic lens with desired properties can be adjusted.

The proposed in this work method for acoustic control by temperature gradients can be advantageous if dynamically adjustment of the properties of SC is needed. As the temperature of wires is controlled by electric current the method is easy to use.

In this study the changes in the temperature that we have produced in the air by applying hot wire method are very weak and therefore the acoustic effects that occur are also very weak (in the order of 5%). The practical utility of these proposals is therefore very limited. However, in optical fibers of type FBG (Fiber Bragg Grating) where relative variations in the refractive index of the periodic structure are of the order of few thousandth, useful practical effects are achieved such as the use of these fibers as deformation and temperature sensors and signal filtering. This is possible by repeating the periodic structure a sufficiently high number of times until the desired reflection coefficient is achieved.

Therefore it can be said that the proposed method in this thesis allows, in principle, get materials and structures with adjustable acoustic properties using temperature control by electric current through the wires, within certain limits. In this way it is easy to carry out experiments of wave propagation phenomena in a macroscopic scale similar to those that occur in microscopic structures for the propagation of electromagnetic waves of high frequency (microwaves and light). The proposed method provides a training environment for research and academic use.

However, due to natural convection, there is always a temperature gradient in the vertical direction and this prevents that the structure of vertical wires can be considered as true 2D structure and therefore the results do not fully coincide with predictions from a 2D simulation. Therefore, the practical usefulness of the proposed method is very limited.

All this work increases our capabilities to study and better understand the propagation of waves in Metamaterials and complex structures and enables us to apply such knowledge to design devices for focusing of acoustic energy for medical applications and non-destructive testing of materials, as well as problems of isolation and control of noise, as for example the cloaking.

Future Work

It has been mentioned that the changes in the temperature that we have produced in the air by applying the hot wires method are very weak and therefore the produced acoustic effects are also very weak. The practical utility of these proposals is therefore very limited. However, some inverse scattering problems using the Born approximation [Kak79] for slightly scattering objects have practical interest in the computerized tomographic imaging. This kind of problems considers that the structure and acoustic properties of a given object (for example, its refraction index spatial distribution) are unknown and they can be deduced by measurements of the scattered acoustic field around the object produced by an incident plane wave.

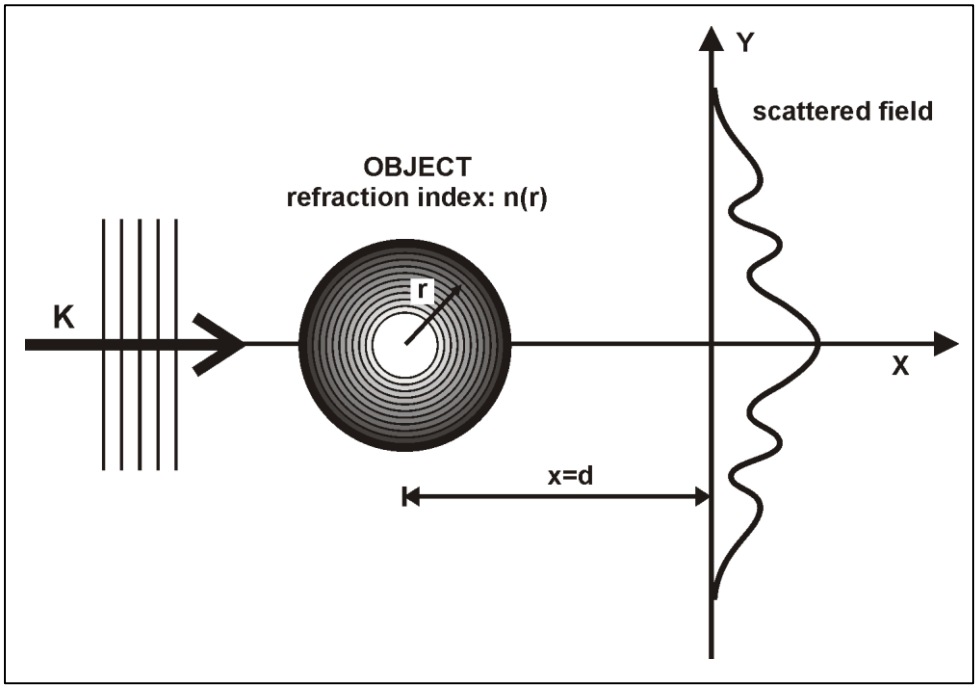

Figure FW-1: From the measured scattered acoustic field along a straight line (Y) perpendicular to the wave vector of the incident plane wave, the unknown radial index law [*n(r)*] of the object can be worked out.

For example, a cluster of heated wires can be disposed in order to form approximately a cylinder whose temperature varies as a function of the radial distance. From the measured scattered acoustic field along a straight line perpendicular to the wave vector of the incident plane wave the unknown radial index law *n(r)* of the cylinder can be worked out using the Fourier diffraction theorem [Kak99] and thus, the object can be acoustically reconstructed. The working frequency must be lower than the Bragg frequency in order to fulfill the homogenization condition.

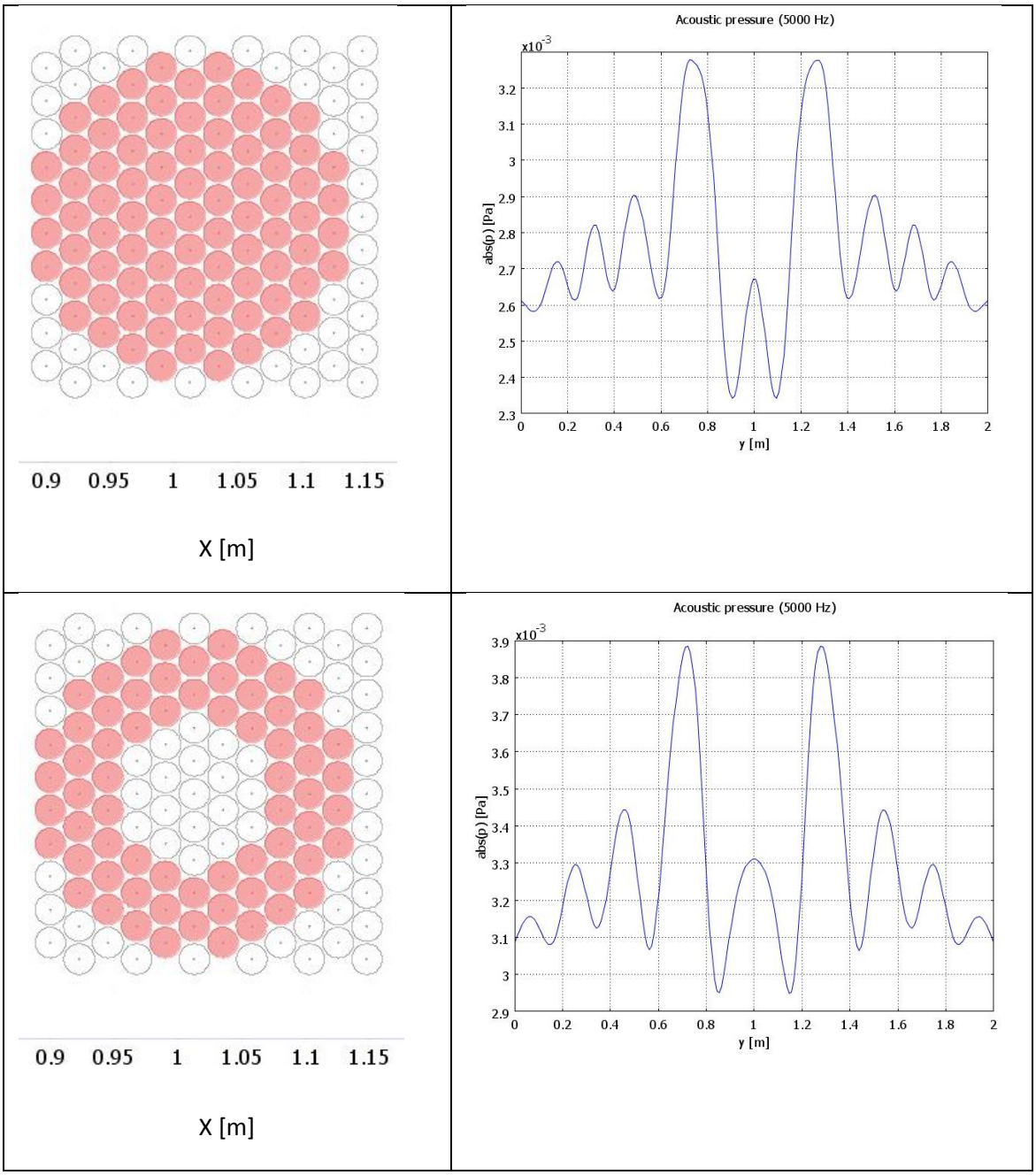

Figure FW-2: On the left of the figures is shown a cluster made of hot wires forming a cylinder (top) and a hollow cylinder (bottom). On the right of the figures is shown a simulation by COMSOL of the acoustic pressure measurements at 5 kHz along a straight line perpendicular to the wave vector of the incident plane wave.

Appendix A

Acoustic Wave Equations Derivation

Generally, the theory in this appendix is extracted from [Kin00] and [Rec00].

A.1. Linearized Equations for Compressible Fluid

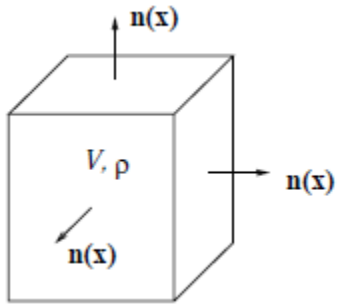

Figure. A.1. A volume element with definition of normal directions**.**

A.1.1. Conservation of mass:

Consider the flow of mass in fluid material with pressure ***P(x,t)***, density ***ρ(x,t)***, and particle velocity **V**(**x**,t). We will be interested mostly in the time-harmonic case, assuming that all waves are steady-state with circular frequency ω. We introduce here the convention that the time variable in a time-dependent scalar field ***F(x,t)*** is separated as:

$$F(x,t) = f(x)e^{-i\omega t}, \qquad (A.1.1.1)$$

where f is a stationary function. A similar convection holds for vector fields.

Let V be a volume element with boundary ∂V, and let $\boldsymbol{n(x)}$, $\boldsymbol{x} \in \partial V$, be the unit normal vector directed into the exterior of V (Fig.A.1). Then $\boldsymbol{V(x,t)}\bullet\boldsymbol{n(x)}$ is the velocity of normal flux through ∂V. The conservation of mass in a unit time interval is expressed by the relation [Inh98]:

$$-\frac{\partial}{\partial t}\int_V \rho dV = \oint_{\partial V} \rho(\boldsymbol{V}.\boldsymbol{n})dS. \qquad (A.1.1.2)$$

The signs in the equation above correspond to the decrease of the mass due of the outflow (in the direction of the exterior normal) of material. A similar relation with opposite signs on both sides is obtained for inflow of material when increase of mass is described.

The surface integral on the right side is transformed into volume integral using the Gauss theorem:

$$\oint_{\partial V}(\rho \boldsymbol{V})\cdot \boldsymbol{n}dS = \int_V \ div(\rho \boldsymbol{V})dV. \qquad (A.1.1.3)$$

Thus is obtained

$$\int_V \left(\frac{\partial \rho}{\partial t} + div(\rho \boldsymbol{V})\right)dV = 0, \qquad (A.1.1.4)$$

which leads to the continuity equation:

$$\frac{\partial \rho}{\partial t} + div(\rho \boldsymbol{V}) = 0, \qquad (A.1.1.5)$$

which describes the law of conservation of mass.

A.1.1.1. Equation of Motion:

Assume that the volume element V is subject to a hydrostatic pressure $P(\boldsymbol{x},t)$. The total force along ∂V is then

$$F = \oint P\boldsymbol{n}dS, \qquad (A.1.2.1)$$

where again $\boldsymbol{n}$ denotes the outward unit normal vector ∂V. The second Newton's law now gives:

$$-\oint_{\partial V} P\boldsymbol{n}dS = \int_V \ \rho\frac{d\boldsymbol{V}}{dt}dV. \qquad (A.1.2.2)$$

The total differential in the integral on the right side is linearized as $d\boldsymbol{V}/dt \approx \partial \boldsymbol{V}/\partial t$. Generally, the total differential $d\boldsymbol{V}/dt$ is expanded into the nonlinear expression [Lan87]:

$$\frac{d\boldsymbol{V}}{dt} = \frac{\partial \boldsymbol{V}}{\partial t} + (\boldsymbol{V}.\nabla)\boldsymbol{V}. \qquad (A.1.2.3)$$

where ∇ is the nabla operator (gradient) in spatial Cartesian coordinates. With the assumption of small oscillations, this relation is linearized in acoustics.

Further, from the Gauss theorem it follows that

$$-\oint_{\partial V} P\boldsymbol{n}dS = -\int_V \ \nabla P dV. \qquad (A.1.2.4)$$

Thus we obtain the equation of motion (Euler equation):

$$\rho\frac{\partial \boldsymbol{v}}{\partial t} = -\nabla P. \qquad (A.1.2.5)$$

Using time-harmonic assumption, we obtain the steady-state expression of the Euler equation:

$$i\omega\rho\boldsymbol{v} = \nabla p, \qquad (A.1.2.6)$$

where we applied the separation of variables to the scalar field $P(\boldsymbol{x},t)$ and vector field $\boldsymbol{V}(\boldsymbol{x},t)$. Introducing the vector field $\boldsymbol{U}(\boldsymbol{x},t)$ of fluid particle displacement, the Euler equation is equivalently written as:

$$\rho \frac{\partial^2 \boldsymbol{U}}{\partial t^2} = -\nabla P. \qquad (A.1.2.7)$$

In stationary form:

$$\rho \omega^2 u = \nabla p. \qquad (A.1.2.8)$$

A.2. Wave Equation and Helmholtz Equation

Assuming a linear fluid, it can be written [Kut91]:

$$P = c^2 \rho, \qquad (A.2.1)$$

where the c is the speed of sound. Then, using the linearized versions of (A.1.1.5) and (A.1.2.5), we obtain:

$$\frac{\partial^2 P}{\partial t^2} = c^2 \frac{\partial^2 \rho}{\partial t^2} = c^2 div(\nabla P). \qquad (A.2.2)$$

Thus we arrive at the wave equation:

$$\Delta P - \frac{1}{c^2}\frac{\partial^2 P}{\partial t^2} = 0. \qquad (A.2.3)$$

Here Δ is the Laplace operator in spatial coordinates.

With the assumption of time-harmonic waves, we finally obtain the Helmholtz equation

$$\Delta p + k^2 p = 0, \qquad (A.2.4)$$

where $k=\omega/c$ is the wave number.

Consider steady-state solutions

$$P(x,t) = p(x)e^{-i\omega t}. \qquad (A.2.5)$$

The stationary part satisfies the Helmholtz equation

$$p'' + k^2 p = 0, \qquad (A.2.6)$$

with general solution $p(x)=Ae^{ikx} + Be^{-ikx}$. This solution is periodic along x; i.e. $p(x+\lambda)=p(x)$ holds for all x with

$$\lambda = \frac{2\pi}{k}. \qquad (A.2.7)$$

The parameter λ is called wavelength of the stationary wave p. Thus k is the number of waves per unit (2π) wavelength.

The magnitude

$$f = \frac{c}{\lambda}, \tag{A.2.8}$$

that relates the speed of sound and the wavelength, is the frequency.

A.3 Reflection and Transmission of acoustic waves

Since the intensity of a harmonic plane progressive wave is $p^2/2r$ [Tow88], the intensity transmission and reflection are real and are defined by:

$$T_I = \frac{I_t}{I_i} = \frac{r_1}{r_2}|T|^2, \tag{A.3. 1}$$

$$R_I = \frac{I_r}{I_i} = |R|^2. \tag{A.3. 2}$$

In practical situations the acoustic beams have a finite cross-sectional area. However, a beam can be described locally by nearly parallel rays and thus can be approximated by a plane wave of finite extent. While there can be some anomalies resulting from diffraction at the edges of the beam, if the cross-sectional area is sufficiently great compared to a wavelength, they can be ignored and the equations developed in this chapter applied.

The power carried by a beam of sound is the acoustic intensity multiplied by the cross-sectional area of the beam. If an incident beam of cross-sectional area A_i is obliquely incident on a boundary, the cross-sectional area A_t of the transmitted beam generally is not the same as that of the incident beam. The power transmission and reflection coefficients are defined by [Kin00]:

$$T_\Pi = \frac{A_t}{A_i}T_I = \frac{A_t}{A_i}\frac{r_1}{r_2}|T|^2, \tag{A.3. 3}$$

$$R_\Pi = R_I = |R|^2. \tag{A.3. 4}$$

From conservation of energy, the power in the incident beam must be shared between reflected and transmitted beams, so:

$$R_\Pi + T_\Pi = 1. \tag{A.3. 5}$$

Consider the plan x=0 at Fig.2.3.1. Let it be the boundary between fluid 1 and fluid 2. Let there be an incident wave traveling in the +x direction

$$P_i = p_i e^{i(\omega t - k_1 x)} \tag{A.3. 6}$$

which, when striking the boundary, generates a reflected wave

$$P_r = p_r e^{i(\omega t - k_1 x)} \tag{A.3. 7}$$

and a transmitted wave

$$P_t = p_t e^{i(\omega t - k_1 x)} \tag{A.3. 8}$$

All the waves must have the same frequency, but, since the speeds c_1 and c_2 are different, the wave numbers $k_1 = \frac{\omega}{c_1}$ in fluid 1 and $k_2 = \frac{\omega}{c_2}$ in fluid 2 are different.

There are two boundary conditions to be satisfied for all times at all points on the boundary: (1) the acoustic pressures on both sides of the boundary must be equal and (2) the normal components of the particle velocities on both sides of the boundary must be equal. The first condition, continuity of pressure, means that there can be no net force on the (massless) plane separating the fluids. The second condition, continuity of the normal component of velocity, requires that the fluids remain in contact. The pressure and normal particle velocity in fluid 1 are P_i+P_r and (U_i+U_r)x so that the boundary conditions are

$$P_i + P_r = P_t \ \ at\ x = 0, \qquad (A.3.\ 9)$$

$$U_i + U_r = U_t \ \ at\ x = 0. \qquad (A.3.\ 10)$$

Division between last equations yields:

$$\frac{P_i+P_r}{U_i+U_r} = \frac{P_t}{U_t} \qquad (A.3.\ 11)$$

which is a statement of the continuity of normal specific acoustic impedance across the boundary.

Since a plane wave has $\frac{P}{U} = \pm r$, the sign depending on the direction of propagation, last equation becomes:

$$r_1 \frac{P_i+P_r}{P_i-P_r} = r_2, \qquad (A.3.\ 12)$$

which leads directly to the reflection coefficient

$$R = \frac{r_2-r_1}{r_2+r_1} = \frac{\frac{r_2}{r_1}-1}{\frac{r_2}{r_1}+1} \qquad (A.3.\ 13)$$

Then, since (A.3.9) is equivalent to 1+R=T, we have

$$T = \frac{2r_2}{r_1+r_2} = \frac{2r_2/r_1}{r_2/r_1+1}. \qquad (A.3.\ 14)$$

The intensity reflection and transmission coefficients follow directly from (A.3.1) and (A.3.2):

$$R_I = \left(\frac{r_2-r_1}{r_2+r_1}\right)^2 = \left(\frac{r_2/r_1-1}{r_2/r_1+1}\right)^2, \qquad (A.3.\ 15)$$

$$T_i = \frac{4r_2r_1}{(r_1+r_2)^2} = \frac{4r_2/r_1}{(r_2/r_1+1)^2}. \qquad (A.3.\ 16)$$

Since the cross-sectional areas of all the beams are equal, the power coefficients in (A.3.3) and (A.3.4) are equal to the intensity coefficients.

From (A.3.13), R is always real. It is positive when $r_1 < r_2$ and negative when $r_1 > r_2$. Consequently, at the boundary the acoustic pressure of the reflected wave is either in phase or 180º out of phase with that of the incident wave. When the characteristic acoustic impedance of fluid 2 is greater than that of fluid 1, a positive pressure in the incident wave is reflected as a positive pressure. On the other hand, if $r_1 > r_2$, a positive pressure is reflected as a negative pressure. When $r_1 = r_2$ then R=0 and there is complete transmission.

From (A.3.14), it is seen that T is real and positive regardless of the relative magnitudes of r_1 and r_2. Consequently, at the boundary the acoustic pressure of the transmitted wave is always in phase with that of the incident wave. Whenever r_1 and r_2 have strongly dissimilar values, the intensity transmission is small. From the symmetries of (A.3.15) and (A.3.16), it is apparent that the intensity

reflection and transmission coefficients are independent of the direction of the wave. For example, they are same from water into air as from air into water. This is a special case of acoustic reciprocity.

In the limit $r_1/r_2 \rightarrow 0$, the wave is reflected with no reduction in amplitude and no change in phase. The transmitted wave has pressure amplitude twice that of the incident wave, and the normal particle velocity at the boundary is zero. In this case the boundary is termed as "rigid".

For $r_1/r_2 \rightarrow \infty$, the amplitude of the reflected wave is again equal to that of the incident wave, and the transmitted wave has zero pressure amplitude. Since the acoustic pressure at the boundary is zero, the boundary is termed as "pressure release".

Appendix B

Theory of Multilayered Scatterer

This chapter describes the multiple scattering approach used in the simulation of the interaction between an ultrasound beam and a single scatterer in which the acoustic properties vary radially. The scatterer consists of a rigid core surrounded by a set of layers with a radial variation of their physical properties. Multiple scattering is solved by considering two canonical problems and one intermediate-series of matrices that represents the incident wave in intermediate cases.

B.1 Two canonical problems

It was explained in chapter 2 that when a wave propagating in a particular medium reaches a region with different acoustical properties, reflected and transmitted waves are generated, leading to the well-known phenomenon of scattering. When a given field like sound impinges one or more obstacles, a scattered field is generated as a result. The complexity of this new field depends on the incident field, the number and location of the scatterers, their acoustic properties and they geometry. In this work sound scatterers are assumed to be infinitely long cylindrical units (if the length of the cylinder is much larger than the radius, it can be considered as a "wire") with circular section.

The theoretical model is based on the concept of "multiple scattering in single scatterer approach" [Cai04b]. The process is illustrated in Fig. B.1 for the case of a multilayered cylindrical scatterer. Wave 5 is the wave scattered by the internal interface. It is then scattered by the external interface and waves 6 and 7 are formed. Again the incident wave 7 is scattered by the internal interface and two new waves 8 and 9 formed and so on. Let's consider a 2D problem configuration in which a cylindrical scatterer is embedded in an unbounded medium. Let us also assume that the unbounded elastic medium is homogeneous and linear, and the scatterer is either linearly elastic, rigid, or void that such problem is linear.

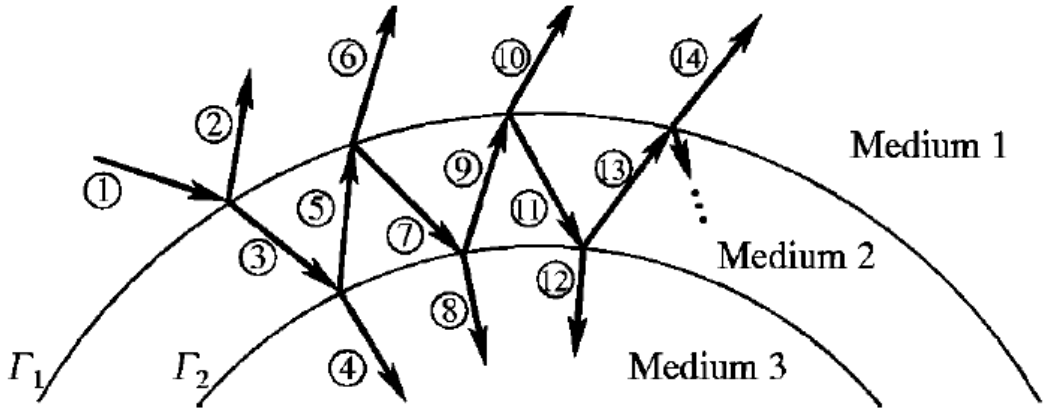

Figure B.1 Scheme of multiple scattering by a single scatterer

The multiple scattering process can be decomposed into two canonical problems. The canonical problems serve as mathematical descriptions of essential wave-interface interactions in the multiple scattering process that occurs in a multilayered scatterer. Each canonical problem consists of the interaction between the incident wave and the surface Γ that separates two media. The first canonical problem treats the wave that propagates inwards (Fig. B.2 a) and the second one treats the wave that propagates outwards (Fig. B.2 b)

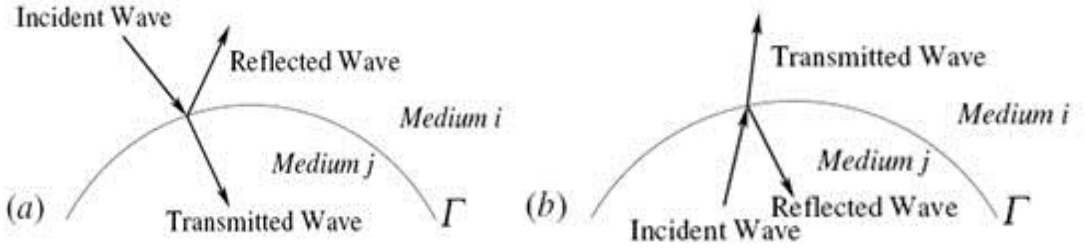

Figure B.2 Two Canonical problems in the multiple scattering process in a multilayer scatterer. a) First canonical problem. b) Second canonical problem.

The medium outside the enclosure of Γ is denoted as medium *i*, and the medium inside the enclosure of Γ is denoted as medium *j*. Mathematical description of each canonical problem is facilitated by a polar coordinate system (r, θ), whose origin is located within the enclosure of Γ.

In steady state, the displacement in either medium can be written as:

$$w(r,\theta,t) = \phi(r,\theta)e^{-\hat{\imath}\omega t}, \qquad (B.1.1)$$

where $\hat{\imath} = \sqrt{-1}$, ω is the angular frequency and ϕ is the complex amplitude of the displacement that satisfies the Helmholtz equation (A.2.4). In polar coordinate system, the general solution for the Helmholtz equation is so-called cylindrical wave functions, which consists of Bessel functions [Abr65].

Using matrix notation, the waves in both canonical problems can be expressed as an inner product between a wave expansion coefficient column matrix and the wave expansion basis column matrix [Ime08]. Table B.1 presents expressions in polar coordinates (r, θ) with center within Γ for the waves in both canonical problems.

Wave	Symbol	Wave Expansion Coefficient	Wave Expansion Basis	
			First Canonical	Second Canonical
Incident	ϕ^I	{A}	$\{J_i(r,\theta)\}$	$\{H_j(r,\theta)\}$
Reflected	ϕ^R	{B}	$\{H_i(r,\theta)\}$	$\{J_j(r,\theta)\}$
Transmitted	ϕ^T	{C}	$\{J_j(r,\theta)\}$	$\{H_i(r,\theta)\}$

Table B.1 Wave Expansion Coefficients and Basis Matrices for Two Canonical Problems

In the table, both matrices of coefficients as matrices of basis are column matrices with indexes between -∞ to + ∞. The expression for a specified wave can be defined as an inner product of the matrix of coefficients and the corresponding basic matrix of wave expansion. For example, the reflected wave in the second canonical problem is $\phi^R = \{B\}^T\{J_j(r, \theta)\}$. The matrices $\{J_j(r, \theta)\}$ and $\{H_j(r, \theta)\}$ are bases used in the expansion of the regular and singular wave, resp., in the medium *j*, whose input values of the *n*-th row are $J_n(k_j r)e^{in\theta}$ and $H_n^{(1)}(k_j r)e^{in\theta}$, resp., where J_n y $H_n^{(1)}$ are Bessel and Hankel functions of first kind and order *n*, resp. and k_j is the wave number.

In linear acoustic the coefficient matrices of the transmitted and reflected wave can be related to the incident wave as follows:

$$\{\boldsymbol{B}\} = [\mathcal{R}_{ij}]\{\boldsymbol{A}\}, \qquad (B.1.2)$$

$$\{\boldsymbol{C}\} = [\mathcal{T}_{ij}]\{\boldsymbol{A}\}, \qquad (B.1.3)$$

When the wave propagates from medium *i* to medium *j* subscript *ij* is used. The case *i*<*j* is considered as first canonical problem and the case *i*>*j* is considered as second canonical problem. Layers are numbered from outside to inside. The characteristic matrices for canonical problems are written in bold. The matrix $[\mathfrak{K}_{ij}]$ denotes first canonical problem when *i*<*j* and second canonical problem when *i*>*j*.

Solutions for canonical problems can be found from the boundary conditions. For a circular surface Γ, with radius *a* and origin in the center of Γ, the boundary conditions are:

$$\phi^T|_{r=a} = (\phi^I + \phi^R)|_{r=a} \qquad (B.1.4)$$

$$\frac{1}{\rho_i}\frac{\partial\phi^T}{\partial r}|_{r=a} = \frac{1}{\rho_i}\left(\frac{\partial\phi^I}{\partial r} + \frac{\partial\phi^R}{\partial r}\right)|_{r=a} \qquad (B.1.5)$$

When $i<j$ the solution for the canonical problems in an acoustic medium is [Ime08]:

$$[\mathcal{R}_{ij}]_{nn} = -\frac{z_i J_n'(k_j a) J_n(k_i a) - z_j J_n(k_j a) J_n'(k_i a)}{z_i J_n'(k_j a) H_n^{(1)}(k_i a) - z_j J_n(k_j a) H_n^{(1)\prime}(k_i a)}, \quad (B.1.6)$$

$$[\mathcal{T}_{ij}]_{nn} = -\frac{2\hat{\imath}}{\pi k_i a} \frac{z_j}{z_i J_n'(k_j a) H_n^{(1)}(k_i a) - z_j J_n(k_j a) H_n^{(1)\prime}(k_i a)}, \quad (B.1.7)$$

$$[\mathcal{R}_{ji}]_{nn} = -\frac{z_i H_n^{(1)\prime}(k_j a) H_n^{(1)}(k_i a) - z_j H_n^{(1)}(k_j a) H_n^{(1)\prime}(k_i a)}{z_i J_n'(k_j a) H_n^{(1)}(k_i a) - z_j J_n(k_j a) H_n^{(1)\prime}(k_i a)}, \quad (B.1.8)$$

$$[\mathcal{T}_{ji}]_{nn} = -\frac{2\hat{\imath}}{\pi k_i a} \frac{z_i}{z_i J_n'(k_j a) H_n^{(1)}(k_i a) - z_j J_n(k_j a) H_n^{(1)\prime}(k_i a)}, \quad (B.1.9)$$

where $z_i=\rho_i c_i$ is the specific acoustic impedance for medium i.

B.2 Formalism for dual-layer scatterer

In Fig.B.1 the outer layer is denoted as 1 and the intermediate layer as 2. The inner layer will be considered as a core of the scatterer and is denoted as 3. Then:

$$\phi^{inc} = \{\mathbf{A}\}^T \{\mathbf{J_1}(r, \theta)\}, \quad (B.2.1)$$

$$\phi^{disp} = \{\mathbf{B}\}^T \{\mathbf{H_1}(r, \theta)\}, \quad (B.2.2)$$

$$\phi^{ref} = \{\mathbf{C}\}^T \{\mathbf{J_3}(r,\theta)\}, \quad (B.2.3)$$

$$\phi^{in} = \{\mathbf{D}\}^T \{\mathbf{J_2}(r,\theta)\} + \{\mathbf{E}\}^T \{\mathbf{H_2}(r,\theta)\}, \quad (B.2.4)$$

where inc, disp, ref and in denote incident, dispersed and refracted wave and the wave in the intermediate layer, resp. Let's write the transformations between the incident wave and preceding waves:

$$\{\mathbf{B}\} = [\mathbf{R}] \{\mathbf{A}\}, \quad (B.2.5)$$

$$\{\mathbf{C}\} = [\mathbf{T}] \{\mathbf{A}\}, \quad (B.2.6)$$

$$\{\mathbf{D}\} = [\mathbf{S}] \{\mathbf{A}\}, \quad (B.2.7)$$

$$\{\mathbf{E}\} = [\mathrm{F}] \{\mathbf{A}\}. \quad (B.2.8)$$

Then for the characteristic matrices is obtained [Cai04]:

$$[\mathbf{S}] = ([\mathrm{I}] - [\mathcal{R}_{21}][\mathcal{R}_{23}])^{-1}[\mathcal{T}_{12}] , \qquad (B.2.9)$$

$$[\mathbf{R}] = [\mathcal{R}_{12}] + [\mathcal{T}_{21}][\mathcal{R}_{23}][\mathbf{S}] , \qquad (B.2.10)$$

$$[\mathbf{F}] = [\mathcal{R}_{23}][\mathbf{S}] , \qquad (B.2.11)$$

$$[\mathbf{T}] = [\mathcal{T}_{23}][\mathbf{S}]. \qquad (B.2.12)$$

B.3 Acoustical scattering by a single multilayer scatterer

The structure of a single multilayered scatterer is shown on Fig.B.3. The single scatterer is composed of N layers with radio r_i (i=1,2,…,N) and $r_1 > r_2 > \ldots > r_N$. The layers are numbered successively inwards, beginning from 1 as the layer adjacent to the host to layer N as the innermost core. The layer between r_{i-1} and r_j is considered as layer i. The region $r > r_1$ is considered layer 0 when necessary. For simplicity the subindex for this layer is omitted. The innermost layer is considered as core.

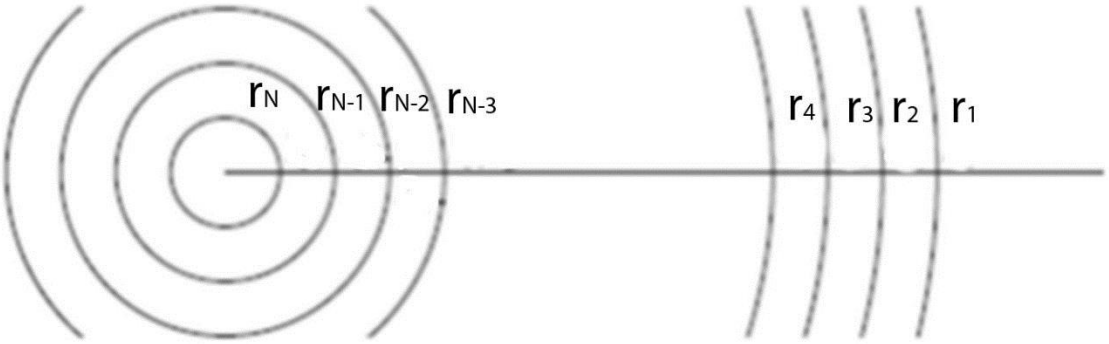

Figure B.3 Multilayer structure

For a general multilayered scatterer, the approach adopted here is using recursively the solution for a dual-layered scatterer. The solution follows the multiple scattering process in the layered scatterer, hence it is formally applicable for all types of waves, and adapting that solution for acoustic waves is straightforward.

The recursive process is the following. In the first step, the innermost two layers are considered as the core and the intermediate layer, and the second layer from the core is considered as host. In the next step, the core and the intermediate layer are considered as a composite new core and one more layer is added to form another dual-layer scatterer. The process is repeated until all the layers are included.

In the external medium coexist both waves, the incident and the scattered, which can be expressed as:

$$\phi^{inc} = \{\mathbf{A}\}^T\{J(k,r)\}, \quad (B.3.\ 1)$$

$$\phi^{disp} = \{\mathbf{B}\}^T\{H(r,\theta)\}, \quad (B.3.\ 2)$$

where, in matrix notation, the wave expansion bases are:

$$\{J(k,r)\}_n = J_n(kr)e^{-\hat{\imath}n\theta}, \quad (B.3.\ 3)$$

$$\{H(k,r)\}_n = H_n^{(1)}(kr)e^{-\hat{\imath}n\theta} \quad (B.3.\ 4)$$

Where $J_n()$ and $H_n()$ are Bessel and Hankel functions of first kind, and k is the wave number.

The transmitted wave in the innermost layer exists only if this layer is penetrable. In this case the transmitted wave can be expressed as:

$$\phi^{trans} = \{\mathbf{C}\}^T\{J(k_n,r)\} \quad (B.3.\ 5)$$

In all other layers, waves contain both components in regular and singular wave expansion basis. For layer i ($1 \leq i \leq N-1$), the wave is expressible as:

$$\phi^{i} = \{D_i\}^T\{J(k_i,r)\} + \{E_i\}^T\{H(k_i,r)\}. \quad (B.3.\ 6)$$

The system is linear, which means all these wave expansion coefficient matrices can be related to that of the incident wave via linear transformations. These linear transformations matrices are the characteristic ones of the scattering system. Denote

$$\{\boldsymbol{B}\} = [\boldsymbol{R}]\{\boldsymbol{A}\}, \quad (B.3.\ 7)$$

$$\{\boldsymbol{C}\} = [\boldsymbol{T}]\{\boldsymbol{A}\}, \quad (B.3.\ 8)$$

$$\{\boldsymbol{D_i}\} = [\boldsymbol{S_i}]\{\boldsymbol{A}\}, \quad (B.3.\ 9)$$

$$\{\boldsymbol{E_i}\} = [\boldsymbol{F_i}]\{\boldsymbol{A}\}. \quad (B.3.\ 10)$$

It is necessary to find a way to express the characteristic matrices **R**, **T**, $\mathbf{S_i}$ and $\mathbf{F_i}$. The strategy is to use the aforementioned recursive process to resolve the dual-layer scatterer and repeat it for each layer.

In the first step, layer N is considered as medium 3, the layer N-1 – as medium 2 and the layer N-2 - medium 1. The solution for dual-layer scatterer is directly accepted, then:

$$[S_{N-1}] = \left([I] - \left[\mathcal{R}_{(N-1)(N-2)}\right]\left[R_{(N-1)N}\right]\right)^{-1}\left[\mathcal{T}_{(N-2)(N-1)}\right], \quad (B.3.\ 11)$$

$$[R_{N-1}] = \left[\mathcal{R}_{(N-2)(N-1)}\right] + \left[\mathcal{T}_{(N-1)(N-2)}\right]\left[R_{(N-1)N}\right][S_{N-1}], \quad (B.3.\ 12)$$

$$[F_{N-1}] = \left[\mathcal{R}_{(N-1)N}\right][S_{N-1}], \quad (B.3.\ 13)$$

$$[T] = \left[\mathcal{T}_{(N-1)N}\right][S_{N-1}]. \quad (B.3.\ 14)$$

Next step is to treat the innermost layers (N and N-1) as a composite core. Then the layer N-2 is considered as medium 2 and the layer N-3 is considered as medium1. There are two important differences:

1. The matrix $[\mathcal{R}_{23}]$ in binary case represents the reflection from the core. In the case of a composite core this matrix must be replaced with matrix that represents the total reflection in the surrounding medium in the previous step, and
2. All the waves in layers N and N-1 in the previous step must be changed as a result of the fact that the interacted wave is no longer incident one.

Let's introduce an intermediate series of matrices $[L_i]$ representing the incident wave in the medium 3 in the intermediate step when the layer *i* is considered as medium 2. Then $[S_i]$ maintains its meaning representing the stationary component of the layer *i* while the $[L_i]$ represents layer effect. In this step:

$$[L_{N-2}] = \left([I] - \left[\mathcal{R}_{(N-2)(N-3)}\right]\left[R_{(N-1)}\right]\right)^{-1}\left[\mathcal{T}_{(N-3)(N-2)}\right]. \quad \textit{(B.3. 15)}$$

Obviously, in the preceding step $[L_i]$ is identical to $[S_{N-1}]$. Then, according to the solution of binary case the wave produced by single multilayer scatterer in medium 1 and 2 are:

$$[S_{N-2}] = [L_{N-2}] \quad \textit{(B.3. 16)}$$

$$[R_{N-2}] = \left[\mathcal{R}_{(N-3)(N-2)}\right] + \left[\mathcal{T}_{(N-2)(N-3)}\right]\left[R_{(N-1)}\right][L_{N-2}], \quad \textit{(B.3. 17)}$$

$$[F_{N-2}] = [\mathcal{R}_{N-1}][L_{N-2}]. \quad \textit{(B.3. 18)}$$

In the composite core the incoming wave represented as $[L_{N-2}]$ is acting as incident one. The expressions for characteristic matrices for all the waves in the composite core are modified by multiplying right side by $[L_{N-2}]$. This is:

$$[S_{N-1}] = [L_{N-1}][L_{N-2}], \quad \textit{(B.3. 19)}$$

$$[F_{N-1}] = [\mathcal{R}_{(N-1)N}][L_{N-1}][L_{N-2}], \quad \textit{(B.3. 20)}$$

$$[T] = \left[\mathcal{T}_{(N-1)N}\right][L_{N-1}][L_{N-2}]. \quad \textit{(B.3. 21)}$$

This procedure can be used recursively until the medium 1 becomes the surrounding environment. This process can be summarized following recursive equations:

$$[L_i] = \left([I] - \left[\mathcal{R}_{i(i-1)}\right]\left[R_{(i+1)}\right]\right)^{-1}\left[\mathcal{T}_{(i-1)i}\right], \quad \textit{(B.3. 22)}$$

$$[R_i] = \left[\mathcal{R}_{(i-1)i}\right] + \left[\mathcal{T}_{i(i-1)}\right][R_{i+1}][L_i]. \quad \textit{(B.3. 23)}$$

This recursion starts from *i*=N-1 and $[R_N]=[\mathcal{R}_{(N-1)N}]$. The recursion moves outward, in direction of decreasing *i*, until *i*=1. Finally, the total scattered wave is represented by

$$[R] = [R_1], \quad \textit{(B.3. 24)}$$

which is what conventionally referred to as the *T-matrix* for multilayer scatterer. Characteristic matrices for the layers can be calculated in this way for layer *i* ($1 \leq i \leq$ N-1):

$$[S_i] = \prod_{j=1}^{i}\left[L_j\right], \quad \textit{(B.3. 25)}$$

$$[F_i] = [R_{i+1}][S_i], \quad \textit{(B.3. 26)}$$

where the cumulative matrix product is to left-multiply by matrices with larger *j* values.

Finally, for the core is obtained:

$$[T] = \left[\mathcal{T}_{N(N+1)}\right][S_{N-1}]. \quad \textit{(B.3. 27)}$$

3.4. Multiple scattering by multilayered scatterers

Once the scattering for a single scatterer has been analyzed, the so-called *T-matrix* being obtained. The multiple scattering is straightforward. Each scatterer is represented by a T-matrix that corresponds to the [R] matrix in the previous section, whose expression is given by *(B.3.24).*

Appendix C

Heat Transfer Equations

C.1 Thermal conduction

The physical mechanism of conduction is most easily explained by considering an ideal gas. Consider a gas in which there exists a temperature gradient and assume that there is no bulk motion. The gas may occupy the space between two surfaces that are maintained at different temperatures, as shown in Figure C.1.1. We associate the temperature at any point with the energy of gas molecules in proximity to the point. This energy is related to the random translation motion, as well as to the internal rotational and vibrational motions, of the molecules.

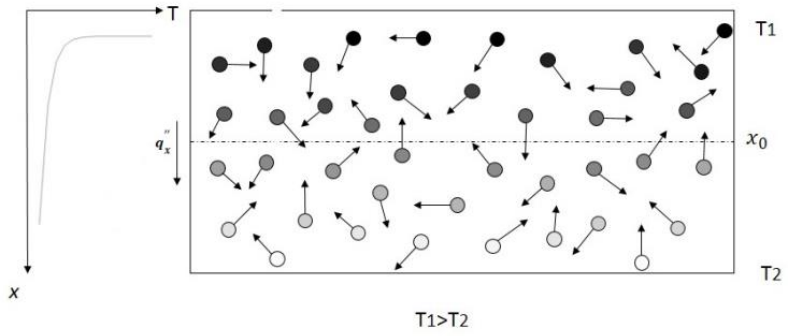

Figure C.1.1 Association of conduction heat transfer with diffusion of energy due to molecular activity

Higher temperatures are associated with higher molecular energies, and when neighboring molecules collide, as they are constantly doing, a transfer of energy from the more energetic molecules must occur. In the presence of a temperature gradient, energy transfer by conduction must then occur in the direction of decreasing temperature. The plane at x_0 is constantly being crossed by molecules from above and below due to their random motion. However, molecules from above are associated with a larger temperature than those from below, in which case there must be a net transfer of energy in the positive x direction. We may speak of the net transfer of energy by random molecular motion as a diffusion of energy.

It is possible to quantify heat transfer processes in terms of appropriate rate equations. These equations may be used to compute the amount of energy being transferred per unit time. For heat conduction, the rate equation is known as Fourier's law. For one-dimensional case the rate equation is expressed as [Inc96]:

$$q''_x = -k\frac{dT}{dx}, \qquad (C.1.1)$$

The heat flux q''_x [W/m^2] is the heat transfer rate in the x direction per unit area perpendicular to the direction of transfer, and it is proportional to the temperature gradient, dT/dx, in this direction. The

symbol ' " ' here does not mean second derivative by time, it simply notes that heat flux through some area. The proportionality constant *k* is a transport property known as the thermal conductivity and is a characteristic of the material. The minus sign is a consequence of the fact that heat is transferred in the direction of decreasing of the temperature.

An essential tool for many heat transfer problem is the first law of thermodynamics – the law of conservation of the energy. A general form of the energy conservation requirement for a differential control volume may be expressed as:

$$\dot{E}_{in} + \dot{E}_g - \dot{E}_{out} = \frac{dE_{st}}{dt} \equiv \dot{E}_{st} \qquad (C.1.\ 2)$$

where $\dot{E}_{\text{in}}$ and $\dot{E}_{\text{out}}$ are the entering and leaving thermal and mechanical energy, respectively. $\dot{E}_{\text{g}}$ is the energy generation – the thermal energy created within the control volume due to conversion from other energy forms. The rate of change of energy stored within the control volume, $\frac{dE_{st}}{dt}$, is designated as $\dot{E}_{\text{st}}$. Equation *(C.1.2)* tells us that the amount of energy inflow and generation act to increase the amount of energy stored within the control volume, whereas outflow acts to decrease the stored energy.

It is important to note that the terms $\dot{E}_{\text{g}}$ and $\dot{E}_{\text{st}}$ represent different physical processes. The term of energy generation, $\dot{E}_{\text{g}}$, is a manifestation of some energy conversion process involving thermal energy on one hand and chemical, electrical or nuclear energy on other. The term is positive (a source) if thermal energy is being generated in the material at the expense of some other energy form; it is negative (a sink) if thermal energy is being consumed. In contrast, the energy storage term $\dot{E}_{\text{st}}$ refers to the rate of change of thermal energy stored by the matter.

Consider a homogeneous medium within which there is no bulk motion (advection) and the temperature distribution *T(x,y,z)* is expressed in Cartesian coordinates. Let the dimensions of the differential control volume in this medium are *dx*, *dy* and *dz* (Figure C.1.2). If there are temperature gradients, conduction heat transfer will occur across each of the control surfaces. The conduction heat rates perpendicular to each of the control surfaces at the *x*, *y* and *z* coordinate locations are indicated by the terms q_x, q_y and q_z, respectively. The conduction heat rates at the opposite surfaces can then be expressed as a Taylor series expansion, neglecting higher order terms:

$$q_{x+dx} = q_x + \frac{\partial q_x}{\partial x} dx, \qquad (C.1.\ 3)$$

$$q_{y+dy} = q_y + \frac{\partial q_y}{\partial y} dy, \qquad (C.1.4)$$

$$q_{z+dz} = q_z + \frac{\partial q_z}{\partial z} dz, \qquad (C.1.\ 5)$$

Within the medium there may also be an energy source term associated with the rate of thermal energy generation:

$$\dot{E}g = \dot{q}dxdydz, \qquad (C.1.\ 6)$$

where $\dot{q}$ is the rate at which energy is generated per unit volume of the medium. In addition, changes in the amount of the internal thermal energy stored by the material in the control volume may occur. If the material is not suffering a change in phase, latent energy effects are not pertinent, and the energy storage term may be expressed as:

$$\dot{E}st = \rho c_p \frac{\partial T}{\partial t} dxdydz, \qquad (C.1.7)$$

where $\rho c_p \frac{\partial T}{\partial t}$ is the time rate of change of the thermal energy of the medium per unit volume.

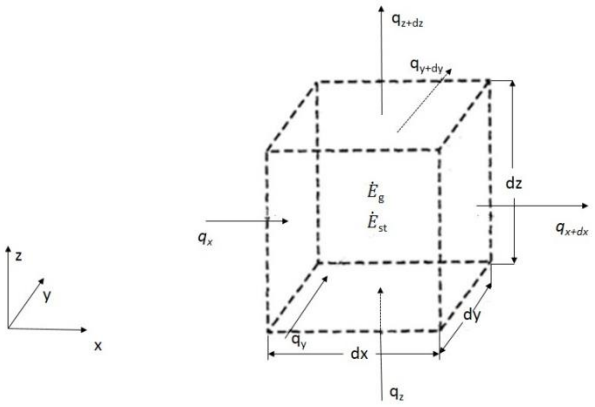

Figure C.1.2 Differential control volume, dx dy dz, for conduction analysis in Cartesian coordinates.

Now we are ready to express conservation of energy using foregoing rate equations. Substituting equations *(C.1.6)* and *(C.1.7)* in *(C.1.2)* we obtain:

$$q_x + q_y + q_z + \dot{q}dxdydz - q_{x+dx} - q_{y+dy} - q_{z+dz} = \rho c_p \frac{\partial T}{\partial t} dxdydz, \qquad (C.1.8)$$

Substituting from equations *(C.1.3 – C.1.5)* it follows that

$$-\frac{\partial q_x}{\partial x}dx - \frac{\partial q_y}{\partial y} - \frac{\partial q_z}{\partial z} + \dot{q}dxdydz = \rho c_p \frac{\partial T}{\partial t} dxdydz, \qquad (C.1.9)$$

The conduction heat rates may be evaluated from Fourier's law:

$$q_x = -kdydz\frac{\partial T}{\partial x}, \qquad (C.1.10)$$

$$q_y = -kdxdz\frac{\partial T}{\partial y}, \qquad (C.1.11)$$

$$q_z = -kdxdy\frac{\partial T}{\partial z}, \qquad (C.1.12)$$

where each heat flux component of equation *(C.1.1)* has been multiplied by the appropriate control surface (differential) area to obtain the heat transfer rate. Substituting equations *(C.1.10 – C.1.12)* into *(C.1.9)* and dividing out the dimensions of the control volume (*dx dy dz*) we obtain

$$\frac{\partial}{\partial x}\left(k\frac{\partial T}{\partial x}\right) + \frac{\partial}{\partial y}\left(k\frac{\partial T}{\partial y}\right) + \frac{\partial}{\partial z}\left(k\frac{\partial T}{\partial z}\right) + \dot{q} = \rho c_p \frac{\partial T}{\partial t}, \qquad (C.1.13)$$

Equation *(C.1.13)* is the general form, in Cartesian coordinates, of the heat diffusion equation. This equation, usually known as the heat equation, provides the basic tool for heat conduction analysis. From its solution we can obtain the temperature distribution *T(x, y, z)* in some medium as a function of time. It describes an important physical condition, that is, conservation of energy. This equation shows that three effects compete in the energy balance: the internal heat generation $\dot{q}$, the rate of change of thermal energy $\rho c_p \frac{\partial T}{\partial t}$ stored within the volume and the net rate of energy transfer by conduction into a unit volume $\frac{\partial}{\partial x}\left(k\frac{\partial T}{\partial x}\right) + \frac{\partial}{\partial y}\left(k\frac{\partial T}{\partial y}\right) + \frac{\partial}{\partial z}\left(k\frac{\partial T}{\partial z}\right)$. Here the word "net" represents the difference between the conduction current that arrives at a given *x* and the conduction current that leaves the control volume.

Frequently the rate of change of thermal energy stored within the volume is called "thermal inertia". It means that a finite sample must be the recipient of net heat transfer if its temperature is to rise. When the net heat transfer input is fixed, the temperature rises faster when the term ρc_p is smaller. The term ρc_p represents the thermal inertia per unit of volume, or the specific heat capacity of the medium.

It is often possible to work with simplified versions of equation *(C.1.13*). For example, if the thermal conductivity is a constant, the heat equation is

$$\frac{\partial^2 T}{\partial x^2}+\frac{\partial^2 T}{\partial y^2}+\frac{\partial^2 T}{\partial z^2}+\frac{\dot{q}}{k}=\frac{1}{\alpha}\frac{\partial T}{\partial t}, \qquad (C.1\ 14)$$

where $\alpha=k/\rho c_p$ is the thermal diffusivity.

Under steady-state conditions, there can be no change in the amount of energy storage; hence equation *(C.1.13)* reduces to

$$\frac{\partial}{\partial x}\left(k\frac{\partial T}{\partial x}\right)+\frac{\partial}{\partial y}\left(k\frac{\partial T}{\partial y}\right)+\frac{\partial}{\partial z}\left(k\frac{\partial T}{\partial z}\right)+\dot{q}=\ 0, \qquad (C.1.15)$$

If the heat transfer is one-dimensional (e.g. in the *x* direction) and there is no energy generation, equation *(C.1.15)* reduces to

$$\frac{\partial}{\partial x}\left(k\frac{\partial T}{\partial x}\right)=0, \qquad (C.1.16)$$

The important implication of this result is that under steady-state, one-dimensional conditions with no energy generation, the heat flux is a constant in the direction of transfer.

C.2 Natural convection

The convection heat transfer mode is comprised of two mechanisms. In addition of energy transfer due to random molecular motion (diffusion), energy is also transferred by macroscopic motion of the bulk. This fluid motion is associated with the fact that at any instant large numbers of molecules are moving collectively or as aggregates. Such motion, in the presence of a temperature gradient, contributes to heat transfer. Because the molecules in the aggregate retain their random motion, the total heat transfer is then due to the superposition of energy transport by the random motion of the molecules and by the bulk motion of the fluid. It is customary to use the term convection when referring to this cumulative transport and the term advection when referring to transport due to bulk fluid motion.

The convection heat transfer mode is sustained both by random molecular motion and by bulk motion of the fluid within the boundary layer. The contribution due to random molecular motion (diffusion) dominates near the surface where the fluid velocity is low. In fact, at the interface between the surface and the fluid (*y=0*), the fluid velocity is zero and the heat is transferred by this mechanism only. The contribution due to bulk fluid motion originates from the fact that the boundary layer grows as the flow progresses in *x* direction. In effect, the heat that is conducted into this layer is swept downstream and is eventually transferred to the fluid outside the boundary layer.

Convection heat transfer may be classified according to the nature of the flow. We speak of forced convection when the flow is caused by external means, such as by a fan, a pump or atmospheric winds.

In contrast, for free (natural) convection the flow is induced by buoyancy forces, which arise from density differences caused by temperature variations in the fluid.

In free convection fluid motion is due to buoyancy forces within the fluid. Buoyancy is due to the combined presence of a fluid density gradient and a body force that is proportional to the density. Usually, the body force is gravitational, although it may be (for example) a centrifugal force in rotating fluid machinery or a Coriolis force in atmospheric and oceanic rotational motions. There are also several ways in which a mass density gradient may arise in a fluid, but for the most common situation it is due to the presence of a temperature gradient. The density of gases and liquids depends on the temperature, generally decreasing with increasing temperature.

In this work we focus on free convection problems in which the density gradient is due to a temperature gradient and the body force is gravitational.

The equations describing momentum and energy transfer in free convection originate from the related conservation principles.

The appropriate rate equation for convection heat transfer process is on the form [Bej93]:

$$q'' = h(T_s - T_\infty), \qquad (C.2.1)$$

where the convective heat flux q'' is proportional to the difference between the surface and fluid temperatures, T_s and T_∞, respectively. This expression is known as Newton's law of cooling. The proportionality coefficient *h* is termed the convection heat transfer coefficient.

In the absence of adjoining force, free boundary flows may occur in the form of a plume (Figure C.2.1) or a buoyant jet. A plume is associated with fluid rising from a submerged heated object. Consider the heated wire of Figure C.2.1, which is immersed in an extensive, quiescent fluid (an extensive medium is, in principle, an infinite medium. Since a quiescent fluid is one that is otherwise at rest, the velocity of the fluid far from the heated wire is zero). Fluid that is heated by the wire rises due to buoyancy forces, entraining fluid from the quiescent region. Although the width of the plume increases with distance from the wire, the plume itself will eventually dissipate as a result of viscous effects and the reduction in buoyancy force caused by cooling of the fluid in the plume.

The description of the phenomenon of convection is not trivial; it depends on numerous fluid properties such as density, viscosity, thermal conductivity and specific heat. The coefficients depend on the surface geometry and the flow conductions. This multiplicity of independent variables results because convection transfer is determined by the boundary layers developing on the surface.

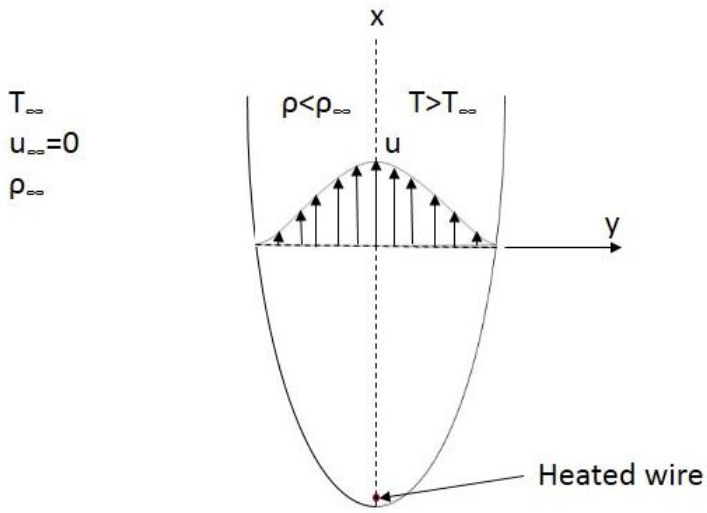

Figure C.2.1 Plume formation above a heated wire. Inside of the plume the density ρ is smaller than the density outside ρ_∞ and the temperature inside T is higher than the temperature outside T_∞. The fluid velocity is greater along the x-axis and gradually decreases toward borders.

C.3 Convection transfer equations

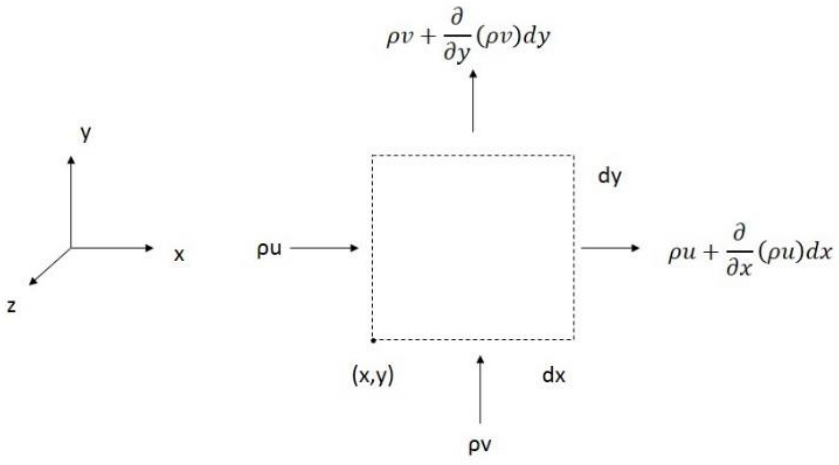

Figure C.3.1 Mass conservation for differential control volume (dx.dy.1).

The conservation law states that matter may neither be created nor destroyed. Stated in the context of the differential control volume of Figure C.3.1 this law requires that, for steady flow, the net rate at which mass enters the control volume (inflow – outflow) must equal zero. Mass enters and leaves

the control volume exclusively through gross fluid motion. Transport due to such motion is often referred

to as advection. If one corner of the control volume is located at (*x*,*y*), the rate at which mass enters the control volume through the surface perpendicular to *x* may be expressed as *(ρu) dy*, where *ρ* is the mass density and *u* is the *x* component of the mass average velocity. The control volume is of unit depth in the *z* direction. Since *ρ* and *u* may vary with *x*, the rate at which mass leaves the surface at *x+dx* may be expressed by a Taylor series expansion of the form:

$$\left[(\rho u) + \frac{\partial(\rho u)}{\partial x} dx\right] dy. \qquad (C.3.1)$$

Using a similar result for the *y* direction, the conservation of mass requirement becomes:

$$(\rho u)\, dy + (\rho v)\, dx - \left[\rho u + \frac{\partial(\rho u)}{\partial x} dx\right] dy - \left[\rho v + \frac{\partial(\rho v)}{\partial y} dy\right] dx = 0. \qquad (C.3.2)$$

After canceling terms and dividing by the infinitesimal area *dxdy*, we obtain:

$$\frac{\partial(\rho u)}{\partial x} + \frac{\partial(\rho v)}{\partial y} = 0 \qquad (C.3.3)$$

The equation *(C.3.3)* is so called continuity equation and it is a general expression of the overall mass conservation requirement.

The second fundamental law that is pertinent is Newton's second law of motion. For a differential control volume in the velocity boundary layer, this requirement states that the sum of all forces acting on the control volume must equal the net rate at which momentum leaves the control volume (outflow – inflow).

Two kinds of forces may act on the fluid in the boundary layer: body forces, which are proportional to the volume, and surface forces, which are proportional to the area. Gravitational, centrifugal, magnetic, and/or electric fields may contribute to the total body force, and we designate the *x* and *y* components of this force per unit volume of fluid as X and Y, respectively. The surface forces F_s are due to the fluid static pressure as well as to viscous stresses. At any point of boundary layer, the viscous stress (a force per unit area) may be resolved into two perpendicular components, which include a normal stress σ_{ii} and shear stress τ_{ij} (Figure C.3.2).

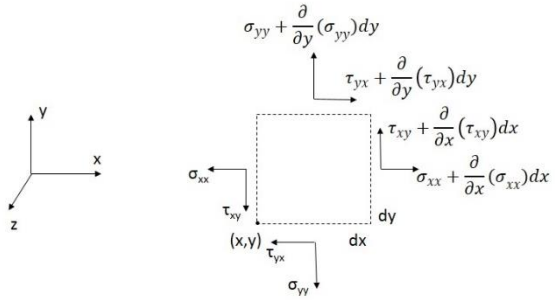

Figure C.3.2 Normal and shear viscous stresses for a differential control volume (dx.dy.1)

A double subscript notation is used to specify the stress components. The first subscript indicates the surface orientation by providing the direction of its outward normal, and the second subscript indicates the direction of the force component. Accordingly, for the *x* surface of Figure C.3.2, the

normal stress σ_{xx} corresponds to a force component normal to the surface, and the shear (tangential) stress τ_{xy} corresponds to a force in the *y* direction along the surface. All the stress components shown are positive in the sense that both the surface normal and the force component are in the same direction. By this

convention the normal viscous stress are tensile stresses. In contrast the static pressure originates from an external force acting on the fluid in the control volume and is therefore a compressive stress.

Several features of the viscous stress should be noted. The associated force is between adjoining fluid elements and is a natural consequence of the fluid motion and viscosity. The surface forces of Figure C.3.3 are therefore presumed to act on the fluid within the control volume and are attributed to its interaction with the surrounding fluid. These stresses would vanish if the fluid velocity, or the velocity gradient, went to zero. In this respect the normal viscous stresses (σ_{xx} and σ_{yy}) must not be confused with the static pressure, which does not vanish for zero velocity.

Each of the stresses may change continuously in each of the coordinate directions. Using a Taylor series expansion for the stresses, the net surface force for each of the two directions may be expressed as

$$F_{s,x} = \left(\frac{\partial \sigma_{xx}}{\partial x} - \frac{\partial p}{\partial x} + \frac{\partial \tau_{yx}}{\partial y}\right) dxdy, \qquad (C.3.4)$$

$$F_{s,y} = \left(\frac{\partial \tau_{xy}}{\partial x} + \frac{\sigma_{yy}}{\partial y} - \frac{\partial p}{\partial y}\right) dxdy, \qquad (C.3.5)$$

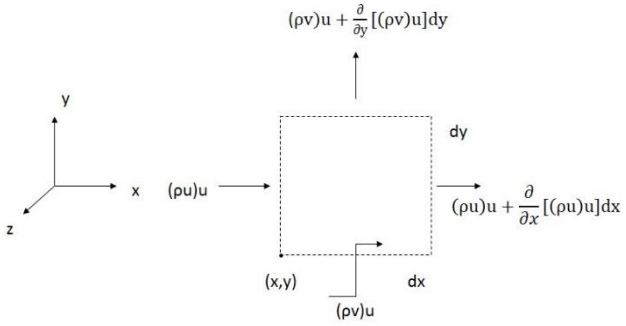

Figure C.3.3 Momentum fluxes for a differential control volume (dx.dy.1)

Figure C.3.3 shows the relevant fluxes in *x* direction. A contribution to the total *x*-momentum flux is made by the mass flow in each of the two directions. For example, the mass flux through the x surface (in the *y*-*z* plane) is (ρu), and the corresponding *x*-momentum flux is (ρu)*u*. Similarly, the *x*-momentum flux due to mass flow through the *y* surface (in the *x*-*z* plane) is (ρv)*u*. These fluxes may change in each of the coordinate directions, and the net rate at which *x* momentum leaves the control volume is

$$\frac{\partial[(\rho u)u]}{\partial x} dx(dy) + \frac{\partial[(\rho v)u]}{\partial y} dy(dx) \qquad (C.3.6)$$

Equating the rate of change in the *x* momentum of the fluid to the sum of the forces in the x direction, we then obtain:

$$\frac{\partial[(\rho u)u]}{\partial x} + \frac{\partial[(\rho v)u]}{\partial y} = \frac{\partial \sigma_{xx}}{\partial x} - \frac{\partial p}{\partial x} + \frac{\partial \tau_{yx}}{\partial y} + X \qquad (C.3.7)$$

This expression may be put in a more convenient form by expanding the derivatives on the left-hand side and substituting from the continuity equation (C.3.3*):*

$$\rho\left(u\frac{\partial u}{\partial x}+v\frac{\partial u}{\partial y}\right)=\frac{\partial}{\partial x}(\sigma_{xx}-p)+\frac{\partial \tau_{yx}}{\partial y}+X \qquad (C.3.8)$$

A similar expression may be obtained for the *y* direction and is of the form:

$$\rho\left(u\frac{\partial v}{\partial x}+v\frac{\partial v}{\partial y}\right)=\frac{\partial \tau_{xy}}{\partial x}+\frac{\partial}{\partial y}(\sigma_{yy}-p)+Y \qquad (C.3.9)$$

The two terms on the left-hand side of each equation *(C.3.8)* and *(C.3.9)* represent the net rate of momentum flow from the control volume. The terms on the right-hand side account for net viscous and pressure forces, as well as the body force. The group $\sigma_{yy}-p$ is so called "the excess normal stress", that is, the normal stress above the level of the local pressure *p*. These equations must be satisfied at each point in the boundary layer, and with equation *(C.3.3)* they may be solved for the velocity field.

It is necessary to relate the viscous stresses to other flow variables. The stresses are associated with the deformation of the fluid and are a function of the fluid viscosity and velocity gradients. From Figure C.3.4 it is evident that a normal stress must produce a linear deformation of the fluid, whereas a shear stress produces an angular deformation. Moreover, the magnitude of stress is proportional to the rate at which the deformation occurs. The deformation rate is, in turn, related to the fluid viscosity and to the velocity gradients in the flow. For a Newtonian fluid, i.e. fluid, for which the shear stress is linearly proportional to the rate of angular deformation, the stresses are proportional to the velocity gradients, where the proportionality coefficient is the fluid viscosity μ. For many fluids, the viscosity μ depends significantly on the temperature and when some temperature gradient exists in flow field it is necessary to regard μ as a function of position. Moreover, there are two types of viscosity: μ is so called dynamic viscosity and λ is dilatational coefficient of viscosity, related to bulk viscosity. The value of λ, which produces a viscous effect associated with volume change, is very difficult to determine. μ and λ are proportionality coefficients associated with the assumption that stress depends on strain linearly. The most approximation is $\lambda\approx$-2/3μ. Then the relations are [Inc96]:

$$\sigma_{xx}=2\mu\frac{\partial u}{\partial x}-\frac{2}{3}\mu\left(\frac{\partial u}{\partial x}+\frac{\partial v}{\partial y}\right) \qquad (C.3.10)$$

$$\sigma_{yy}=2\mu\frac{\partial v}{\partial y}-\frac{2}{3}\mu\left(\frac{\partial u}{\partial x}+\frac{\partial v}{\partial y}\right) \qquad (C.3.11)$$

$$\tau_{xy}=\tau_{yx}=\mu\left(\frac{\partial u}{\partial y}+\frac{\partial v}{\partial x}\right) \qquad (C.3.12)$$

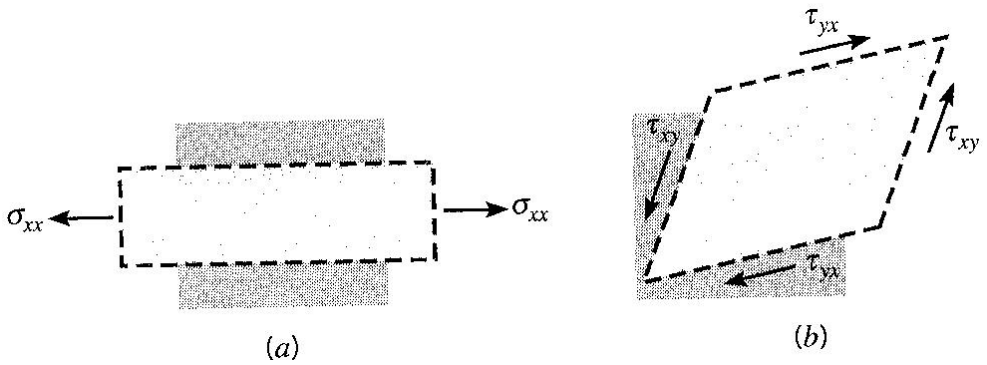

Figure C.3.4 Deformations of a fluid element due to viscous stresses. (a) Linear deformation due to a normal stress. (b) Angular deformation due to shear stress.

Substituting equations (C.3.10–C.3.12) into (C.3.8) and (C.3.9), the *x*- and *y*-momentum equations become:

$$\rho\left(u\frac{\partial u}{\partial x}+v\frac{\partial u}{\partial y}\right)=-\frac{\partial p}{\partial x}+\frac{\partial}{\partial x}\left\{\mu\left[2\frac{\partial u}{\partial x}-\frac{2}{3}\left(\frac{\partial u}{\partial x}+\frac{\partial v}{\partial y}\right)\right]\right\}+\frac{\partial}{\partial y}\left[\mu\left(\frac{\partial u}{\partial y}+\frac{\partial v}{\partial x}\right)\right]+X \qquad (C.3.13)$$

$$\rho\left(u\frac{\partial v}{\partial x}+v\frac{\partial v}{\partial y}\right)=-\frac{\partial p}{\partial y}+\frac{\partial}{\partial y}\left\{\mu\left[2\frac{\partial v}{\partial y}-\frac{2}{3}\left(\frac{\partial u}{\partial x}+\frac{\partial v}{\partial y}\right)\right]\right\}+\frac{\partial}{\partial x}\left[\mu\left(\frac{\partial u}{\partial y}+\frac{\partial v}{\partial x}\right)\right]+Y \qquad (C.3.14)$$

Equations *(C.3.13)* and *(C.3.14)* are the momentum equations for the flow of a Newtonian fluid. The momentum equations are known also as the Navier-Stokes equations.

It is useful to present the equations *(C.3.13)* and *(C.3.14)* in other, more convenient form. The stress tensor σ_{ij} can be represented like this:

$$\sigma_{ij}=\begin{pmatrix}\sigma_{xx} & \tau_{xy}\\ \tau_{yx} & \sigma_{yy}\end{pmatrix} \qquad (C.3.15)$$

where σ_{ij} and τ_{ij} are the normal and shear stresses, respectively. The stress tensor σ_{ij} can be expressed as the sum of two other stress tensors:

1. A volumetric stress tensor, $p\delta_{ij}$, which tends to change the volume of the stressed body; and
2. A deviatoric component called the stress deviator tensor, s_{ij}, which tends to distort it.

Then

$$\sigma_{ij}=s_{ij}+p\delta_{ij}, \qquad (C.3.16)$$

This tensor σ_{ij} is split up into two terms:

$$\sigma_{ij}=\begin{pmatrix}\sigma_{xx} & \tau_{xy}\\ \tau_{yx} & \sigma_{yy}\end{pmatrix}=-\begin{pmatrix}p & 0\\ 0 & p\end{pmatrix}+\begin{pmatrix}\sigma_{xx}+p & \tau_{xy}\\ \tau_{yx} & \sigma_{yy}+p\end{pmatrix}=-pI+T, \qquad (C.3.17)$$

where I is the 2x2 identity matrix and T is the deviatoric stress tensor. The pressure p is:

$$p=-\frac{1}{3}\left(\sigma_{xx}+\sigma_{yy}\right). \qquad (C.3.18)$$

For a Newtonian isotropic fluid equation *(C.3.12)* can be written as:

$$T_{ij}=\mu\left(\frac{\partial u}{\partial y}+\frac{\partial v}{\partial x}\right)+\delta_{ij}\lambda\nabla\cdot\boldsymbol{u}, \qquad (C.3.19)$$

where $\boldsymbol{u}$ = (u,v). A straightforward substitution of T_{ij} into the momentum conservation equation *(C.3.13)* and *(C.3.14)* will yield the Navier-Stokes equations for a compressible Newtonian fluid for steady-state analysis in the form:

$$\rho(\boldsymbol{u}\cdot\nabla)\boldsymbol{u}=\nabla\cdot\left[-p\boldsymbol{I}+\mu(\nabla\boldsymbol{u}+(\nabla\boldsymbol{u})^{T})-\left(\frac{2\mu}{3}-\lambda\right)(\nabla\cdot\boldsymbol{u})\boldsymbol{I}\right]+\boldsymbol{F}\,, \qquad (C.3.20)$$

where I denotes the identity tensor. If the body force is only the gravity, then X = 0 and Y = -ρg.

Another interesting case is about heated vertical plate (Figure C.3.5). The plate is immersed in an extensive, quiescent fluid, and with $T_s>T_\infty$ the fluid close to the plate is less dense than the fluid that is further removed. Therefore, the buoyancy forces introduce a free convection in vertical direction – the heated fluid rises vertically and fluid from the quiescent region occupies its place. The velocity is zero when $y\to\infty$, as well as at the plate surface. If $T_s<T_\infty$ also temperature gradient rises but in this case the fluid motion is downward.

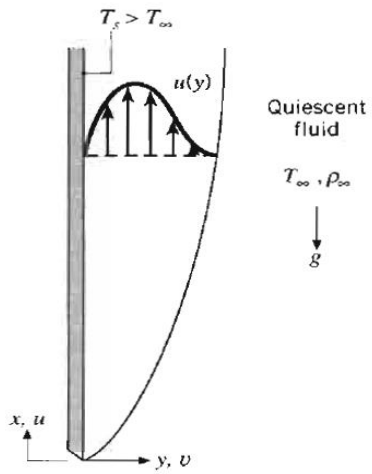

Source: Incropera *et al.*, Fundamentals of heat and mass transfer, 6th edition, Wiley, 2006

Figure C.3.5 Heated plate in an extensive, quiescent fluid. The velocity has maximum value at certain distance from the plate and 0 at the surface and when y→∞.

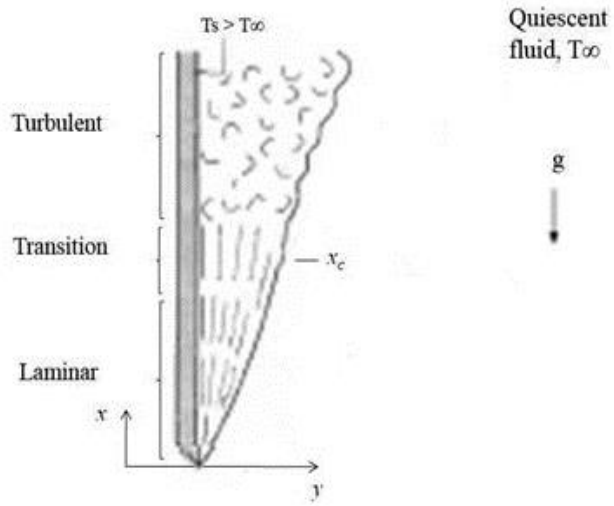

Source: Incropera *et al.*, Fundamentals of heat and mass transfer, 6th edition, Wiley, 2006

Figure C.3.6. Laminar and turbulent motion in free convection.

In free convection there are two forms of fluid motion – laminar and turbulent. In the laminar form the fluid flow is highly ordered and it is possible to identify streamlines along which the fluid particle moves (Figure C.3.6). Fully turbulent fluid flow is, generally, highly irregular and is characterized by random motion of relatively large parcels of fluid. Between the laminar and turbulent regions of fluid motion there is a transition zone, across which a conversion from laminar to turbulent conditions occurs. In this work only the laminar motion will be considered.

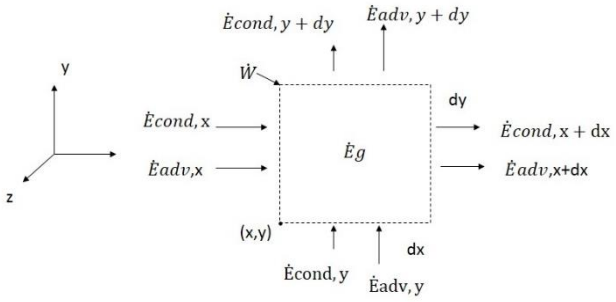

Figure C.3.7 Differential control volume (dx.dy.1) for energy conservation

To apply the energy conservation requirement to a differential control volume (Figure C.3.7), it is necessary to first delineate the relevant physical processes. The energy per unit mass of the fluid includes the thermal internal energy e and the kinetic energy $V^2/2$, where $V^2 = u^2 + v^2$. Accordingly, thermal and kinetic energy are advected with the bulk fluid motion across the control surfaces, and for the x direction, the net rate at which this energy enters the control volume is:

$$\dot{E}_{adv,x} - \dot{E}_{adv,x+dx} = \rho u\left(e + \frac{V^2}{2}\right)dy -$$

$$-\left\{\rho u\left(e+\tfrac{V^2}{2}\right) + \frac{\partial}{\partial x}\left[\rho u\left(e+\tfrac{V^2}{2}\right)\right]dx\right\}dy = -\frac{\partial}{\partial x}\left[\rho u\left(e+\tfrac{V^2}{2}\right)\right]dxdy \qquad (C.3.21)$$

Energy is also transferred across the control surface by molecular processes. There may be two contributions: that due to conduction and energy transfer due to the diffusion. However, it is only in chemically reacting boundary layers that species diffusion strongly influences thermal conditions. Hence the effect is neglected in this development. For the conduction process, the net transfer of energy into the control volume is:

$$\dot{E}_{cond,x} - \dot{E}_{cond,x+dx} = -k\left(k\frac{\partial T}{\partial x}\right)dy - \left[-k\frac{\partial T}{\partial x} - \frac{\partial}{\partial x}\left(k\frac{\partial T}{\partial x}\right)\right]dy = \frac{\partial}{\partial x}\left(k\frac{\partial T}{\partial x}\right)dxdy \qquad (C.3.22)$$

Energy may also be transferred to and from the fluid in the control volume by work interactions involving the body and surface forces. The net rate at which work is done on the fluid by forces in the x direction may be expressed as:

$$\dot{W}_{net,x} = (Xu)dxdy + \frac{\partial}{\partial x}[(\sigma_{xx} - p)u]dxdy + \frac{\partial}{\partial y}(\tau_{yx}u)dxdy \qquad (C.3.23)$$

The first term on the right-hand side of Eq. *(C.3.23)* represents the work done by the body force, and the remaining terms for the net work done by the pressure and viscous forces. Using Eqs. *(C.3.21)* and *(C.3.23)* the energy conservation requirement may be expressed as:

$$-\frac{\partial}{\partial x}\left[\rho u\left(e+\tfrac{V^2}{2}\right)\right] - \frac{\partial}{\partial y}\left[\rho u\left(e+\tfrac{V^2}{2}\right)\right] + \frac{\partial}{\partial x}\left(k\frac{\partial T}{\partial x}\right) + \frac{\partial}{\partial y}\left(k\frac{\partial T}{\partial y}\right) + (Xu + Yv) - -\frac{\partial}{\partial x}(\rho u) - \frac{\partial}{\partial y}(\rho v) + \frac{\partial}{\partial x}(\sigma_{xx}u +$$
$$\tau_{xy}v) + \frac{\partial}{\partial y}(\tau_{yx}u + \sigma_{yy}v) + \dot{q} = 0, \qquad (C.3.24)$$

where $\dot{q}$ is the rate at which the energy is generated per unit volume. This expression provides a general form of energy conservation requirement for the thermal boundary layer.

Because Equation *(C.3.24)* represents conservation of kinetic and thermal internal energy, it is rarely used in solving heat transfer problems. Instead, a more convenient form, which is termed the thermal energy equation, is obtained by multiplying Equations *(C.3.8)* and *(C.3.9)* by *u* and *v*, respectively, and subtracting the results from Equation *(C.3.24)*. It follows that [Bej93]:

$$\rho u\frac{\partial e}{\partial x}+\rho v\frac{\partial e}{\partial y}=\frac{\partial}{\partial x}\left(k\frac{\partial T}{\partial x}\right)+\frac{\partial}{\partial y}\left(k\frac{\partial T}{\partial y}\right)-p\left(\frac{\partial u}{\partial x}+\frac{\partial v}{\partial y}\right)+\mu\Phi+\dot{q} \qquad (C.3.25)$$

where the term $p\left(\frac{\partial u}{\partial x}+\frac{\partial v}{\partial y}\right)$ represents a reversible conversion between kinetic and thermal energy, and $\mu\Phi$, the viscous dissipation, is defined as:

$$\mu\Phi=\mu\left\{\left(\frac{\partial u}{\partial y}+\frac{\partial v}{\partial x}\right)^2+2\left[\left(\frac{\partial u}{\partial x}\right)^2+\left(\frac{\partial v}{\partial y}\right)^2\right]-\frac{2}{3}\left(\frac{\partial u}{\partial x}+\frac{\partial v}{\partial y}\right)^2\right\} \qquad (C.3.26)$$

The first term on the right-hand side of Equation *(C.3.26)* originates from the viscous shear stresses, and the remaining terms arise from the viscous normal stresses. Collectively, the terms account for the rate at which kinetic energy is irreversibly converted to thermal energy due to viscous effects in the fluid.

To express the left-hand side of the thermal energy equation in terms of the temperature, it is necessary to specify the nature of the medium. If, for example, the medium is ideal gas, then equation *(C.3.25)* becomes:

$$\rho C_p\left(u\frac{\partial T}{\partial x}+v\frac{\partial T}{\partial y}\right)=\frac{\partial}{\partial x}\left(k\frac{\partial T}{\partial x}\right)+\frac{\partial}{\partial y}\left(k\frac{\partial T}{\partial y}\right)+\left(u\frac{\partial p}{\partial x}+v\frac{\partial p}{\partial y}\right)+\mu\Phi+\dot{q} \qquad (C.3.27)$$

It is useful to represent the equation *(C.3.27)* in more convenient form. For two-dimensional steady state analysis without considering the viscous heating of a fluid it can be wrote:

$$\nabla\cdot(-k\nabla T)=Q-\rho C_p\boldsymbol{u}\cdot\nabla T \qquad (C.3.28)$$

The theoretical model considered in this work is based on the solutions of equations *(C.3.20)* and *(C.3.28)*.

Appendix D

The Finite Element Method

In this chapter a short introduction to the fundamentals of the finite element method is presented in order to understand how the software package COMSOL Multiphysics, used in this investigation, works. The presentation is based on the Oden's book [Bec81] and also on [Bha05].

The Finite Element Method (FEM) is one of the numerical methods for obtaining approximate solution of ordinary and partial differential equations. It is especially powerful when dealing with boundary conditions defined over complex geometries that are common in practical applications. Because of its adaptability in applying to wide variety of physical areas (for example: heat transfer, fluid dynamics, structural analysis, electrostatics, electromagnetism and others) and versatility in handling arbitrary domains the finite element method has become the preferred method for solution of many practical problems.

The key idea of the finite element method is to discretize the solution domain into a number of simpler domains called elements. An approximate solution is assumed over an element in terms of unknown solutions at selected points called nodes. The unknown solutions at the nodes are generally referred to as the nodal degrees of freedom. The appropriate choice of nodal degrees of freedom depends on the order of the governing differential equation. Several practical elements are available that assume a simple linear solution. Other elements use more sophisticated functions to describe solution over elements.

D.1 Mathematical foundation of the Finite Element Method

The Finite Element Method emerged in the seventh decade of the XX century, when computers where available. From a mathematical point of view, is a special form of the classical (beginning of XX century) Galerkin and Rayleigh-Ritz methods for finding approximate solution of differential equations. In both methods the governing differential equation, first, is converted into an equivalent integral form.

The Rayleigh-Ritz method employs calculus of variations to define a variational or energy functional $F(u(x))$ associated to the original differential equation. A function $u(x)$ that minimizes this energy functional represents a solution of the governing differential equation. Therefore, to solve the differential equation is equivalent to minimizing this functional.

The Galerkin method uses a more direct approach. An approximate solution, with one or more unknown parameters, is chosen. In general, this assumed solution will not satisfy the differential equation exactly. The integral form represents the residual obtained by integrating the error over the solution domain. Employing a criterion adopted to minimize the residual gives equations for finding the unknown parameters.

For most practical problems, solutions of differential equations are required to satisfy not only the differential equation but also the specified boundary conditions at one or more points along the boundary of the solution domain. In both methods some of the boundary conditions must be satisfied explicitly by the assumed solutions while others are satisfied implicitly through the minimization process. The essential boundary conditions are those that must explicitly be satisfied by the assumed solutions, while the natural boundary conditions are incorporated implicitly into the integral formulation. In general, therefore, the approximate solutions will not satisfy the natural boundary conditions exactly. For the second-order problems considered in this work, a boundary condition in which only assumed solution is specified is essential, and the one involving its first derivative, is natural.

D.2 A Model problem given by a differential equation.

To fix ideas let us begin by considering the boundary-value problem of finding a function u(x), $0 \leq x \leq 1$which satisfies the following differential equation and boundary conditions:

$$\left.\begin{aligned} -u'' + u = x \quad 0 < x < 1 \\ u(0) = 0, \quad u(1) = 0 \end{aligned}\right\} \tag{D.2.1}$$

where the primes denote differentiation with respect to x.

The data of the problem consist of all information given in advance:

The domain of the solution (the interval [0,1]); the right-hand side nonhomogeneous part of the differential equation, sometimes called excitation or load function, (f(x)=x);

The coefficients of various derivatives (the trivial functions -1 and +1); and the boundary conditions we want the solution fulfills at the interval ends.

The data in our model are "smooth", that is, the right-hand side *f(x) = x* and the coefficients of the derivatives are differentiable infinitely many times. As a consequence of this smoothness, there exist a unique function *u(x)* which satisfies the differential equation at every point in the domain as well as the boundary conditions.

Sometimes in most technical applications the data are not so smooth, for instance suppose that instead of *f(x)=x* we had a unit "impulse" or "point source" concentrated at $x = 1/2$ and represented by a Dirac delta: $f(x) = \delta(x - \frac{1}{2})$. In this case u(x) must have a discontinuity in its first derivative at $x = 1/2$ and therefore its second derivative does not exist (in the classical or traditional sense) at this point. It seems that something goes wrong.

The difficulty is that our requirement that a solution *u(x)* satisfies the differential equation at every point x in the domain is too strong. To overcome this difficulty, we shall reformulate the boundary-value problem in a way that will admit weaker conditions on the solution and its derivatives. Such

reformulation is called weak *or* variational formulation of the problem and is designed to accommodate irregular (not smooth) data and irregular solutions as well as very smooth solutions.

Whenever a smooth "classical" solution to a problem exist, it is also the solution of the weak problem.

D.3 The variational statement of the model problem

Translating all terms in the differential equation (D.2.1) to the left-hand side we obtain the residual function r(x):

$$r(x) = -u'' + u - x$$

This function represents the error committed when an assumed approximated solution (or trial function $\tilde{u}$) is substituted in the differential equation. When the exact solution *u(x)* is substituted, the residual function is identically zero (for every x).

The total error for the entire solution domain can be obtained by integrating *r(x)* over the domain. However, in a straight integration of *r(x)*, the negative and positive errors at different points may cancel each other giving the false feeling that the error is zero.

To avoid error cancellation, *r(x)* is multiplied by any smooth enough weighting function (or test function) *v(x)* and then integrated over the solution domain.

The weak statement of the model problem (D.2.1) is given as follow:

Find the function *u(x)* such that the averaged weighted residual is zero for every test (or weight) function *v(x)* belonging to a suitable class of functions.

$$\left.\begin{aligned} &\int_0^1 (-u'' + u - x)\boldsymbol{v}dx = 0 \qquad \text{for all } \boldsymbol{v} \in H \\ &u(0) = 0 \\ &u(1) = 0 \end{aligned}\right\} \qquad \text{(D.3.1)}$$

It is clear that if (D.3.1) is true the differential equation (D.2.1) is satisfied in an average sense. The solution of (D.2.1) also satisfies (D.3.1), in fact is the only solution of (D.3.1)

D.4 A symmetric variational formulation

If u and v are sufficiently smooth functions we can apply the integration-by-parts formula to the first term of (D.3.1):

$$\int_0^1 -u"vdx = \int_0^1 u'v'dx - u'v|_0^1 \qquad \text{(D.4.1)}$$

If we demand that the test functions $\boldsymbol{v}$ vanish at the end points, then (D.3.1) can be replaced by (D.4.2) in order to obtain an alternative, symmetric, weak formulation problem:

Find $u \in H_0^1$ such that

$$\int_0^1 \left(u'v' + uv - xv\right)dx = 0 \qquad \text{for all } \boldsymbol{v} \in H_0^1 \qquad \text{(D.4.2)}$$

wherein H_0^1 is a new class of functions that we shall describe below. Now there is a certain symmetry in the formulation: the same order of the derivatives of both trial *u* and test *v* functions appear.

Since (D.3.1) contains second derivatives whereas (D.4.2) has only firs derivatives we see that we have progressively weakened the smoothness requirements on our solution and, thereby, enlarged the class of data for which these statements of the problem make sense. We shall refer to the particular weak formulation defined in (D.4.2) as a variational boundary-value problem.

The set H_0^1 of test and trial functions represent the class of admissible functions for problem (D.4.2), since it contains only those functions which satisfy the boundary conditions and are sufficiently regular that the integral in (D.4.2) has meaning.

The most irregular term inside the integral is *u'v'*: if u and v are irregular, then their derivatives are even less regular. Since v is allowed to be any function in the set of admissible functions, we must consider the possibility that v=u. Thus it will be necessary that $(v')^2$ be smooth enough for its integral to be calculated. Hence, we shall define the set H_0^1 of admissible functions as the set of all functions that vanish at the end points and whose first derivatives are square-integrable. Thus, a function *w(x)* is a member of H_0^1 if

$$\int_0^1 (w')^2 dx < \infty \qquad \text{and } w(0)=0=w(1) \qquad \text{(D.4.3)}$$

Henceforth we consider that (D.4.2) is the given model boundary-value problem that we wish to solve instead of (D.2.1); this make it possible for us to consider broad classes of variational boundary-value problem which have no classical solutions as well as equivalent variational formulations of nice problems with classical solutions.

D.5 Galerkin approximations

Let us consider N basis functions $\{\phi_1, \phi_{2,} \ldots, \phi_N\}$ belonging to H_0^1 that are linearly independent; that is, it is impossible to find N coefficients $\{\beta_1, \beta_{2,} \ldots \beta_N\}$ not all of which are zero, such that $\sum_{i=1}^{N} \beta_i \emptyset_i(x) = 0$ for all x.

We can build an approximation v_N of *v* in the N-dimensional subspace $H_0^{(N)}$ of H_0^1:

$$v_N(x) = \sum_{i=1}^{N} \beta_i \emptyset_i(x) \qquad \text{(D.5.1)}$$

Where the β_i are arbitrary constants.

The Galerkin's method consist of seeking an approximate solution to (D.4.2) in a finite dimensional subspace $H_0^{(N)}$ of the space H_0^1 of admissible functions of the form

$$u_N(x) = \sum_{j=1}^{N} \alpha_j \emptyset_j(x) \tag{D.5.2}$$

which satisfies (D.4.2) with H_0^1 replaced by $H_0^{(N)}$. In other words, the variational statement of the approximate problem is this:

Find $u_N \in H_0^{(N)}$ such that

$$\int_0^1 \left(u_N{}' v_N{}' + u_N v_N - x v_N\right) dx = 0 \qquad \text{for all } \boldsymbol{v_N} \in H_0^{(N)} \tag{D.5.3}$$

To determine the specific values, α_j of these coefficients we introduce (D.5.1) and (D.5.2) into (D.5.3) to obtain the condition

$$\int_0^1 \left\{ \frac{d}{dx}\left[\sum_{i=1}^{N} \beta_i \emptyset_i(x)\right] \frac{d}{dx}\left[\sum_{j=1}^{N} \alpha_j \emptyset_j(x)\right] + \left[\sum_{i=1}^{N} \beta_i \emptyset_i(x)\right]\left[\sum_{j=1}^{N} \alpha_j \emptyset_j(x)\right] - x\left[\sum_{i=1}^{N} \beta_i \emptyset_i(x)\right] \right\} dx = 0 \tag{D.5.4}$$

for all β_i i=1,2, ...N

Expanding the above expression and factoring the coefficients β_i gives

$$\sum_{i=1}^{N} \beta_i \left(\sum_{j=1}^{N} \left\{ \int_0^1 \left[\phi'_i(x) \phi'_j(x) + \phi_i(x) \phi_j(x) \right] dx \right\} \alpha_j - \int_0^1 x \phi_i(x) dx \right) = 0 \tag{D.5.5}$$

for all β_i i=1,2, ...N

where $\phi'_i = \frac{d\phi_i(x)}{dx}$

The structure of the above expression is most easily seen by rewriting it in the more compact form

$$\sum_{i=1}^{N} \beta_i \left(\sum_{j=1}^{N} K_{ij} \alpha_j - F_i \right) = 0 \tag{D.5.6}$$

for all choices of β_i, where

$$K_{ij} = \int_0^1 \left[\phi'_i(x) \phi'_j(x) + \phi_i(x) \phi_j(x) \right] dx \tag{D.5.7}$$

and

$$F_i = \int_0^1 x \phi_i(x) dx \tag{D.5.8}$$

being i,j=1,2, ...N

The NxN square array of numbers $\boldsymbol{K} = [\boldsymbol{K_{ij}}]$ is usually referred to as the stiffness matrix for problem (D.5.3) for the basis functions $\{\phi_i\}_{i=1}^{N}$.

The Nx1 column vector **F={F$_i$}** is referred to as the load vector. Since the ϕ_i are known, the numbers K_{ij} and F_i can be calculated directly by the formulas (D.5.7) and (D.5.8).

Because the β_i are arbitrary, (D.5.6) represents N equations to be satisfied by the α_j rather than the single equation it may appear to be. To see this, consider the following natural choices for the set of parameters: β_1=1, β_i=0 for i≠1. Then (D.5.6) yields...

$$\sum_{j=1}^{N} K_{\mathbf{1}j}\alpha_j = F_1$$

repeating the process, for β_2=1, β_i=0 for i≠2 and so on, we arrive at the system of N linear equations in the N unknown coefficients α_j:

$$\sum_{j=1}^{N} K_{ij}\alpha_j = F_i \quad \text{i=1,2, ...N} \qquad \text{(D.5.9)}$$

Since the functions ϕ_i have been chosen to be independent, equations (D.5.9) will be independent, and therefore the stiffness matrix **K** will be invertible. It follows that the coefficients α_j are uniquely determined by

$$\alpha_j = \sum_{i=1}^{N} (K^{-1})_{ji} F_i \qquad \text{(D.5.10)}$$

The approximate solution $\boldsymbol{u_N}$ is now determined by introducing (D.5.10) into (D.5.2)

D.6 Finite element basis functions

The finite element method provides a general and systematic technique for constructing basis functions for Galerkin approximations of boundary value problems. The main idea is that the basis functions ϕ_i can be defined piecewise over subregions of the domain called finite elements and that over any subdomain, the ϕ_i can be chosen to be very simple functions such as polynomials of low degree.

To construct a set of piecewise basis functions, we first partition the domain (i.e., the interval

$x_1 \leq x \leq x_5$, where x_1=0 and x_5=1, in our previous problem) into a finite number of elements. Figure (D.6.1) shows, for example, the domain of our problem partitioned into four elements, denoted e_i, *i={1,2,3,4}*. The length of each finite element will be denoted $\boldsymbol{h_i}$. Within each element, certain points are identified, called nodes or nodal points, which play an important role in finite element constructions. In this example, the five nodes are taken to be the end points of each element; these are numbered *1* to *5* in the figure. The collection of elements and nodal points is sometimes referred to as finite element mesh.

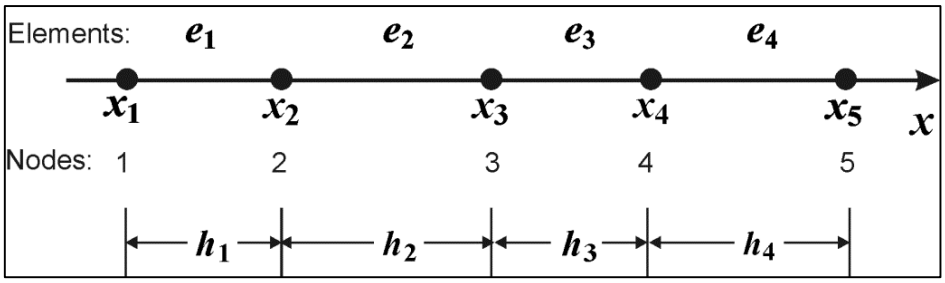

Figure D.6.1 A finite element partition of the region $x_1 \leq x \leq x_5$ comprised of four elements with nodes at element end points.

Having constructed a finite element mesh, we proceed to construct a corresponding set of basis functions (see Figure D.6.2):

$$\emptyset_i(x) = \begin{cases} \frac{x-x_{i-1}}{h_{i-1}} = \psi_2^{e_{i-1}}(x) & for\ x_{i-1} \leq x \leq x_i \\ \frac{x_{i+1}-x}{h_i} = \psi_1^{e_i}(x) & for\ x_i \leq x \leq x_{i+1} \\ 0 & for\ x \leq x_{i-1}\ and\ x \geq x_{i+1} \end{cases} \quad \text{(D.6.1)}$$

where $h_i = x_{i+1} - x_i$ is the length of element e_i. Their first derivatives are

$$\emptyset'_i(x) = \begin{cases} \frac{1}{h_{i-1}} & for\ x_{i-1} \leq x \leq x_i \\ \frac{-1}{h_i} & for\ x_i \leq x \leq x_{i+1} \\ 0 & for\ x \leq x_{i-1}\ and\ x \geq x_{i+1} \end{cases} \quad \text{(D.6.2)}$$

These basis functions satisfy the following criteria:

Each function $\emptyset_i(x)$ is the result of patching together piecewise-linear functions defined over each finite element. For example the "hat"-shaped function $\emptyset_2(x)$ associated with node *2* is produced by combining a linear function $\psi_2^1(x) = \frac{x-x_2}{h_1}$ defined on element e_1 and a linear function

$\psi_1^2(x) = \frac{x_3-x}{h_2}$ defined on element e_2.

Each $\emptyset_i(x)$, is a continuous function and its value is *1* for the node x_i and zero for the other nodes, that is, $\emptyset_i(x_j) = \delta_{ij}$. This makes possible to express the assumed solution as:

$$u_N(x) = \sum u_i \emptyset_i(x) \quad \text{(D.6.3)}$$

where, comparing with (D.5.2), the parameters α_i defining the approximate solution $u_N(x)$ are precisely the values of u_N at the nodal points, $\alpha_i = u_N(x_i)$.

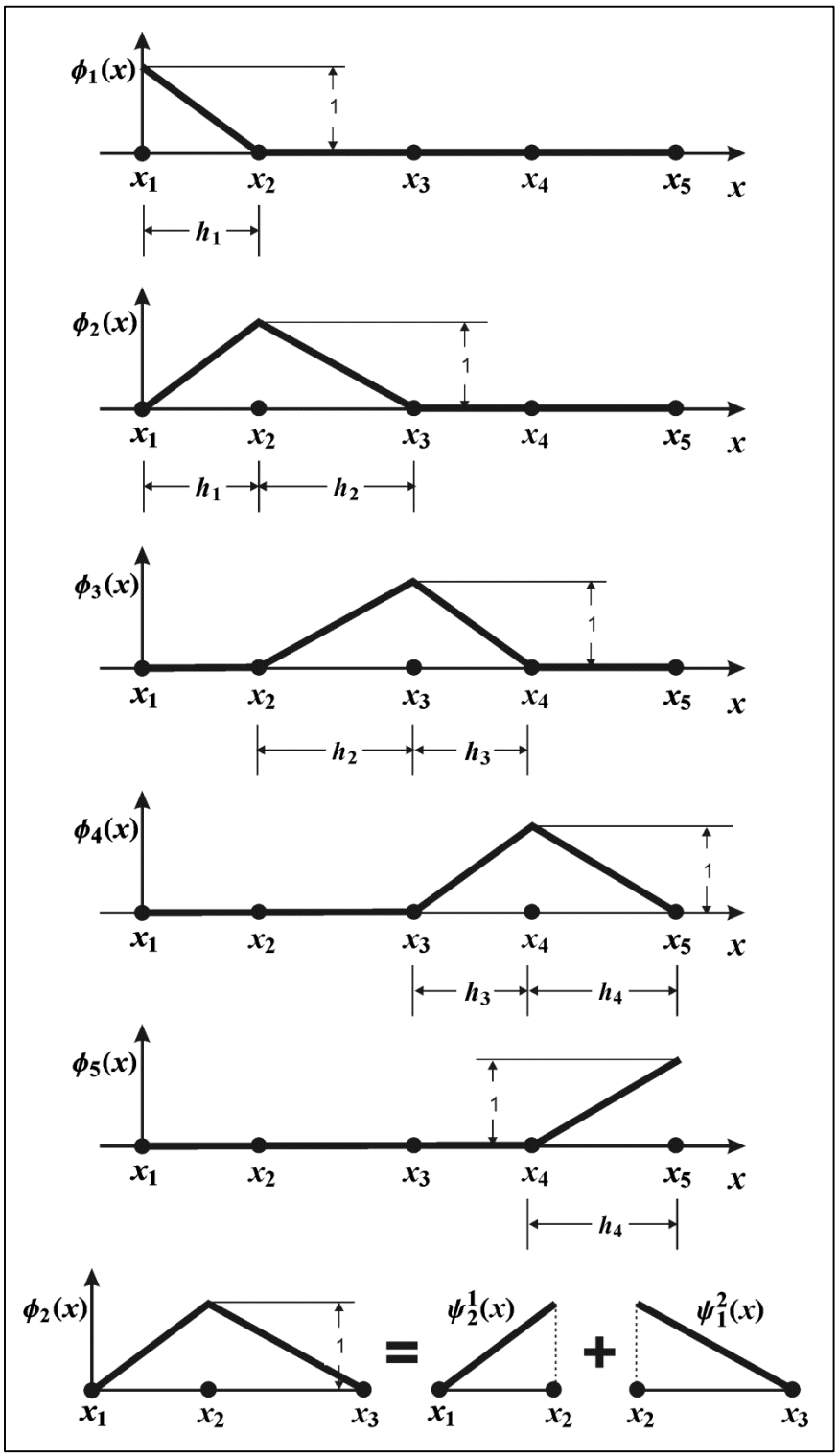

Figure D.6.2 Example of piece-wise continuous finite element basis functions.

By the way, each $\emptyset_i(x)$ has square-integrable fist derivative, (see fig. D.6.3).

For example, suppose that the values of $\boldsymbol{u_i}$ at nodes *{u_1, u_2, u_3, u_4, u_5}* are *{0.2, 0.5, 0.3, 0.8, 0.4}* respectively. Then, substituting these values into (D.6.3) gives

$$u(x) = \sum_{i=1}^{5} u_i \emptyset_i(x) = 0.2\emptyset_1(x) + 0.5\emptyset_2(x) + 0.3\emptyset_3(x) + 0.8\emptyset_4(x) + 0.4\emptyset_5(x)$$

So that these components combine to give the continuous piece-wise linear function shown in figure D.6.4

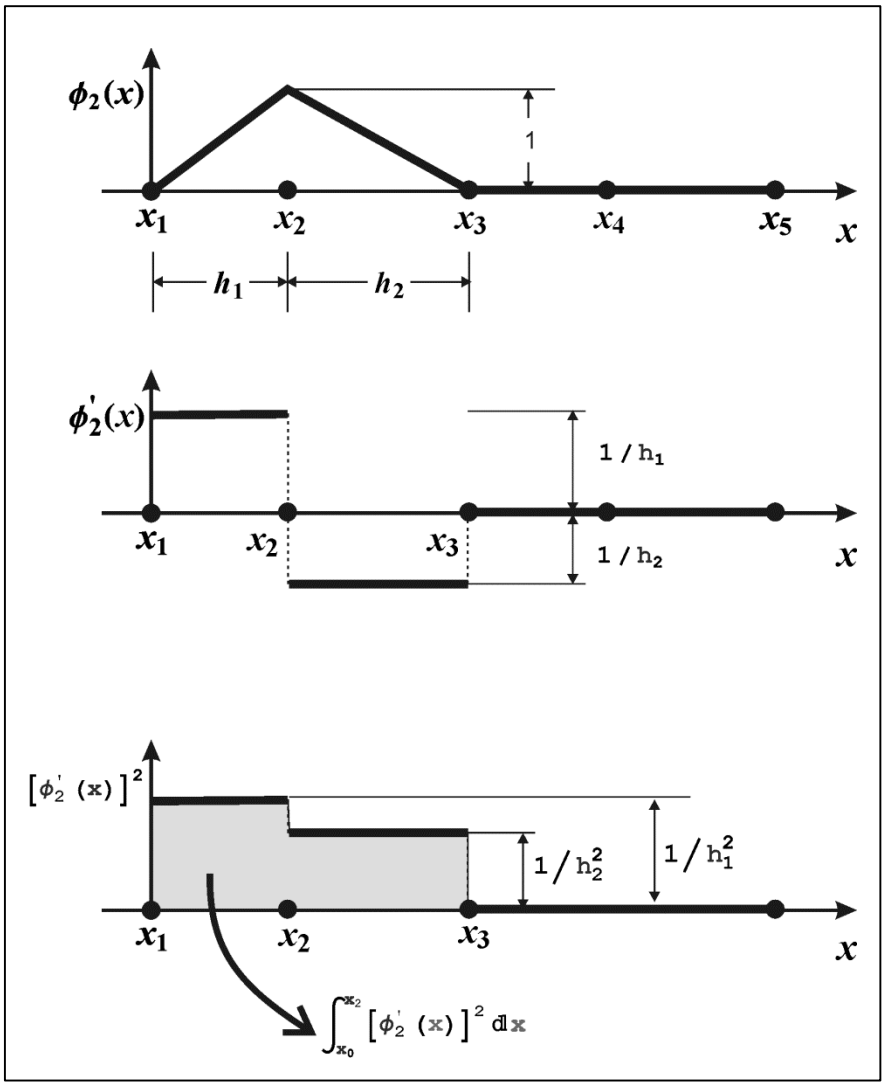

Fig. D.6.3 Finite element basis functions whose derivatives are square-integrable.

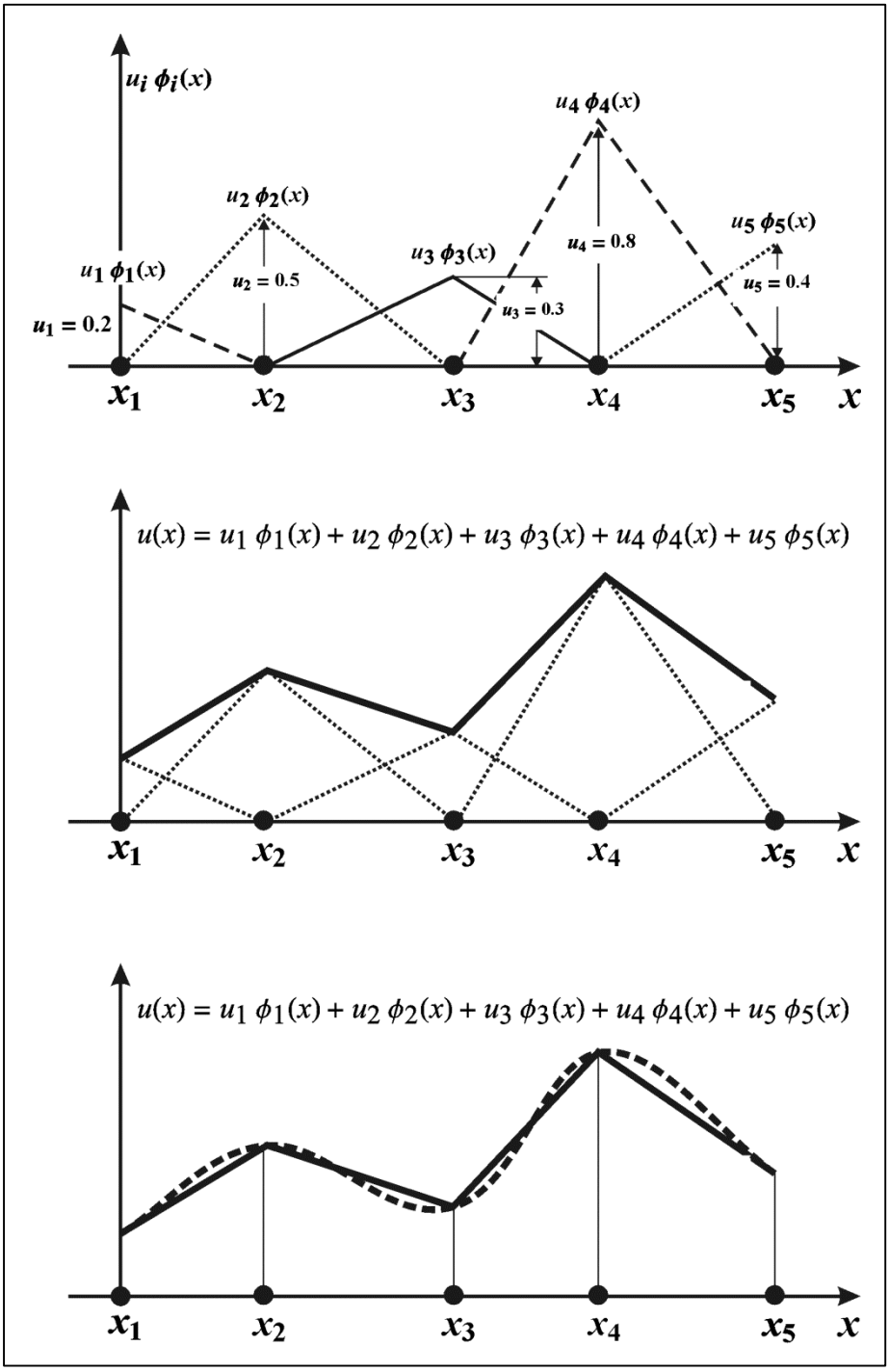

Figure D.6.4. Piecewise local linear approximation of a smooth function.

D.7 Finite element calculations

We apply the Galerkin approximation method to the boundary-value problem (D.2.1) generalized when in (D.4.1), the term $-[\![u'v]\!]_{x_1}^{x_n}$ is different from zero.

$$-[\![u'v]\!]_{x_1}^{x_n} + \int_{x_1}^{x_n}(u'v' + uv - xv)dx = 0 \qquad \text{(D.7.1)}$$

Using the finite element decomposition and the basis functions above defined we arrive at a generalization of (D.5.6), where the stiffness matrix is

$$K_{ij} = \int_{x_1}^{x_n}[\emptyset'_i(x)\,\emptyset'_j(x) + \emptyset_i(x)\emptyset_j(x)]\text{dx} \qquad \text{(D.7.2)}$$

and the load vector is

$$F_i = \int_{x_1}^{x_n} x\emptyset_i(x)dx \qquad \text{(D.7.3)}$$

We can rewrite the generalization of (D.5.6) in the next form

$$[\![-u'(x)\emptyset_i(x)]\!]_{x_1}^{x_n} + \sum_j K_{ij}u_j = F_i \quad \text{for } i=1\ldots n \qquad \text{(D.7.4)}$$

There are three important properties of the stiffness matrix ***K*** and the load vector ***F*.**

1.-Summability of stiffness matrix: Each element of the stiffness matrix is obtained by integrating some product of basis functions and its derivatives over the entire domain $x_1 \le x \le x_n$. But the operation of integration is additive, that is

$$K_{ij} = \int_{x_1}^{x_n}[\emptyset'_i\,\emptyset'_j + \emptyset_i\emptyset_j]dx = \int_{x_1}^{x_2}(\ldots)dx + \int_{x_2}^{x_3}(\ldots)dx + \ldots\int_{x_{n-1}}^{x_n}(\ldots)dx =$$

$$= \sum_{e=1}^{4}\int_e [\emptyset'_i\,\emptyset'_j + \emptyset_i\emptyset_j]dx \qquad \text{(D.7.5)}$$

where $\int_e$ denotes integration over element e.

Let the terms

$$K_{ij}^e = \int_e [\emptyset'_i\,\emptyset'_j + \emptyset_i\emptyset_j]dx \qquad \text{(D.7.6)}$$

represent components of the element stiffness matrix for the element *e*. Thus,

$$K_{ij} = \sum_{e=1}^{4} K_{ij}^e \qquad \text{(D.7.7)}$$

Similarly,

$$F_i^e = \int_e x\emptyset_i(x)dx, \quad F_i = \sum_{e=1}^{4} F_i^e \qquad \text{(D.7.8)}$$

where F_i^e are components of the element load vector for the element *e*.

Because of this elementary summability property, it is possible to generate $\boldsymbol{K}$ and $\boldsymbol{F}$ by computing only the element matrices $\boldsymbol{K^e}$ and $\boldsymbol{F^e}$ for a typical element e and then to construct $\boldsymbol{K}$ and $\boldsymbol{F}$ as the sums indicated above.

2.-Sparseness of *K*: For our model problem, we must compute nine numbers K_{ij} $(i,j=1,2,3)$. However, an examination of figure D.6.2 reveals that $\emptyset_1$and $\emptyset'_1$are different from zero only in elements e_1 and e_2 adjacent to node *1*. Similarly the same thing happens with the other elements. Consequently, products of functions $\emptyset_i\emptyset_j$ are nonzero only where the support for basis functions overlap. For example, the products $\emptyset_1\emptyset_2$ are nonzero only in element *2*, whereas $\emptyset_1\emptyset_3$ are zero everywhere. Hence, the integrals K_{12}, K_{21} are nonzero, but $K_{13}=K_{31}=0$.

It follows that if nodes **i** and **j** do not belong to the same element, then $\mathbf{K_{ij} = 0}$. This implies that in a mesh consisting of many elements, most of the matrix entries will be zero, and the matrix is called sparse. The sparsity of *K* is a consequence of our particular choice of basis functions.

The matrix *K* nonzero entries appear clustered near the main diagonal. Outside this "band" of nonzero terms, all entries are zero. Matrices of this type are said to be banded.

3.-Symmetry of *K*: Interchanging ***i*** and ***j*** in the integral expression for K_{ij} does not change the value calculated, so that $K_{ij} = K_{ji}$ and the stiffness matrix for this problem is symmetric. Not always is the matrix symmetric, yet in most physical problems based on conservation laws this symmetry will arise quite naturally. This symmetry of *K* has nothing to do with the choice of basis functions and is entirely dependent on the form of the variational problem to be solved.

D.8 Physical origins of one dimensional second order boundary value problems

Most physical problems are formulated in terms of two functions whose values are to be determined. We refer to these functions as the state variable $\boldsymbol{u}$ (displacement, temperature) and the flux $\boldsymbol{\sigma}$ (stress, heat). These quantities are related to each other by a constitutive equation (or law) which contains all the information descriptive of the particular material in which the process is taking place.

For example, the following constitutive equation

$$\sigma(x) = -k(x)\frac{du(x)}{dx} \qquad \text{(D.8.1)}$$

describes the linear behavior of a material having a given modulus $k(x)$.

A conservation law is a statement, involving the flux, which requires that in every subdomain the entering flux is zero (i.e. the flux is conserved). Flux can enter a part of the body in two ways: it can be supplied by a distribution of internal sources, denoted by the given function $\boldsymbol{f}$, and it can enter through the boundary of the region.

In addition, $\boldsymbol{u}$ is required to be a continuous function and we frequently require that this state variable assume a given value on either (or both) boundaries of the body. If the particular physical problem includes this requirement, this condition is called essential boundary condition. All other conditions in the boundary-value problem are derivable from the conservation principle.

To fix ideas, let us now consider a representative one-dimensional model of a physical system. Consider, for example, a one-dimensional body (e. g. a rod) occupying the region $0 \leq x \leq l$, as shown in figure D.8.1. The body is composed of two materials, one occupying the region $0<x<x_2$ and the other the region $x_2<x<l$. At this point x_2, the material modulus $\boldsymbol{k}$ suffers a simple discontinuity, as

indicated, but is continuous within each of the two material sections. In this example, the distribution $\boldsymbol{f}$ of internal sources is assumed to be continuous al all points except at $x=x_3$, where a simple discontinuity in the source distribution exist and at $x=x_4$, where a concentrated source of intensity $\hat{f}$, represented by a Dirac delta, is imposed. Thus, the data k and f are such that the body is naturally composed of four subdomains $\boldsymbol{e_i}$ within each of which all data are smooth, and five points (including the boundaries) at which discontinuities in some data occur. We shall refer to the $\boldsymbol{e_i}$ as smooth subdomains.

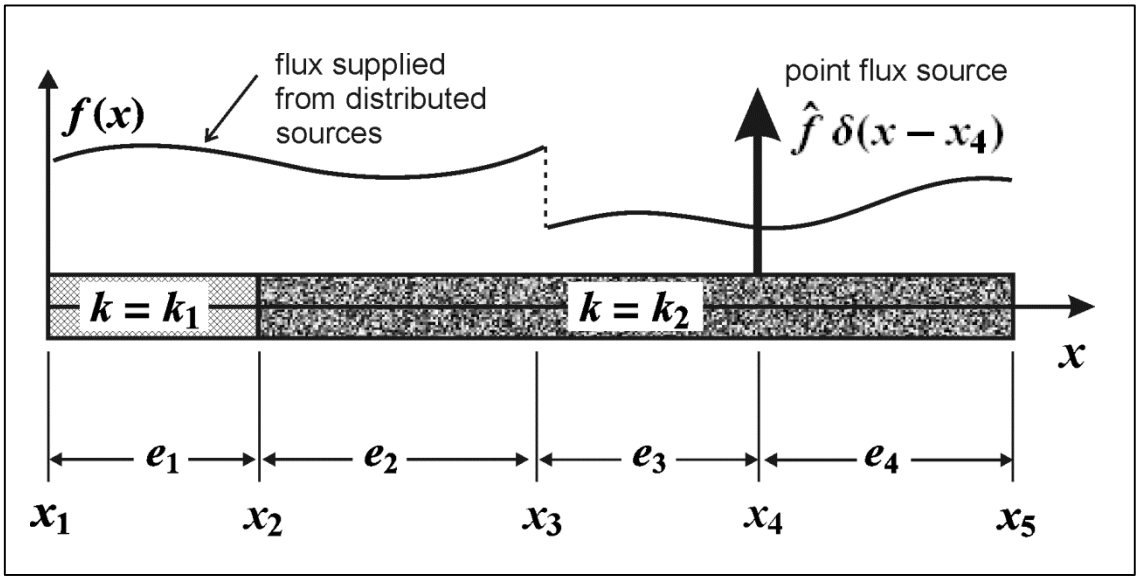

Figure D.8.1 A one-dimensional bar naturally subdivided into four regions between discontinuities in the material modulus k and the source f

Using only essential conditions on u, the conservation law, the constitutive equation, and the given data, we now formulate a classical mathematical description of this one-dimensional physical problem:

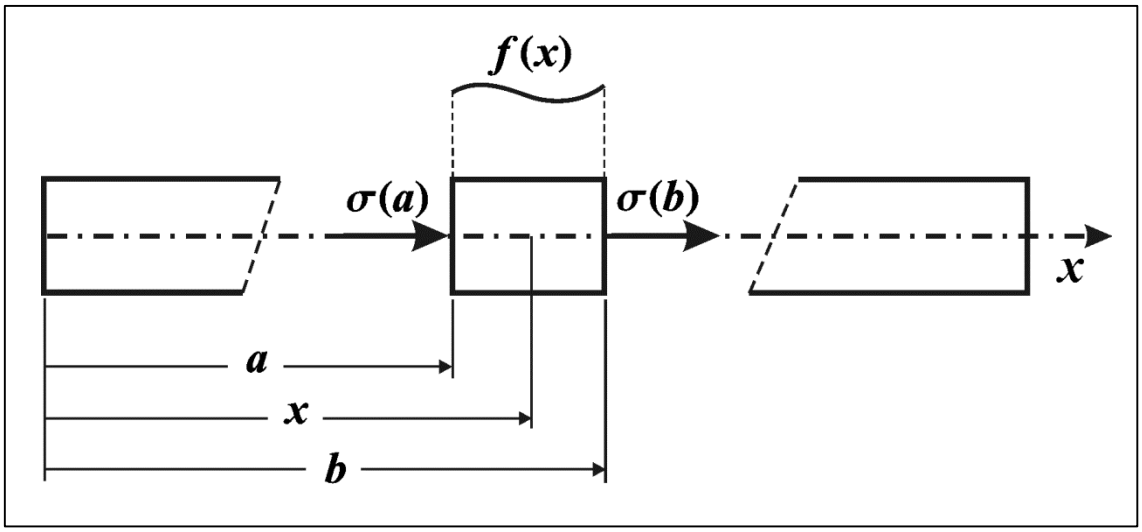

Figure D.8.2 Fluxes on an interior element of the bar shown in figure D.8.1

1.- The flux must be conserved at every point in the body. Consider first a typical point $\bar{x}$ in the interior of a region of smooth data and a region $a \le x \le b$ containing $\bar{x}$, as shown in the Figure D.8.2. The fluxes on the boundaries of this material element are indicated by arrows in the figure and the element also contains internal sources of intensity *f(x)*. The conservation flux states that

$$\sigma(b) - \sigma(a) = \int_a^b f(x)\, dx \qquad \text{(D.8.2)}$$

output - input = generation

2.- To determine the form of this conservation law at the point $\bar{x}$, we take the limit of each side of (D.8.2) as a approaches $\bar{x}$ from the left (written $a \to \bar{x}^-$) and as b approaches $\bar{x}$ from the right ($b \to \bar{x}^+$). Since the source term *f* is bounded, the limit of the integral vanishes and we have

$$\lim_{b \to \bar{x}^+} \sigma(b) - \lim_{a \to \bar{x}^-} \sigma(a) = \lim_{\substack{a \to \bar{x}^- \\ b \to \bar{x}^+}} \int_a^b f(x)\, dx = 0$$

or $$[\![\sigma(\bar{x})]\!] = 0 \qquad \text{(D.8.3)}$$

where

$$[\![\sigma(\bar{x})]\!] = \lim_{b \to \bar{x}^+} \sigma(b) - \lim_{a \to \bar{x}^-} \sigma(a)$$

is the jump in σ at $\bar{x}$. Thus (D.8.3) states that, having no jumps, the flux is continuous at all points inside the smooth subdomains.

3.- Since the integrand *f(x)* in (D.8.2) is continuous, we know from the mean- value theorem of integral calculus that $\int_a^b f(x)dx = (b-a)f(\xi)$, ξ being some point such that $a < \xi < b$ and $f(\xi)$ being the average of *f* over this interval. Thus,

$$\sigma(b) - \sigma(a) = (b-a)f(\xi)$$

Dividing by (b-a) and taking the limit as before, we obtain

$$\lim_{\substack{a \to \bar{x}^- \\ b \to \bar{x}^+}} \frac{\sigma(b) - \sigma(a)}{b-a} = f(\bar{x})$$

Thus, we have for all points *x* in the interior of the smooth regions,

$$\frac{d\sigma(x)}{dx} = f(x) \qquad \text{(D.8.4)}$$

Substitution of the constitutive equation (D.8.1) into (D.8.4) produces a linear second-order differential equation for our boundary-value problem of the form

$$-\frac{d}{dx}\left[k(x)\frac{du(x)}{dx}\right] = f(x) \qquad \text{(D.8.5)}$$

Of course, at points where the material modulus *k(x)* is smooth, (D.8.5) can be expanded to read

$$-k(x)\frac{d^2u(x)}{dx^2} - \frac{dk(x)}{dx}\frac{du(x)}{dx} = f(x) \qquad \text{(D.8.6)}$$

4.- We consider next the points at which some of the data are discontinuous but finite, such as the point $x=x_3$. As in the preceding discussion, the conservation principle requires that the jump in the flux vanishes,

$$[\![\sigma(x\ \ )]\!] = 0 \qquad \text{for } x=x_3$$

Because of the discontinuity in the integrand, we cannot use the mean-value theorem; *ku'* is continuous at x_3 but *(ku')'* is not defined. Hence, we do not have a differential equation at the point $x=x_3$.

At the point $x=x_2$ where *k* is discontinuous, the conservation principle again gives a null jump condition$[\![\sigma(x_2)]\!] = 0$. At this point we easily verify that the differential equation (D.8.4) must be satisfied, but since *k* is not differentiable, we cannot expand (D.8.5) to obtain the form given in (D.8.6).

5.- Next we consider the point x_4 at which the concentrated source is applied

$f = \hat{f}\delta(x - x_4)$. Writing the balance of the flux equation for the region containing $x=x_4$, we have

$$\sigma(b) - \sigma(a) = \int_a^b f(x)\,dx = \int_a^b \bar{f}(x)\,dx + \int_a^b \hat{f}\delta(x - x_4)\,dx \qquad \text{(D.8.7)}$$

where $\bar{f}$ is the smooth part of *f*, and in the last integral we have employed he symbolism for Dirac deltas. Taking the limit as *a* and *b* approaches x_4, we find that the integral of $\bar{f}$ goes to zero while the contribution due to the concentrated source has the constant value of $\hat{f}$, independent of a and b. Thus, we have the non-homogeneous jump condition

$$[\![\sigma(x\ \ )]\!] = \hat{f} \qquad \text{for } x=x_4$$

Since the value of the last integral is independent of *a* and b we cannot obtain a differential equation for $x=x_4$.

6.- Finally, we consider the boundaries of the body, i.e. $x=x_1$ and $x=x_5$. All finite physical system must interact in some way with their surrounding environment, and the effects of this interaction are incorporated prescribing the value of the flux, or the state variable, or a linear combination of both at the boundaries.

When the state variable ***u*** is prescribed, the boundary condition is named essential.

The boundary condition is called natural when the flux or a linear combination of the flux and the state variable is specified at the boundary.

D.9 State-dependent sources and transport terms

For completeness, we note that there are two other terms which may appear in the governing differential equation. First is a term that arises when there is a source in the physical system which is proportional to the state variable. Letting the constant of proportionality be the given function *–b(x)*, the differential equation incorporates the term *b(x)u(x)*.

Second in steady-state transport processes, the domain is viewed as a fixed region of space with material flowing through it. The flux quantity to be conserved is transmitted through the material, as in the discussion above, but also is carried, or convected, through the region of interest by the moving material having a velocity *c(x)*.

The general governing differential equation is then

$$-\frac{d}{dx}\left[k(x)\frac{du(x)}{dx}\right]+c(x)\frac{du(x)}{dx}+b(x)u(x)=f(x) \qquad \text{(D.9.1)}$$

Which must be satisfied at all points where the data are smooth.

D.10 Variational formulation of two-point boundary-value problems

In relation with the figure (D.8.1), consider a general boundary-value problem defined in the interval $0 \le x \le l$ by the system

$$\left.\begin{aligned} &-\frac{d}{dx}\left[k(x)\frac{du(x)}{dx}\right]+c(x)\frac{du(x)}{dx}+b(x)u(x)=f(x) \\ &\text{for points } x \in \boldsymbol{e}_i,\ \text{i=\{1, 2, 3, 4\}} \\ &\left[\!\left[k(x_2)\frac{du(x_2)}{dx}\right]\!\right]=0 \quad \text{flux continuity at } x_2 \\ &\left[\!\left[k(x_3)\frac{du(x_3)}{dx}\right]\!\right]=0 \quad \text{flux continuity at } x_3 \\ &-\left[\!\left[k(x_4)\frac{du(x_4)}{dx}\right]\!\right]=\hat{f} \quad \text{flux discontinuity at } x_4 \\ &\alpha_0\frac{du(0)}{dx}+\beta_0 u(0)=\gamma_0, \qquad \alpha_l\frac{du(l)}{dx}+\beta_l u(l)=\gamma_l \quad \text{boundary conditions} \end{aligned}\right\} \qquad \text{(D.10.1)}$$

wherein the domain [0, *l*] is divided into the four smooth subdomains $\boldsymbol{e}_i$ indicated in the figure.

We construct the residual error function r(x),

$$r(x)=-[k(x)u'(x)]'+c(x)u'(x)+b(x)u(x)-f(x)$$

$$\text{for points } x \in \boldsymbol{e}_i,\ \text{i=\{1, 2, 3, 4\}}$$

multiply *r(x)* by a sufficiently smooth test function $v=\delta u$ defined over the entire interval, $0 \leq x \leq l$, and integrate the first term in the product *rv* by parts over each subdomain. The result over subdomain $\boldsymbol{e}_i$ is of the form

$$\int_{e_i} rv\,dx = -ku'v|_{x_i}^{x_{i+1}} + \int_{e_i} (ku'v' + cu'v + buv)dx - \int_{e_i} fv\,dx \qquad \text{(D.10.2)}$$

for points $x \in \boldsymbol{e}_i$, i={1, 2, 3, 4}

Now, since u is the solution of our problem,

$$\int_{e_i} rv\,dx = 0 \text{ and therefore } \sum_{i=1}^{4} \int_{e_i} rv\,dx = 0 \qquad \text{(D.10.3)}$$

Thus, substituting (D.10.2) into (D.10.3) yields

$$\int_0^l (ku'v' + cu'v + buv)dx + k(0)u'(0)v(0) + [\![k(x_2)u'(x_2)]\!]v(x_2)$$

$$+[\![k(x_3)u'(x_3)]\!]v(x_3) + [\![k(x_4)u'(x_4)]\!]v(x_4) - k(l)u'(l)v(l) = \int_0^l \bar{f}\,v\,dx \qquad \text{(D.10.4)}$$

for all smooth test functions $v=\delta u$. Where $\bar{f}$ is the "smooth part" (i.e., the integrable part) of the source function *f*.

Substituting in (D.10.4) the jump conditions in x_2, x_3 y x_4 shown in (D.10.1) and resolving in for the first derivatives in the boundaries

$$u'(0) = \frac{\gamma_0 - u(0)\beta_0}{\alpha_0} \qquad \text{and} \qquad u'(l) = \frac{\gamma_l - u(l)\beta_l}{\alpha_l}$$

We reduce (D.10.4) to

$$\int_0^l (ku'v' + cu'v + buv)dx$$

$$= \int_0^l \bar{f}\,v\,dx + \hat{f}v(x_4) - \frac{k(0)}{\alpha_0}[\gamma_0 - u(0)\beta_0]v(0)$$

$$+\frac{k(l)}{\alpha_l}[\gamma_l - u(l)\beta_l]v(l) \qquad \text{(D.10.5)}$$

for all admissible test functions $v = \delta u$.

A variational statement of the two-point boundary value problem (D.10.1) now takes on the following form: find a function $\boldsymbol{u}$ such that (D.10.5) holds for all test functions $\boldsymbol{v} = \boldsymbol{\delta u}$ in a suitable class of admissible functions.

This is a rather remarkable result. We have managed to transform the entire system of differential equations, jump conditions, and boundary conditions in (D.10.1) into a single equation in which all the features of the solution and the discontinuous and the discontinuous data are intrinsically present.

The variational problem (D.10.5) characterizes the solution as a function defined over the entire interval, $0 \le x \le l$, rather than piecewise as in (D.10.1). Nevertheless, it is clear that any solution of (D.10.1) is automatically a solution of (D.10.5). That is, the variational statement (D.10.5) always include the classical problem as a special case whenever the solution is sufficiently smooth.

Let us study which is the appropriate space of admissible functions:

1.- By integrating *[(ku')'v]* once by parts, we have produced an integral involving products of the first derivatives of trial functions $\boldsymbol{u}$ and test functions $\boldsymbol{v} = \boldsymbol{\delta u}$. Thus it is sufficient to take *u* and *v* to be members of a class of functions, denoted $\boldsymbol{H^1}$, whose derivatives of order 1 and less are square-integrable over the whole interval *[0,l]*. That is

$$\int_0^l [(v')^2 + v^2]\, dx < \infty. \qquad \text{(D.10.6)}$$

We also encounter frequently the subclass of functions in $\boldsymbol{H^1}$ that vanish at *x=0* and *x=l*. We denote this class by $\boldsymbol{H_0^1}$; that is, *v(x)* is a member of $\boldsymbol{H_0^1}$ if satisfies (D.10.6) and *v(0)=0=v(l)*.

2.-Another useful feature of the variational formulation is that whenever the boundary conditions can be incorporated naturally into an integration-by-parts formula, they are automatically compatible with the differential equation. That is, the problem is well-posed.

3.-Boundary conditions enter variational boundary-value problems in two distinct ways: the essential boundary conditions, which involves the specification of values of the solution function, enter the problem in the definition of the space of admissible functions, whereas the natural boundary conditions, which implies the specification of derivatives of the solution function, appears as explicit terms in the actual form of the variational equation.

To fix ideas, consider as examples the problems

i) $$-u''(x) + u(x) = f(x), \qquad 0 \le x \le l$$
$$u(0) = 0, \quad u(l) = 0$$

ii) $$-u''(x) + u(x) = f(x), \qquad 0 \le x \le l$$
$$u'(0) = \gamma_0, \quad u'(l) = \gamma_l$$

According to (D.10.5), the variational statements of these problems are:

(V-i) Find $\boldsymbol{u}$ in $\boldsymbol{H_0^1}$ such that

$$\int_0^l (u'v' + uv)dx = \int_0^l fv\, dx \quad \text{for all } \boldsymbol{v} = \boldsymbol{\delta u} \in \boldsymbol{H_0^1}$$

that is, when *u* is specified in the boundary then $\delta u=0$ there, and therefore all admissible test function *v* must be null in the boundary, thus restricting the space of admissible functions to H_0^1.

(V-ii) Find $\boldsymbol{u}$ in $\boldsymbol{H^1}$ such that

$$\int_0^l (u'v' + uv)dx = \int_0^l fv\,dx - \boldsymbol{\gamma_0} v(0) + \boldsymbol{\gamma_l} v(l) \qquad \text{for all } \boldsymbol{v} = \boldsymbol{\delta u} \in \boldsymbol{H^1}$$

In this case, the given natural boundary conditions enter as data on the right-hand side of the equation, but no special restrictions is imposed on the general admissible function space H^1 .

4.-To measure the error in the function approximation problems like (D.10.5), two norms are frequently employed:

i) For problems where b(x)>0, the energy norm:

$$\|v\|_E = \left[\int_0^l \left(kv'^2 + bv^2\right)dx\right]^{1/2}$$

ii) The H^1-norm:

$$\|v\|_1 = \left[\int_0^l \left(v'^2 + v^2\right)dx\right]^{1/2}$$

D.11 Galerkin approximations

We identify a finite set of basis functions $\{\emptyset_1, \emptyset_2, \ldots \emptyset_N\}$ in H^1 that define a finite-dimensional subspace of test functions H^h in H^1. We then seek a function $u_h \in H^h$ of the form

$$u_h = \sum_{j=1}^N \alpha_j \emptyset_j(x) \qquad \text{(D.11.1)}$$

Which satisfies the variational problem on H^h. For problem (D.10.5), this procedure leads to the discrete problem

$$\int_0^l \left(ku_h'v_h' + cu_h'v_h + bu_hv_h\right)dx = \int_0^l \bar{f}\, v_h dx + f v_h(x_4)$$

$$-\frac{k(0)}{\alpha_0}[\gamma_0 - u_h(0)\beta_0]v_h(0) + \frac{k(l)}{\alpha_l}[\gamma_l - u(l)\beta_l]v_h(l) \qquad \text{(D.11.2)}$$

for all $v_h = \sum_{i=1}^N \beta_i \emptyset_i \in H^h$

or, equivalently,

$$\sum_{j=1}^N K_{ij}\alpha_j = F_i, \quad i = 1,2, \ldots N \qquad \text{(D.11.3)}$$

where K_{ij} is the stiffness matrix

$$K_{ij} = \int_0^l \left(k\emptyset_j'\emptyset_i' + c\emptyset_j'\emptyset_i + b\emptyset_j\emptyset_i\right)dx - \frac{k(0)\beta_0}{\alpha_0}\emptyset_j(0)\emptyset_i(0) + \frac{k(l)\beta_l}{\alpha_l}\emptyset_j(l)\emptyset_i(l) \qquad \text{(D.11.4)}$$

And the components of load vector are

$$F_i = \int_0^l \bar{f}\emptyset_i dx + \hat{f}\emptyset_i(x_4) - \frac{k(0)}{\alpha_0}\gamma_0\emptyset_i(0) + \frac{k(l)}{\alpha_l}\gamma_l\emptyset_i(l) \qquad \text{(D.11.5)}$$

with $1 \le i, j \le N$.

Solving (D.11.3) for the coefficients α_j, our Galerkin approximation of the problem is obtained immediately from (D.11.1). We note that the stiffness matrix $\mathbf{K_{ij}}$ is not symmetric whenever the coefficient $\boldsymbol{c}$ in (D.11.4) is not identically zero.

D.12 Finite element approximations

D.12.1.-Partitioning the domain and selection of shape functions

We will assume, for definiteness, that the domain of our problem is composed of four natural smooth subdomains indicated in Figure D.8.1. Suppose that the concentrated source term in *f* shown in this figure is located at the coordinate $x = \bar{x} = x_4$. Then the flux $\sigma = -ku'$ will experience a jump $[\![\sigma]\!] = \hat{f}$at x_4. However, our element shape functions will always have the property that their derivatives are continuous within each element, and, therefore, they cannot accommodate a jump such as this. For this reason, we will always construct our mesh so that a nodal point is located at all points of discontinuity of the data. Then terms such as $\hat{\boldsymbol{f}}\boldsymbol{v_h}(\bar{\boldsymbol{x}})$ representing prescribed jumps will never enter in the local equations which characterize the approximation over individual elements. These terms enter in the analysis when the contributions over individual elements are summed in the assembling process.

For simplicity we will employ linear functions as shape functions, on a typical element.

D.12.2.-Calculation of Element Matrices and Equations

Having selected an appropriate set of shape functions, we calculate the local approximation of the problem over each element, and the element statements are patched together (assembled) to form the final approximation of the problem. Let us see how this is done.

For any typical smooth subdomain $\boldsymbol{e_i}$, between points s_1^e and s_2^e, we have for all admissible functions v_1^e,

$$\int_{s_1^e}^{s_2^e}(ku_h^{e\prime}v_h^{e\prime} + cu_h^{e\prime}v_h^e + bu_h^e v_h^e)dx = \int_{s_1}^{s_2}\bar{f}v_h^e dx + \boldsymbol{\sigma}(\boldsymbol{s_1^e})v(s_1^e) - \boldsymbol{\sigma}(\boldsymbol{s_2^e})v(s_2^e) \quad \text{(D.12.2.1)}$$

where $\boldsymbol{\sigma}(s_i^e)$ are the true values of the flux at the interval end points s_i^e, *i=1,2*, and not their approximations, thus appearing as given natural boundary data in the right-hand side of this equation. Note also that, unlike (D.11.5), no point-source terms such as $\hat{f}v_h^e(\bar{x})$ appear in (D.12.2.1) because our decision to locate end nodal points of elements at these points. Only in the assembly process will be taken into account these source terms.

Note that in (D.12.2.1) u_h^e is defined in terms of the shape functions ψ_j^e for this element, and the nodal values $\{u_1^e, u_2^e\}$ corresponding at nodes $\{x_1^e, x_2^e\}$ of the element, as follows

$$u_h^e(x) = \sum_{j=1}^{2} u_j^e \psi_j^e(x) \quad \text{(D.12.2.2)}$$

where N_e =2 is the number of nodes in the element $\boldsymbol{e}$, and

$$u_j^e = u_h^e(x_j^e), \quad j = 1, 2 \quad \text{(D.12.2.3)}$$

Upon substituting (D.12.2.2) into (D.12.2.1) and taking $v_h^e = \delta u_h^e = \psi_j^e$, we arrive at a system of linear equations of the form

$$\sum_{j=1}^{2} k_{ij}^e u_j^e = f_i^e + \sigma(s_1^e)\psi_i^e(s_1^e) - \sigma(s_2^e)\psi_i^e(s_2^e), \quad i=1, 2 \qquad \text{(D.12.2.4)}$$

where k_{ij}^e are the entries in the element stiffness matrix and f_i^e are the components of the element load vector, defined as

$$k_{ij}^e = \int_{s_1^e}^{s_2^e} \left(k\psi_i^{e\prime}\psi_j^{e\prime} + c\psi_i^{e\prime}\psi_j^e + b\psi_i^e\psi_j^e \right) dx$$

$$i, j=1, 2 \qquad \text{(D.12.2.5)}$$

$$f_i^e = \int_{s_1^e}^{s_2^e} \bar{f}\psi_i^e dx$$

In actual finite element calculations, the integral in (D.12.2.5)

are rarely evaluated in closed form. Instead, the entries k_{ij}^e are generally computed using numerical integration rules. Also, it is common practice to calculate f_i^e using the interpolant of *f* rather than *f* itself; for example, if $\bar{f}$ is the continuous part of *f* (excluding concentrated point sources) and if

$$f_h^e(x) = \sum_{i=1}^{2} \bar{f}(x_i^e)\psi_i^e(x)$$

Then, instead of the formula in (D.12.2.5), we use

$$f_i^e = \int_{s_1^e}^{s_2^e} f_h^e \psi_i^e dx \qquad \text{(D.12.2.6)}$$

In this way we can define the data *f* in our approximation by only specifying its values at the nodal points.

D.12.3 Element assembly

Having calculated the matrices and equations describing our approximation over each finite element, the next step in our analysis is to assemble the equations describing the approximation of the entire mesh by adding up the contributions to these equations furnished by each element.

To fix ideas, consider the special case in which linear shape functions are used. Each element then has two nodes, and therefore there are two equations per element of the following form:

$$\left.\begin{aligned} k_{11}^e u_1^e + k_{12}^e u_2^e &= f_1^e + \sigma(s_1^e) \\ k_{21}^e u_1^e + k_{22}^e u_2^e &= f_2^e - \sigma(s_2^e) \end{aligned}\right\} \qquad \text{(D.12.3.1)}$$

Here the subscripts 1 and 2 are labels of the end point nodes on a typical element and $\sigma(s_1^e)$ and $\sigma(s_2^e)$ represent the actual values of the flux $\sigma = -ku'$ at the nodes. Of course, these subscripts are

to be relabeled upon assembling the elements so as to coincide with appropriate node numbers in the final mesh. For example, if the element is to fit between nodes 6 and 7 in a mesh, u_1^e in (D.12.3.1) is actually u_6, u_2^e is u_7, $\sigma(s_1^e)$ is the value of *–ku'* as the node at x_6 is approached from the right, and $\sigma(s_2^e)$ is *–ku'* as the node at x_7 is approached from the left.

We now assemble the equations describing the entire collection of elements comprising our mesh by sweeping through all elements, one at time, and using (D.12.3.1) to calculate the contributions of each of them. Consider, for example, a mesh containing *N-1* elements and *N* nodes, numbered consecutively, as shown in Figure D.8.1. This means that there results N equations in N degrees of freedom describing the assembled system of elements, and we must allocate space in the computer for a system of this size. Thus we anticipate calculating an *NxN* stiffness matrix $K=[K_{ij}]$ and *Nx1* load vector $F=\{F_{ij}\}$.

We initiate the assembly process by setting $K_{ij}=0$ and $F_i=0$. For element $\boldsymbol{e_1}$, between nodes *1* and *2*, (D.12.3.1) yields the equations

$$\left.\begin{aligned} k_{11}^1 u_1 + k_{12}^1 u_2 &= f_1^1 + \sigma(x_1^+) \\ k_{21}^1 u_1 + k_{22}^1 u_2 &= f_2^1 - \sigma(x_2^-) \end{aligned}\right\} \quad \text{Element 1}$$

where $\sigma(x_1^+)$ is the flux at node 1 as this node is approached from the right and $\sigma(x_2^-)$ is the flux at node *2* as this node is approached from the left. These equations are added into the first and second rows of the *NxN* system describing the entire mesh.

We next go to element $\boldsymbol{e_2}$. Since it lies between nodes *2* and *3*, its contributions, calculated using (D.12.3.1), are added to the equations in rows *2* and *3*. Since two elements and three nodes have been "activated", we now have the three equations,

$k_{11}^1 u_1 + k_{12}^1 u_2 = f_1^1 + \sigma(x_1^+)$	Element 1
$k_{21}^1 u_1 + (k_{22}^1 + k_{11}^2) u_2 + k_{12}^2 u_3 = f_2^1 + f_1^2 - \sigma(x_2^-) + \sigma(x_2^+)$	and
$k_{21}^2 u_2 + k_{22}^2 u_3 = f_2^2 - \sigma(x_3^-)$	Element 2

Continuing this process through the entire system of *N* elements, we arrive at the system

$$\begin{aligned} k_{11}^1 u_1 + k_{12}^1 u_2 &= f_1^1 + \sigma(x_1^+) \\ k_{21}^1 u_1 + (k_{22}^1 + k_{11}^2) u_2 + k_{12}^2 u_3 &= f_2^1 + f_1^2 + [\![\sigma(x_2)]\!] \end{aligned}$$

$$k_{21}^2 u_2 + \left(k_{22}^2 + k_{11}^3\right)u_3 + k_{12}^3 u_4 = f_2^2 + f_1^3 + [\![\sigma(x_3)]\!] \qquad \text{D.12.3.2)}$$

$$k_{21}^3 u_3 + k_{22}^3 u_4 = f_2^3 - \sigma(x_4^-)$$

Wherein $[\![\sigma(x_j)]\!]$ denotes the jump in σ at node j:

$$[\![\sigma(x_j)]\!] = \sigma(x_j^+) - \sigma(x_j^-), \quad j=2,3,\ldots,N-1 \qquad \text{(D.12.3.3)}$$

Recall that $[\![\sigma(x)]\!]=0$ at all interior points at which the flux is continuous. If there are no point sources in the data *f* located at interior nodes, all of the interior jump terms in (D.12.3.2) must be zero and only the values of σ at the boundaries remain. If, however, a

Point source $\hat{f}_j\delta(x-x_j)$ is prescribed at any interior node x_j, then we must set

$$[\![\sigma(x_j)]\!] = \hat{f}_j$$

in (D.12.3.2). In our previous example, a point source $\hat{f}_j\delta(x-\bar{x})$ is located at point $\bar{x}=x_4$. Then the linear system of equations for the entire mesh assumes the form

$$\begin{bmatrix} k_{11}^1 & k_{12}^1 & 0 & 0 & 0 \\ k_{21}^1 & k_{22}^1+k_{11}^2 & k_{12}^2 & 0 & 0 \\ 0 & k_{21}^2 & k_{22}^2+k_{11}^3 & k_{12}^3 & 0 \\ 0 & 0 & k_{21}^3 & k_{22}^3+k_{11}^4 & k_{12}^4 \\ 0 & 0 & 0 & k_{21}^4 & k_{22}^4 \end{bmatrix} \begin{bmatrix} u_1 \\ u_2 \\ u_3 \\ u_4 \\ u_5 \end{bmatrix} = \begin{bmatrix} \tilde{F}_1 \\ F_2 \\ F_3 \\ F_4 \\ \tilde{F}_5 \end{bmatrix} \qquad \text{(D.12.3.4)}$$

where

$$\begin{bmatrix} \tilde{F}_1 \\ F_2 \\ F_3 \\ F_4 \\ \tilde{F}_5 \end{bmatrix} = \begin{bmatrix} f_1^1 + \sigma(x_1^+) \\ f_2^1 + f_1^2 \\ f_2^2 + f_1^3 \\ f_2^3 + f_1^4 + \hat{f} \\ f_2^4 - \sigma(x_5^-) \end{bmatrix} \qquad \text{(D.12.3.5)}$$

D.12.4 Boundary conditions

Up to this point no boundary conditions have been applied. Thus (D.12.3.4) is applicable to a wide range of boundary conditions. We consider the following cases:

1. **General Natural Boundary Conditions:** These correspond to the general case in which a linear combination of ***u*** and ***u'*** are prescribed:

$$\alpha_0 u'(0) + \beta_0 u(0) = \gamma_0\,, \quad \alpha_l u'(l) + \beta_l u(l) = \gamma_l \qquad \text{(D.12.4.1)}$$

In our approximation of this case, we solve for ***u'***

$$u_h'(0) = \frac{\gamma_0}{\alpha_0} - \frac{\beta_0}{\alpha_0} u_h(0) \text{ and } u_h'(l) = \frac{\gamma_l}{\alpha_l} - \frac{\beta_l}{\alpha_l} u_h(l) \qquad \text{(D.12.4.2)}$$

where $u_h(0)=u_1$ and $u_h(l)=u_5$. Then, remembering that the flux $\sigma = -ku'$, (D.12.3.4) reduces to

$$\begin{bmatrix} k_{11}^1 - \frac{k(0)\beta_0}{\alpha_0} & K_{12} & 0 & 0 & 0 \\ K_{21} & K_{22} & K_{23} & 0 & 0 \\ 0 & K_{32} & K_{33} & K_{34} & 0 \\ 0 & 0 & K_{43} & K_{44} & K_{45} \\ 0 & 0 & 0 & K_{54} & k_{22}^4 + \frac{k(l)\beta_l}{\alpha_l} \end{bmatrix} \begin{bmatrix} u_1 \\ u_2 \\ u_3 \\ u_4 \\ u_5 \end{bmatrix} = \begin{bmatrix} f_1^1 - \frac{k(0)\gamma_0}{\alpha_0} \\ f_2^1 + f_1^2 \\ f_2^2 + f_1^3 \\ f_2^3 + f_1^4 + \hat{\boldsymbol{f}} \\ f_2^4 - \frac{k(l)\gamma_l}{\alpha_l} \end{bmatrix} \qquad \text{(D.12.4.3)}$$

If the final stiffness matrix in (D.12.4.3) is invertible, we can solve for the unknown nodal values. Other features of the approximation, such as the approximate flux $\sigma_h = -ku'_h$, can then be easily evaluated.

2. Dirichlet Boundary Conditions:

Boundary conditions of the type

$$u(0) = \frac{\gamma_0}{\beta_0}\,, \quad u(l) = \frac{\gamma_l}{\beta_l} \qquad \text{(D.12.4.4)}$$

are a special case of (D.12.4.1) when $\alpha_0 = \alpha_l = 0$. Essential boundary conditions of this form are usually called Dirichlet boundary conditions.
In this case, $u_h(0) = u_1 = \frac{\gamma_0}{\beta_0}$ and $u_h(l) = u_5 = \frac{\gamma_l}{\beta_l}$, so that only N-2 unknown nodal values $\{u_2, u_3, u_4\}$ remain. Then (D.12.3.4) reduces to the (N-2)x(N-2) system

$$\begin{bmatrix} K_{22} & K_{23} & 0 & 0 \\ K_{32} & K_{33} & K_{34} & 0 \\ 0 & K_{43} & K_{44} & K_{45} \end{bmatrix} \begin{bmatrix} u_2 \\ u_3 \\ u_4 \end{bmatrix} = \begin{bmatrix} f_2^1 + f_1^2 - \frac{K_{21}\gamma_0}{\beta_0} \\ f_2^2 + f_1^3 \\ f_2^3 + f_1^4 + \hat{\boldsymbol{f}} - \frac{K_{45}\gamma_l}{\beta_l} \end{bmatrix} \qquad \text{(D.12.4.5)}$$

And the two auxiliary equations corresponding to nodes 1 and N,

$$\left.\begin{aligned} K_{11}\left(\frac{\gamma_0}{\beta_0}\right) + K_{12}\boldsymbol{u_2} &= f_1^1 + \boldsymbol{\sigma}(0) \\ K_{54}\boldsymbol{u_4} + K_{55}\left(\frac{\gamma_l}{\beta_l}\right) &= f_2^4 - \boldsymbol{\sigma}(l) \end{aligned}\right\} \qquad \text{(D.12.4.6)}$$

The reduced system (D.12.4.5) can be solved for the unknown nodal values {u_2, u_3, u_4}. Once {$\mathbf{u_2}$, $\mathbf{u_4}$} are known, the approximations of the end point fluxes { $\boldsymbol{\sigma}(0), \boldsymbol{\sigma}(l)$} can be computed directly using the auxiliary equations (D.12.4.6)

3. Neumann Boundary Conditions:

When only the derivative of u is specified at each end, (D.12.4.1) reduces to

$$u'(0) = \frac{\gamma_0}{\alpha_0}\ ,\ \ u'(l) = \frac{\gamma_l}{\alpha_l} \qquad \text{(D.12.4.7)}$$

Whenever $\beta_0 = \beta_l = 0$. Natural boundary conditions of this type are called Neumann boundary conditions. This kind of problem frequently requires some special consideration for certain forms of the governing differential equation (D.12.4.2). In particular, consider the case in which the coefficients *c(x)* and *b(x)* are identically zero so that the boundary–value problem becomes one of solving the differential equation

$$-\big(k(x)u'(x)\big)' = f(x) \qquad \text{(D.12.4.8)}$$

subject to the end conditions (D.12.4.7). In this case, the solution $\boldsymbol{u}$ is determined only to within an arbitrary constant $\boldsymbol{c_0}$; that is u+ $\boldsymbol{c_0}$ is also a solution. Because of the analogy of this problem with equations describing mechanical systems, the constant $\boldsymbol{c_0}$ is sometimes referred to as a rigid motion, and this rigid motion must be specified if we are to obtain a unique solution to our problem. Moreover, the finite element approximation (D.12.3.4) of this Neumann problem will also contain an arbitrary rigid motion. Since solutions to (D.12.3.4) will then be non-unique, the stiffness matrix will necessarily singular.

The presence of a rigid motion in the solution to a Neumann problem leads to another consideration of fundamental importance: the data *f*, α_0, α_l, γ_0, γ_l, cannot be specified arbitrarily, they must be *compatible* in a sense we will now make clear. Since the variational form of this Neumann problem (with c,b ≡ 0) is to find $u \in H^1$ such that

$$\int_0^l ku'v'dx = \int_0^l \bar{f}vdx + \hat{f}v(\bar{x}) - k(0)\left(\frac{\gamma_0}{\alpha_0}\right)v(0) + k(l)\left(\frac{\gamma_l}{\alpha_l}\right)v(l) \qquad \text{(D.12.3.9)}$$

for all $v \in H^1$. Since $u=c_0=constant$ is a solution, this equation must also hold for $u=c_0$ and the choice $v=1$. Hence, the data must be such that

$$\int_0^l \bar{f}dx + \hat{f} - k(0)\left(\frac{\gamma_0}{\alpha_0}\right) + k(l)\left(\frac{\gamma_l}{\alpha_l}\right) = 0 \qquad \text{(D.12.3.10)}$$

The compatibility condition (D.12.4.10) is a necessary condition for the existence of a solution to (D.12.4.9). We remark that from a physical viewpoint, (D.12.4.10) is a global conservation law; it reflects the requirement that the flux σ be conserved over the entire body.

For the discrete problem corresponding to (D.12.4.9), this compatibility condition assumes the form (see (D.12.3.5))

$$\tilde{F}_1 + \sum_{i=2}^{N-1} F_i + \tilde{F}_N = 0 \qquad \text{(D.12.4.11)}$$

To eliminate the rigid motion, we can specify the value of u_j at any node j equal to an arbitrary constant c_0. For instance, setting $u_1=c_0$ in (D.12.4.5).

4. Mixed Boundary Conditions:

When an essential boundary condition is applied at one boundary point and a natural boundary condition at the other, a mixed boundary-value problem for the function $\boldsymbol{u}$ is obtained. For example, one mixed problem is characterized by the end conditions

$$u(0) = \frac{\gamma_0}{\beta_0}, \qquad u'(l) = \frac{\gamma_l}{\alpha_l} \qquad \text{(D.12.4.12)}$$

and another by

$$\alpha_0 u'(0) + \beta_0 u(0) = \gamma_0, \qquad u(l) = \frac{\gamma_l}{\beta_l} \qquad \text{(D.12.4.13)}$$

Since at least one of these conditions specifies the value of $\boldsymbol{u}$ at an endpoint, the solution will contain no rigid motions.

Appendix E

Publications

E.1 International Journals

1. Jose Sánchez-Dehesa, Mitko Angelov, Francisco Cervera, Liang-Wu Cai. S*ound control by temperature gradients*, Applied Physic Letters, 95, (20), 204102, 2009

2. Jose Sánchez-Dehesa, Mitko Angelov, Francisco Cervera, Liang-Wu Cai. S*ound control by temperature gradients*, The Journal of the Acoustical Society of America, 127, (3),2014, 2010

E.2 International Meetings and Conferences

1. Mitko Angelov, Daniel Torrent, Francisco Cervera, José Sánchez-Dehesa, *Pendellosung phenomenon in two-dimensional sonic crystals,* Acoustics '08, Paris, 2008.

2. Liang-Wu Cai, Mitko Angelov, Francisco Cervera, José Sánchez-Dehesa, *Focusing of airborne sound by heated wires,* ASME International Mechanical Engineering Congress and Exposition, Boston, 2008

Bibliography

[Abr65] Abramovitz, M., Stegun, I., *Handbook of Mathematical Functions*, Dover, New York, 1965

[ASTM] Standards E 1137 for Industrial Platinum Resistance Thermometers

[Bas80] Bass, H.E., Absorption of Sound by Air: High Temperature Predictions *J. Acoust. Soc.Am.* 69(1), 124-138 (1980)

[Bec81] Becker. E., Carey, G., Oden, J., *Finite Elements. An Introduction*, Prentice-Hall, Inc, Englewood Cliffs, New Jersey, 1982

[Bej93] Bejan, A., *Heat Transfer*. John Wiley & Sons, New York, 1993

[Ber86] Beranek, L.L. *Acoustics.* Acoustical Society of America, New York, 1986

[Bey69] Beyer, R.T., S.V.Letcher, *Physical Ultrsonics*, Academic, New York, 1969

[Bha57] Bhatia, A.B. Sound and Ultrasound Absorption Resulting from Heat Radiation, *J. Acoust. Soc.Am*. 29(7), 823-824 (1957)

[Bha05] Bhatti,A. *Fundamental Finite Element Analysis and Applications* New Jersey, John Wiley&Sons, 2005

[Bog93] Bogen, S.D., Hinders, M.K.,*Dynamics stress concentration in fiber-reinforced composites with interface layers*, J.Compos. Mater. **27**, 1272-1311, 1993.

[Bog94] Bogen, S.D., Hinders, M.K., *Interface Effect in Elastic Wave Scattering*, Springer, Berlin, 1994

[Cai04a] Cai, L.-W. Scattering of antiplane shear waves by layered circular elastic cylinder, *J. Acoust. Soc.Am.* 115(3), 515-522., 2004

[Cai04b] Cai, L.-W. Multiple scattering in single scatterer, *J. Acoust. Soc.Am.* 115(3), 986-995, 2004

[Cai05] Cai, L.-W. Scattering of elastic anti-plane shear wave by multilayered eccentric scatterers, *Quart. J. Mech. Appl. Math*. 25 (2), 165 – 183, 2005

[Cai07] Cai, L.-W. and J. Sánchez-Dehesa, Microlens array for focusing airborne ultrasound using heated wire grid, *Appl. Phys. Lett.* 91, 181915, 2007

[Cai99] Cai, L.W. and J.H.Williams, Jr., Large-scale multiple scattering problems *Ultrasonics* 37, 453-462 (1999).

[Car59] Carslaw, H.S. and J.C.Jaeger, *Conduction of Heat in Solids*, 2nd ed. Oxford University Press, Oxford, 1959

[Cer01] Cervera, F., L. Sanchis, J.V. Sanchez-Perez, R. Martinez-Sala, C. Rubio, F. Meseguer, C. Lopez, D. Cabalero and J. Sanchez-Dehesa, "Refractive acoustic Devices for Airborne Sound", Phys. Rev. Lett. 88, 023902 (2001).

[Cli10] Climente, A., Torrent, D., Sánchez-Dehesa, J., Sound focusing by gradient-index sonic lenses, *Applied Physics letters,* **97**, 104103, 2010

[Coc96] Cocis, S. and Z.Figura, *Ultrasonic Measurements and Technologies*, 1-st ed. Chapman & Hall and Ister Science Limited, London, 1996

[Cro98] Crocker, M.J., *Handbook of Acoustics* John Wiley&Sons, Canada

[Dow92] Dowling, J. Sonic band structure in fluids with periodicity density variations, *J. Acoustic Soc. Am.,* 91 2539-2543, 1992

[Gar12] Garcia-Chocano, V.M., Torrent, D. Sánchez-Dehesa, J., Reduced acoustic cloaks based on temperature gradients, *Appl. Phys.Lett., **101** 084102, (2012)*

[Gha09] Ghatak, A., *Optics*, 4th edition, Tata McGraw-Hill, New Delhi, 2009

[Hal01] Hallaj, I. M., R.O. Cleveland, K. Hynynen, Simulations of the thermo-acoustic lens effect during focused ultrasound surgery, *J. Acoust. Soc.Am.* 109(5), 2245-2253 (2001)

[Ime08] IMECE2008-69219 - ASME international Mechanical Engineering Cingress and Exposition, November 5-10, 2008, Boston, Ma, USA

[Inc96] Incropera, P.F., David P. D., *Fundamentals of Heat and Mass Transfer*, 4th Edition, School of Mechanical Engineering, Purdue University, USA, 1996

[Inh98] Inhlenburg, F., *Finite Element Analysis of Acoustic Scattering,* Springer-Verlag, New York, 1998

[ITS90]International Temperature Standard 90.

[Kak79] Kak, A.C. Computerized tomography with x-ray, emission, and ultrasound sources. *Proceeding of the IEEE,* 67:1245-1272, 1979.

[Kak99] Kak, A.C., Slaney, M., *Principles of computerized topographic imaging.* IEEE Press, New York, 1999.

[Khe04] Khelif, A., Choujaa, A., Benchabane, S., Laude, V. Guiding and filtering acoustic waves in a two-dimensional phononic crystal, *IEEE Ultrasonics Symposium,* pages 654-567, 2004

[Kin00] Kinsler *Fundamentals of Acoustics.* 4th Ed, Wiley, 2000

[Kit56] Kittel, Ch. *Introduction to Solid State Physics*, John Wiley & Sons, New York, 1956

[Kut91] Kuttruf, H., *Ultrasonics*, Elsevier Science Publishers Ltd, New York, 1991

[Lan36] Landau, L.D., Teller E., Zur Theorie der Schalldispersion , *Phys. Z. Sowjet-Union, Vol.*10, 1936

[Lan87] Landau, L.D., Lifshitz, E.M., *Fluid mechanics*, Pergamon Press, Oxford,1987.

[Lau15] Laude, V., *Phononic Crystals: Artificial Crystals for Sonic, Acoustic, and Elastic Waves.*, Walter de Gruyter, Berlin/Boston, 2015.

[Lin09] Lin, S.-Ch., Huang, T.J., Sun, J.H., Wu, T.-T., Gradient-index phononic crystals, *Physical review B*, **79**, 094302.

[Lin12] Lin, S.-Ch., *Acoustic metamaterials*, Lap Lambert Academic Publishing, Saarbrüken, 2012

[Lor03] Lorenzo Martínez, *Diseño y Caracterización de Dispositivos Basados en Cristales Acústicos/Fotónicos: Aplicación de la teoría de Dispersión Múltiple y de los Algoritmos Genéricos* – Tesis Doctoral, Departamento de Física Teórica de la Materia Condensada, Facultad de Ciencias, Universidad Autónoma da Madrid

[Mal94] Mal A.K., Yang R.-B. The influence of fiber-matrix interfacial layer properties on wave characteristics in metal matrix composites, *Review of Progress in Quantitative Nondestructive Evaluation*, vol. 13B, pp. 1453-1460, 1994

[Mey72] Meyer, E., Neumann, E.,*Physical and Applied Acoustics*, Academic, New York, 1972

[Mor86] Morse, P.M., Ingard, K.U., *Theoretical Acoustics*, Princeton Univ. Press, 1986

[Nyb81] Nyborg, W.L. Heat Generation by Ultrasound in a Relaxing Medium, *J. Acoust. Soc.Am*. 70(2), 310-312 (1981)

[Raj04] Raj, B., V.Rajendran, P. Palanichamy, *Science and Technology of ultrasonics* Pangbourn, Alpha Science Internacional, 2004

[Rec00] Recuero, M. *Ingeniería acústica*, Paraninfo, Madrid, 2000

[Rom13] Romero-Garcia, V., Cebrecos, A., Picó, R., Sánchez-Morcillo, V.J., García-Raffi, L.M., Sánchez-Pérez, J.V., Wave focusing using symmetry matching in axisymmetric acoustic gradient index lenses, *Appl. Phys.Lett,**103**264106 (2013)* .

[San01] Sanchis L., Cervera, F. Reflectance properties of two-dimensional sonic band-gap crystals., *J. Acoust. Soc.Am.*, 109 2598-2605, 2001

[San98] Sanchez-Perez, J., Caballero, D., Martinez-Sala, R., Rubio, C. Sanchez-Dehesa, J., Meseguer, F., Linares, J. Galvez, F. Sound attenuation by a two-dimensional array of rigid cylinders, *Phys.Rev.Lett.*, 80 5325-5328, 1998

[Sán03] Sánchez-Dehesa, J., Cervera, F., Häkansson, A., Sanchis, L., Acoustic interferometers based on two-dimensional arrays of rigid cylinders in air, Physical review B **67**, 035422, 2003

[Sch79] Schlichting, H., *Boundary Layer Theory*, 7th ed., Mc-Graw-Hill, New York, 1979

[Shi96] Shindo, Y., Niwa, N. Scattering od antiplane shear wave in a fiber-reforced composite medium with interfacial layers, *Acta Mech.* **117**, 181-190, 1996

[Sin93] Sinclair, A.N., Addison, R.C.,Jr. Acoustic diffraction spectrum of a SiC fiber in a solid elastic medium, *J. Acoust. Soc. Am*, **94**, 1126 - 1135, 1993

[Tor07] Torrent, D. and Sánchez-Dehesa J. Acoustic metamaterials for new two-dimensional sonic devices, *New Journal of Physics* 9 (2007) 323

[Tow88] Towne, D.H., *Wave Phenomena*. General Publishing Company, Toronto, 198

[Woo41] Wood, A.B. *A textbook of Sound* MacMilian, New York, 1941

[Yim95a] Yim, H., Williams, J.H., Jr. Formulation and its energy balance verification for ultrasonic nondestructive characterization of a single fiber composite interphase, *Ultrasonics **33**, 377-387.*

[Yim95b] Yim, H., Williams, J.H., Jr. Database generation and parametric study for ultrasonic nondestructive characterization of a single fiber composite interphase, *Ultrasonics **33**, 389-401*.